Numerical analysis of surface Rayleigh wave interaction with seismic barriers and pile fields accounting elastic-plastic soil behaviour

Aleksandr Dudchenko

Communauté UNIVERSITÉ Grenoble Alpes

MOSCOW STATE (NATIONAL RESEARCH) UNIVERSITY OF CIVIL ENGINEERING

THÈSE

Pour obtenir le grade de

DOCTEUR DE LA COMMUNAUTE UNIVERSITE GRENOBLE ALPES

préparée dans le cadre d'une cotutelle *entre la Communauté Université Grenoble Alpes* et *Université d'Etat de génie civil de Moscou*

Spécialité : **2MGE : Matériaux, Mécanique, Génie civil, Electrochimie**
Arrêté ministériel : 25 mai 2016
Présentée par

Dudchenko Aleksandr

Thèse dirigée par **Daniel DIAS** , Professeur, UGA
et codirigée par **Sergey KUZNETSOV** , Professeur, IPMech RAS

préparée au sein du **Laboratoire Sols, Solides, Structures et Risques**
dans **l'École Doctorale I-MEP2 - Ingénierie - Matériaux, Mécanique, Environnement, Energétique, Procédés, Production**

Analyse numérique de l'interaction des ondes de Rayleigh en surface avec des barrières sismiques et des champs de pieux prenant en compte le comportement élastoplastique du sol.

Numerical analysis of surface Rayleigh wave interaction with seismic barriers and pile fields accounting elastic-plastic soil behaviour.

Thèse soutenue publiquement le **20/12/2018**
devant le jury composé de :

Monsieur Marwan SADEK
Professeur Université Libanaise à Beyrouth (Liban), Président, Rapporteur
Monsieur Jean-François SEMBLAT
Professeur, IMSIA - Institut des Sciences de la Mécanique et Applications Industrielles, Rapporteur
Monsieur Stéphane BRULE
Directeur d'agence Entreprise Menard et Docteur de Aix Marseille Université, Examinateur
Monsieur Christophe DANO
Maître de Conférences, Polytech Grenoble et Laboratoire 3SR, Examinateur
Monsieur Daniel DIAS
Professeur, Communauté Université Grenoble Alpes, Directeur de thèse
Monsieur Sergey KUZNETSOV
Professeur, Institute for Problems in Mechanics RAS, Co-directeur de thèse

Abstract

The present work is focused on numerical simulation (FEM) and analysis of surface Rayleigh wave interaction with vertical seismic barriers (underground walls, screens, trenches, etc.) as well as pile fields within the framework of linear elastic and plastic mechanical material models. The aim of the research is to estimate the degree of protection that vertical barriers and pile fields provide against vibrations transferred by surface Rayleigh waves and generated by various sources. The main idea behind this type of protection is to prevent seismic waves form transmitting wave energy into the protected zone decreasing the amplitude of displacements, velocities and accelerations at the points behind the barrier (pile field). The attention is paid to Rayleigh waves as they can be generated by both external (located on the Earth's surface) and internal (located beneath the Earth's surface) vibration sources and this type of waves can transfer a significant portion of vibration source energy.

First, numerical simulations of Rayleigh wave interaction with vertical seismic barriers and pile fields are performed assuming soil and barrier materials to behave according to the linearly-elastic constitutive law. This regards the vibrations that induce shear strains in the soil not exceeding 10^{-5} during their propagation. Based on this, the principal dimensionless complexes are formulated. Geometrical along with mechanical parameters of the barrier (pile field), that determine vibration reduction effect, are identified. The obtained results reveal the validity of this way of vibration protection. In addition to that, the approach towards vertical seismic barrier optimization (which can also be extended to the pile field) is adopted in finite difference form to use for particular soil conditions and design vibration frequency.

Several models of soil behaviour are analysed and their validity as well the applicability to approximate real dynamic soil behaviour along with the mechanism of vibration energy dissipation are identified. Based on this analysis, Mohr-Coulomb constitutive model is selected as it has a broad experimental database for various soils and appropriately reflects shear modulus reduction with an increase in the shear strain as well as energy dissipation effects. Afterwards, this model is used in the analysis of Rayleigh wave interaction with the vertical barriers and pile fields accounting for non-linear character of soil deformation at different shear strain level. As a result, the influence of shear strain level on the effectiveness of the considered ways of vibration protections is shown and the appropriate conditions to use these methods are identified within the scope of this research.

Keywords:Numerical simulation; vibration; ground vibration, vibration isolation; Rayleigh wave scattering; seismic protection; vibration mitigation; vertical seismic barrier; pile wave barrier.

Résumé

Le travail présent est axé sur la simulation numérique et l'analyse de l'interaction des ondes de surface de Rayleigh avec des barrières sismiques verticales (murs souterrains, écrans, tranchées, etc.) ainsi que des champs de pieux dans des modèles de matériaux mécaniques élastiques et plastiques linéaires. Le but de la recherche est d'estimer le degré de protection que les barrières verticales et les champs de pieux fournissent contre les vibrations transférées par les ondes de surface de Rayleigh et générées par diverses sources. L'idée principale de ce type de protection est d'éviter que les ondes sismiques ne transmettent l'énergie des vagues dans la zone protégée, diminuant les amplitudes des déplacements, les vitesses et les accélérations aux points situés derrière la barrière (champ de pieux). Les principaux complexes sans dimension sont formulés. L'attention est portée sur les ondes de Rayleigh car elles peuvent être générées à la fois par des sources de vibrations externes (situées à la surface de la Terre) et internes (situées sous la surface de la Terre) et ses ondes peuvent transmettre une portion significative de l'énergie de source de la vibration.

Premièrement, des simulations numériques de l'interaction des ondes de Rayleigh avec les barrières sismiques verticales et les champs de pieux sont effectuées en supposant que le sol et les matériaux de barrière se comportent conformément à la loi de comportement linéaire élastique. Cela concerne les vibrations qui induisent des contraintes de cisaillement dans le sol n'excédant pas 10^{-5} lors de leur propagation. Les principaux complexes sans dimension sont formulés sur cette base. Des paramètres géométriques et mécaniques de la barrière (champ de pieux) déterminant l'effet de réduction de vibration sont identifiés. Les résultats obtenus révèlent la validité de cette onde de protection contre les vibrations. En outre, l'approche de l'optimisation de la barrière sismique verticale (qui peut également être étendue au champ de pieux) est adoptée sous forme de différences finies pour des conditions de sol particulières et une fréquence de vibration de conception.

Plusieurs modèles de comportement du sol sont analysés et leur validité, ainsi que l'applicabilité à l'approximation du comportement dynamique réel du sol, ainsi que le mécanisme de dissipation d'énergie des vibrations, sont identifiés. Sur la base de cette analyse, modèle le Mohr-Coulomb a été choisir car il dispose d'une base de données expérimentale étendue pour divers sols et reflète de manière appropriée la réduction du module de cisaillement avec l'augmentation de la contrainte de cisaillement ainsi que les effets de dissipation d'énergie. Par la suite, ce modèle est utilisé dans l'analyse de l'interaction des ondes de Rayleigh avec les barrières verticales et les champs de pieux, en tenant compte du caractère non linéaire de la déformation du sol à différents niveaux de déformation de cisaillement. En conséquence, l'influence du niveau de contrainte de cisaillement sur l'efficacité des moyens de protection contre les vibrations considérées est démontrée et les conditions appropriées pour utiliser ces méthodes sont identifiées dans le cadre de cette recherche.

Mots clés: Simulation numérique; vibration; vibrations du sol, isolation des vibrations; Diffusion d'ondes de Rayleigh; protection sismique; atténuation des vibrations; barrière sismique verticale; barrière à ondes de pile.

CONTENTS

CHAPTER 1

INTRODUCTION

Introduction

Nowadays, the issue of vibration isolation of buildings and structures from surface waves of Rayleigh type, which can be induced by natural or artificial sources of vibration, is of utmost importance for the modern civil and geotechnical engineering. In the case of artificial vibration sources, such as above-ground and under-ground railway roads, highways, heavy vibration loaded equipment, etc. it is often impracticable to construct a new residence or operating building away from existing vibration sources under restrain urban conditions. This is also the case for new above-ground and under-ground traffic lines as well as new plants with dynamically loaded equipment if the existing buildings and facilities are located nearby. For natural vibration sources as well as artificial sources generating vibrations with high amplitudes (blasts), the significance of creating new protection equipment and methods is related to the requirement to maintain load-bearing capacity of buildings and facilities under strong ground motion conditions like strong earthquakes (with the magnitude more than 7 according to the European scale).

When waves from artificial vibration sources except blasts are propagated, strains in the soil usually do not exceed 10^{-4} [132] (hereinafter these vibration sources are classified as the low-amplitude sources), whereby non linear character of strain-stress relation for soils as well as the shear modulus decrease with the increase in shear strain can be neglected. At the same time, the dissipation of vibration energy during wave propagation through the soil may be taken into account by use of visco-elastic models for the soil or Rayleigh damping. In the case of high amplitude vibration sources, such as earthquakes and blasts shear strain in the soil may reach 0.002 and 0.01 respectively [132] (*Remark.* Here, it is related to the areas that are located quite remotely from vibration sources, where buildings and facilities may be located; as far as shear strain may reach even higher values in blast or earthquake epicentres, that will require use of models that take into account the damage of the soil). At such shear strain level in soils, their deformation character is strictly non-linear and requires the application of plastic or elasto-plastic models and, in the case of blast exposures, the plasticity models that will account for the damage of soil.In addition to that, shear modulus of a soil may vary by more than two times with the shear strain change. Hence, for such vibration sources (hereinafter, these sources are identified as high-amplitude ones) the non-linear character of stress-strain relation in the process of deformation at high shear strains has to be taken into account.

In the present work, the possibility to protect buildings and structures from vibrations generated by natural and artificial sources with the use of vertical seismic barriers or pile fields is analysed. In addition to that, the non-linear character of soil deformation is considered.

Research motivation

Topic relevance arises due to imperfections of present-day vibration protection devices and methods. For example, when vibration isolation systems are designed to ensure the required noise and vibration level in residence and operating buildings or to isolate dynamically loaded equipment, the major disadvantage shall be the increase in the structural complexity of the construction designed. This results in an increase of the design and construction cost. In addition to that, the implementation of a vibration insulation system into an existing building or structure is an even more complicated problem. In the case of high-amplitude natural or artificial vibrations, such as earthquakes,blasts etc. systems of vibration protection have to maintain load-bearing capacity of a structure during and after dynamic loading. Modern systems provide, in most cases, an adequate seismic and blast protection level for buildings and structures. As a result, these constructions may withstand earthquakes or blast loading of the assumed intensity without considerable damage and progressive failure. Nevertheless, there are some examples when buildings equipped with seismic protection systems were destroyed by the earthquakes of the intensity not exceeding the estimated level. For instance, during the earthquake in Kobe (Japan) in 1995, approximately 180,000 buildings were destroyed although many of them were equipped with seismic protection systems. The shared disadvantage of the above mentioned protection systems from low and high amplitude vibrations is that they do not ensure vibration protection of underground constructions directly affected by vibrations coming from the soil. Meanwhile, even modern methods and approaches towards underground construction design might not ensure its bearing capacity as well as the absence of cracks in the case of concrete constructions, which is evidenced by the earthquake in Japan in 2011, when Fukusima-1 NPP foundation slab was damaged.

Hence, the development of alternative vibration protection facilities which would address the above issues is a significant task for the present-day civil and geotechnical engineering. The possible methods that may resolve the issues above are seismic barriers and pile fields meant to protect the territories against surface waves which are one of the major vibration exposure component in the case of surface sources as well as a measurable component of vibration exposure generated by underground vibration sources.

Research Hypothesis

The major research concept of the present work that determines the subsequent study line is seismic barriers and pile fields may be used for vibration attenuation within the protected area due to the scattering and reflection of surface seismic waves, when they interact with such barriers as well as plastic yielding within the area of these barriers at high residual and shear strains.

Objectives of the present work

This work is targeted to the determination of the optimal vertical seismic barrier and pile field geometry as well as the mechanical parameters of the material from which such barriers are made, in order to ensure maximum decrease of the vibration energy transmitted to the protected zone by surface Rayleigh waves. In addition to that, the shear strain level at which the barrier and pile field are the most efficient is also estimated.

As the parts of the set purpose, the following objectives have been met:

- the features of plasticity models that are used in soil mechanics to describe static and dynamic soil behaviour have been reviewed and studied; the most relevant model with respect to available experimental data and required accuracy of soil stress-strain state description is selected;

- numerical simulation of seismic wave interaction with vertical seismic barriers has been performed without account for non-linear soil deformation behaviour in order to select the factors being crucial for control of vibration energy entering the protected area;

- seismic wave interaction with pile fields has been modelled numerically assuming the soil to deform within the elastic strain range to select the pile field parameters that significantly affect vibration decrease within the protected zone;

- a method for vertical seismic barrier optimization has been chosen and implemented in a finite difference form to get the optimal barrier size with potential restrictions on the material amount or the required vibration level within the protected area if prescribed soil conditions and design vibration exposure are specified;

- based upon barrier and pile field configurations obtained in the process of addressing the optimization procedure, numerical simulations of the vertical barrier and the pile field interaction with the surface Rayleigh waves have been performed with account of non-linear soil deformation character at different shear strain levels, which provides the most favourable conditions when such barriers can utilized.

Thesis outline

The thesis paper consists of the introduction, 5 chapters, the conclusion and bibliography. The total thesis content makes 132 pages, including 105 figures and 7 tables. The reference list includes 137 items.

In the introduction part the relevance , actuality, hypothesis, main purpose and objectives of the research are stated.

The second chapter overviews theoretical as well as experimental researches related to diffraction,scattering and reflection of body and surface elastic waves by obstructions and inhomogeneities (including the ones on the semi-space surface) in continuum media as well as experimental and theoretical studies related to protection against vibrations transferred by surface Rayleigh waves using vertical barriers of various types.

The third chapter overviews the main constitutive equations and models of the granulated media mechanics that are used to simulate static and dynamic soil behaviour. Constitutive equations for hyper-elastic, elastic and plastic mediums (Mohr Coulomb's, Drucker-Prager's and Cam-Clay-based models) are reviewed. Their comparison along with the assessment of the effect of the numerical parameters that are used to ensure solution procedure convergence are performed. Admissibility of actual soil behaviour approximation with these models and their comparison with the most accurate present-day approaches based upon hypoplasticity models are reviewed.

The fourth chapter presents the results of numerical simulation of surface waves interaction with vertical seismic barriers using 2D plain strain and 3D models within the framework of the linear elastic constitutive relations for soil and barrier materials. The effect of barrier geometry and its material mechanical parameters are analysed, then, the recommendation for the practical barrier design are given to ensure maximum vibration energy decrease inside the protected region. The possible method of a vertical seismic barrier optimization is introduced and implemented in a finite-difference form to use in practical design accounting for prescribed geological conditions and design vibration exposure and allowing for taking into account potential restrictions upon the barrier material amount or vibration level within the protected area. The results of the optimization procedure for particular soil conditions and vibration source are shown.

The fifth chapter presents the results of numerical simulation of seismic Rayleigh wave interaction with piles and pile fields. The deformation of soil and piles are considered to be linearly

elastic. Effect of pile field geometry upon vibration control within the protected area is analysed and the recommendation towards the pile field design are given.

In the sixth chapter, the summary of numerical simulation of vertical seismic barrier as well as pile field interaction with surface Rayleigh waves is presented at different levels of shear strains with account of non-linear character of soil deformation.

CHAPTER 2

REVIEW OF MAJOR VIBRATION SOURCES AND METHODS TO MITIGATE VIBRATION MOTION

Contents

This chapter overviews vibration sources with respect to their dynamic parameters and nature of caused vibration motion as well as scientific researches related to diffraction and dissipation of the energy of body and surface elastic waves by the obstructions and inhomogeneities in the continuous media (including inhomogeneities on the surface of a continuous half-space). The results of experimental and theoretical works related to protection against vibrations transferred by seismic waves with various types of seismic barriers are shown.

Soil motion and vibration Sources

Major vibration types and their evaluation techniques.

Structural vibrations in buildings and facilities may be caused by both external and internal sources. Internal sources include heavy equipment installed in buildings for different purposes, indoor blasts, etc. Earthquakes, transport vehicles, such as motor vehicles and high-speed trains, heavy dynamic equipment in the construction sites as well as blasts can be referred to external

vibration sources. It is worth noting that all the sources mentioned above induce vibration motion of different nature, duration and having various acceleration, velocity and motion amplitudes. Moreover, earthquakes and blasts can be classified as the most dangerous types of vibration exposure upon structures due to the high amplitude of vibration and irregular hard-to-predict nature. Subsequently, the external sources of vibration generating surface Rayleigh waves will be reviewed.

According to the character, vibrations may be grouped as follows [39]:

- sustained vibrations (long duration reaching sometimes several hours; availability of steady frequency parameters);
- impulse vibration (short duration, high initial exposure amplitude, fast attenuation);
- Interrupted vibration (discrete periods of broken sustained vibration, repeated impulses of vibration motion).

Sustained vibration (a) is generally caused by transport vehicles (motor vehicles, trains, near-surface or aboveground lines of subways), dynamic equipment, construction machinery, etc. This vibration type may be evaluated with respect to weighted acceleration mean squares which is shown in the regulatory documents for different regions such as [136],[40], [39], [7], [134], [24] and [52]. According to , for example Russian construction code, [24], to estimate sustained low-amplitude vibrations (a) the values L_a,L_υ and L_u, called vibration acceleration, vibration velocity and vibration displacement amplitudes that are measured in decibels (dB), are introduced. Equation for estimation of vibration acceleration can be written as:

$$L_a = 20 \lg \frac{a}{a_0}, \tag{2.1}$$

where a - vibration acceleration amplitude, (m/s^2),$a_0 = 3 * 10^{-4} m/s^2$ is the reference vibration acceleration. Equations for the estimation of vibration velocities and displacements are introduced similarly:

$$L_\upsilon = 20 \lg \frac{\upsilon}{\upsilon_0}, \tag{2.2}$$

$$L_u = 20 \lg \frac{u}{u_0}, \tag{2.3}$$

where υ and u are vibration velocity and displacement amplitudes, respectively, meanwhile $\upsilon_0 = 5{*}10^{-8} m/s$ and $u_0 = 5{*}10^{-14} m$ are the reference vibration velocity and displacement amplitudes as appropriate.

The values similar to the ones defined by equations (2.1) and (2.2) are also introduced by German construction code, [40] to measure and assess vibration velocities and accelerations, however, with different reference vibration velocity and acceleration amplitudes equalling $a_0 = 1 * 10^{-6} m/s^2$ and $\upsilon_0 = 1 * 10^{-9} m/s$ respectively. Additionally, [40] introduces vibratory force level:

$$L_F = 20 \lg \frac{F}{F_0}, \tag{2.4}$$

which is missed in [24].In equation(2.4) is the reference vibration force value equalling $F_0 = 1 * 10^{-6} m/s$. The values described above and other ones mentioned in particular construction codes can be used to estimate vibration level and set the limit values upon it to ensure the required working and living conditions for people as well as to maintain building and structures, for example [136].

Impulse vibration, including blast exposure (b), is typically related to blasts, heavy equipment falling and impact, for example, when a transport vehicle collides a structure. Unlike the sustained vibration, a small number of regulatory documents for the evaluation of impulse

or blast vibration is available, for example [7] and [137] (part 1.7). This vibration type can be estimated by its maximum acceleration.

It is worth noting that load-bearing capacity of some buildings and facilities (bridges, high-rise facilities, tunnels, etc.) are assessed with account of this exposure type by designating such an exposure as an equivalent static load or directly simulating it using time domain dynamic approach. Numerical simulation of a multi-storey building progressive collapse due to blast loading as well as transport vehicle collision with a tunnel are the examples of such design computations that can be used to ensure structural resistance of such structures to progressive collapse or impulsive loading.

Interrupted vibration (c) includes pile driving, above-ground and underground trains (this vibration type may be related to this group as well because discrete vibration sections corresponding to 1 train passing are practicable to select), etc. For this vibration type different criteria shall be introduced including vibration dose (VDV,$[m/s^{1.75}]$) [39]:

$$VDV = \left(\int_0^T a^4(t)\,\mathrm{d}t \right)^{0.25}, \tag{2.5}$$

where $a(t)$ is a frequency-weighted acceleration and T is the period of vibration. Hourly equivalent noise level can be estimated as:

$$L_{eq}(hours) = 10 \lg \left[\frac{1}{T} \int_{t_1}^{t_2} 10^{L_A(t)}\,\mathrm{d}t \right], \tag{2.6}$$

where the equation under logarithm corresponds to total 1-hour sound energy. To evaluate average daily vibrations, similar values might be introduced [52].

Major vibration sources.

The most probable vibration sources for civil and geotechnical engineering objects are considered in this chapter including transport vehicles, operating equipment, construction activities, earthquakes, etc. General information regarding principal frequencies and shear strain range in the soil during vibration propagation is provided in this paragraph. The problem of vibration energy distribution among various wave types for each source is discussed in paragraph 2.1.3 as it relates to the source position in relation to the earth surface.

Transport vehicles usually generate vibrations at which shear strains in the soil do not exceed 10^{-5}, hence, the character of soil deformation remains almost linearly elastic. Exposure frequency and amplitude depend upon the following parameters:

- transport vehicle speed;
- transport vehicle mass;
- transport vehicle speed – Rayleigh wave soil velocity ratio [84],[111];
- soil conditions.

At the same time, building codes or standards prescribing the frequency range and methods to estimate the noise and vibration for some sources of that type at different distances are available. For example, the USA Codes for the prediction of noise and vibrations from trains [52] and Russian Federation code characterizing the noise from the underground subway [117].

Generally, this vibration type affects indoor comfort within the high frequency range ($> 10Hz$), hence, the wavelength of the waves propagating through soils shall not be more than $30m$ in the case of weak soils with S- waves propagation speeds not exceeding $360m/sec$.

Operating equipment Vibrations generated by heavy equipment induce shear strains in soils of the same level as transport vibration not exceeding $< 10^{-5}$. Therefore, soil straining may be considered as linearly elastic. High frequency vibration motion resulting in high noise and vibrations affecting comfort and operating conditions in the adjacent buildings are considered the most frequently.

Construction activities, which cause vibrations and noise, include tunnelling machines, pile driving, dynamic soil compaction, etc. Within the area of these activities shear and residual strains in the soil can be high, however, when the vibrations reach buildings or constructions they usually do not exceed 10^{-5}, hence, the major effect of the vibrations from such sources is related to the comfort of people and labour conditions in the buildings and facilities.

Blast exposure may cause the destruction of the entire structure and should be considered separately. Shear strain in the soil during the process of blasting may reach $10^{-3} \div 10^{-2}$, hence, the deformation of soil is strictly non-linear which requires the models accounting for such a behaviour. In several cases, to correctly describe soil straining due to blast exposures, soil failure should be taken into account.

Earthquakes is, probably, one the most hazardous soil motion source for buildings and facilities. It is because of the fact that an earthquake causes soil vibration with up to $2g$ (PGA) acceleration. In addition to that, earthquakes can affect soil structure and cause its liquefaction resulting in the foundation destruction. Hence, an earthquake effect can be disastrous and result in the collapse of buildings, villages, cities and city infrastructure.

When seismic waves propagate from the hypocentre of an earthquake shear strains in the soil may reach $2 * 10^{-3}$,meanwhile the most hazardous frequencies for structures that are required to be taken into account in the design process vary between $0.1 \div 20Hz$ [132]. Hence, an earthquake directly affects bearing structures of buildings and may result in their destruction in the case of strong ground motion.

Table 2.1.2 represents the most probable vibration sources for civil and geotechnical engineering objects, their specific frequency ranges and the range of shear strains in soil when waves are propagated from these sources through the soil. All the vibrations caused by these sources may be classified into 2 groups:

- vibrations affecting the equipment and people staying in the buildings and facilities but not affecting load-bearing capacity of the structures;
- vibrations affecting load-bearing capacity of constructions.

The first group includes all the sources causing vibrations with shear strains in soils not exceeding 10^{-5}, i.e. vibrations due to transport vehicles, construction activities and operating equipment. When the vibrations of this type be propagated, soil deforms virtually according to the linear law and no plastic or damage properties shall be taken into consideration

The second group includes vibrations causing significant shear strains in the soil during their propagation. For example, vibrations from earthquakes and blasts. When these vibrations propagate, shear strains in the soil may reach 10^{-2}, i.e. soil behaviour is strictly non-linear and the character of soil deformation along with the shear modulus of soil depend upon the value of the shear strain. Obviously, the dependency of shear modulus upon the shear strain,plastic character of soil deformation as well as the damage of soil can not be neglected in this case.

Types of waves generated by the vibration sources and the distribution of the vibration energy between various wave types for different sources.

All the sources of vibration considered above can be divided into external and internal according to their location in respect to the surface of a half-space. External vibration sources including high-speed trains, above and near-ground construction activities, heavy equipment in industrial buildings, etc. act on the Earth's surface or in the near-surface zone. Internal vibration sources

Vibration source	Soil shear strains, m/m	Frequency, Hz
Earthquake	$10^{-4} \div 2 * 10^{-3}$	$0.1 \div 20^{*}$
Transport vehicles**	$< 10^{-5}$	$2 \div 125$
Heavy equipment (industrial vibrations)	$< 10^{-5}$	> 10
Explosions (including construction activities)	$10^{-3}10^{-2}$	–
Construction activities	$< 10^{-5}$	–
* -the most hazardous frequencies for load-bearing of structures ** - subway trains according to [117].		

Table 2.1: Main Vibration Exposure Parameters [132].

such as subway, underground construction works, underground blasts, earthquakes, etc. generate vibration below the earth's surface.

In the case of overground (external) vibration sources, Rayleigh surface waves carry the major portion of vibration energy and their amplitude attenuates with the distance as $\frac{1}{\sqrt{rx}}$ (where r is a wave number and x is a distance from the vibration source) in the case of spatial problem and point harmonic loading [81]. At the same time, body waves attenuate with distance much faster than surface Rayleigh waves and their amplitudes decrease with the distance from the epicentre as $\frac{1}{|rx|}$. Work [82] generalizes the outer Lamb's problem for the case of moving loading. In [102], it is shown that Rayleigh wave can transfer up to 67% of the vibration source energy, whereas longitudinal and transverse waves transfer 26% and 7% energy of the source respectively.

At the same time, the mechanism of wave propagation from inner vibration sources e.g. earthquakes, subway, underground explosions is more complex. It becomes even more complicated because of the layered structure of the medium where this vibration exposure spreads. However, according to the asymptotic estimations performed in [105] for inner harmonic loading no Rayleigh wave is observed at the distance from the epicentre which meets the condition:

$$d_1 < \frac{c_R H}{\sqrt{c_P^2 - c_R^2}}, \tag{2.7}$$

where C_R and C_P are Rayleigh and P wave speeds respectively and H is the depth of the source. Additionally, at the distance $a \in (d_1, d_2)$ where d_2 is calculated by equation:

$$d_2 < \frac{c_R H}{\sqrt{c_S^2 - c_R^2}}, \tag{2.8}$$

Rayleigh surface waves exists, but body waves continue to dominate.In (2.8) c_S is shear wave velocity. Finite element (FE) simulation of plane inner Lamb problem in [77] shows that Rayleigh wave appears at the distance $d_3 \approx 2.25H$ from the epicentre which is in a good agreement with equations (2.7) and (2.8). Moreover, it is observed that for a point source with impulsive time variation loading described by the delta-Dirac function (δ) Rayleigh waves begin dominating in magnitude of displacement at the distances greater than $3H$ from the epicentre [77]. In addition to that, it is worth noting that surface Rayleigh waves attenuate with distance as $\frac{1}{\sqrt{rx}}$ whereas body waves as $\frac{1}{|rx|}$ in 3D-problems with harmonic vibration source [81].

In addition to that, in some papers, particularly [118], it is claimed that up to 60% of the earthquake source energy generated by shallow-focus earthquakes (the origin depth is less than 70 km) can be spent on the surface seismic waves. Taking this into account along with body and surface wave attenuation character with distance, it can be concluded that in some cases, that can be determined based on seismic microzonation, surface Rayleigh waves may be one of the most hazardous components of earthquakes.Particularly, in [72] it is stated that at the distances from the epicentre which are more than double earth crust thickness, surface waves (Rayleigh and Love waves) can be the main components of the soil motion.

The main principles behind vibration protection by seismic barriers and pile fields and their theoretical foundation.

The main ideas behind the protection by horizontal and vertical seismic barriers including pile fields

Present-day vibration and seismic protection methods and approaches can be classified into the following groups [41]:

- techniques focused on the design of earthquake-resistant structural schemes, components and assemblies including installation of special dampers or vibration absorbers into the load-bearing structures to dissipate vibration energy;
- methods for creating a kind of a barrier preventing the transmitting of wave energy into the protected region (such waves can be generated both by earthquakes and artificial vibration sources, for example, by trains).

Firstly, it is worth noting the method of resonant masses proposed by P Cacciola et al. in [25]. Although this method is called a barrier, it is based on the effect of structure-soil-structure interaction and consists in the construction of an additional resonant mass outside a protected structure. Shake table tests in [25] showed that this method can provide up to 7% decrease in the acceleration of the structure. Meanwhile, numerical computations showed more than 75% decrease for vibration displacements. On the other hand, this method has the disadvantages concerning the weight of the resonant part and the requirement to have 3 degrees of freedom to ensure decrease of seismic impact in all three directions.

One of the most interesting approach to seismic protection using wave barriers is the application of metamaterials. For example in [69], Kim and Das study metamaterials implementing «negative» shear modulus concept and representing a kind of Helmholtz resonator. Figure 2.1 shows the appearance of such a filler material and their layout. This barrier modifies a real part of a wave vector decreasing vibration motion. Numerical simulation in [69] showed that the vibration motion decreases virtually to zero in the shadow zone and the effectiveness of such barrier in terms of vibration reduction is much higher than that of the trench filled with standard materials.

Generally, seismic metamaterials is quite promising research direction in the field of earthquake and vibration protection. Field experiments along with numerical simulation in [23] and [21] show the reduction effect of such seismic metamaterial barrier.These studies also represent lensing effect (increase in vibration displacements) that can take place in the center of the barrier ring [23] or in the borehole mesh zone [21].Deep foundations and underground components of structures can also be considered as elements forming metamatierial which in that case is the city area. The effect of these structures on wave propagation is studied in [22].

Another interesting approach towards seismic barrier construction is the use of gas field cushions [98], where the gas pressure equilibrates the external soil pressure. This barrier provides a dramatic change in the stiffness inside the media, thus, decreasing the amplitudes of vibration

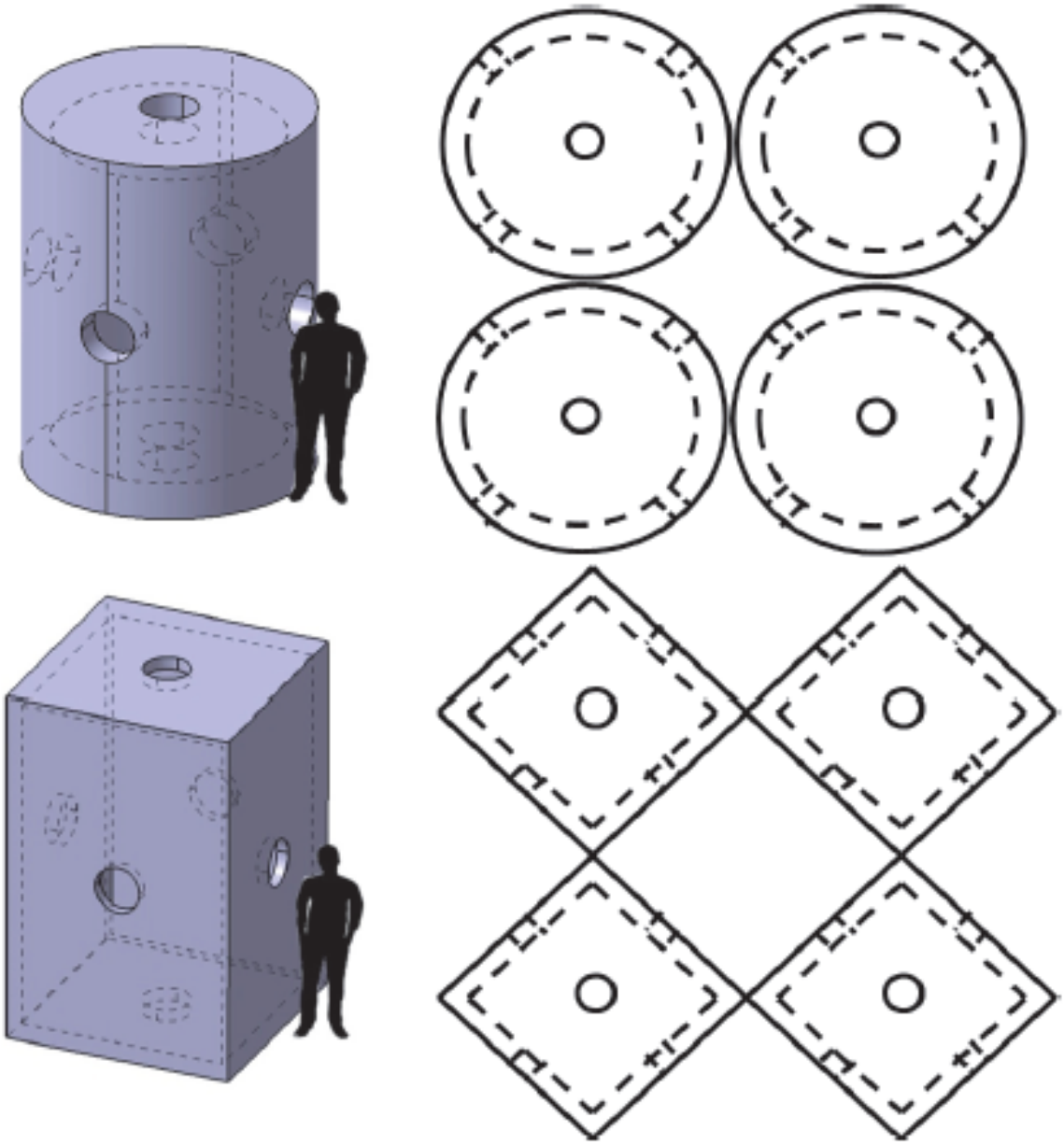

Figure 2.1: Metamaterial elements and their orientations [69]

displacements within the protected area. According to the measurements performed, such a decrease in the vibration displacements may achieve 70% within the protected area [98]. Figure 2.2 shows the scheme of the gas cushion used for vibration control [98]. In addition to that, this work provides the examples of the method implementation.

The main concept of protection by horizontal and vertical seismic barriers from the vibrations transmitted by surface Rayleigh waves are established in [41] and [76]. The main principle of vertical seismic barrier (pile fields can be classified as a kind of vertical seismic barriers) is to diffract, reflect and dissipate wave energy preventing it from transmission into the protected zone.Vertical seismic barriers can be constructed as underground concrete walls , empty trenches or trenches filled with any material like concrete, EPS geofoam etc. The main principle of horizontal seismic

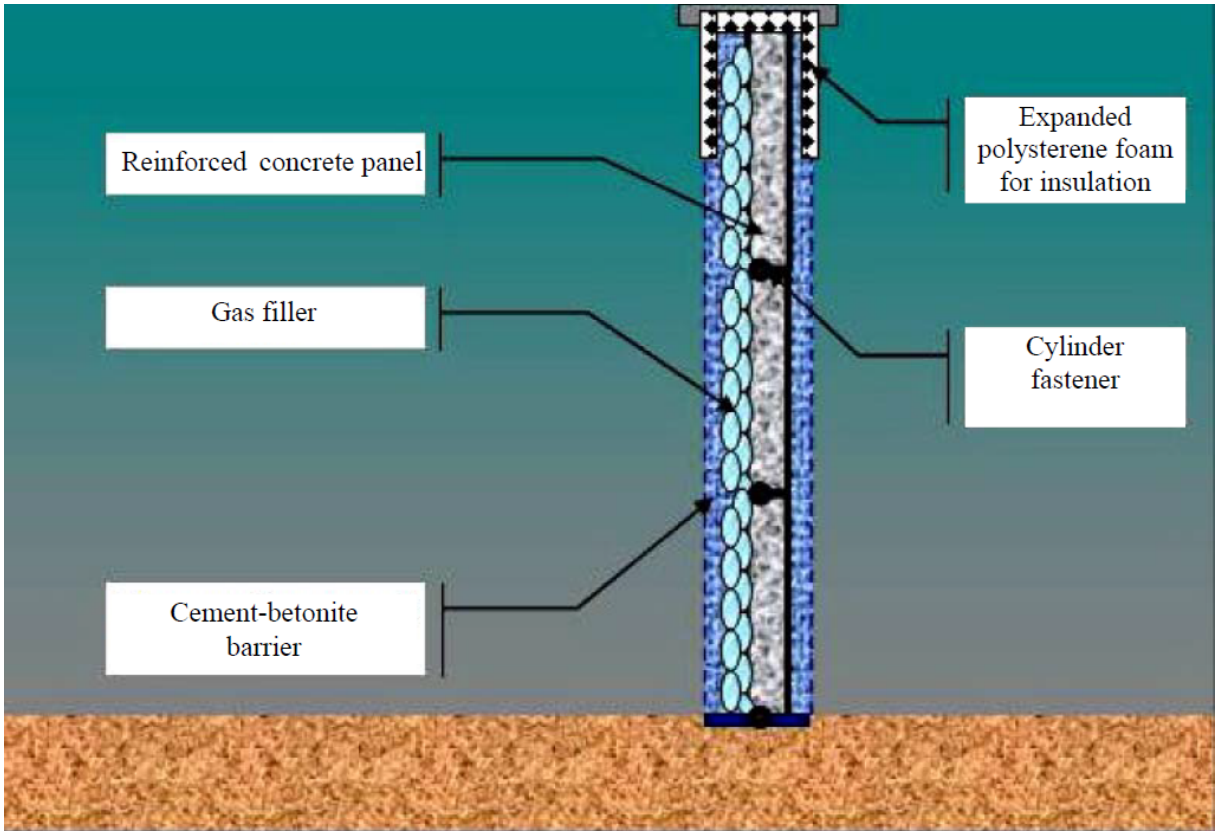

Figure 2.2: Gas Pad Arrangement Option [98]

barrier is based on Chadwick and Smith [30] postulating incapability of surface Rayleigh wave to propagate along the fixed surface of the half-space. Therefore, a horizontal seismic barrier is the modification of the surface layer approximating its properties to the properties of the fixed half-space. In addition to that it is possible to design a horizontal barrier for protection against Love waves based upon Love's theorem [91].

One of the methods of the surface layer modification for protection against Rayleigh waves is the roughening of the surface that can be implemented by construction of the series of trenches. Rayleigh wave dissipation and attenuation by such surfaces with random roughness is studied in [135],[96] and [133]. The authors have concluded that to ensure efficient application of this technique, it is required to ensure commensurability of the periods and vertical dimensions of the surface roughness with the wavelength. In addition to that, this type of seismic barrier decreases only vibrations transported by the waves moving in a direction transverse to the roughness and the efficiency of these barriers depends on the wave frequency. Hence, this technique has significant restrictions not allowing for its wide application.

One of the effects of Rayleigh wave propagation along the rough surface is the change of its velocity [51]. For real frequencies the wave velocity and its attenuation with the distance are obtained in relation to the frequency [86]. Roughness scale-effect for large wavelengths of Rayleigh, Scholte and Stoneley waves is studied in [109].

Horizontal acoustic barriers are studied quite well in [80]. Based upon numerical FE analysis, it is shown that this type of seismic barriers decreases the vibrations transferred by surface Rayleigh waves within the protected area. According to the obtained results, the density and Young's modulus of the barrier material and their ratio to those parameters of the soil as well as the width and depth in relation to the wavelength are the main parameters that affect vibration reduction effect of horizontal seismic barriers. Based upon the numerical simulation the authors provide recommendations for practical barrier design for a particular soil condition and the

expected frequency range during vibration action. It is important to emphasize that Poisson's ratio does not affect vibration decrease within the protected area. The major disadvantage of this protection technique against surface Rayleigh waves is related to the required material parameters. This barrier shall be arranged from non stiff and very dense material which is difficult to implement in practice. For example, high dense concrete ($\rho > 5000 kg/m^3$) is stiff and vice versa,in general, small stiffness materials are lightweight . Hence, practical application of horizontal seismic barriers is extremely difficult.

In the following part, the review of theoretical and experimental researches on seismic wave interaction with inhomogeneities in a half space and vertical wave barriers including pile fields is given.

Theoretical and experimental researches related to wave scattering and diffraction by inhomogeneities in a continuous media

The analytical works in the field of wave barriers as a mean of vibration isolation are based on the theory of linear elastodynamics as wells wave scattering and diffraction by heterogeneities in a continuous media including surface imperfections. The majority of these researches up to 1973 year are described in [104]. The main methods used for the analysis of diffraction by various obstacles described in this work are the methods of integral equations and transforms as well as perturbation method for elastic waves. In addition to that, it is worth noting the work of Hudson [59], who developed the theory of Rayleigh wave scattering due to surface irregularities.

Knopoff's papers [70, 71] are one of the first works on the scattering of compression and shear waves by rigid spherical obstacles respectively. The obstacle size in these works varies from very small in comparison with the wavelength to the size compared with the wavelength. Scattering of plane P waves by a finite stiffness spherical obstacle is studied in [110] by Pao and Mow for the cases of rigid, fluid and empty spheres.

Reflection and transmission of Rayleigh waves at a corner (figure 2.3) is studied in [60] theoretically using a Green's function method. In this research, the approximate values of transmission and reflection coefficients as the functions of the wedge angle and Poisson's ratio are obtained numerically. These coefficients are obtained experimentally in [113] as an angle function of two-dimensional Rayleigh waves. The experimental scheme is shown in figure 2.4. These results are in a good agreement with the first order theory for angles in the range between 110 and 180 degrees. Experiments with smaller angles showed a considerable discrepancy with the theory.

Diffraction of shear waves by parabolic semi-cylindrical and semi-elliptical canyons are studied by Trifunac as well as Wong and Trifunac in [141, 147] respectively. As a result, the solution of the problem related to the propagation of plane shear waves through semi-circular and semi-elliptical canyons is obtained. In [83] similar problem for longitudinal waves is considered. The obtained results show the potential increase in the vibration displacements amplitude within the area of such inhomogeneities.

Scattering, reflection and transmission of surface and body elastic waves by a surface - breaking crack (figure 2.5) are studied in [101, 6] using integral equations. As a result, the values of scattering ratios as well as displacement field within the crack area are obtained for different types of elastic waves at various incident angles (in this case – the angle between the wave direction and direction perpendicular to the transverse crack section) and crack depths [6]. Additionally, the displacement fields in the crack vicinity at different angles of incidence are obtained for the case of body wave propagation [101].

The studies above concerning body and surface waves diffraction and scattering by inhomogeneities in the continuous media and on the surface of a half-space do not cover the complete list of the researches devoted to this topic. However, these works describing individual cases of interaction of elastic waves with inhomogeneities (canyons, cracks, corner areas, etc.) demonstrate reflection, diffraction and scattering effects of the inhomogeneities in the media for travelling

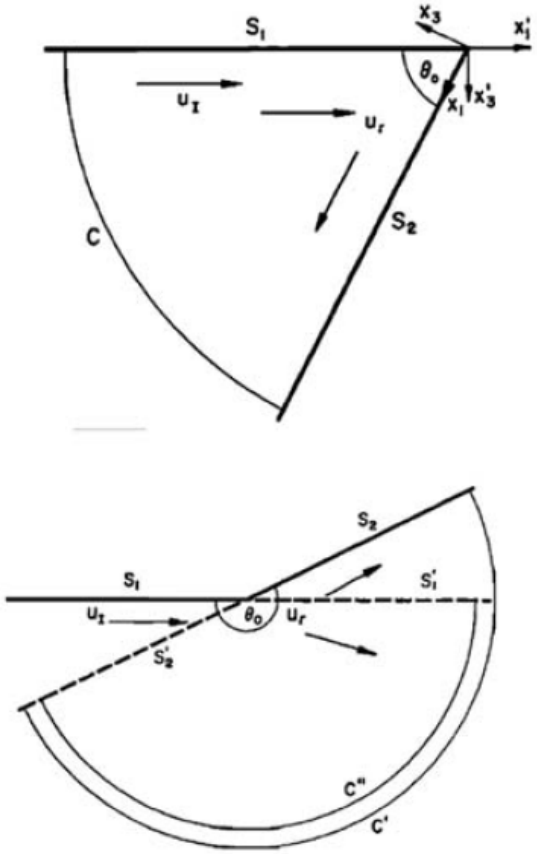

Figure 2.3: Surface wave scattering in corner zones [60].Problem geometry.
u_I, u_r- directions of original and reflected waves respectively; S_1, S_2- free surfaces of the half-space and S_1', S_2' their extensions;

body and surface waves. General analytical solution of the problem concerning a vertical seismic barrier or a pile field interaction with elastic waves with analytical methods is extremely difficult. However, for particular cases of interaction the analytical solutions are obtained.

For example, in [63] the study of screening properties of composite wave barrier using Green's function technique is performed. The obtained results reveal that the obstacles with low Rayleigh wave velocity in their material demonstrate higher screening properties than high velocity obstacles at small angles of incidence . At the same time, screening properties of the barriers made of high wave velocity material increase with the growth of the incident angle. The minimum of screening parameters of a low velocity obstacle is observed at the angles which are in the vicinity of 60 degrees. At larger values of the incident angle, screening properties of the both barrier types increase. In addition to that, a composite barrier that is composed of one high velocity layer sandwiched between two low velocity layers shows higher screening effect than the low-velocity one at small incident angles and its screening effect does not decrease with the growth of the incident angle.

In [65], the decrease of vibrations caused by high-speed train movement is obtained by using the trenches installed along the rail road is studied. This problem is solved analytically with Fourier series and Fourier transform at a fixed trench depth and different frequency ranges. The obtained results reveal that at supercritical train speed equalling to $200km/h$ the important frequency range is placed between $2Hz$ and $8Hz$. Whereas, at the speed of $70km/h$ the most critical frequencies vary between 0 and $1.1Hz$. At the same time, for this case the trench shows good attenuation properties only at the frequencies larger than 1.1 Hz. Consequently, it is

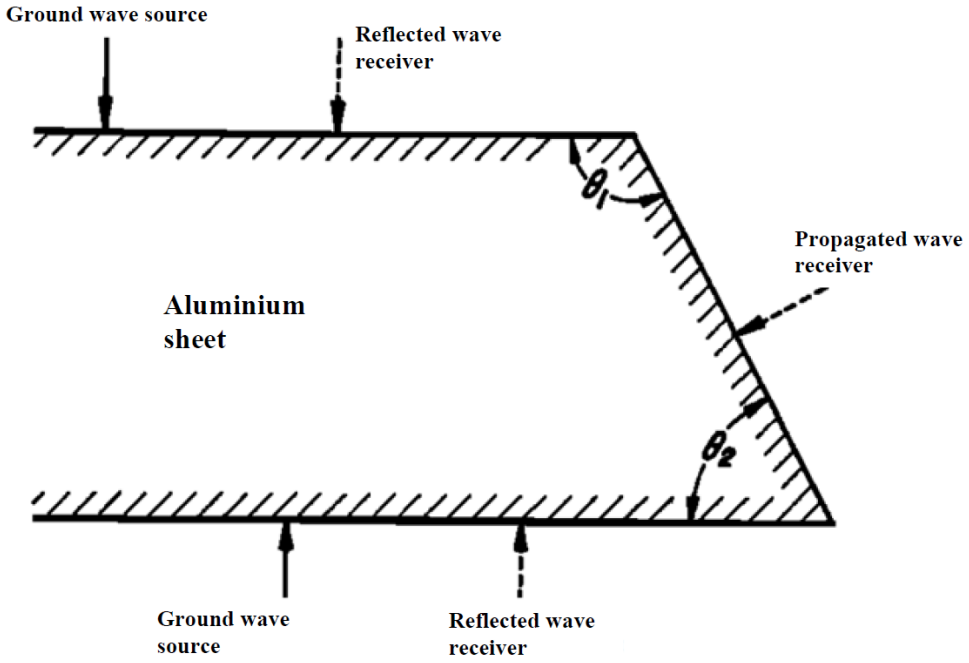

Figure 2.4: The scheme of the experimental device for study of wave propagation and reflection in corner zones. [113]

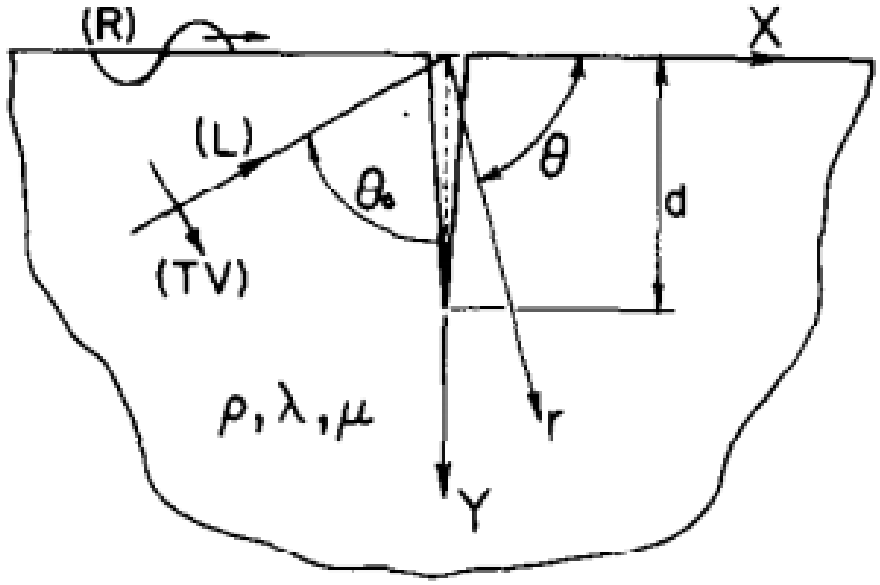

Figure 2.5: The scheme of surface elastic wave diffraction and scattering on the surface crack [101]
(R) –Rayleigh surfaced wave;
(L) and (TV) – longitudinal and transverse waves;
(r) – vector showing direction of reflected wave movement;
(θ) and (θ_0)– angles of wave incidence and reflection respectively;
(d) – crack depth.

obtained that if the main frequency equals to $4Hz$ the trench may decrease the vibrations almost by 90%. Additionally, the trench may demonstrate reasonably good performance as well at the

frequencies placed between 1.1 Hz and 4Hz, while for lower frequencies the trench practically does not decrease but even may increase the vibrations. The authors also claimed that a trench can be considered as a wave barrier only if the surface waves are generated.

The study of seismic waves interaction with piles and pile fields is even more complicated and requires various numerical schemes, thus, few analytical works related to this topic can be found. Such works include [8] and [9] where the particular solution of pile - body wave interaction [8] as well as pile-surface wave interaction [9] problems are obtained. In addition to that, for the 2D pile-body wave interaction problem the precise analytical solution is obtained in [9].

Apparently, most of these analytical work are devoted to simple models of materials and geometries with idealized conditions, because more realistic and complicated cases require numerical calculations using various realization of finite and boundary element methods or other kinds of numerical methods.

Vibration mitigation using vertical seismic barriers

Experimental researches

One of the first works devoted to the studying of trenches and underground screens as a mean of vibration protection is the one of Barkan [11] where some experimental results for high frequency vibration sources are obtained. In addition to that, the terms «passive vibration isolation» and «active vibration isolation» are introduced to determine the isolation of a specific territory from the vibrations coming from the sources outside and the isolation of the vibration source itself, thus, decreasing the radiated vibration energy respectively.Figures 2.6 and 2.7 show the examples of experimental design for active and passive isolation for protection against the vibrations generated by transport vehicles [11].The author, probably, is the first who described the shadow zone (screened zone) behind the barrier and showed the influence of the screen depth – wavelength ratio on the vibration decrease. According to the obtained results, a barrier (a trench or a screen) produces a shadow zone behind it where the vibration is decreased to its minimum followed by the decrease of the barrier effect with the distance. The applicability of this techniques for high-frequency vibrations is stated. However, it is shown that in some cases this mean of protection can be ineffective , for example, in the one shown in figure 2.7. Which, according to the author's opinion, can be caused by misunderstanding in the theory of wave diffraction by obstacles.

Some successfully applications of trenches and wave barriers for vibration protection are presented in [42, 106, 100]. Figure 2.8 shows the scheme of a barrier used in [42, 106] by Dolling and Neumeuer respectively. The installation of the bentonite trench gave a double decrease in the vibration amplitude of the printing plant which is located near the subway. In [100], RL McNeill et al. use a complex system including a trench with a sheet-wall barrier installed before the trench to protect a laboratory with precision equipment (figure 2.9). The trench with sheet pile wall on the vibration source side and a foundation slab on the building side are used for protection. Additionally, the foundation slab is constructed on the base made of light material . Supplementary vibration insulators are installed between the foundation and the floor where the equipment is installed. As a result,the slab acceleration decreased and met the owner's requirements after the laboratory was equipped with this vibration isolation system (figure 2.9). In this case, it is difficult to estimate the quantitative effect of the trench and sheet pile wall upon the vibration control, however, the combination of the measures produced the required effect.

More detailed and extensive experimental studies of trenches as a mean of passive and active vibration isolation against Rayleigh waves are performed in [150, 148, 43, 122] which resulted in the recommendations towards practical trench design in soil depending on soil conditions along with the vibration source frequency. These recommendations can allow ensuring maximum vibration decrease within the protected zone. Moreover, the values of the reduction ratios at

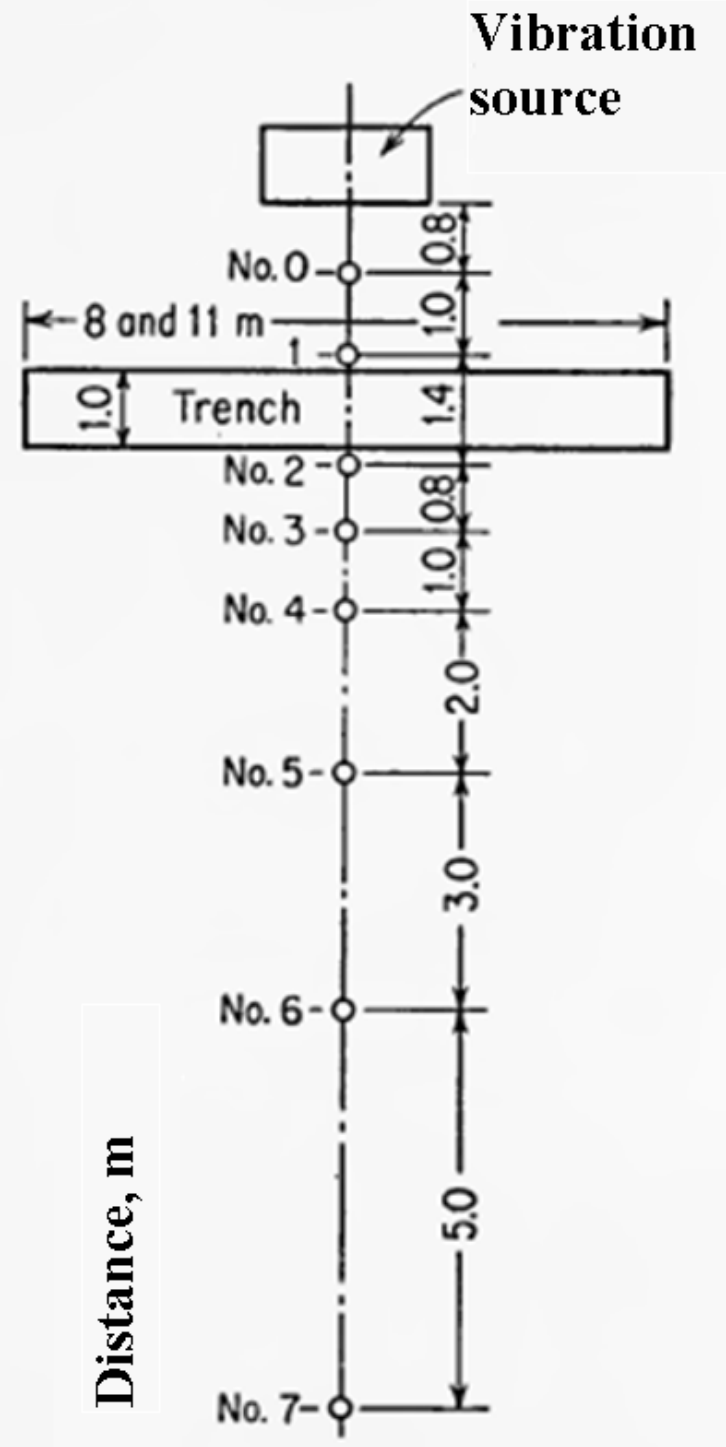

Figure 2.6: Active Vibration Protection Experiment Scheme [11]

which a trench could be considered as an effective mitigation measure are specified.

In [28], field experiments related to the interaction of surface waves with a wave barrier filled with various materials are carried out for the cases of passive and active vibration protection. In this study, wave barriers such as trenches, underground walls etc., are found to be more effective for passive vibration isolation. In addition to that, it is shown that open trenches provide larger vibration decrease than the filled ones. However, the necessity of supporting measures imposes the restrictions on the open trench depth. This is the reason why the cases of the trenches filled

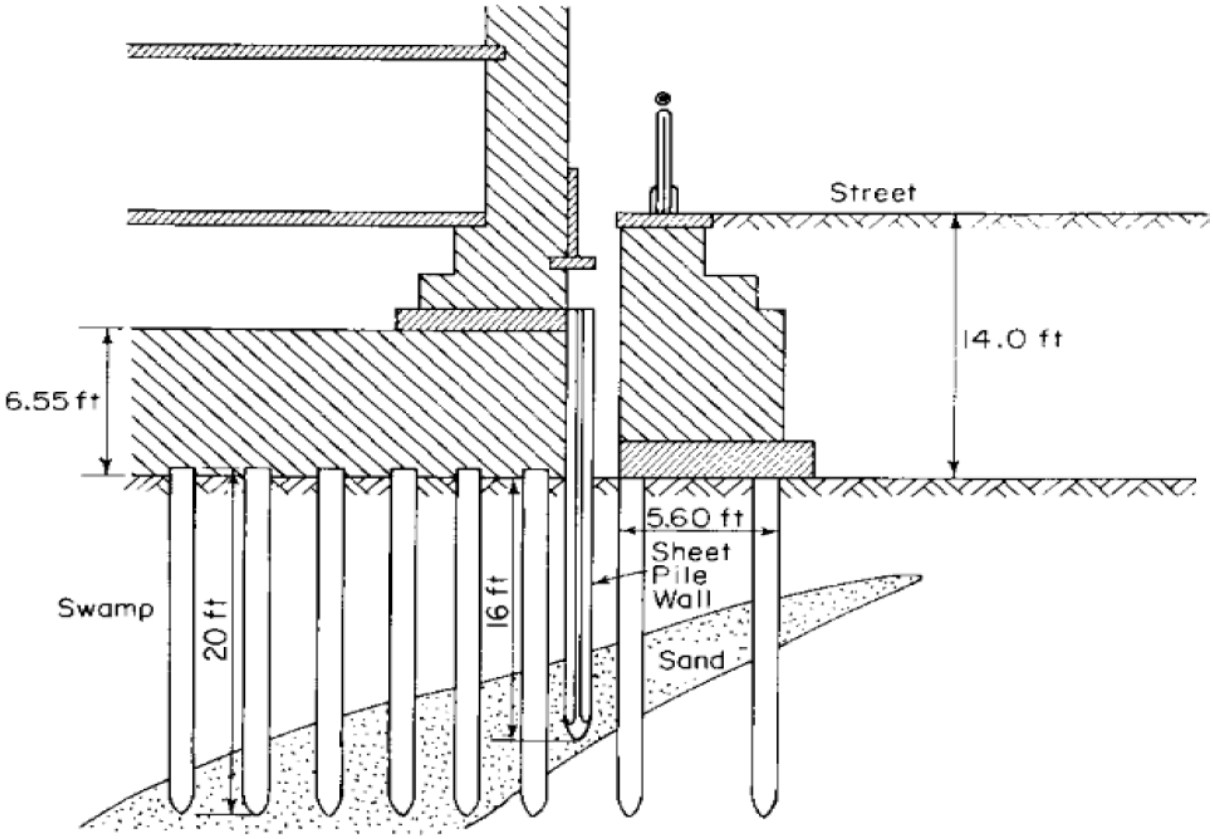

Figure 2.7: Example of Passive Insulation for Protection with the Screen against Vibration Due to Transport Vehicle [11]

with materials which are softer than the considered soils (bentonite slurry) and harder (concrete) than the soil are studied as well. Consequently, it is obtained that the trench filled with light and soft material demonstrates better vibration mitigation than the one filled with hard and heavy material.

Similar experiments are performed for a GeoFoam wave barrier and an open trench in [4]. In addition to that, the obtained results are compared with numerical simulation in Abaqus. This comparison shows that the vibration reduction effect obtained from numerical computations follows the same trend as the one obtained from the experiment. Thus, numerical simulation can be used to compute vibration attenuation effect given by the barriers in other soil conditions.

The attenuation properties of a stiff wave barrier are studied in [34] experimentally and numerically using coupled FE-BE computation. Prior to the calculation and the barrier construction dynamic soil characteristic are determined and used for the layered model of the soil. The full scale experimental study is carried out for jet grouting columns installed along a railway track. The barrier length, height and width are 55 m, 7.5 m and 1 m respectively. Two vibration measurements are performed before installation of the barrier and after it. It is shown that a relation between the Rayleigh wave velocity in the surrounding soil and the velocity of bending waves in the barrier determines the effectiveness of the barrier in vibration reduction. The barrier is found to be a good way to decrease vibration level and it is shown that the largest vibration reduction can be observed directly beyond the barrier followed by the decrease in barrier performance with distance, although, reduction effect is still significant.

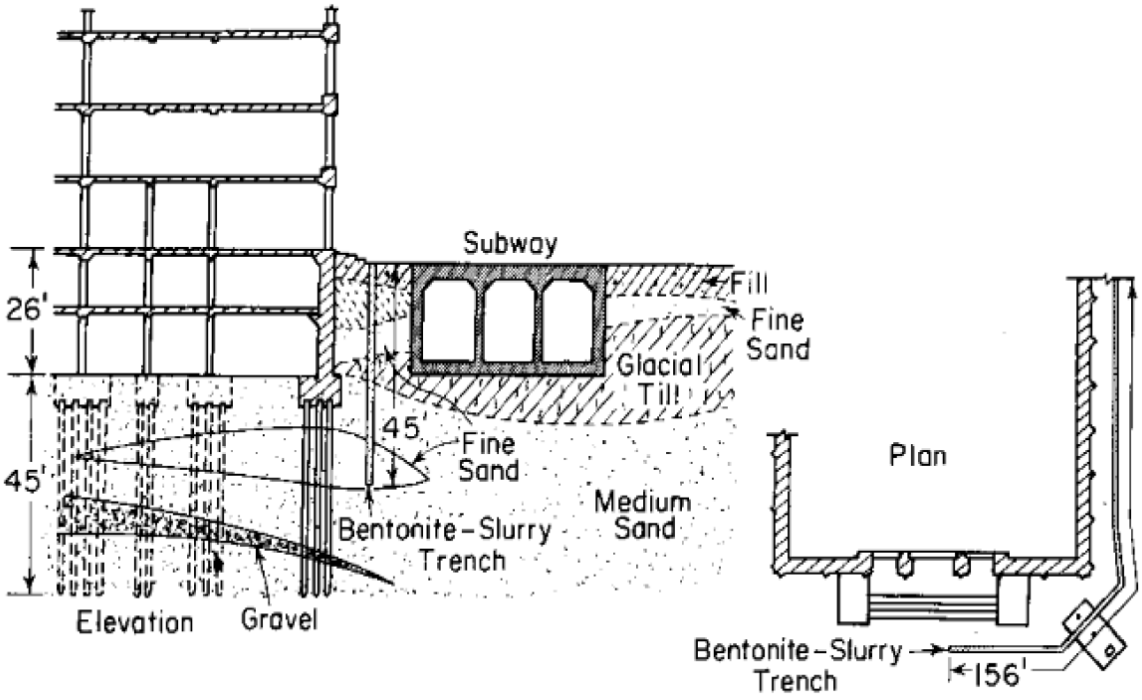

Figure 2.8: Usage of the Barrier for Subway Vibration Protection [42].

Numerical researches

Along with the development of computers and numerical schemes it has become possible to deal with the problems of waves diffraction and scattering using numerical methods. These methods allow creating more realistic models and conditions comprising non-linear material properties and finite deformation.

Finite difference method (FDM)

In [2, 3], Aboudi studies screening and diffraction of waves by a surface obstacle and a thin barrier combining finite difference and perturbation methods. The waves in [2, 3] are generated by impulsive loading. The obtained results reveal that the surface obstacle highly affects Rayleigh and the reflected waves. Hence, this heterogeneity can be used for vibration protection purposes [2]. Meanwhile, the screening effect of the thin barrier occurs at some conditions described by the authors in [3].

In [48], finite difference scheme with absorbing boundary conditions are used to study the scattering of waves by a trench. The transmission and reflection coefficients are obtained from the surface waveforms and compared with experimental results at a given moment.

Boundary element method (BEM)

In some cases BEM can be more useful than FEM as it does not require absorbing boundary conditions or large model sizes to avoid the reflection of waves at the boundaries. In [16, 38, 85], the effectiveness of trenches for active and passive vibration isolation is studied using BEM.

In [16], plane strain problem for active and passive isolation is considered. The obtained results demonstrate the effectiveness of a trench as a mean of active and passive vibration protection. In addition to that, it is shown that an empty trench is more effective than the concrete filled one. In [38, 85], these problems are studied using three-dimensional formulation for homogeneous soils and using plane strain formulation for non-homogeneous ones. It is shown that the

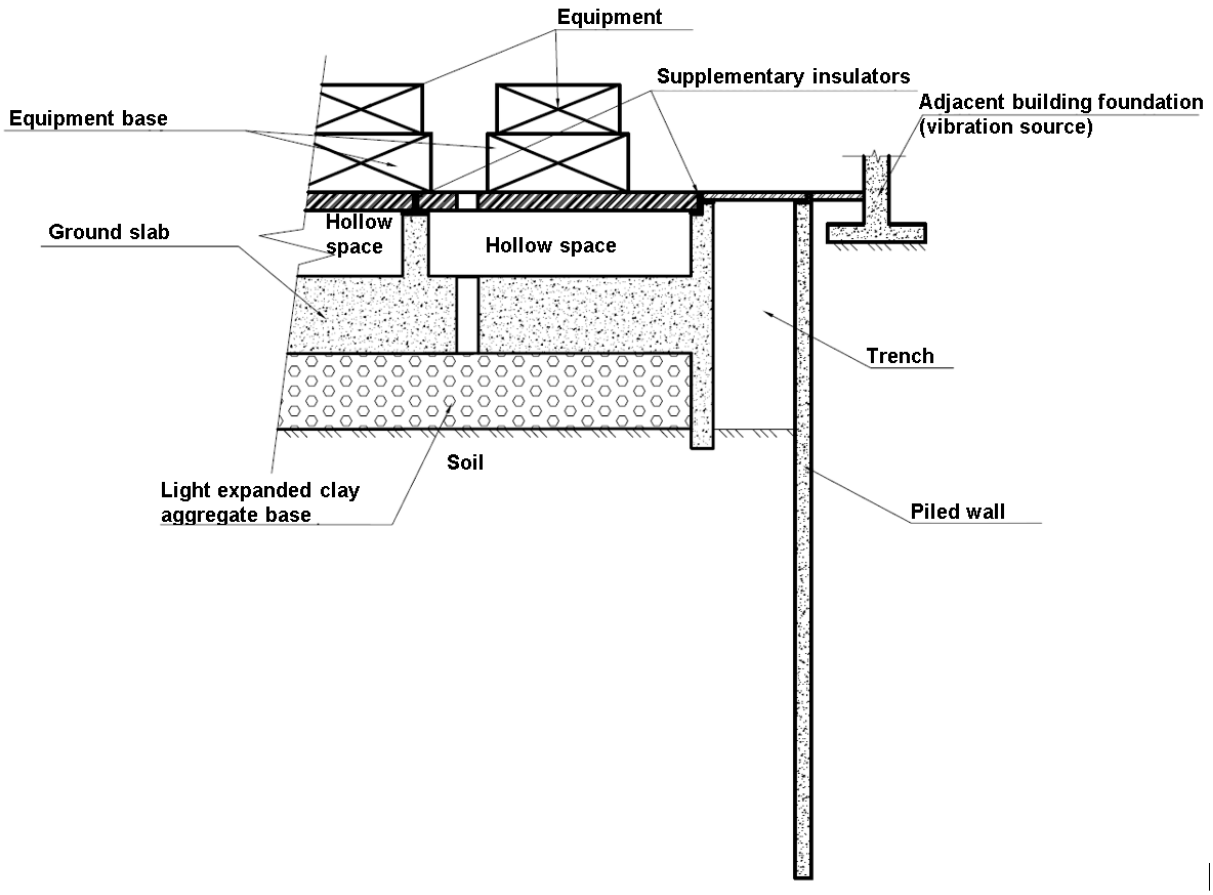

Figure 2.9: Precision Equipment Insulation with the Wall in Piled Soil [100].

depth and the width of a trench should depend upon the stiffness of the most rigid layer in order to ensure maximum vibration decrease.

In [10], the problem of active and passive vibration isolation by trenches is studied for the case of multi-layered three-dimensional soil media. Similarly to [85], the results for two layered media are obtained assuming the soil to be isotropic linearly elastic or viscoelastic.

Finite element method (FEM)

[130, 99] are probably the first works devoted to vibration reduction by trenches using FEM. All the results obtained in these researches are in a good agreement with the previous experimental studies mentioned above.In [130], it is obtained that the effectiveness of a trench is a function of the trench depth to the wavelength ratio. According to this work, the trench with the depth which is greater than or equal to 0.6 of the considered wavelength reduces vibration within the protected zone significantly . In comparison with an empty trench, the filled one shows less vibration decrease. Similar results are obtained in [130]for SH and vertical component of SV waves propagating in a layer over a half-space within the frequency range of $4 \div 6$ Hz. Meanwhile for the frequencies which are less than $3 \div 4$ HZ the amplification of horizontal component is observed. Haupt in [54] investigates the reduction effect of core walls by using FEM method. In [56], similar results are obtained for train induced vibration by Hu et. al using FEM. Additionally, it is also shown that the growth in the trench length increases its attenuation properties.

Finite element study (FE) of open, infilled trenches and elastic foundations as a mean of protection from train induced vibrations are carried out in [153] under plane strain conditions.

Train loading, that generates Rayleigh waves, is simulated as a vertical harmonic loading on the free surface. The soil is assumed to be viscoelastic which is simulated by hysteretic damping. The obtained results are in a good agreement with the results in [130, 99] as well as the experimental works described above. It is shown that the effectiveness of a trench is a function of the ratio of its height to the wavelength of the waves propagating in the underlying soil (in the case of active vibration isolation, body waves wavelength). The effectiveness of an open trench in terms of vibration decrease significantly depends on its height, while for an in-filled trench the width also affects the resultant vibration decrease. In order to ensure a significant vibration decrease the geometrical parameters of an in-filled trench should satisfy the following conditions:

$$W > \lambda \quad D > 0.6\lambda, \tag{2.9}$$

where W and D are the height and the width of the filled trench, λ is the wavelength of the Rayleigh wave propagating in soil. Additionally, stiff trenches are shown to be more effective than the soft ones, while for the foundations the situation is opposite. Hence soft elastic foundation provides better vibration decrease. In addition to that, it is claimed that the density, damping ratio and the location of the in-filled trench affect vibration reduction insignificantly.

Ekanayake et al. study the infilled wave barriers using finite element method with the verification of a model on the field experiments performed using the EPF geofoam barrier [45]. The study of open and water infilled trenches as well as EPS geofoam barriers is carried out. The constitutive model for the geofoam is based on Drucker-Prager yield criterion with the hardening law implemented. Water in the trench is simulated by using the Mie-Grüneisen equation of state implemented in Abaqus [140]. The obtained results reveal that the EPS geofoam barrier is close to the open trenches in vibration attenuation effect providing a good level of vibration protection. In addition to that, this barrier is better for passive vibration isolation than active. At the same time, the EPS geofoam barrier is more effective than the water filled one, however the latter outperforms the EPS geofoam barrier if the width significantly increases along with the distance from the source.

In [64], Jesmani et al. study the influence of a trench geometrical properties on vibration reduction in sandy-soil using 3D FE model. Bi-linear elasto-plastic constitutive law is used to simulate the soil behaviour. It is obtained that the optimal trench arc angle (the angle characterizing arc length along which the barrier surrounds the protected area) equals to 150 degrees , meanwhile the trench radius does not affect the screening properties of such barrier. Additionally, it is worth noting the vibration amplitude increase near the trench.

The main disadvantage of FEM for addressing the problems considered in this work is the requirement to increase the model sizes to prevent the waves reflected from the model borders from returning to the observation zone. One of the methods allowing for reduction of the model sizes is so-called not-reflecting boundaries (in [140] “the infinite element” term is used). In [103], Motamedi et al. use Abaqus for parametric study of wave barriers along with the possibility to use the non-reflected boundaries or so called infinite elements. The authors carry out the results verification on seismic wave propagation from a surface loading using the data from the centrifuge tests. Then, accounting for the verification results,a parametric study of the barrier vibration reduction effect is carried out. The analysis shows that the increase in the barrier stiffness and height improves the attenuation properties significantly. While barrier width influences its vibration attenuation effect only for the barriers made of soft materials.

The reduction of blast induced vibration by vertical barriers is studied by Wang et al. using Ls-Dyna in [145]. Model proposed by Kreig in [74] is used for the GeoFoam and soil, compression hardening model is used for the concrete. The obtained results reveal a trench to be the most effective barrier, however due to the possibility of soil collapse such a barrier is not appropriate for the protection from blast induced shock waves. On the other hand, concrete walls are able to resist the inertia loading but could not reduce the ground shock impact significantly. Meanwhile,

the Geofoam barrier is found to be effective in shock wave energy reduction and it is easier to construct and maintain than open trenches.

Vibration reduction by dual trenches is studied by Saikira et al. under plane strain conditions using elastic constitutive law for the proposed materials [127]. It is found that a relative shear wave velocity of the in-filled trench (the ratio of the shear wave velocity in the barrier material to that in the surrounding soil) influences barrier reduction effect. The decrease in the relative shear wave velocity ratio results in the growth of the barrier reduction effect. However, this value has a certain limit below which the decrease in relative shear wave velocity not necessary increases the screening efficiency of the barrier. The optimal values of relative shear wave velocity are found for some barrier heights. In addition to that, it is found that dual in-filled trenches require less depth than the single one to obtain the targeted degree of vibration reduction.

One of the most comprehensive studies of vertical seismic barriers is performed in [119]. The effect of barrier material stiffness, density and barrier depth upon vibration energy attenuation within the protected area is shown. Applicability of vertical barriers for blast protection is also studied. The main disadvantage of this work is the complexity of some design solutions proposed for practical implementation and disregard of soil deformation character, depending on shear strain level in the case of blast exposure.

In [5, 112], coupled FE-BEM is used to study protection from the vibrations induced by passing trains using wave barriers. The effect of the train speed is shown [5]. In addition to that, other methods of vibration reduction like soil improving or replacement (soil stiffening) are studied [5]. Generally, trench is found to be effective measure for vibration reduction, while concrete barrier is more effective for low speed and frequencies.

In [33, 89], the mechanism of vibration propagation generated by railway transport along with potential protection measures are analysed. It is shown that the distance between the trench and railway track is a significant factor. Close to the track, body waves dominate and carry much vibration energy , therefore, a trench is useless as these waves can go under it and thus be unaffected by a barrier. Moreover, the cost of this type of protection is estimated for polyurethane foam as backfill material.

It is important to emphasize that none of the above works proposes the optimization algorithm for the practical barrier design accounting for prescribed soil and vibration conditions and ensuring minimum vibration level within the protected zone. One of the few exceptions is [151], where to optimize physical parameters of the underground trench (trench slope, inclination angle, vertical size and enclosure wall thickness) Taguchi approach is proposed [126]. However, in this work material properties of the barrier are not taken into account, which can be very important. As a result, the author obtained the optimal values of the inclined angle, the top thickness, the depth and the width of the trench with the value of transmission ratio equalling to 0.306.

Vibration mitigation using piles and pile fields

The study of piles as a vibration barrier started from the work of Richart and Woods [122], where the performance of this type of protection is investigated experimentally. In addition to that, the authors suggested the initial design guidelines for pile barriers. Later, Woods [149] confirmed the screening effect of cylindrical hole barriers on Rayleigh waves using holography. One of the first theoretical studies is performed by Javier Aviles and Sánchez-Sesma [8, 9], who theoretically analysed interaction of pile rows with body waves [8] as well as Rayleigh waves [9] using planar and spatial models. The authors suggest the values of pile length, spacing and the width of the barrier for effective vibration isolation.

In [66], Kattis et al. adopt Boundary Element Method (BEM) in the frequency domain to analyse vibration isolation by pile rows. Further development of this approach in [67] allow to model a pile row as an in-filled effective trench by using the homogenization method which is implemented in the mechanics of fibre-reinforced composite materials. In that work, the interac-

tion of pile row with Rayleigh waves is considered accounting one of the most important factors which is the volume fraction of the piles. It is worth noting, that this simulation method slightly overestimates the reduction effect of a pile row comparatively to the modelling of independent piles. Additionally, the authors show that trench barriers have a better reduction effect than pile rows and the type of a pile cross-section has virtually no effect on the vibration reduction.

Afterwards, this solution technique is extended for spatial simulation of pile row interaction with Rayleigh waves in frequency domain [68]. In addition to that, BEM is utilized in the work of Tsai [143] to study active vibration protection for different types of piles as well as pile length and spacing.

Another interesting approach based on the periodicity theory and FEM is implemented by Jiankun Huang [57] for the analysis of horizontal vibration attenuation by pile rows. Then, this method is further developed for plane waves in [58] and pile barriers with initial stress in [88]. In these works the authors propose the concept of the dispersion curves and analyse the attenuation zones produced by pile fields. The waves with the frequencies within the attenuation zone cannot propagate through the periodic pile barriers. It is shown that the reduction ratio of pile rows relates to relative Young's modulus, the density of the piles (ratio between these values corresponding to piles and soil) and the pile fraction [57]. Meanwhile, initial stress affects [88] the width as well as the lower and upper bounds of the attenuation zones having virtually no effect on the reduction effect.

Vibration attenuation properties of pile rows in porous media are analyzed in the works [27] and [26] of Yuan-Qiang Cai et al. for surface Rayleigh waves and body waves respectively by using Fourier-Bessel series. In this research, such key factors as pile spacing, relative pile Young's modulus and density are underlined. Moreover, it is shown that vibration isolation from Rayleigh waves in porous media is less effective than that in the non porous elastic media, which is not in the agreement with the study carried out by Lu [92] which presents better effectiveness of pile barrier for the case of two phase media.

Multiple body wave scattering by several pile rows is analyzed in [139] by the method proposed by the authors. It is shown that the increase in the number of rows improves vibration reduction properties of a pile barrier. At the same time, such method is found to have better screening effect for lower frequencies of body waves.

Conclusion

Based upon the bibliographical review of the international construction codes vibration protection standards as well as research works on seismic wave propagation and their interaction with inhomogeneities as well as seismic barriers and pile fields, it can be concluded that:

1. Existing international building codes and standards prescribe permissible vibration levels in buildings and facilities; their exceedance requires special-purpose activities related to vibration level decrease to the permissible value. In the case of earthquakes the accelerations, velocities and displacements of construction bases are regulated for different seismicity and construction sites, for example by [138].

2. Rayleigh waves transfer the major part of vibration energy in the case of external vibration sources and can transfer measurable portion of vibration energy when it is generated by underground sources . Based upon this, the development of techniques for protection against surface waves of this type is a significant issue for the present-day civil engineering.

3. The main principle of vibration protection by a vertical seismic barrier and a pile field is to diffract, reflect and dissipate wave energy preventing it from the transmitting into the protected zone, thus, reducing vibration displacements, velocities and accelerations of the

points within the protected area. It is theoretically proven by researches related to seismic wave scattering and reflection by obstacles and inhomogeneities in the elastic half-space.

4. Existing experimental and numerical studies related to the interaction of Rayleigh seismic waves with trenches,wave barriers of different types as well as pile fields support the applicability of these techniques for passive protection against vibrations transferred by Rayleigh waves. Active vibration protection with these barriers is less efficient due to waves passing around this obstacles and recovery of the vibration motion level behind the "shadow" zone.

5. Whereas the above studies evaluate the vibration mitigation within the protected area behind the barrier at different barrier parameters, the complex effect of the barrier material and geometrical parameters has not been shown. The suitable algorithm of barrier optimization in the case of prescribed soil conditions and design vibration loading has not been proposed.

6. Most of the researches related to vibration attenuation by piles and pile fields deal with the parameters of pile field independently regardless their complex effect on the vibration attenuation properties. Apart from that, the parameters of the pile fields obtained are difficult to implement in practice in terms of technology and construction codes.

7. In the majority of the researches described above, interaction of surface Rayleigh waves with vertical seismic barriers as well as pile fields is analysed under assumption of linear deformation character of the soil and barrier (pile field). This is possible only for low shear strain level in soil during wave propagation (less than 10^{-4}) which relates to traffic vibrations, construction works , etc. In the case of earthquakes and blast exposure, soil deformation character is strictly non-linear, thus, the results obtained are limited by the low amplitude vibration sources.

CHAPTER 3

CONSTITUTIVE EQUATIONS AND MATERIAL MODELS

Contents

The third chapter reviews the main constitutive laws and models that are used in soil mechanics to address static and dynamic problems. Constitutive equations for hyperelastic,elastic and elastoplastic media (Mohr Coulomb's, Drucker-Prager's and Cam-Clay-based models) are reviewed. Their comparative study as well as the assessment of the numerical parameters influence (these parameters are used to ensure solution procedure convergence) are performed. The possibility to approximate dynamic soil behaviour by using these models is analysed resulting in the selection of the model for the further dynamic computations. Additionally, boundary and initial conditions for the problems considered in the following chapters are formulated.

Basic notation

In this paragraph, the basic notation used in the following text is represented. Let $\boldsymbol{\sigma} = \sigma_{ij}$ is a second order symmetric stress tensor:

$$\boldsymbol{\sigma} = \begin{pmatrix} \sigma_{11} & \sigma_{12} & \sigma_{13} \\ \sigma_{21} & \sigma_{22} & \sigma_{23} \\ \sigma_{31} & \sigma_{32} & \sigma_{33} \end{pmatrix} \tag{3.1}$$

with its invariants defined as:

$$I_\sigma = tr(\sigma), \tag{3.2}$$

$$II_\sigma = \sigma_{12}^2 + \sigma_{23}^2 + \sigma_{13}^2 - (\sigma_{11}\sigma_{22} + \sigma_{22}\sigma_{33} + \sigma_{33}\sigma_{11}), \tag{3.3}$$

$$III_\sigma = det(\sigma). \tag{3.4}$$

Denoting $p = -I_\sigma/3$ (in some books this value is also called hydrostatic pressure), the deviatoric part of $\boldsymbol{\sigma}$ can be written in the form:

$$S = \begin{pmatrix} \sigma_{11} + p & \sigma_{12} & \sigma_{13} \\ \sigma_{21} & \sigma_{22} + p & \sigma_{23} \\ \sigma_{31} & \sigma_{32} & \sigma_{33} + p \end{pmatrix}. \tag{3.5}$$

In equations (3.1) and (3.5) $\sigma_{11}, \sigma_{22}, \sigma_{33}$ are the normal stresses ($\sigma_x, \sigma_y, \sigma_z$ in the case of orthogonal coordinate system XYZ), while $\sigma_{12} = \sigma_{21}, \sigma_{23} = \sigma_{32}, \sigma_{13} = \sigma_{31}$ are the shear stresses (they can also be denoted as $\tau_{xy} = \tau_{yx}, \tau_{yz} = \tau_{zy}, \tau_{xz} = \tau_{zx}$ in the case of orthogonal coordinate system XYZ). The following stress measures are considered:

$$q = \sqrt{\frac{3}{2} * (S : S)} \tag{3.6}$$

$$r = \left(\frac{9}{2} S \cdot S : S\right)^{\frac{1}{3}} \tag{3.7}$$

where (3.6) are the Mises equivalent stress and (3.7) is the third invariant of the deviatoric part of the stress tensor. In addition to that, the deviatoric polar angle [32] is also used when, for example, singular yield functions such as Mohr-Coulomb and Tresca ones are replaced by their smoothed approximation surfaces. This measure is determined as:

$$\Theta = \frac{1}{3} \arcsin\left(\frac{r}{q}\right)^3 \tag{3.8}$$

Similarly, symmetric second order strain tensor $\boldsymbol{\varepsilon} = \varepsilon_{ij}$ can be introduced:

$$\boldsymbol{\varepsilon} = \begin{pmatrix} \varepsilon_{11} & \varepsilon_{12} & \varepsilon_{13} \\ \varepsilon_{21} & \varepsilon_{22} & \varepsilon_{23} \\ \varepsilon_{31} & \varepsilon_{32} & \varepsilon_{33} \end{pmatrix} \tag{3.9}$$

with its invariants:

$$I_\varepsilon = tr(\boldsymbol{\varepsilon}), \tag{3.10}$$

$$II_\varepsilon = \varepsilon_{12}^2 + \varepsilon_{23}^2 + \varepsilon_{13}^2 - (\varepsilon_{11}\varepsilon_{22} + \varepsilon_{22}\varepsilon_{33} + \varepsilon_{33}\varepsilon_{11}), \tag{3.11}$$

$$III_\varepsilon = det(\varepsilon). \tag{3.12}$$

Similarly to the stress tensor, it is possible to change equations (3.9-3.12) to the conventional form by using x, y, z instead of $1, 2, 3$. Apart from that, the notation equivalent to the one used in Abaqus explicit solver [94] is utilized in the following text.

Reduction ratio. In order to estimate the efficiency of the barrier (pile field) in terms of the vibration decrease in the protected zone, the following ratio is introduced:

$$k_{red,E} = \frac{K_{bar}}{K_{hom}}, \tag{3.13}$$

where K_{hom} - is the kinetic energy field of the area Δ in the homogeneous model, while K_{bar} is the kinetic energy field of the area Δ in the model with the seismic barrier (pile field). It

shows the decrease of vibration energy in the protected zone after the installation of the barrier. Similar quantity is introduced for the displacements:

$$k_{red,u} = \frac{u_{bar}}{u_{hom}}, \tag{3.14}$$

where u_{hom} - is the displacement field in the area Δ in the homogeneous model, while u_{bar} is the displacement field in the area Δ in the model with the seismic barrier (pile field). This value allows to assess the displacement decrease in the protected zone.

Initial and boundary conditions

Initial conditions

The following ordinary initial conditions are considered:

$$\mathbf{u}(\mathbf{x},t)\Big|_{t=0} = \mathbf{0}, \quad \partial_t \mathbf{u}(\mathbf{x},t)\Big|_{t=0} = \mathbf{0}, \tag{3.15}$$

that are sufficient for the first stage calculations using the elastic constitutive law. In that case, the initial stress distribution in the half-space(half-plane) is neglected as it has virtually no effect on the displacements, velocities and accelerations of the points in the protected zone.

In the case of numerical simulation involving non-linear constitutive laws which are affected by initial stress distribution (elasto-plasticity, plasticity, etc.), instead of initial conditions defined by equation (3.15), the following conditions for initial stress and velocity fields are used:

$$\sigma(\mathbf{x},t)|_{t=0} = \sigma_0(\mathbf{x}), \quad \partial_t \mathbf{u}(\mathbf{x},t)\Big|_{t=0} = \mathbf{0}, \tag{3.16}$$

where $\sigma_0(\mathbf{x})$ is the initial stress distribution calculated from the static problem.

Boundary conditions

For isotropic media on the free surface of the half-space Π_ξ (Figure 3.1),the boundary condition of zero stress is used:

$$\mathbf{t}_\xi \equiv \boldsymbol{\sigma} \cdot \boldsymbol{\xi} = 0, \mathbf{x}' \in \boldsymbol{\Pi_\xi}, \tag{3.17}$$

where $\mathbf{I}$ is the unit diagonal matrix, $\boldsymbol{\xi}$ is the unit outward normal to the surface $\boldsymbol{\Pi_\xi}$ and $\mathbf{t}_\xi$ is surface stress. In the case of elastic media equation (3.17) can be written in the form:

$$\mathbf{t}_\xi \equiv (\lambda tr(\boldsymbol{\varepsilon})\mathbf{I} + 2\mu\boldsymbol{\varepsilon}) \cdot \boldsymbol{\xi} = 0, \quad \mathbf{x}' \in \boldsymbol{\Pi_\xi}, \tag{3.18}$$

where $\boldsymbol{\varepsilon}$- small strain tensor.

In the case of seismic barrier installed in the medium (Figure 3.1), the condition of perfect mechanical contact is applied to the contact surfaces between the barrier and the soil $\boldsymbol{\Omega_\eta}$:

$$\begin{aligned} \mathbf{t}_{bar}\Big|_{\mathbf{x}\cdot\boldsymbol{\eta}\in\Omega_\eta} &= \mathbf{t}_{soil}\Big|_{\mathbf{x}\cdot\boldsymbol{\eta}\in\Omega_\eta}, \\ \mathbf{u}_{bar}\Big|_{\mathbf{x}\cdot\boldsymbol{\eta}\in\Omega_\eta} &= \mathbf{u}_{soil}\Big|_{\mathbf{x}\cdot\boldsymbol{\eta}\in\Omega_\eta} \end{aligned} \tag{3.19}$$

where $\mathbf{t}_{bar}$, $\mathbf{t}_{soil}$ are the stresses on the contact surface from the barrier and soil sides respectively; $\boldsymbol{\eta}$ is the unit normal to the interface between the barrier and soil Ω_η; $\mathbf{u}_{bar}$, $\mathbf{u}_{soil}$ are the displacement vectors on the contact surface from the barrier and soil sides respectively; the indexes *bar* and *soil* correspond to the barrier and soil accordingly.

Similar contact condition is used to simulate contact between piles and soil. Let $\mathbf{\Theta}_\zeta$ denotes the interface between the pile and soil with the unit outward normal $\boldsymbol{\zeta}$.Then, the condition of perfect mechanical contact for the lateral pile surface takes the following form:

$$\begin{aligned} \mathbf{t}_{pile}\Big|_{\mathbf{x}\cdot\boldsymbol{\zeta}\in\mathbf{\Theta}_\zeta} &= \mathbf{t}_{soil}\Big|_{\mathbf{x}\cdot\boldsymbol{\zeta}\in\mathbf{\Theta}_\zeta} \\ \mathbf{u}_{pile}\Big|_{\mathbf{x}\cdot\boldsymbol{\zeta}\in\mathbf{\Theta}_\zeta} &= \mathbf{u}_{soil}\Big|_{\mathbf{x}\cdot\boldsymbol{\zeta}\in\mathbf{\Theta}_\zeta} \end{aligned} \tag{3.20}$$

where the indexes *pile* and *soil* correspond to the piles and soil respectively.

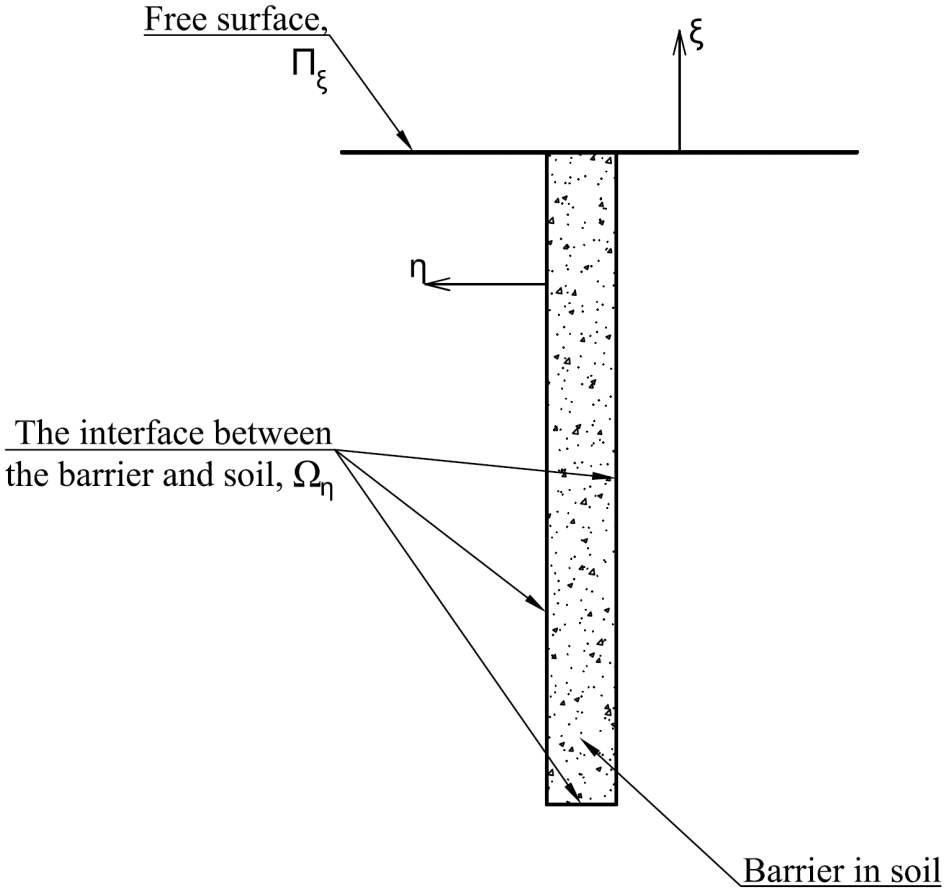

Figure 3.1: Boundary conditions.$\boldsymbol{\xi}$ and $\boldsymbol{\eta}$ are the unit normals to the free surface of the half-space and contact interface between the barrier and soil respectively.

Hyperelastic media

Constitutive equations for hyperelastic media

The first part of the present work is targeted to the search for the optimal configuration of the wave barrier (the dimensions of the barrier and the mechanical characteristics of its material) as well as a pile field (planar dimensions of a pile field as well as pile depth) ensuring maximum vibration reduction in the protected zone. The solution is performed assuming the soil and barrier material to deform according to linear elastic constitutive law, which is appropriate if shear strains in the soil do not exceed 10^{-4} (low amplitude vibration sources). Therefore, it is necessary to introduce constitutive relations for hyperelastic media (linear elastic constitutive law is a particular case in this category of elastic models).

Hyperelastic material is the one for which it is possible to define elastic potential in the form [142]:

$$\Psi = \Psi(I_\varepsilon, II_\varepsilon, III_\varepsilon), \tag{3.21}$$

where $I_\varepsilon, II_\varepsilon, III_\varepsilon$ are defined according to equations (3.10 - 3.11). In that case, the stresses are calculated as:

$$\sigma = \nabla_\varepsilon \Psi(I_\varepsilon, II_\varepsilon, III_\varepsilon), \tag{3.22}$$

or:

$$\sigma = \lambda(I_\varepsilon, II_\varepsilon, III_\varepsilon) I_\varepsilon \mathbf{I} + 2\mu(I_\varepsilon, II_\varepsilon, III_\varepsilon)\varepsilon. \tag{3.23}$$

Lame's constants λ and μ must satisfy the condition:

$$3\lambda + 2\mu > 0, \mu > 0, \tag{3.24}$$

in order to ensure the deformation energy to be positive [142].

In the case of a linearly elastic material and infinitesimal strains the equation of motion can be written as:

$$\mathrm{div}_{\mathbf{x}} \mathbf{C} \cdot \cdot \nabla_{\mathbf{x}} \mathbf{u} - \rho \ddot{\mathbf{u}} = 0, \tag{3.25}$$

where $\mathbf{u}(\mathbf{x}, \mathbf{t})$ is the displacement vector;$\mathbf{C}$ is positively defined elasticity tensor (in the case of isotropic elastic media equation (3.24) is the condition of positive definiteness of the elastic tensor $\mathbf{C}$); ρ is the material density.

For isotropic homogeneous media equation (3.25) can be written in Navier-Clapeyron form:

$$(\lambda + 2\mu)\nabla \mathrm{div}\mathbf{u}(\mathbf{x}, t) + \mu \mathrm{rotrot}\mathbf{u}(\mathbf{x}, t) + \mathbf{f}(\mathbf{x}, t) = \rho \ddot{\mathbf{u}}(\mathbf{x}, t), \tag{3.26}$$

where $\mathbf{f}(\mathbf{x}, t)$ is a body forces field. Denoting longitudinal (P-wave) and shear (S-wave) velocities as:

$$c_P = \sqrt{\frac{\lambda + 2\mu}{\rho}}, \quad c_S = \sqrt{\frac{\mu}{\rho}} \tag{3.27}$$

respectively equation (3.26) can rewritten to the form:

$$c_P^2 \nabla \mathrm{div}\mathbf{u}(\mathbf{x}, t) - c_S^2 \mathrm{rotrot}\mathbf{u}(\mathbf{x}, t) + \frac{1}{\rho}\mathbf{f}(\mathbf{x}, t) = \ddot{\mathbf{u}}(\mathbf{x}, t). \tag{3.28}$$

Major wave types

Major wave types generated by external and internal sources of vibration, that are considered in this work, are body waves including longitudinal and shear waves as well as surface waves including Rayleigh, Stoneley, Love and Lamb waves. In this thesis, the main attention is paid to Rayleigh surface waves and body waves. Therefore, wave equations for these waves are shown in the following text.

Plane P-waves and S-waves

Theory of body waves propagation in an infinite space is mainly developed in the works of Poisson [115],[116], etc. Wave equation for a travelling body wave with plane wavefront has the following form:

$$\mathbf{u}(\mathbf{x},t) \equiv \mathbf{m}\exp\left(ir(\mathbf{n}\cdot\mathbf{x}-ct)\right), \tag{3.29}$$

where $\mathbf{m}$ is the oscillation amplitude, $\mathbf{n}$ is a unit wave vector that determines the direction of wave propagation; c is a phase velocity; $r = \frac{\omega}{2\pi c}$ is a wave number and ω is a circular frequency.Substitution of equation (3.29) into (3.26) produces Christoffel equation:

$$\left((\lambda+2\mu)\mathbf{n}\otimes\mathbf{n}+\mu(\mathbf{I}-\mathbf{n}\otimes\mathbf{n})-\rho*c^2\mathbf{I}\right)\cdot\mathbf{m}=0. \tag{3.30}$$

Solution of equation (3.30) gives the wave velocities and directions of polarization. As a result, three waves having mutually orthogonal polarization are obtained from the solution of equation (3.30). Which are P -wave (longitudinal wave polarized in the direction of propagation) as well as SH and SV waves (shear waves polarized in the directions orthogonal to the propagation direction). SV and SH wave are polarized in vertical and horizontal directions respectively [47].

Surface waves

Based on the approach in [78, 79] the equation of a surface wave travelling in a half-space or in a layer with arbitrary anisotropy has the form:

$$\mathbf{u}(\mathbf{x},t) \equiv \mathbf{f}(x")\exp\left(ir(\mathbf{n}\cdot\mathbf{x}-ct)\right), \tag{3.31}$$

where $x'' = ir(\boldsymbol{\nu}\cdot\mathbf{x})$ is a dimensionless complex variable; $\mathbf{f}(x")$ is an undetermined functions defining the amplitudes on the wavefront; $\mathbf{n}$ is a unit wave vector that determines the direction of the wave propagation; $\boldsymbol{\nu}$ is an outward normal to the boundary Π_ν along which the wave propagates. Substitution of equation (3.31) into (3.25) produces Christoffel equation for the surface wave propagating in an anisotropic half-space:

$$-r^2\left(\mathbf{A}\partial^2_{x"}+\mathbf{B}\partial^2_{x"}+\mathbf{D}\right)\cdot\mathbf{u}=0, \tag{3.32}$$

where $\mathbf{A}$, $\mathbf{B}$ and $\mathbf{D}$ are defined by equation (3.33) with $\mathbf{I}$ being a unit matrix of the third order.

$$\mathbf{A}=\boldsymbol{\nu}\cdot\mathbf{C}\cdot\boldsymbol{\nu};\mathbf{B}=\boldsymbol{\nu}\cdot\mathbf{C}\cdot\mathbf{n}+\mathbf{n}\cdot\mathbf{C}\cdot\nu;\mathbf{D}=\mathbf{n}\cdot\mathbf{C}\cdot\mathbf{n}+\rho c^2\mathbf{I}. \tag{3.33}$$

Introducing $\mathbf{w}=\partial^{\mathbf{2}}_{\mathbf{x}"}$ and Jacobian $\mathbf{G}$ defined by equation (3.34), equation (3.32) can be transformed to the form (3.35).

$$\mathbf{G}=\begin{pmatrix}\mathbf{0} & \mathbf{I}\\ -\mathbf{A}^{-1}\mathbf{D} & -\mathbf{A}^{-1}\mathbf{B}\end{pmatrix}. \tag{3.34}$$

$$\partial^2_{x"}\begin{pmatrix}\mathbf{f}\\ \mathbf{w}\end{pmatrix}=\mathbf{G}\cdot\begin{pmatrix}\mathbf{f}\\ \mathbf{w}\end{pmatrix}; \tag{3.35}$$

In equation (3.34) $\mathbf{0}$ is a square zero matrix of the third order. Taking equations (3.34-3.35) into account, the solution of equation (3.32) can be written in the form:

$$\begin{pmatrix}\mathbf{u}(\mathbf{x},t)\\ \mathbf{z}(\mathbf{x},t)\end{pmatrix}=\left(\exp(x''\mathbf{G})\cdot\mathbf{C}\right)\exp\left(ir(\mathbf{n}\cdot\mathbf{x}-ct)\right), \tag{3.36}$$

where $\mathbf{z}(\mathbf{x},t)=\mathbf{w}(x'')\exp\left(ir(\mathbf{n}\cdot\mathbf{x}-ct)\right)$. It is worth noting that equation (3.36) holds for $\mathbf{G}$ having Jordan blocks in the canonical form.

Rayleigh waves in anisotropic half-space

Wave equation for a plane Rayleigh wave propagating in anisotropic half-space has the following form:

$$\mathbf{u}(\mathbf{x},t) \equiv \mathbf{m}(ir\boldsymbol{\nu}\cdot\mathbf{x})\exp\left(ir(\mathbf{n}\cdot\mathbf{x}-ct)\right), \tag{3.37}$$

In this case the polarization of the wave ($\mathbf{m}$) depends upon the depth and the wave number (r). Additional condition for the complex coordinate $Im(x'') < 0$ is applied on the half-space. Other variables are the same as in equation (3.31). Christoffel equation for this case can be obtained by the substitution of equation (3.37) into (3.25):

$$\left(\boldsymbol{\nu}\cdot\mathbf{C}\cdot\boldsymbol{\nu}\frac{\partial^2}{\partial x''^2}+(\boldsymbol{\nu}\cdot\mathbf{C}\cdot\mathbf{n}+\mathbf{n}\cdot\mathbf{C}\cdot\boldsymbol{\nu})\frac{\partial^2}{\partial x''^2}+\mathbf{n}\cdot\mathbf{C}\cdot\mathbf{n}-\rho c^2\mathbf{I}\right)\cdot\mathbf{m}(x'')=0 \tag{3.38}$$

Introducing a new variable $\mathbf{v}(x'')=\frac{\partial}{\partial x''}\mathbf{m}(x'')$ the equation can be transformed to the form:

$$\left(\mathbf{A_1}\cdot\frac{\partial}{\partial x''}\mathbf{v}(x'')+\boldsymbol{\nu}\cdot\mathbf{C}\cdot\mathbf{n}+\mathbf{A_2}\frac{\partial}{\partial x''}\mathbf{v}(x'')+\mathbf{A_3}\right)\cdot\mathbf{m}(x'')=0, \tag{3.39}$$

where $\mathbf{A_1}$,$\mathbf{A_2}$ and $\mathbf{A_3}$ are defined as:

$$\mathbf{A}=\boldsymbol{\nu}\cdot\mathbf{C}\cdot\boldsymbol{\nu};\mathbf{B}=\boldsymbol{\nu}\cdot\mathbf{C}\cdot\mathbf{n}+\mathbf{n}\cdot\mathbf{C}\cdot\nu;\mathbf{D}=\mathbf{n}\cdot\mathbf{C}\cdot\mathbf{n}-\rho\cdot c^2\mathbf{I}. \tag{3.40}$$

As a result, similarly to equation (3.36) the system of first order equations is obtained:

$$\frac{\partial}{\partial x''}\vec{X}=\mathbf{G}\cdot\vec{X}, \tag{3.41}$$

where $\vec{X}=\begin{pmatrix}\mathbf{m}\\ \mathbf{v}\end{pmatrix}$ and $\mathbf{G}=\begin{pmatrix}\mathbf{0} & \mathbf{I}\\ -\mathbf{A}^{-1}\mathbf{D} & -\mathbf{A}^{-1}\mathbf{B}\end{pmatrix}$. In order to formulate closed system of equations defining Rayleigh wave velocity it is necessary to adopt boundary conditions (3.17) and the condition of Sommerfeld (the absence of the solutions growing exponentially at $Im(x'')\rightarrow-\infty$). One of the most important research directions related to Rayleigh wave propagation in anisotropic elastic half-space is the search for the "forbidden directions" for Rayleigh wave (in that particular directions Rayleigh wave cannot propagate in the considered material). However, it is shown [79],[30],[12],[13], [90], [29] and [31] that there is no such "forbidden directions". Therefore , vibrations transferred by surface Rayleigh waves can be decreased only due to the processes of wave scattering and reflection by inhomogeneities and obstacles in the media as well as energy dissipation in soil because of its plastic deformation nature.

Rayleigh waves in isotropic half-space

If a half space is an isotropic and hyperelastic, equation (3.37) defining Rayleigh wave, that propagates in this media, can be simplified to the form:

$$\mathbf{u}(\mathbf{x},t)=\sum_{k=1}^{2}t_i\mathbf{m}_k\exp\left(ir(\gamma_k\boldsymbol{\nu}\cdot\mathbf{x}+\mathbf{n}\cdot\mathbf{x}-ct)\right), \tag{3.42}$$

where m_k defines the polarization of partial waves. Other variables are the same as in equations (3.37-3.41). Christoffel equation for a Rayleigh wave propagating in elastic half-space has the form:

$$\begin{aligned}\left(\gamma_k^2((+2\mu)\boldsymbol{\nu}\otimes\boldsymbol{\nu}+\mu\mathbf{n}\otimes\mathbf{n})+\gamma_k((\lambda+\mu)(\boldsymbol{\nu}\otimes\mathbf{n}+\mathbf{n}\otimes\boldsymbol{\nu}))+\right.\\ \left.+(\lambda+2\mu)\mathbf{n}\otimes\mathbf{n}+\mu\boldsymbol{\nu}\otimes\boldsymbol{\nu}-\rho c^2\mathbf{I}\cdot\mathbf{m}_k=0,\right.\end{aligned} \tag{3.43}$$

where γ_k can be calculated from the condition of zero determinant:

$$\begin{aligned}det\left(\gamma_k^2((+2\mu)\boldsymbol{\nu}\otimes\boldsymbol{\nu}+\mu\mathbf{n}\otimes\mathbf{n})+\gamma_k((\lambda+\mu)(\boldsymbol{\nu}\otimes\mathbf{n}+\mathbf{n}\otimes\boldsymbol{\nu}))+\right.\\ \left.+(\lambda+2\mu)\mathbf{n}\otimes\mathbf{n}+\mu\boldsymbol{\nu}\otimes\boldsymbol{\nu}-\rho c^2\mathbf{I}=0.\right.\end{aligned} \tag{3.44}$$

Rayleigh wave velocity can be calculated by adding boundary condition (3.18) resulting in quite complex equation. Therefore, the approximation of Bergmann and Victorov [144] is used to calculate Rayleigh wave velocity:

$$c_R = \frac{0.87 + 1.12\nu}{1 + \nu} c_S, \tag{3.45}$$

where c_R and c_S are Rayleigh and shear waves velocities respectively, ν - Poisson's ratio.

Non-linearly deformable media

Basic principles

In this work only infinitesimal deformations are considered as even at strong earthquakes shear strains do not exceed $2 \cdot 10^{-3}$ (in the case of an explosion shear strains in the soil can achieve 10^{-2}) [62, 132]. Therefore, small deformation tensor is considered:

$$\varepsilon_{ij} = \frac{1}{2}\left(\frac{\partial u_i}{\partial x_j} + \frac{\partial u_j}{\partial x_i}\right). \tag{3.46}$$

Here u_i are the components of the displacement vector $\mathbf{u}(\mathbf{x})$ and dx_j is the initial size of the element for which the strain is calculated.

Remark. It is worth noting that this approach with the use of infinitesimal strains can be inappropriate for the vicinity of vibration source, especially in the case of earthquake and explosion sources. However, this approach is valid at a certain distance from the source because the strains decrease due to the geometric and material damping in soil.

The integration of elsto-plastic constitutive equations is based upon strain increment decomposition into plastic $d\varepsilon_{ij}^{pl}$ and elastic $d\varepsilon_{ij}^{el}$ parts [50]

$$d\varepsilon_{ij} = d\varepsilon_{ij}^{el} + d\varepsilon_{ij}^{pl}. \tag{3.47}$$

The character of stress-strain condition is determined with the use of smooth yield surface of the form [50]:

$$f\left(I_\sigma, II_\sigma, III_\sigma, I_{\varepsilon^{pl}}, II_{\varepsilon^{pl}}, III_{\varepsilon^{pl}}\right). \tag{3.48}$$

If $f < 0$ then the deformation is elastic, otherwise ($f = 0$) the material experiences plastic deformation.

Numerical integration of constitutive equations (plasticity, nonlinear elasticity) is usually performed by using approximate numerical schemes, for example, Newton's one. In this case, the loading of a body and the numerical integration of its stress-strain condition is performed in several steps (increments). This means that the body is loaded over some time period (in the case of static problems this is quasi time) which is divided into several time steps depending on the solution procedure convergence as well as the type of numerical scheme. At which step, stress-strain condition of the body is calculated. Numerical aspects of the implementation of these methods within the framework of spatial discretization using FEM for dynamic and static problems are given in [155, 156, 19]. Here it is important to emphasize that all these approaches require incremental forms of constitutive equations. Therefore,stress and strain rates are considered at each step. As an example, the Jauman rate equation for Hooke's law in the case of linear elasticity can be written in the form:

$$\triangle\, \dot{\sigma}_{ij}^{J} = \lambda \delta_{ij} \triangle\, \dot{\varepsilon}_{kk} + 2\mu \triangle\, \dot{\varepsilon}_{ij}, \tag{3.49}$$

where $\dot{\sigma}_{ij}^{J}$ and $\dot{\varepsilon}_{ij}$ are stress and strain rate tensors accordingly; $\dot{\varepsilon}_{kk}$ is the first invariant of strain rate tensor; λ, μ are Lame's parameters. All the constitutive equations in the following text will be written using incremental form according to the numerical schemes implemented in the software.

Perfectly plastic media

In the case of perfect plasticity no hardening is observed (the corresponding part of the curve $\sigma - \varepsilon$ is a straight line which is parallel to the axis σ) and stresses in the media are defined solely by elastic part of the deformation(ε_{ij}^{el}). Then, yield potential G is introduced as a function:

$$G\left(I_\sigma, II_\sigma, III_\sigma, I_{\varepsilon^{pl}}, II_{\varepsilon^{pl}}, III_{\varepsilon^{pl}}\right), \tag{3.50}$$

that coincides with the yield surface function (3.48) in the case of associated flow rule. If these functions are described by different equations, flow rule is called non-associated. In the following text non-associated flow rule is considered, as it is more general case and more suitable for soils. In that case plastic deformations are defined as:

$$\dot{\varepsilon}_{pl} = \mathrm{d}\lambda \frac{\mathrm{d}G}{\mathrm{d}\sigma_{ij}}, \tag{3.51}$$

where $\mathrm{d}\lambda$ is a positive scalar and the operator $\frac{\mathrm{d}G}{\mathrm{d}\sigma_{ij}}$ is the gradient of the plastic potential in the stress space taking the form $\left(\frac{\mathrm{d}G}{\mathrm{d}\sigma_{xx}}; \frac{\mathrm{d}G}{\mathrm{d}\sigma_{yy}}; \frac{\mathrm{d}G}{\mathrm{d}\sigma_{zz}}; \frac{\mathrm{d}G}{\mathrm{d}\sigma_{xy}}; \frac{\mathrm{d}G}{\mathrm{d}\sigma_{yz}}; \frac{\mathrm{d}G}{\mathrm{d}\sigma_{zx}}\right)$ (it can also be denoted as $\nabla_{\boldsymbol{\sigma}}$). The scalar $\mathrm{d}\lambda$ can be obtained using Geiringer's condition [50], which contains the requirement for the stresses to belong to the yield surface at each step if plastic flow occurs. It can be formulated in the form:

$$\nabla_{\boldsymbol{\sigma}} G \cdot\cdot \dot{\boldsymbol{\sigma}} = 0. \tag{3.52}$$

Taking into account that the stress is determined by elastic deformation part:

$$\dot{\varepsilon}_{el} = \dot{\varepsilon} - \mathrm{d}\lambda \frac{\mathrm{d}G}{\mathrm{d}\sigma_{ij}} \tag{3.53}$$

and Hooke's law:

$$\boldsymbol{\sigma} = C^E \dot{\boldsymbol{\varepsilon}}, \tag{3.54}$$

the equation from which the scalar $\mathrm{d}\lambda$ can be obtained can be written as:

$$\mathrm{d}\lambda = \frac{\{\nabla_{\boldsymbol{\sigma}} G\}^T \cdot\cdot \{C^E \cdot \dot{\boldsymbol{\varepsilon}}\}}{\{\nabla_{\boldsymbol{\sigma}} G\}^T \cdot\cdot \{C^E \cdot \nabla_{\boldsymbol{\sigma}} G\}}. \tag{3.55}$$

In equations (3.54-3.55) C^E is an elasticity tensor;$\{\nabla_{\boldsymbol{\sigma}}\}$ is the transposed matrix of the gradient of the plastic potential in stress space; $\dot{\boldsymbol{\varepsilon}}$ is the strain rate tensor.

Hardening plasticity

It is possible to define three types of hardening: (1) isotropic; (2) kinematic and (3) mixed hardening. In the case of isotropic hardening yield surface growths equally in all directions expanding the zone of elastic deformations. Therefore, the initial yield stress equaling to σ_{Y_0} changes after unloading to the value $\sigma_Y \geq \sigma_{Y_0}$ (Figure 3.2, [19]). In the case of kinematic hardening yield surface moves in the direction of loading (Figure 3.2, [19]).Mixed hardening type comprises the main features of kinematic and isotropic hardening. Apart from that, other types of hardening that are beyond the scope of the present work can be considered, [32, 19, 55, 44]

For plasticity models with hardening, hardening module k is defined to determine the relation between plastic stresses and strains as well as the size of the yield surface [32, 50]:

$$\dot{\sigma} = k\dot{\varepsilon}. \tag{3.56}$$

It is worth noting that it is possible to implement linear and non-linear hardening (in the case of non-linear hardening k can depend on the chosen stress or strain measure). Positive scalar $d\lambda$ is

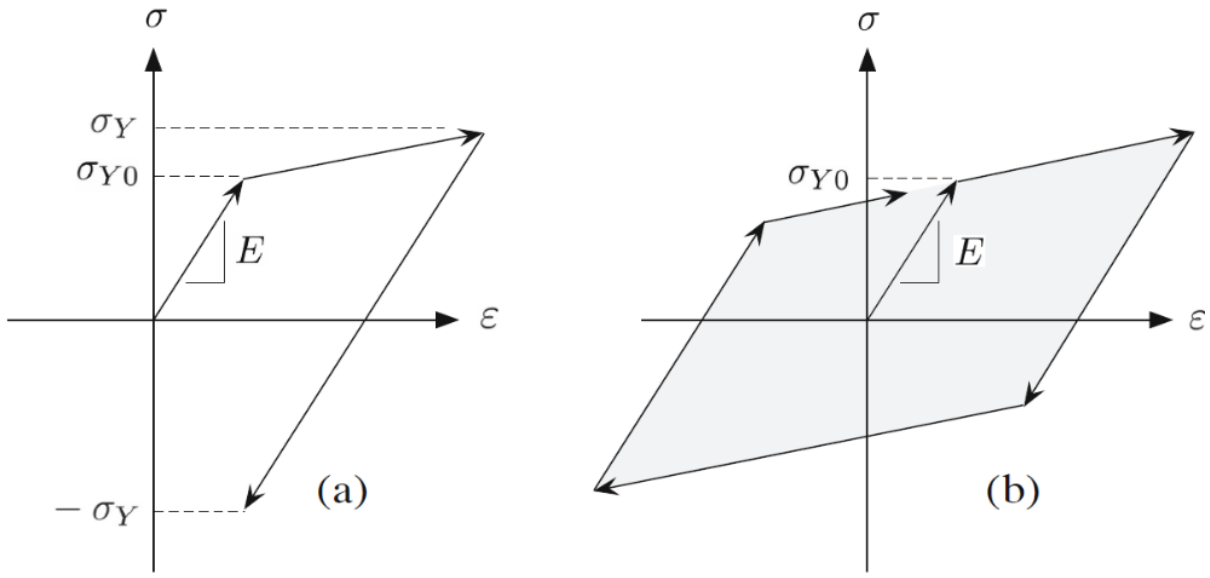

Figure 3.2: Isotropic (a) and kinematic hardening (b), [19]

calculated assuming that a new point in stress space belongs to the new yield surface obtained as a result of hardening:

$$\mathrm{d}\lambda = \frac{1}{k}\frac{\{\nabla_{\boldsymbol{\sigma}} G\}^T \cdot\cdot \{C^E \cdot \dot{\boldsymbol{\varepsilon}}\}}{\{\nabla_{\boldsymbol{\sigma}} G\}^T \cdot\cdot \{C^E \cdot \nabla_{\boldsymbol{\sigma}} G\}}. \tag{3.57}$$

Additionally, constitutive equation in this case is usually complemented by Drucker's postulate [50]:

$$\mathrm{d}\lambda = \dot{\boldsymbol{\sigma}} \cdot\cdot \dot{\boldsymbol{\varepsilon}} \geq 0. \tag{3.58}$$

In the case of isotropic hardening, yield surface depends on k and the plastic strain measure chosen for the model. Obviously, this approach has its disadvantages including impossibility to account for Bauschinger effect and possible exhaustion of plasticity if a large number of cycles takes place [50]. However, this approach can be used at low number of loading -unloading cycles.

If kinematic hardening occurs, the yield surface moves in the direction of loading, thus, this hardening type is the most appropriate for the simulation of hysteresis behaviour in the case of cyclic loading. Mathematically this hardening rule can be written in the form:

$$\mid f - c(k) \mid = f_0, \tag{3.59}$$

where $c(k)$ is a function depending upon hardening parameter k and f_0 is an initial yield surface. [32].

In the present work a linear isotropic hardening with small $k \leq 0.001$ is considered as it is typical to the majority of soils as well as the number of cycle considered is less than 20.Thus, this approach allows the modelling of soil hysteresis behaviour in the case of cyclic loading. However, other effects such as the Masing rules are not taken into account [62].

Models based on the Mohr-Coulomb and Drucker-Prager criteria

Models based on the Mohr-Coulomb and Drucker-Prager criteria (in the following text they are denoted as Mohr-Coulomb and Drucker-Prager models) relate to the yield criteria depending on the first invariant of the stress tensor $\mathbf{I}_\sigma$ (hydrostatic pressure).In the following text the mathematical formulation of these criteria and the corresponding plastic potentials are given. Additionally, the effect of the numerical parameters introduced in these models upon the hysteresis loops is shown.

Mohr-Coulomb model

Mohr-Coulomb yield criteria has the following form:

$$\tau_{max} = \frac{\sigma_{max} - \sigma_{min}}{2} \leq f(\mathbf{I}_\sigma, \mathbf{II}_\sigma), \tag{3.60}$$

where σ_{max}, σ_{min} are the maximal and minimal principal stresses respectively. The yield surface that satisfies this criterion is a hexagonal pyramid in the space of principal stresses. The principal idea behind this approach is that a medium goes into a plastic state when the shear stresses exceed the value $f(\mathbf{I}_\sigma, \mathbf{II}_\sigma)$ that can be defined as:

$$(\mathbf{I}_\sigma, \mathbf{II}_\sigma) = c - p\tan\phi, \tag{3.61}$$

where c is cohesion stress, ϕ is friction angle and p is hydrostatic pressure or $(-\mathbf{I}_\sigma/3)$.

In the models based on Mohr-Coulomb approach both perfect and hardening plasticity can be implemented.This model is one of the most oftenly used in soil mechanics as the shear damage mechanism is inherent to many soils. Nevertheless, this model has its drawbacks one of which is the loss of smoothness in the vertex zone and the angles of the pyramid which complicates numerical integration of the constitutive equations. it can be resolved by using smooth approximating yield surface [19], that can be described by the following equation [140]:

$$f\left(p, q, \|\boldsymbol{\varepsilon_{pl}}\|\right) \equiv R_{MC}(\Theta, \phi)q - c(\|\boldsymbol{\varepsilon}_{pl}\|) - p * tan(\phi) = 0, \tag{3.62}$$

where $\|\boldsymbol{\varepsilon}_{pl}\|$ is a predefined strain measure in the model; ϕ and $c(\|\boldsymbol{\varepsilon_{pl}}\|)$ are friction angle and cohesion respectively; p,q and Θ are defined by equations (3.6-3.8). R_{mc} is determined by the following equation:

$$R_{MC}(\Theta, \phi) = \frac{1}{\sqrt{3}\cos\phi}\sin\left(\Theta + \frac{\pi}{3}\right) + \frac{1}{3}\cos\left(\Theta + \frac{\pi}{3}\right)\tan\phi. \tag{3.63}$$

In the case of potential plastic flow, plastic strains are calculated as [94]:

$$\begin{aligned} d\varepsilon_{pl} &= \frac{d\overline{\varepsilon_{pl}}}{g}\frac{\partial G}{\partial \sigma} \\ g &= \frac{1}{c}\sigma : \frac{\partial G}{\partial \sigma} \end{aligned} \tag{3.64}$$

and plastic flow potential G has the following form:

$$G\left(p, q, \|\boldsymbol{\varepsilon}_{pl}\|\right) = \sqrt{(\epsilon c_0 \tan\phi)^2 + (R_{mw}q)^2} - p\tan\phi \tag{3.65}$$

where ψ is the dilation angle , c_0 is the initial value of the cohesion and ϵ is the parameter used to smooth the yield surface in the meridional stress plane; θ is Lode's angle defined by equation (3.8) . $R_{mw}\left(\Theta, e\right)$ defines the approximation of the Mohr-Coulomb yield surface in the deviatoric plane and has the form:

$$R_{mw}\left(\Theta, e\right) = \frac{4 * (1-e^2)\cos^2\theta + (2e-1)^2}{2(1-e^2)\cos\theta + (2e-1)\sqrt{4(1-e^2)\cos^2\theta + 5e^2 - 4e}}\frac{3 - \sin\phi}{6\cos\phi}. \tag{3.66}$$

In equations (3.65) and (3.66), numerical parameters e and ϵ determine the smoothness of the yield surface and flow potential in meridional and deviatoric plans. This approach avoids the loss of smoothness during numerical integration procedure in the zone of the pyramid vertex and in the areas of its edges. Nevertheless, it is rather complicated for numerical realization because of the necessity to differentiate trigonometric functions. In addition to that, there is another approach allowing to avoid the differentiation of the trigonometric functions during numerical integration process of the plasticity equations. It is based on the polar decomposition of the stress and strain tensors while the integration is carried out by the return mapping method for various sections of the yield surface. In more details, this technique and numerical implementation are described in [19, 44, 152].

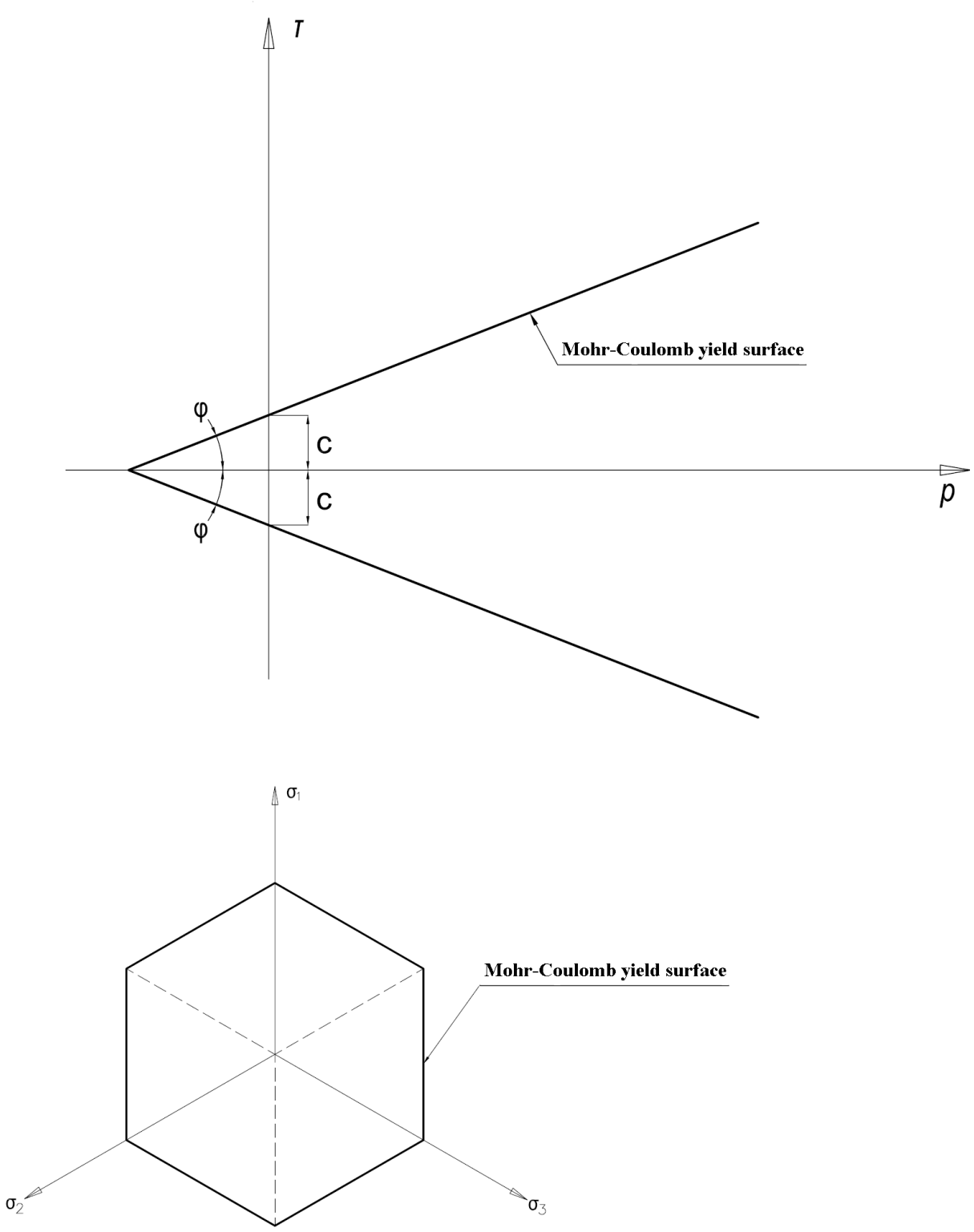

Figure 3.3: Mohr-Coulomb model in meridional (top scheme) and deviatoric plane (bottom scheme)

Drucker-Prager model

Drucker-Prager criteria implemented in Abaqus [94] has the following form:

$$f\left(p,q,\|\boldsymbol{\varepsilon}_{pl}\|\right) \equiv \frac{q}{2}\left(1+\frac{1}{k}-(1-\frac{1}{k})(\frac{r}{q})^3\right) - c(\|\boldsymbol{\varepsilon}_{pl}\|) - p*tan(\phi), \tag{3.67}$$

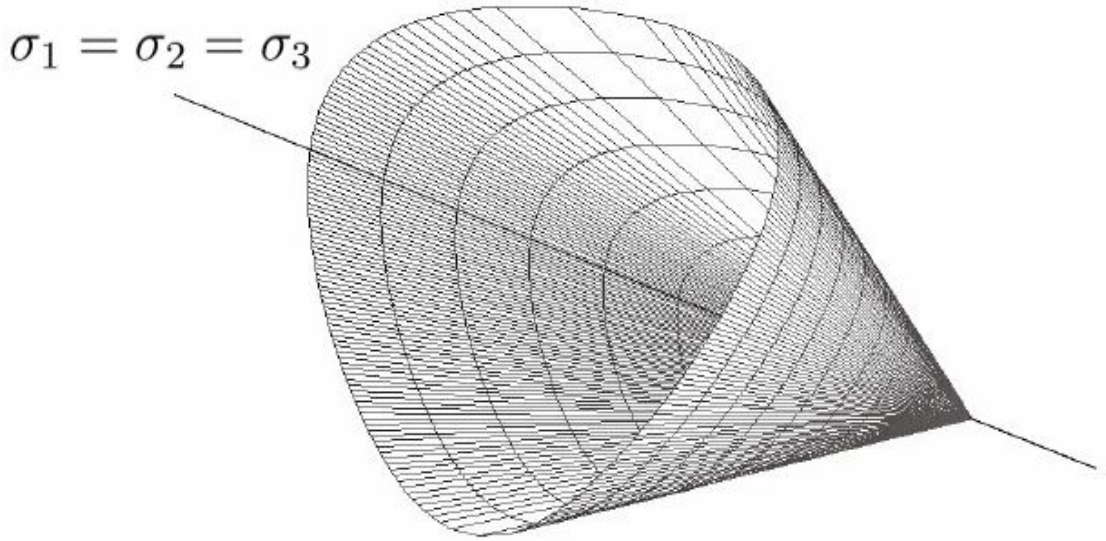

Figure 3.4: Smooth approximation of Mohr-Coulomb yield surface

where $c(\|\boldsymbol{\varepsilon}_{pl}\|)$ and ϕ are the cohesion and friction angle corresponding to Drucker-Prager yield criteria (in general case these values differ from friction angle and cohesion related to Mohr-Coulomb criteria); K is flow stress ratio. It is worth noting that direct comparison of the results obtained using Mohr-Coulomb and Druker-Prager models requires matching the parameters $c(\|\boldsymbol{\varepsilon}_{pl}\|)$ and ϕ of the both models. Such comparison is performed, for example, in works [146], [93] and [128] showing that these models are equivalent for plane strain conditions. Meanwhile, for spatial problems Mohr-Coulomb and Drucker-Prager models can produce different results. For instance,it is shown that Drucker-Prager model gives discrepancies on the friction angle and it is less appropriate to simulate soil behaviour, [93] and [128]. On the other hand, Rani et al. show that both the models produces similar results for undrained behaviour of clayey soils [121]. Therefore, it is possible to use both the models, but for Drucker-Prager one parameter fitting is required so that it would correspond to engineering geological surveys.

Drucker-Prager yield surface in meridional and deviatoric plans is represented in figure 3.5. Drucker-Prager yield surface is a cone in the stress space with a non-smooth vertex zone. Therefore, a smooth approximation for plastic flow potential is used [94] :

$$G\left(p, q, \|\boldsymbol{\varepsilon}_{pl}\|\right) = \sqrt{q^2 + \gamma^2 (c_0 - p_{t0} \tan\psi)^2} - p \tan\psi - c' = 0, \tag{3.68}$$

where γ is flow potential eccentricity defining the smoothness of flow potential in deviatoric plan, p_{t0} and c_0 are the initial cohesion and hydrostatic strength respectively, c' is the cohesion at the current step and ψ is dilatancy angle determined similarly to Mohr-Coulomb model.

Influence of eccentricity and numerical damping on hysteresis loop and energy loss

Equations (3.62, 3.65) and (3.67,3.68) demonstrate the possibility to match the models based on Mohr-Coulomb and Drucker-Prager criteria. In the following part the influence of the numerical parameters defining yield surface and flow potential smoothness is presented. All these parameters do not have physical meaning and only ensure solution procedure stability and convergence. Parameters e and ϵ of Mohr-Coulomb model varies in the ranges $0.5 < e \leq 1$ and $0.5 < \epsilon \leq 1$ affecting the shape of the yield surface and flow potential. In the case of Drucker-Prager model, the parameters K and γ vary in the range $0.778 \leq K \leq 1$ and $0 < \gamma < 1$ similarly as for Mohr-Coulomb model affecting the yield surface and flow potential.

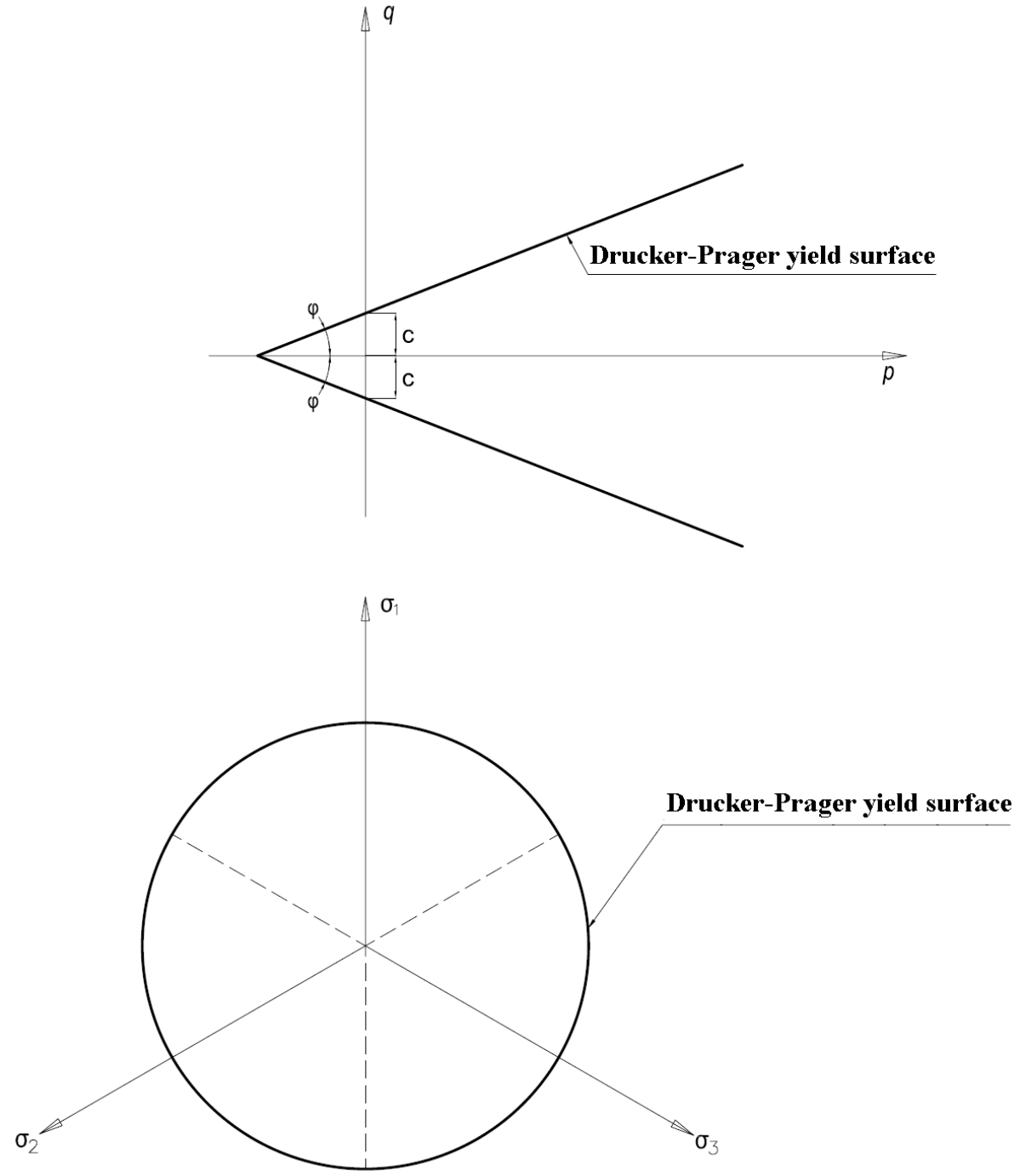

Figure 3.5: Drucker-Prager yield surface in meridional (top scheme) and deviatoric (bottom scheme)

To assess the effect of these numerical parameters on the final results, quasy-static problem is simulated using finite element method (FEM) along with Newton's method to resolve non-linear system of equations in Abaqus 2016 software, [94]. Eight-node hexahedral finite elements of C3D8 type with a linear shape function [94] are used for the simulation. More detailed description of the element formulation as well as numerical scheme including convergence and error control are presented in [94].

For locally unstable problems involving material nonlinearities, for example plasticity, ad-

ditional stabilization techniques can be included in the solution procedure ,[94].In this work constant damping factor is used for automatic stabilization of static problems during non-linear quasi-static solution procedure. In that case viscous forces are added to the global equilibrium equations to in the form:

$$F = dM\upsilon, \tag{3.69}$$

where d is the damping factor, M is the mass matrix, $\upsilon = \frac{\delta u}{\delta t}$ is vector of nodal velocities (in the context of this problem it does not have a physical meaning). This value is used to ensure the stability of the solution procedure. Nevertheless, there is no guarantee that the value of damping will be suitable for the problem. Therefore, it is important to estimate whether the quantity is appropriate for the solution stability without affecting the final results or not. This can be estimated through comparing stress-strain curves obtained at different values of damping factor. If the selected value is appropriate, then further decrease in the damping factor should not affect the result, which means that the results are close to the ones obtained without non-physical additions into the global equation.

To estimate the influence of the numerical parameters of Mohr-Coulomb and Drucker-Prager models along with damping factor a single element model is created. The model is a cube with horizontal and vertical sizes equalling to $1m$. The displacements along the x axis on the face of the cube which is parallel to YOZ are fixed, while on the opposite face cyclic loading is applied (Figure 3.6). This loading can be given as a kinematic or force factor with the frequency f. Other faces of the model are free. In addition to that, volumetric kinematic loading will be also considered. In that case, the displacements along the Z, X and Y axis are fixed on the three faces which are parallel to XOY, YOZ and XOZ respectively. On the opposite faces cyclic kinematic loads are applied.

Comparing the energy dissipated by plastic deformation as well as strain-stress curves gives the information regarding the influence of the variables included in the mathematical models of plastic media (damping factor and eccentricities). The energy of plastic deformation is defined by equation below:

$$\int_{\Lambda} \sigma_{ij}, d\varepsilon_{ij}^{pl}, \tag{3.70}$$

where Λ is the model volume on which the integration is carried out. As single element model is considered, strain and stress is evenly distributed on the element volume.

The hardening, as a result of the influence of symmetric and asymmetric cyclic loading, is simulated using Mohr-Coulomb plasticity model. Variation of the character of stress-strain curves due to variation of the damping factor at fixed other parameters in the model subjected to cyclic loading is presented in figure 3.7. The charts in figure 3.7 are plotted at $\phi = \psi = 0$,$c = 0.001$, $e = 1$ and $\epsilon = 0.1$. As can be seen from the charts below, large values of the damping factor can ensure the convergence of the solution procedure. However, the large values are not suitable because a further decline in the damping factor affects the solution significantly. Thus, the maximum value for damping is 10^{-6} as further decreases do not cause any substantial changes, which means that the results are close to the ones obtained without non-physical additions into the global equation. It is worth noting, that the values of damping factor less than 10^{-7} does not ensure problem stability and the convergence is not achieved.

Similar results are obtained for asymmetric loading (figure 3.8). The charts in figure 3.8 are plotted at the same values of the parameters as the ones in figure 3.7.

Figure 3.9 demonstrates the variation of the character of stress-strain curves due to variation of the damping factor at fixed other parameters for the case of perfect plasticity defined by Mohr-Coulomb model. The curves in the figure 3.9 are plotted at $\phi = 30$, $\psi = 0$,$c = 0.001$, $e = 0.56$ and $\epsilon = 0.005$ and $f = 5Hz$ (here f is the frequency of cyclic loading).

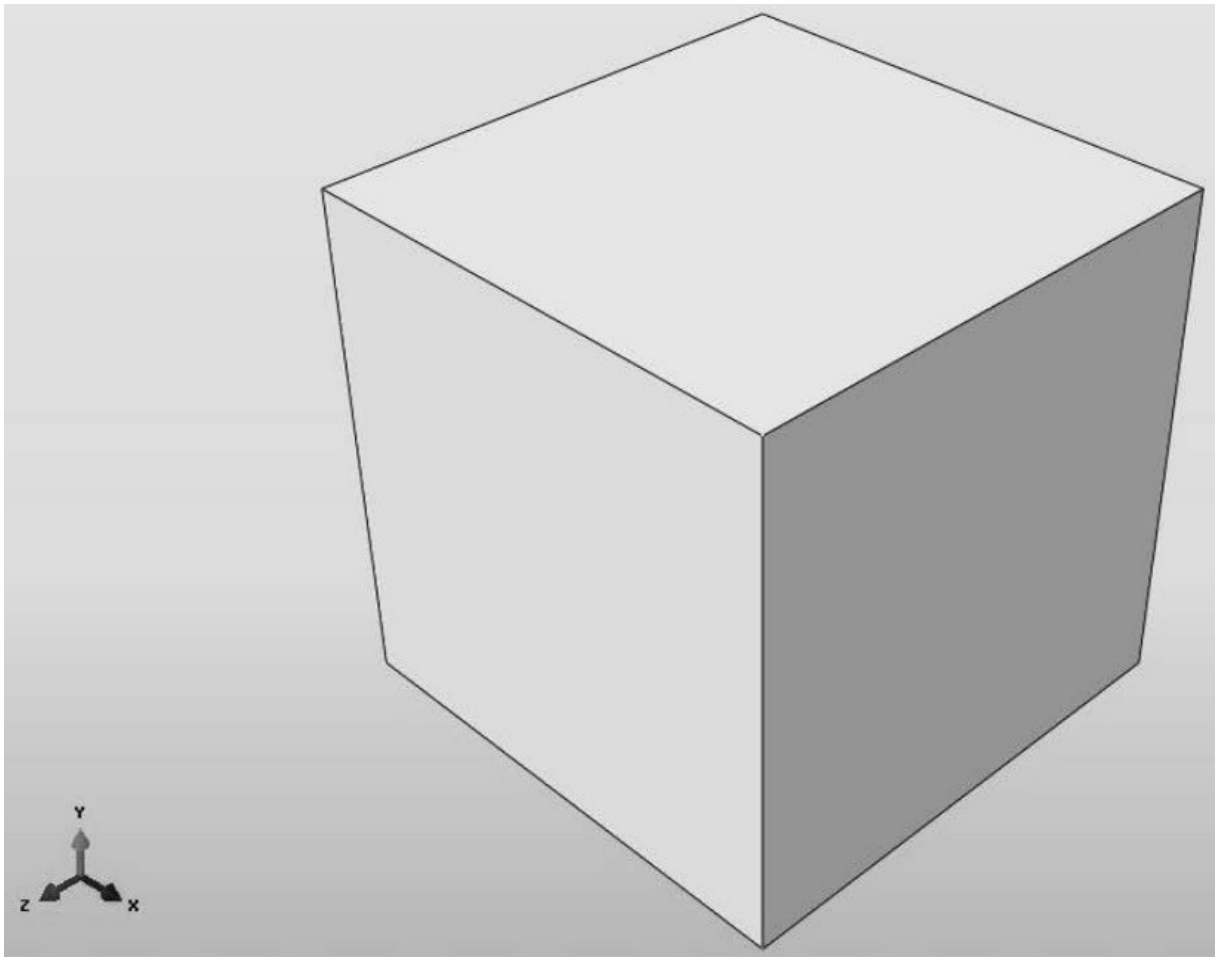

Figure 3.6: Finite element model

Variation of the character of stress-strain curves due to variation of the damping factor for Drucker-Prager model at fixed other parameters is presented in figure 3.10. The charts in figure 3.10 are plotted at $\phi = 30$, $\psi = 0$,$c = 0.001$ and $f = 5Hz$ (here f is the frequency of cyclic loading). Here γ is flow eccentricity and K is flow ratio.

The obtained results reveal that for both hardening and non – hardening types of plasticity models the damping factor affects the result of the solution dramatically. Large values of damping factor can cause substantial change in the character of stress- strain curves, while a damping factor equalling to or less than 10^{-5} may ensure the convergence of the solution, meanwhile negligibly influencing the final results. Additionally, increase in damping factor value from 10^{-5} does not affect the results significantly while in more complicated cases the solution convergence will not be achieved. Thus, damping factor affects the solution procedure convergence and the calculation results, so its values should be selected for each particular problem.

The influence of deviatoric and meridional eccentricities on the result can be estimated by comparing the energy dissipated by plastic deformation at different values of these parameters. Variation of the energy dissipated by plastic deformations described by Mohr-Coulmb model due to the change of both meridional and deviatoric eccentricities is shown in figure 3.11. The surface in figure 3.11 is plotted at $\phi = 30$, $\psi = 0$,$c = 0.001$ and $f = 5Hz$.

As can be seen from the surface in figure 3.11, the influence of deviatoric eccentricity on the energy of plastic deformation is insignificant. In addition to that, the variation of meridional eccentricity has virtually no effect on the energy of plastic deformation, excluding abrupt peaks, probably, caused by numerical errors, although error control is satisfied. These effects can be ob-

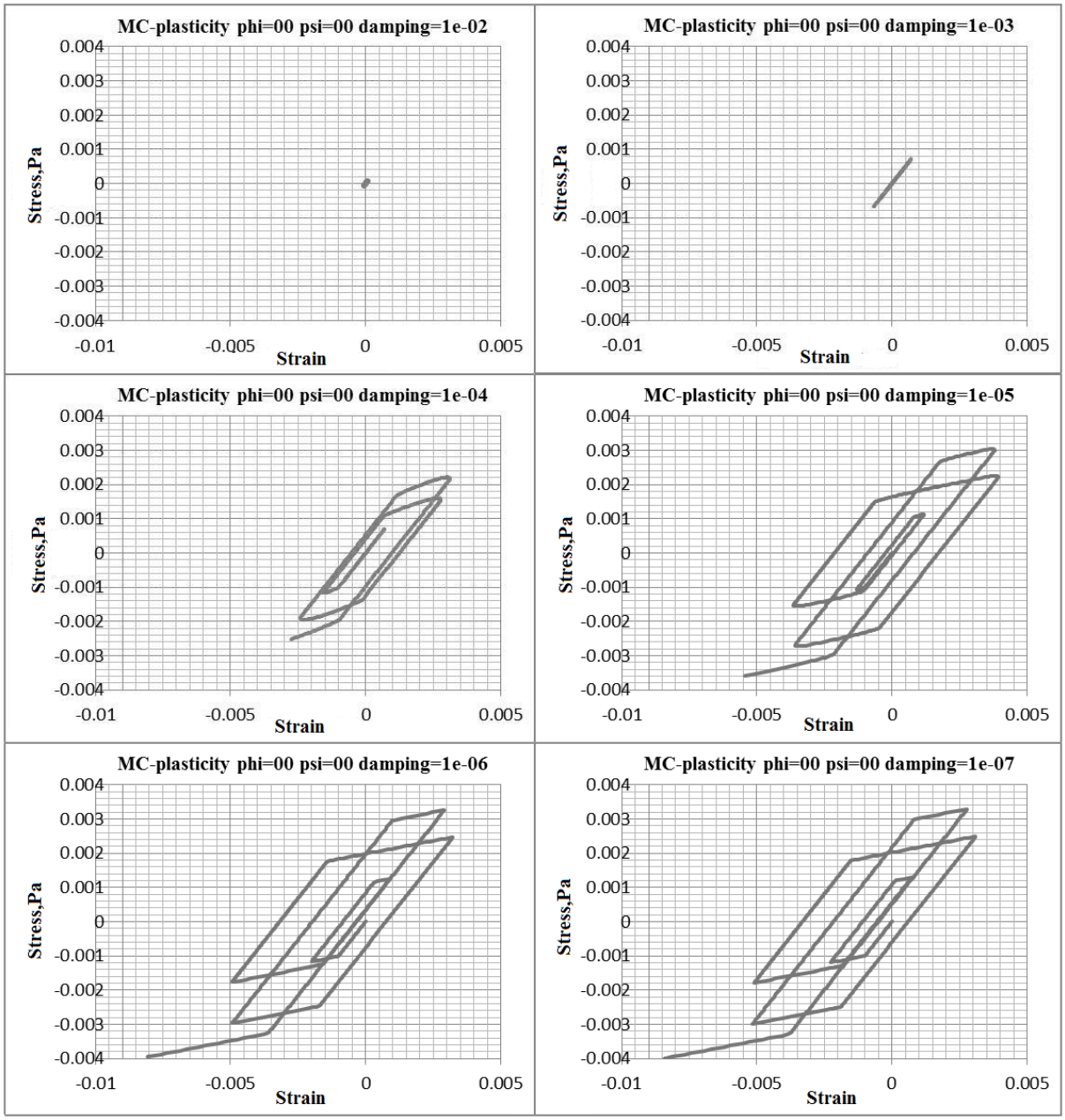

Figure 3.7: : Stress-strain curves for symmetric cycle loading at different values of damping

served when the value of deviatoric eccentricity is greater than 0.75. Nevertheless, the maximum difference in the results is lower than 1% One possible reason behind the energy independence on the value of meridional eccentricity is that this eccentricity may be fixed in the software. In this case is possible to define this value by comparing the stress-strain curves with the yield surface.

Similarly to Mohr-Coulomb model, it is possible to estimate the influence of the flow eccentricity and flow rate in Drucker-Prager model on the calculation results. The variation of the energy dissipated by plastic deformations described by Drucker-Prager model with the change of flow eccentricity and flow rate is shown in figure 3.12. The surface in figure 3.12 is plotted at $\phi = 30$, $\psi = 0$,$c = 0.001$ and $f = 5Hz$.

The obtained results reveal that the variation of flow potential eccentricity does not affect the energy of plastic deformation, while the flow ratio affects the energy significantly. In contrast to Mohr-Coulomb model there are no such deviations from the mean energy in Drucker-Prager

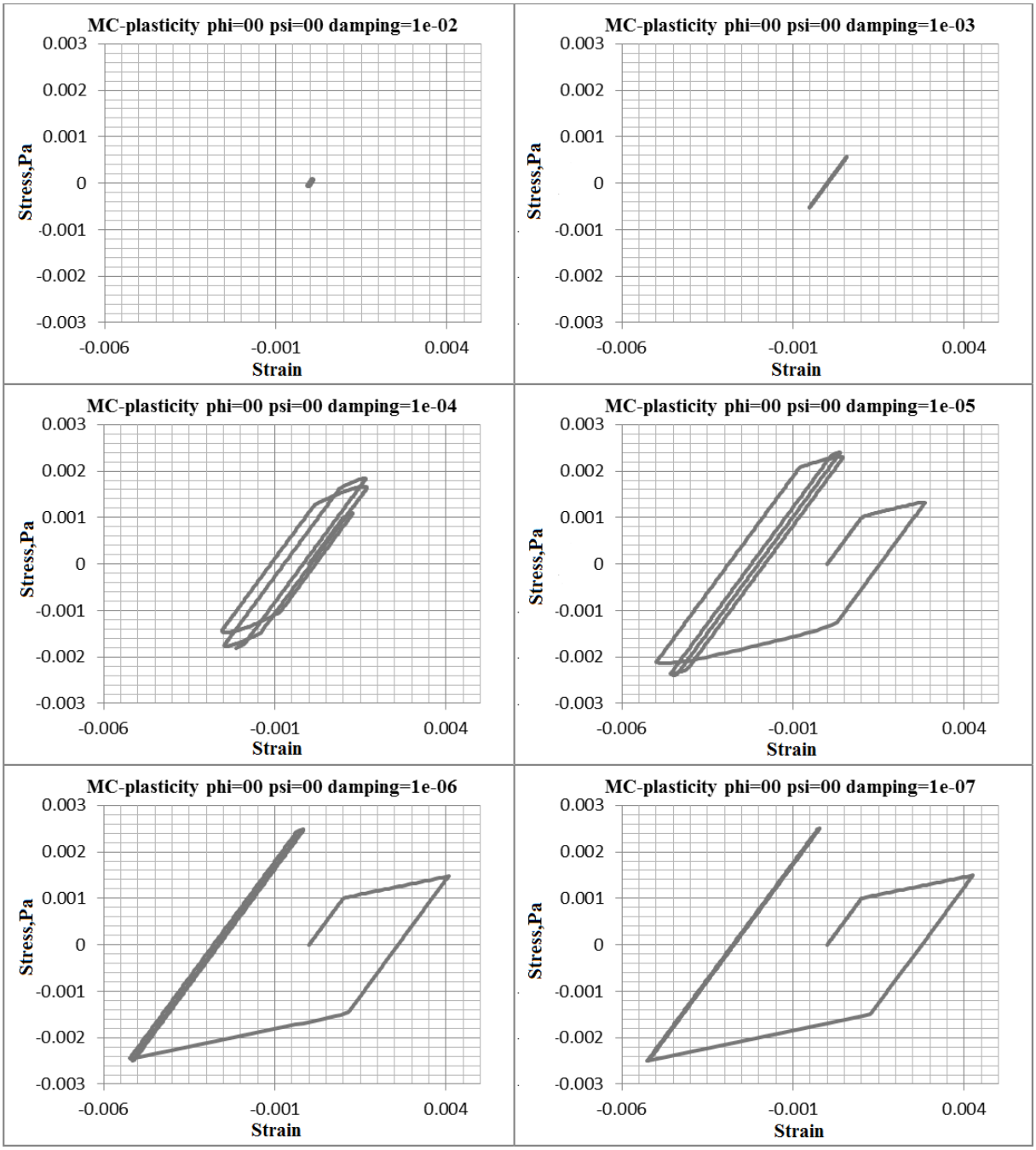

Figure 3.8: : Stress-strain curves for asymmetric cycle loading at different values of damping

model, which means that Drucker-Pruger model is more stable. Additionally, the value of flow potential eccentricity may be estimated by comparing the stress-strain curve and the yield surface.

The Mohr-Coulomb yield surface and the loading in meridional plane along with the resulting stress-strain curve are shown in figure 3.13. The curves in figure 3.13 are plotted at $\phi = 30$, $\psi = 0$,$c = 0.001$,$f = 5Hz$ $e = 0.56$ and $\epsilon = 0.005$. The strain stress curve for these parameters of the model and loading is plotted in the top part of the figure .

The actual value of meridional eccentricity that are implemented in the model can be found from equation:

$$e = \frac{p_{yield}}{c} \tan \phi, \tag{3.71}$$

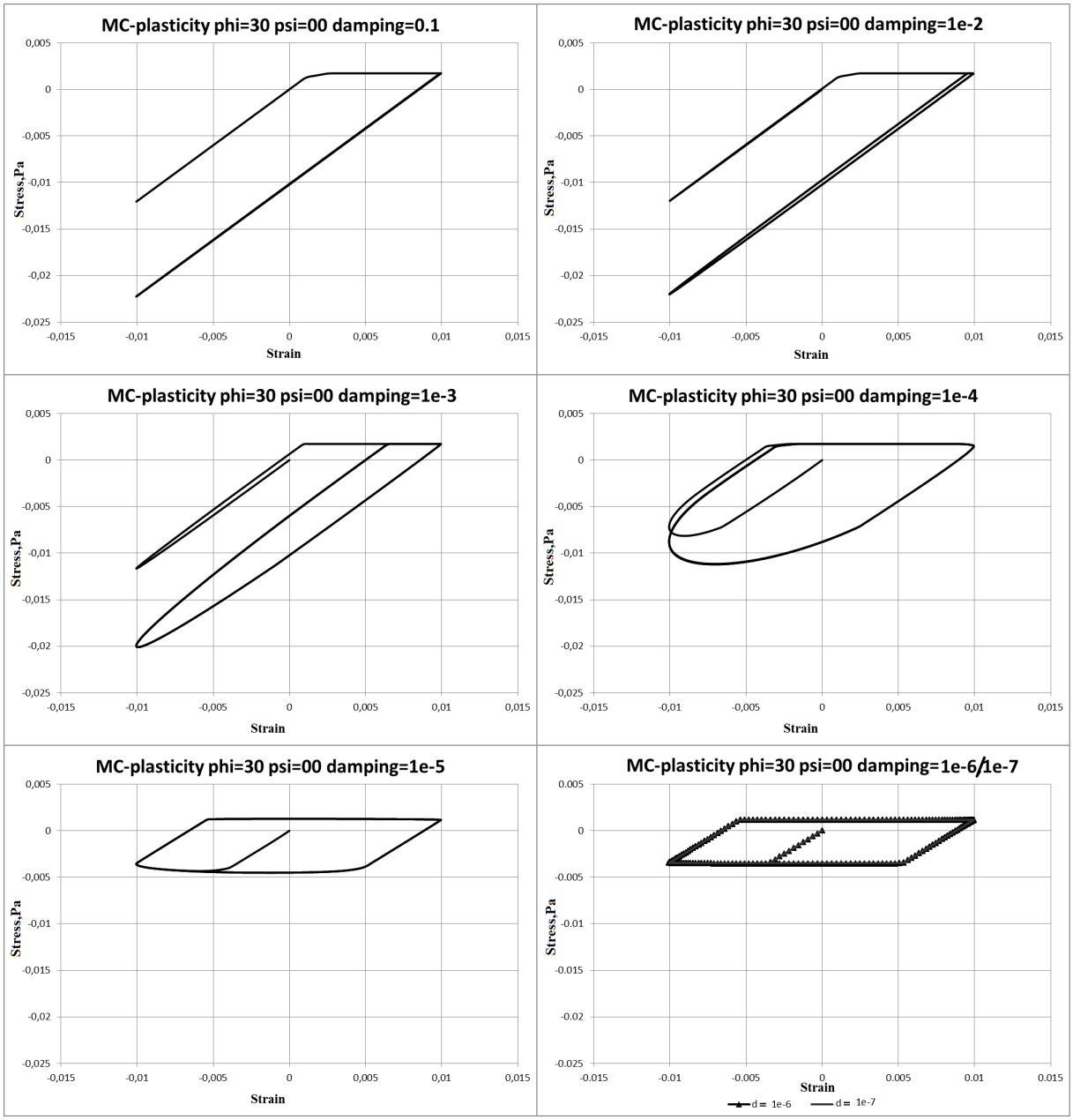

Figure 3.9: Stress-strain curves for Mohr - Coulomb model at different values of damping in the case of perfect plasticity

where p_{yield} is the stress corresponding to the beginning of the plastic flow.

Drucker-Prager yield surface along with the loading in meridional plane are shown in the top part of the figure . The curves in figure 3.72 are plotted at $\phi = 30$, $\psi = 0$,$c = 0.001$ and $f = 5Hz$. The resulting stress-strain curve for these parameters of the model and loading is plotted in bottom part of the figure .

Similarly to Mohr-Coulomb model, the flow eccentricity in Drucker-Prager model can be found from the following equation:

$$\gamma = \frac{p_{yield}}{c} \tan \phi. \tag{3.72}$$

In sum, both Mohr-Coulomb and Drucker-Prager models are appropriate to simulate hysteresis soil behaviour and energy dissipation during wave propagation in soil.

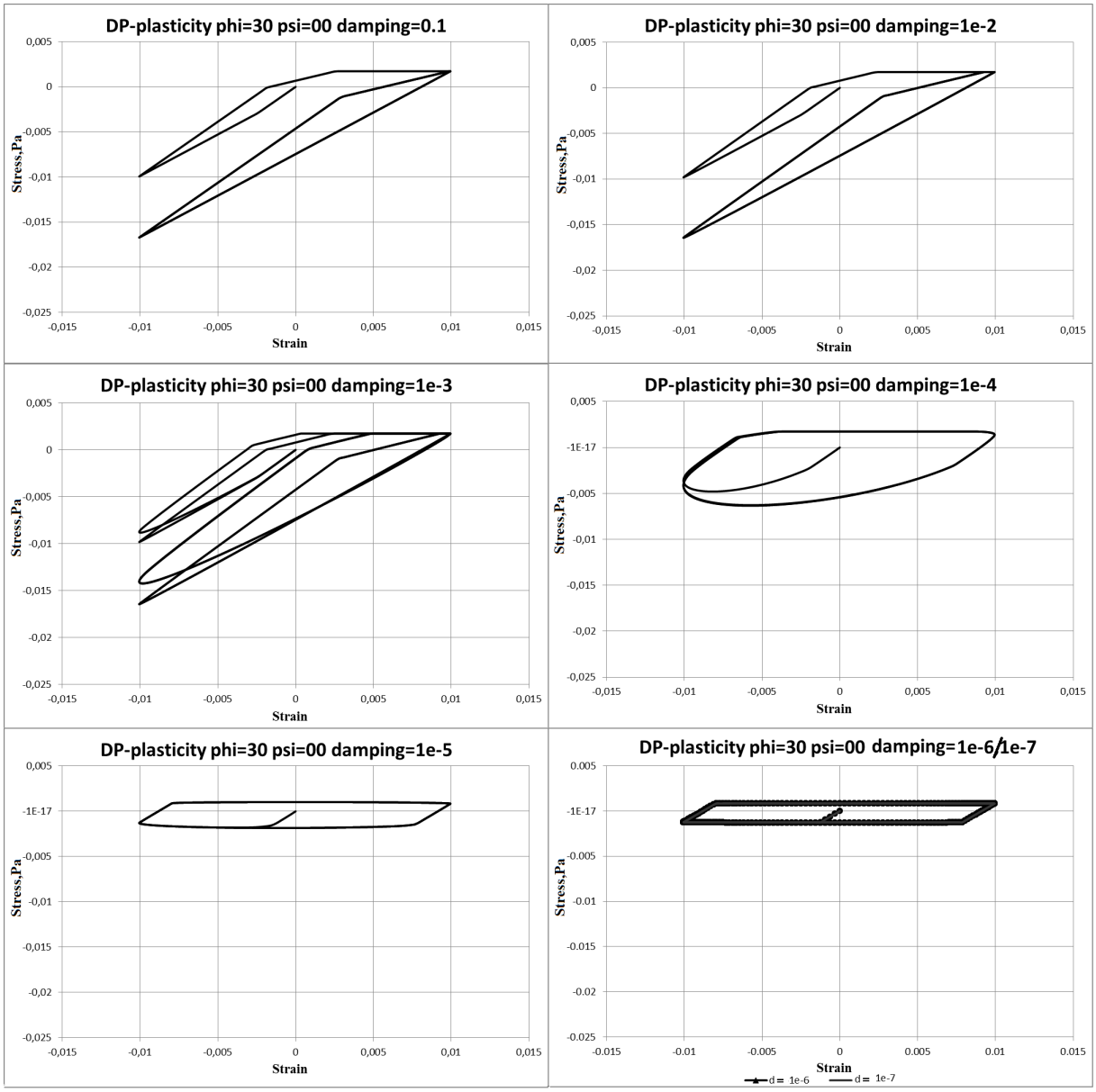

Figure 3.10: Stress-strain curves for Drucker - Prager model at different values of damping in the case of perfect plasticity

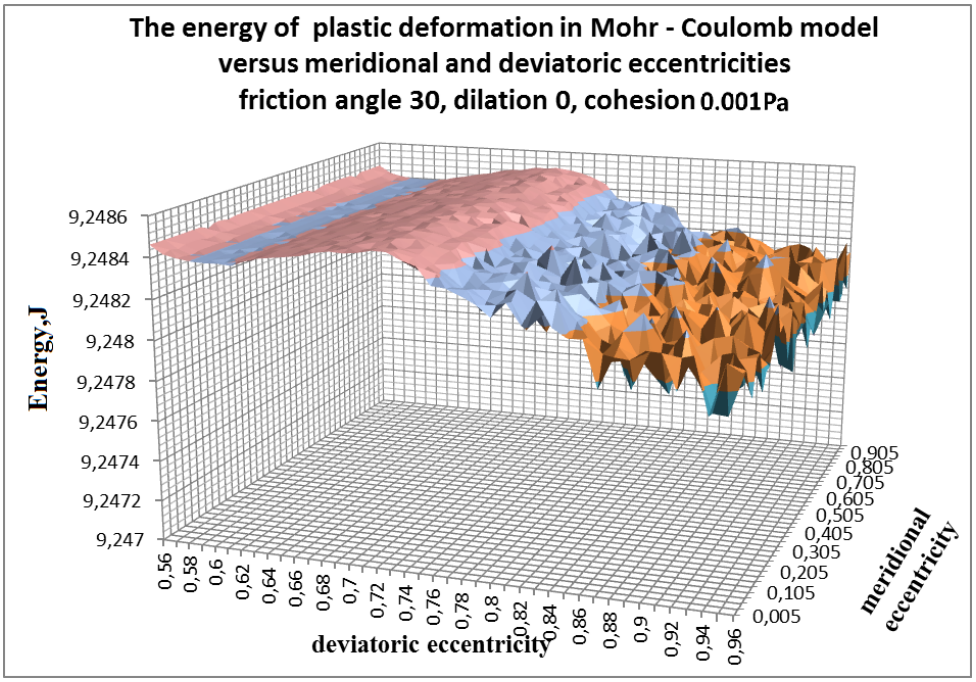

Figure 3.11: Variation of the energy dissipated by plastic deformation with the change of meridional and deviatoric eccentricities

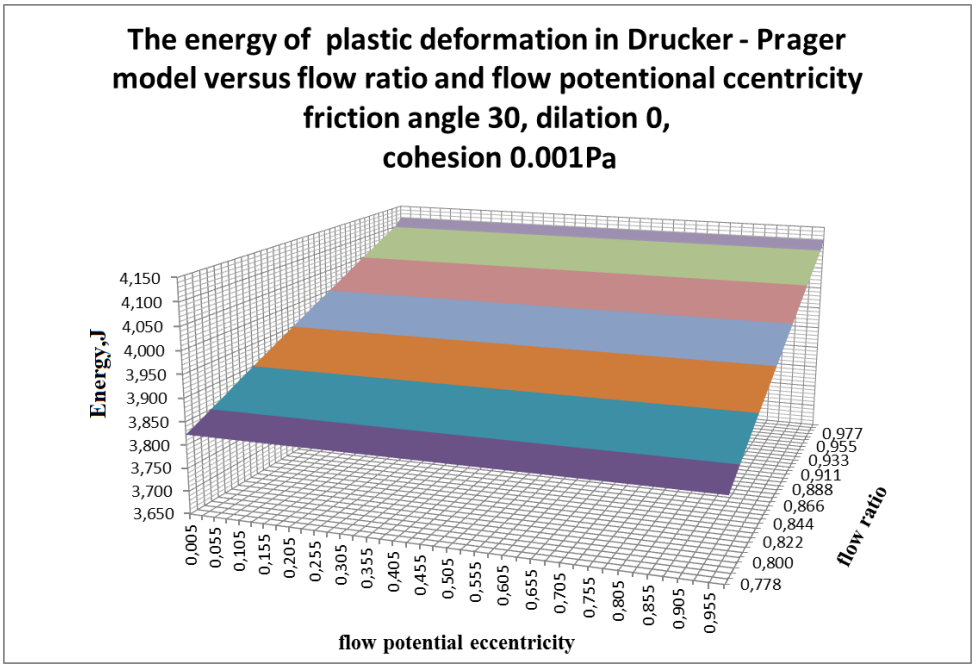

Figure 3.12: Variation of the energy dissipated by plastic deformation with the change of flow eccentricity and flow rate

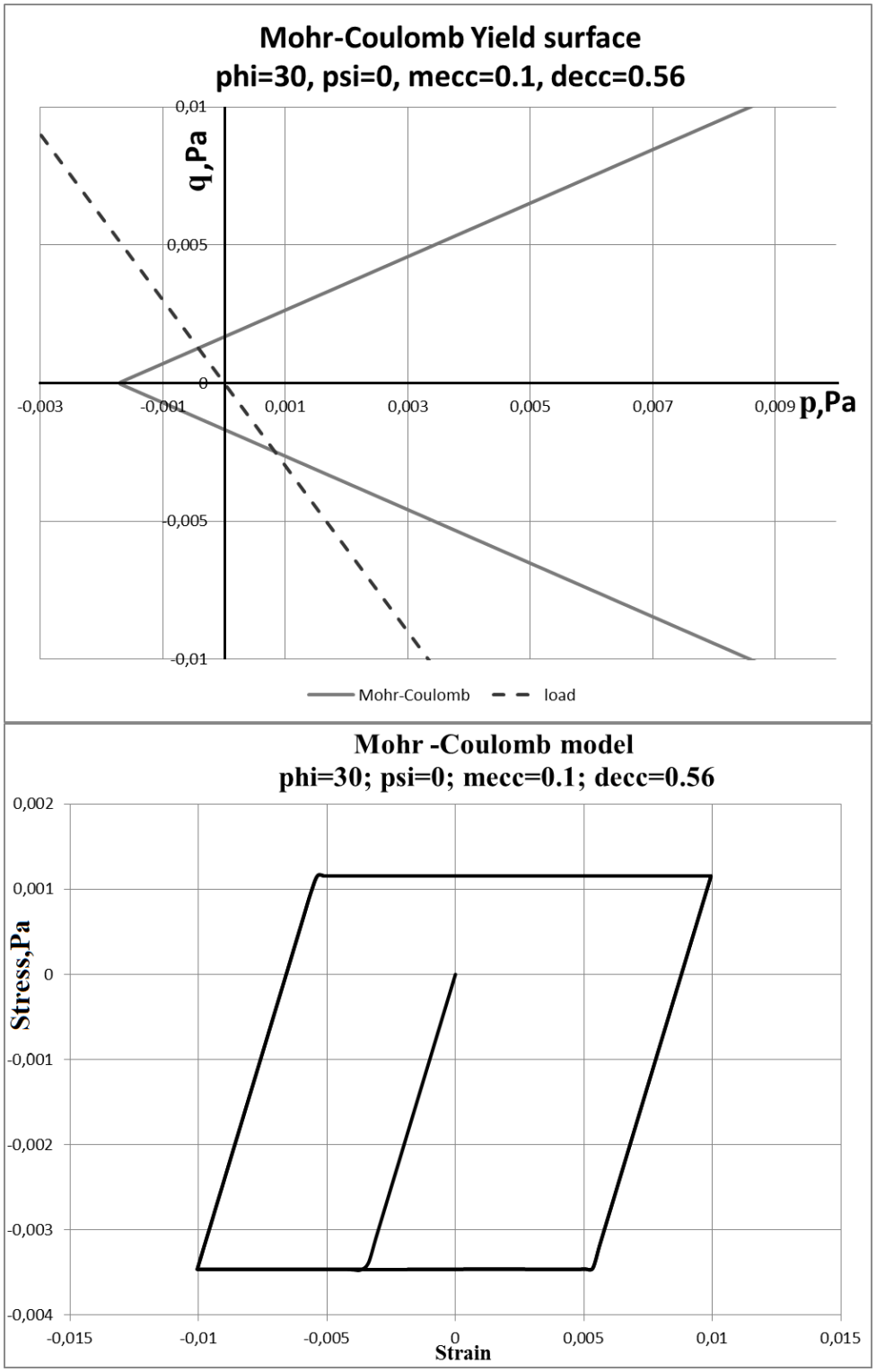

Figure 3.13: Yield surface for Mohr – Coulomb model and loading path (top chart) as well as the resulting stress-strain curve (bottom curve)

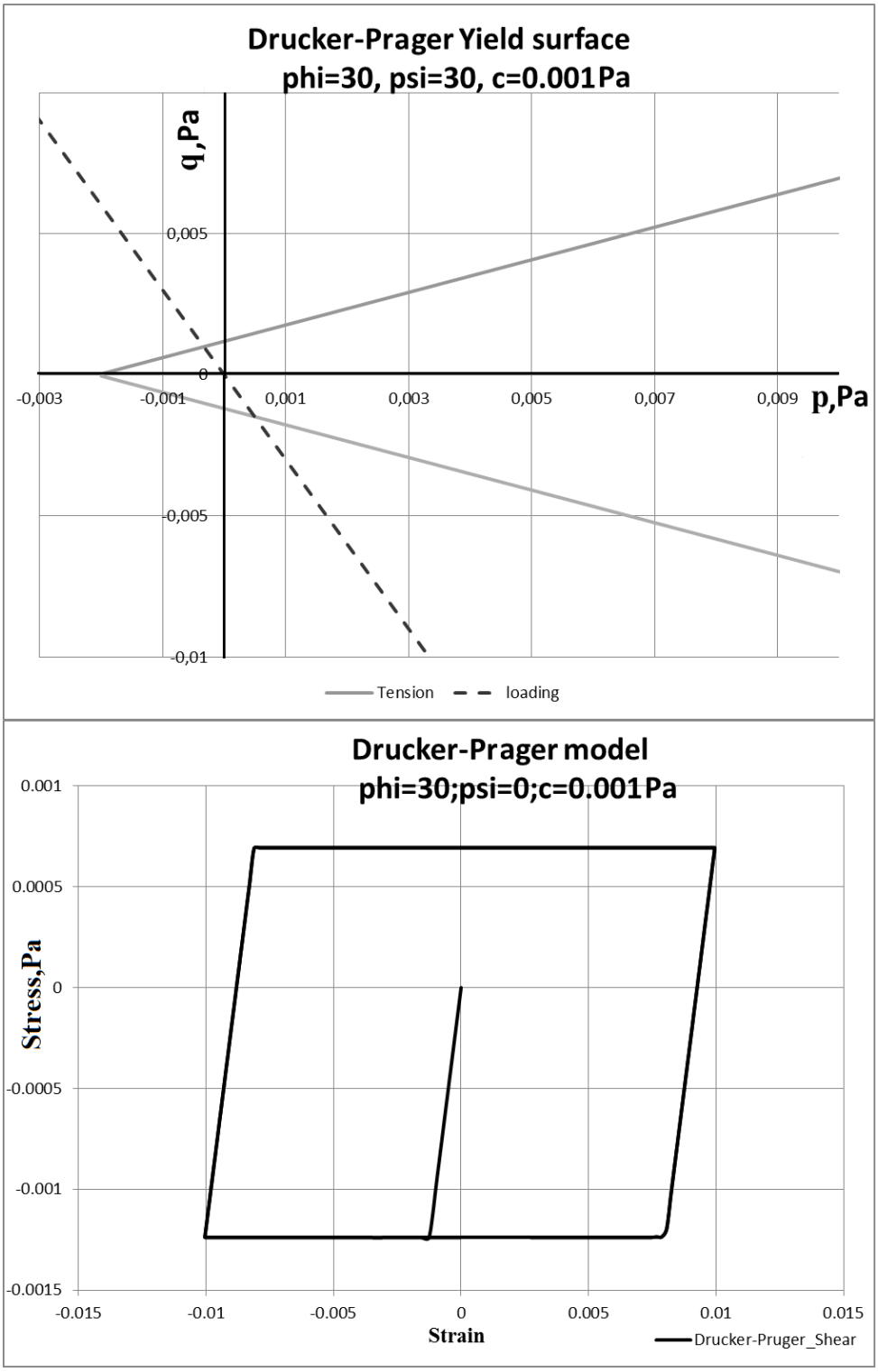

Figure 3.14: Yield surface for Drucker-Prager model and loading path (top chart) as well as the resulting stress-strain curve (bottom curve)

Models based on the critical state concept (Cam-Clay and Modified Cam-clay)

Model description

The original version of Cam-Clay model was proposed in the works [125, 123]. Later, the original logarithmic yield surface was replaced by the ellipsoidal one, [124]. The critical surface equation has the following form [124]:

$$f(p,q,p_c) \equiv \frac{1}{b}(\frac{p}{a}-1)^2 + (\frac{q}{Ma})^2 = 0, \tag{3.73}$$

where b is a dimensionless parameter specifying the ellipsoid shape: in a subcritical zone $b = 1$ (left side), in a supercritical zone $b \geq 1$ (right side); the dimensionless parameter M specifies ellipsoid dimension along q -axis; a is the "central" point of the ellipsoid. This parameter defines ellipsoid dimension along p -axis:

$$a = \frac{p_c}{1+b}, \tag{3.74}$$

where p_c is the current yield pressure value. Actually, parameter p_c specifies the evolution of the ellipsoidal surface (3.73).

Subcritical and supercritical zones are also associated with dry and wet conditions when this model is used to describe the behaviour of porous materials and the use of the exponential hardening law. This model is proposed to describe the material softening at high hydrostatic pressure values. The cross-section of Cam-Clay model in the meridional plan is shown in figure 3.15.

The model is described in more details in [50]. It is quite suitable for describing the behaviour of cohesionless soils at high confining pressure. However, it has a number of disadvantages, such as a larger number of input parameters and, as a result, it requires more complicated experiments on soils to determine these parameters and fit it to the model. In contrast to that, Mohr-Coulomb and Drucker-Prager models allow using the data obtained from conventional triaxial soil tests.

Model behaviour under deviatoric kinematic loading

The modified Cam-Clay (MCC) model with linear volumetric hardening and linear elastic initial response is considered. The applied kinematic loading produces uniform strain field that is split in two parts:

$$\varepsilon(\tau) = -\frac{1}{3}\tau + \mathbf{I} + e(\tau), \tag{3.75}$$

where τ is the loading "time". Variation of τ and $e(\tau)$ is given in figure 3.16, where volumetric strain gradually increases to $(1) = 0.03$ and, then, is held fixed at the attained value; variation of the deviatoric components starts from $\tau = 1$.

The elastic volumetric and shear moduli are as follows $K_e = 0.67$ and $\mu = 0.67$ while plastic module equals to $K_p = 0.2$. The MCC ellipsoid parameters in equation (3.74) are taken as $b = 1, M = 1, p_{c0} = var$ the value of , p_{c0} is varied so that the volumetric (elastic) pressure would be placed in either (i) subcritical (dry) zone at $p < a$, or (ii) supercritical (wet) zone at $a < p_{c0}$, or (iii) take inelastic pressure values related to $p > p_{c0}$.

Deviatoric loading at subcritical zone ($p < a$) At $p_{c0} = 0.06$ and $\theta(1) = 0.03$, the volumetric kinematic loading yields (elastic) pressure value $p = 0.02 < a$. The deviatoric stress component variation vs. time for the considered subcritical zone is plotted in figure 3.17. The corresponding deviatoric stress-strain relations in terms of signed Tresca measure ($\tau_{tresca} = \sigma_{max} - \sigma_{min}$, where $\sigma_{max}, \sigma_{min}$ are the maximal and minimal principal stresses respectively) is presented in figure 3.18.

Figure 3.19 shows variation of stress invariants at cyclic deviatoric kinematic loading: the plot is drawn in terms of the pressure and signed Tresca measure. This plot reveals rather peculiar

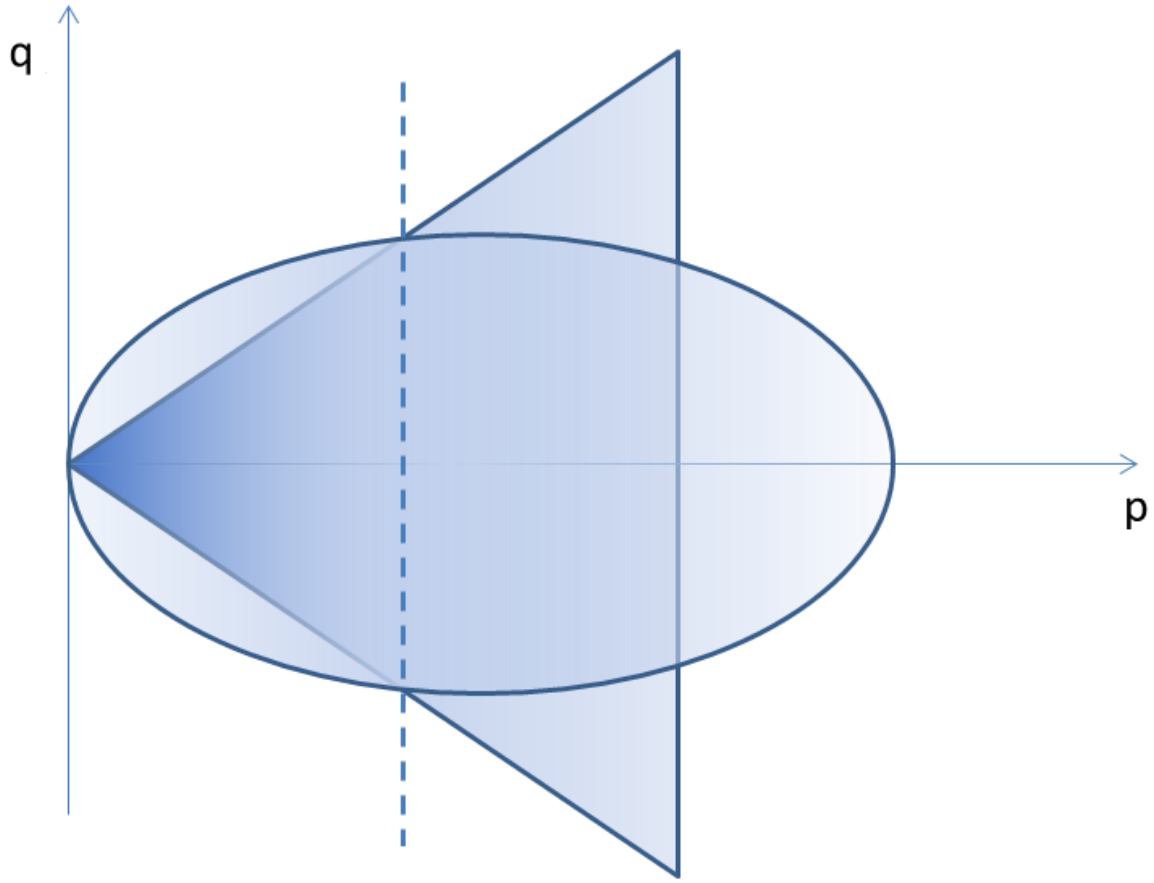

Figure 3.15: Yield and critical state surfaces for the MCC model: dashed line corresponds to intersection of the ellipsoidal yield surface with critical state cone

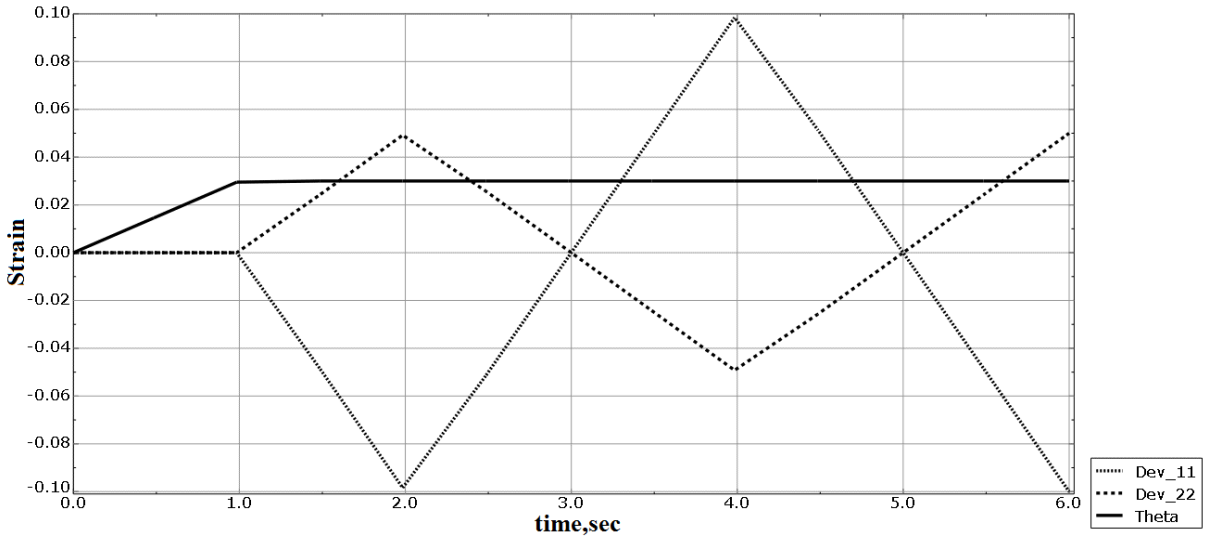

Figure 3.16: Deviatoric and volumetric strain component variation

behavior of the Tresca stress: at the sufficiently large amplitude of the deviatoric kinematic loading.The corresponding signed Tresca stress growths till the value $p = p_{c0}/2$ demonstrating "apparent " hardening and, then, oscillates at almost constant pressure equalling to $p = p_{c0}/2$.

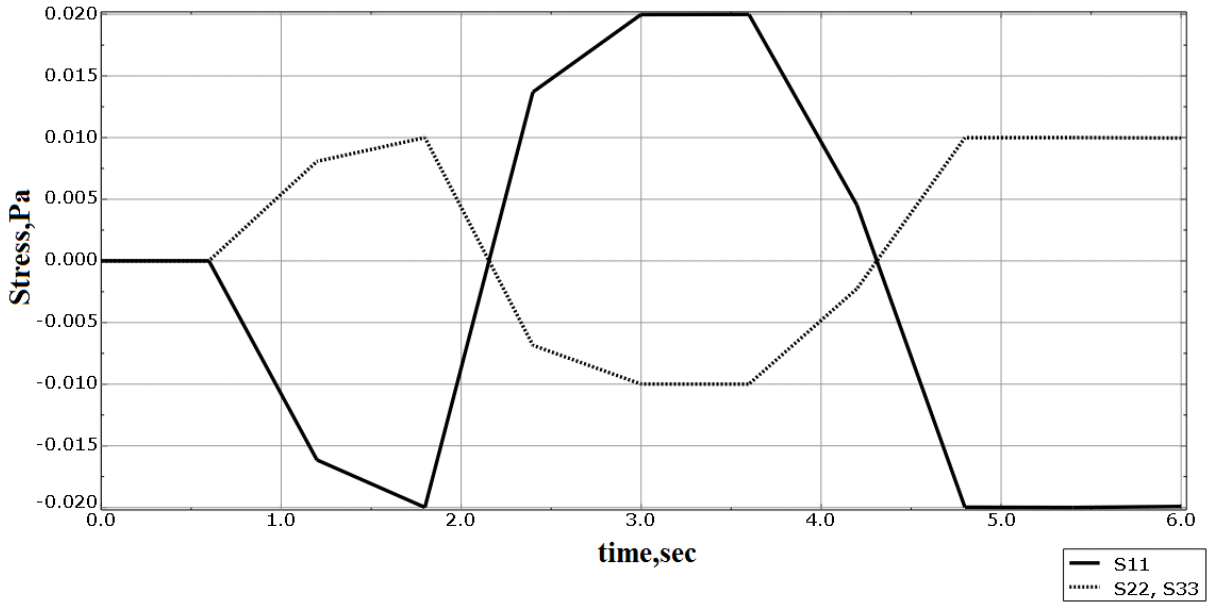

Figure 3.17: Subcritical zone: deviatoric stress component variation vs. time

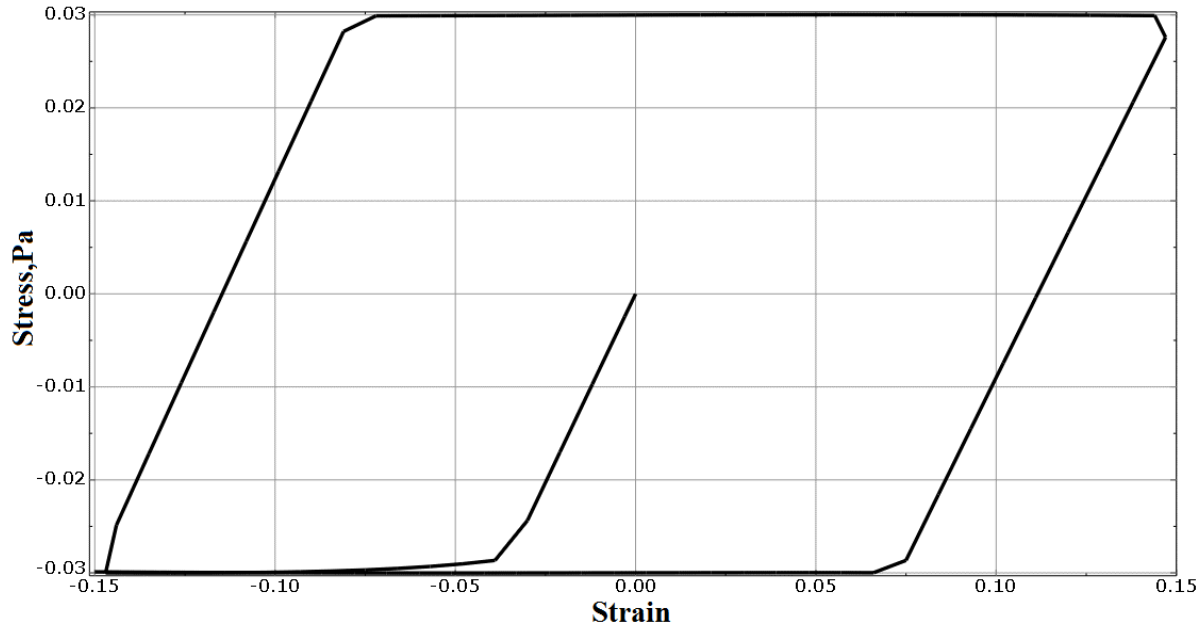

Figure 3.18: Subcritical zone: deviatoric stress-strain plot in terms of signed Tresca measures

Deviatoric loading at supercritical zone $(a < p \leq p_{c0})$ At $p_{c0} = 0.015$ and $\theta(1) = 0.03$, the volumetric kinematic loading yields (elastic) pressure value equalling to $p = 0.01$. The deviatoric stress component variation vs. time for the considered supercritical zone is plotted in figure 3.20. The corresponding deviatoric stress-strain relations in terms of signed Tresca measure is presented in figure 3.21.

Figure 3.22 shows the variation of stress invariants at cyclic deviatoric kinematic loading in the supercritical zone: the plot is drawn in terms of pressure and signed Tresca measure. Again, as it is shown for the subcritical zone, the plot in the figure 3.22 reveals peculiar behaviour of the Tresca stress: at the sufficiently large amplitude of the deviatoric kinematic loading. The corresponding signed Tresca measure declines with the decrease in the pressure equalling

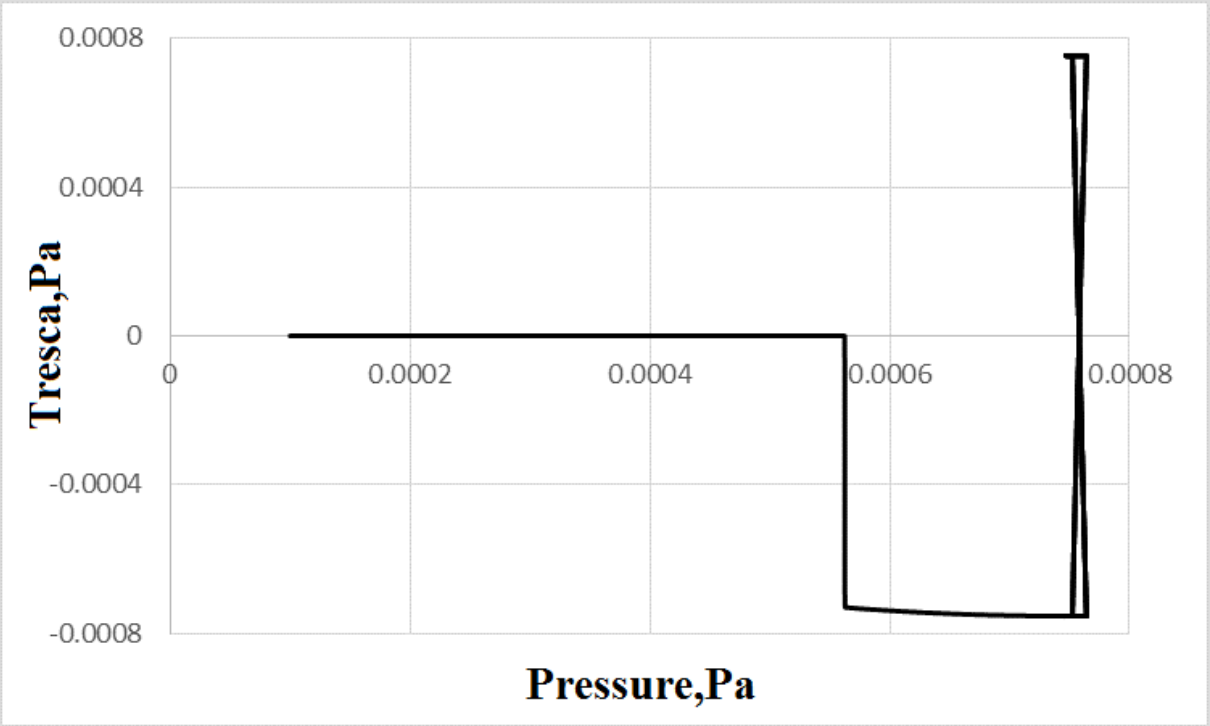

Figure 3.19: Subcritical zone: stress plot in terms of pressure and signed Tresca stress

$p = p_{c0}/2$, thus ,showing "apparent" softening. Afterwards,the stress oscillates at almost constant pressure valued $p = p_{c0}/2$.

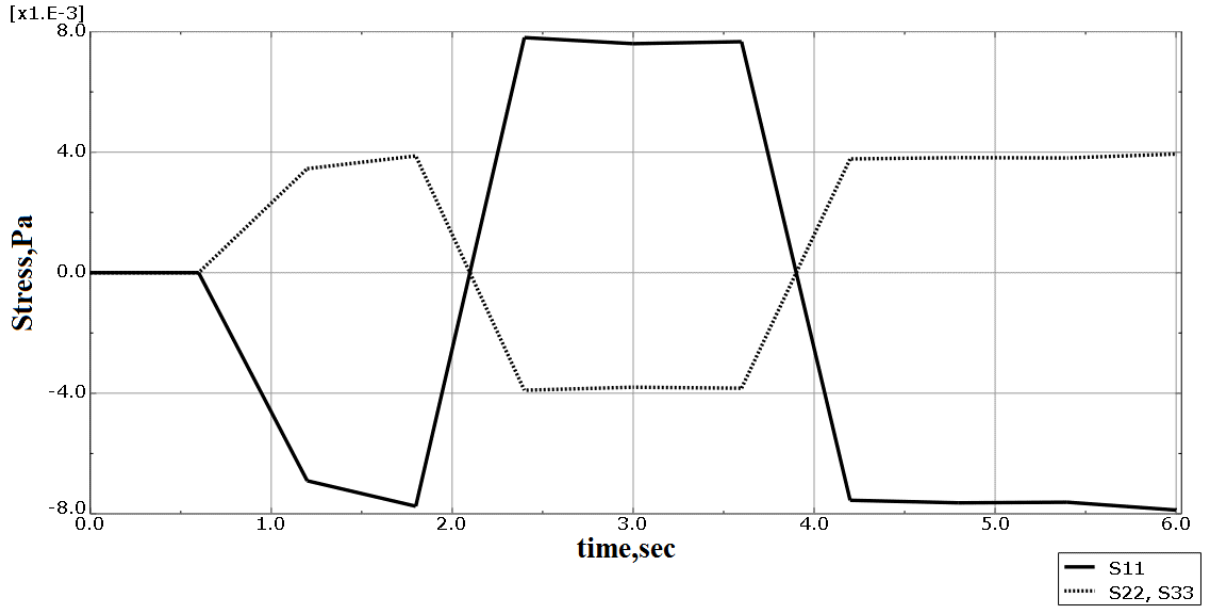

Figure 3.20: Supercritical zone: deviatoric stress component variation vs. time

Deviatoric loading at high confining pressure ($p > p_{c0}$) At $p_{c0} = 0.02$ and $(1) = 0.15$, the volumetric kinematic loading yields (elastic) pressure value equalling to $p = 0.01 > p_{c0}$. The deviatoric stress component variation vs. time for the considered supercritical zone is plotted in figure 3.20. The stress components variation vs. time for the considered outer zone is plotted

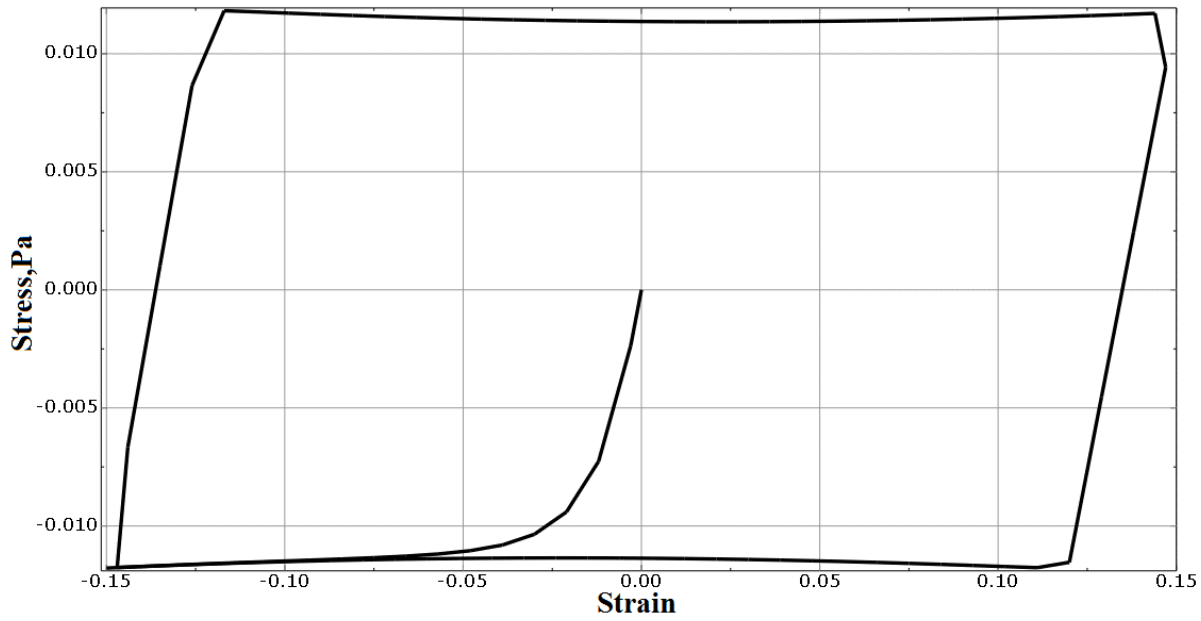

Figure 3.21: Supercritical zone: deviatoric stress-strain plot in terms of signed Tresca measures

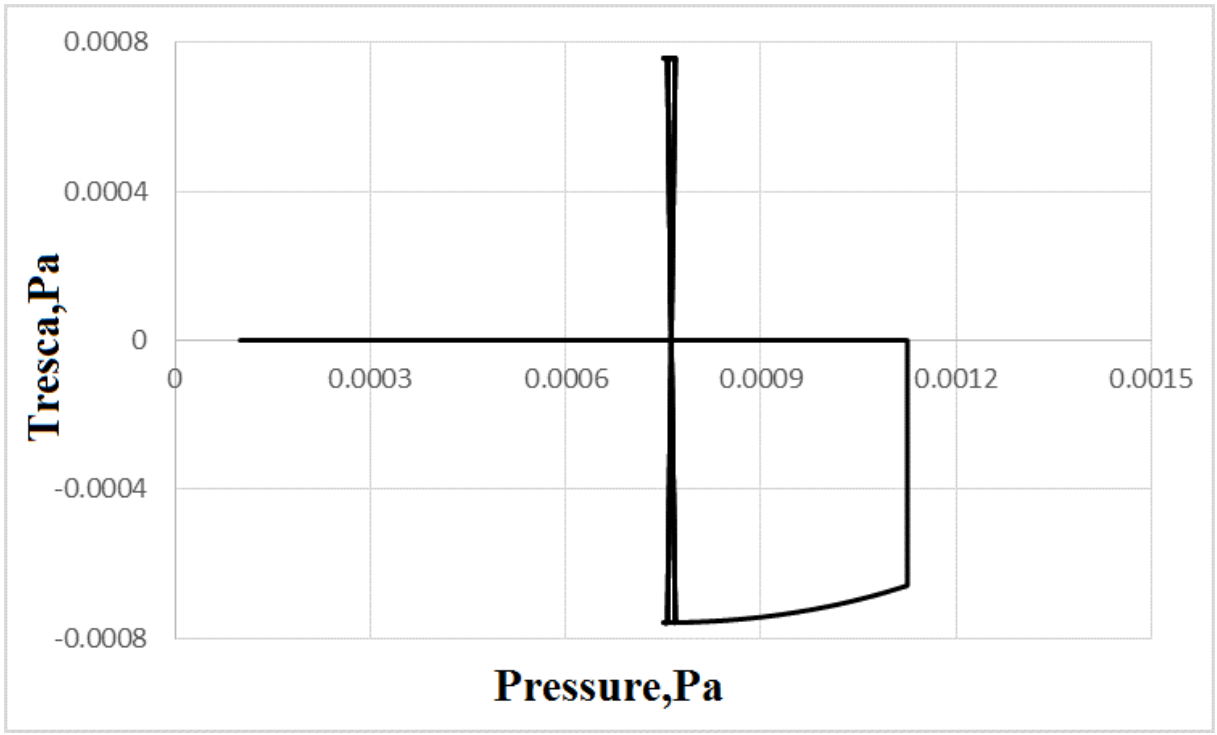

Figure 3.22: Supercritical zone: stress plot in terms of pressure and signed Tresca stress

at 3.23. Figure 3.24 shows variation of stress invariants at cyclic deviatoric kinematic loading at the supercritical outer zone: the plot is drawn in terms of pressure and signed Tresca measure. For such a case the corresponding plots for deviatoric components are similar to the previous case.

A significant result is that the hysteresis behaviour of Tresca strain measure at subcritical, supercritical and supercritical at $p > p_{c0}$ has virtually the same character. Additionnaly, after the periods of "apparent" hardening/softening the value of deviatoric stress oscillates around the

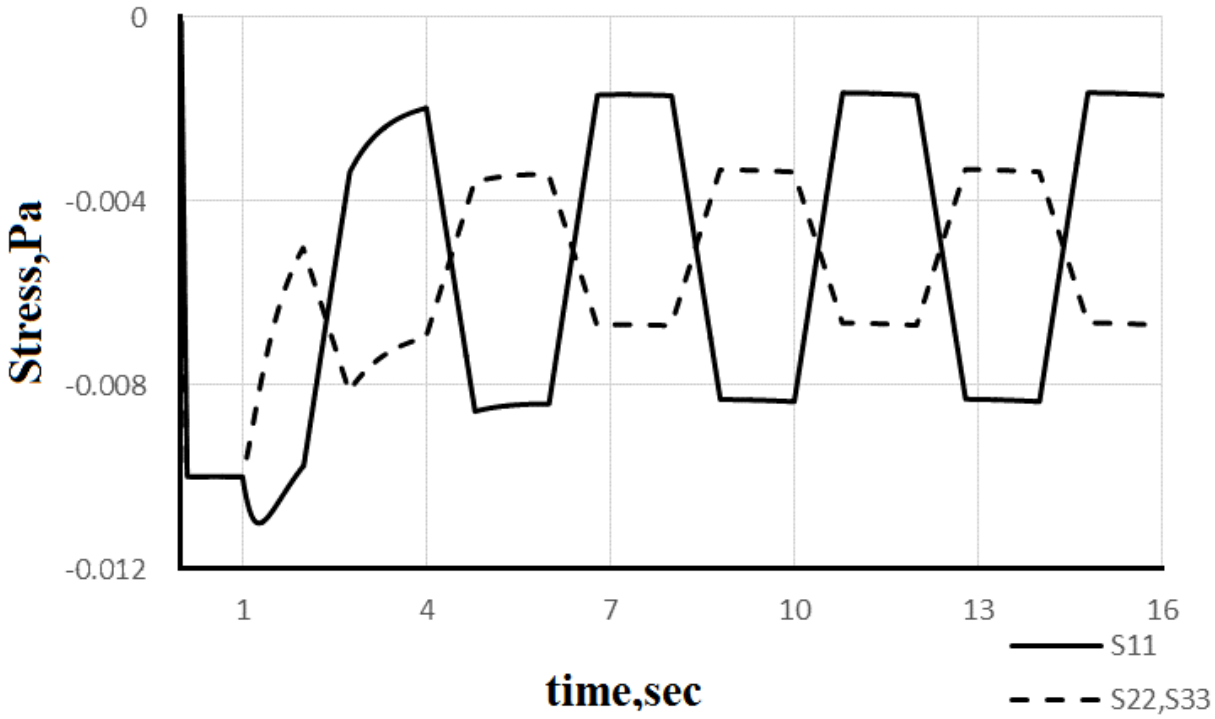

Figure 3.23: Supercritical zone: deviatoric stress component variation vs. time

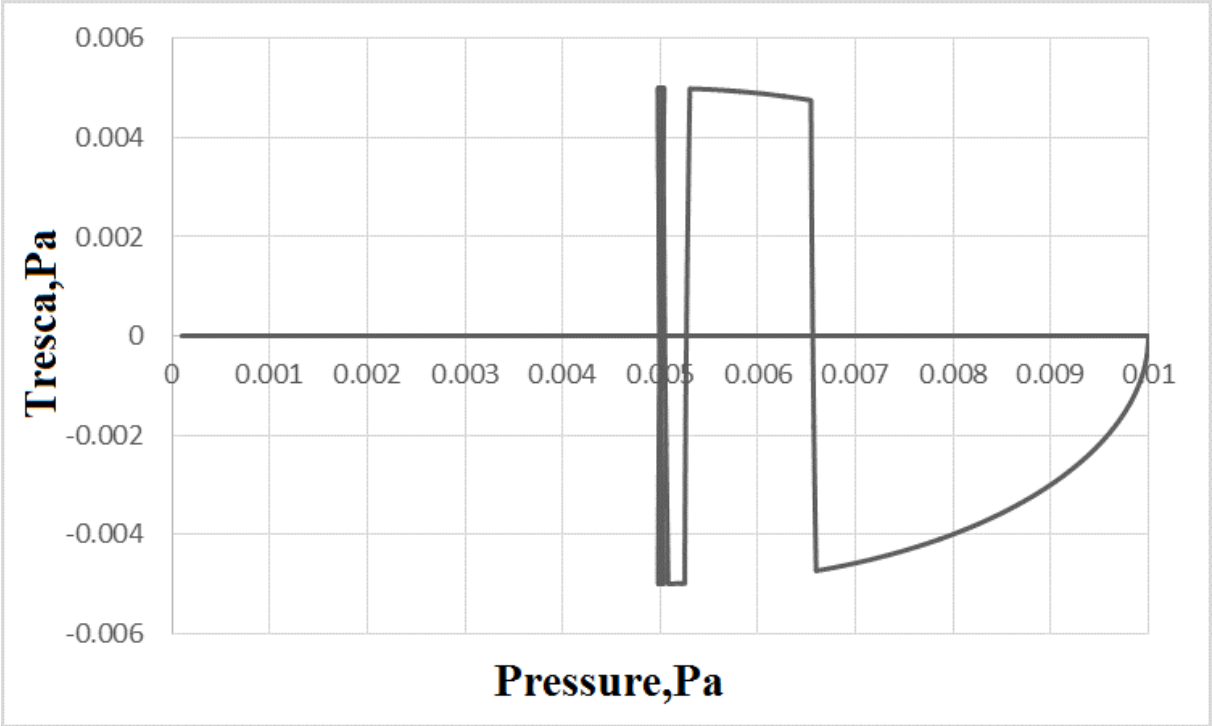

Figure 3.24: Supercritical zone: stress plot in terms of pressure and signed Tresca stress

value of hydrostatic pressure $p = p_{c0}/2$.

MCC model allows accounting for the soil softening at high confining pressure and its hardening at low confining pressures [50]. At the same time, the propagation of surface Rayleigh waves takes place in the near-surface zone. Herein, no such "apparent" softening is required but the so-called post-peak softening of the soil is required (the process of hardening is followed by

the softening after the deviatoric stress reaches a certain value depending on soil). This effect can be taken into account by using more complex models, for example, [97, 107]. However, they are even more complex and there is a small database for various soils.

Soil behaviour under dynamic loading condition

One of the main factors determining the character of soil behaviour under static and dynamic loading is the amplitude of shear strains depending on which it is necessary to underline elastic, viscoelastic, elastoplastic behaviour or soil failure. Soil deformation character as well as main characteristics of the models used at different amplitudes of shear strain according to [62, 37] is shown in table 3.25 . The change of the shear modulus and damping of soil depending on the

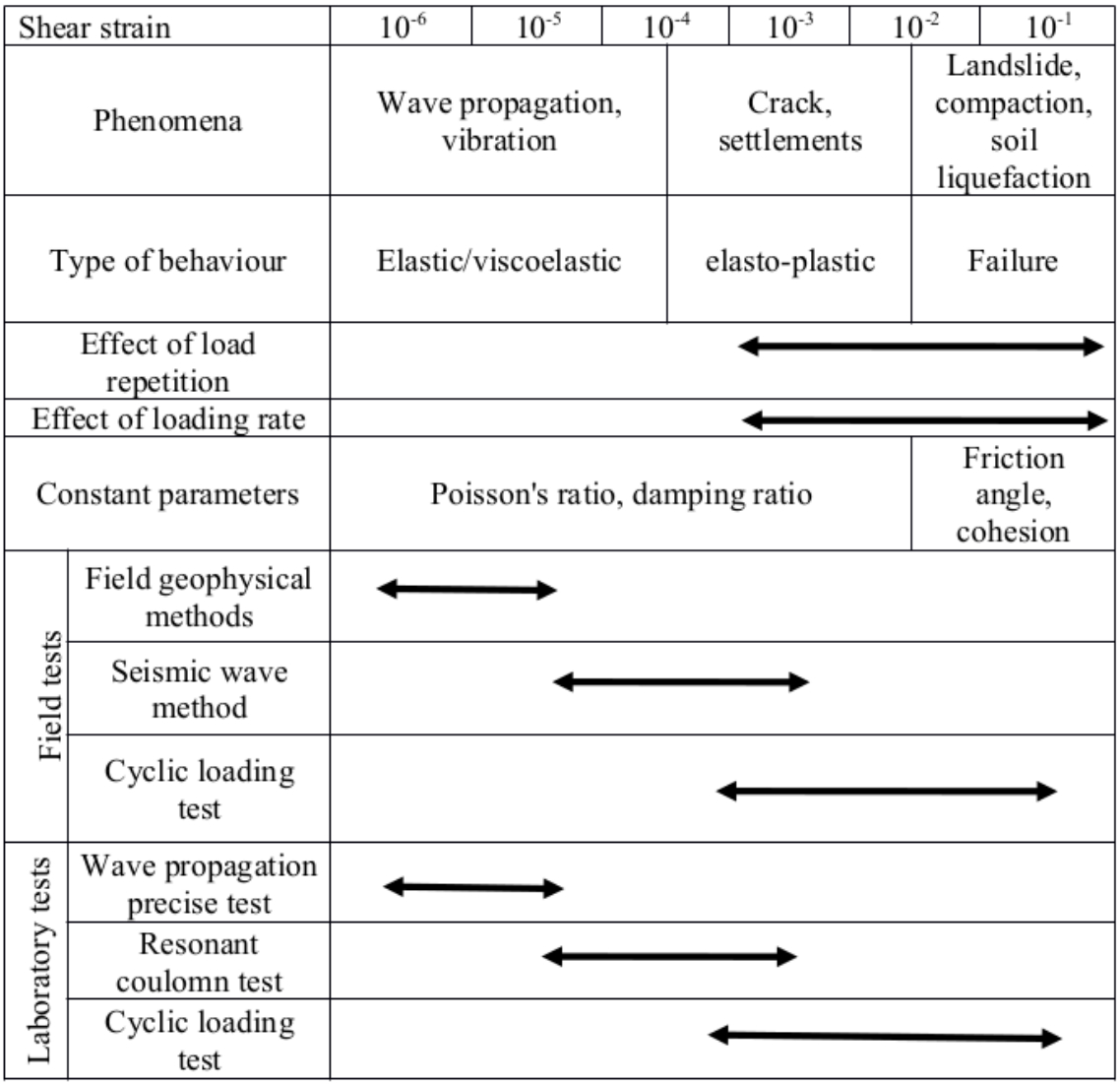

Figure 3.25: The variation of soil deformation character

shear strain is studied in [53, 53, 129] and other similar works. The approximation of the shear modulus change with the shear strains is shown in equation (3.76).

$$G = G_0 \frac{1}{1 + \frac{\gamma}{\gamma_{ref}}}, \tag{3.76}$$

where γ is shear strain, γ_{ref} is the reference shear strain depending on a soil, G_0, G are initial and current shear moduli of a soil. works [62, 37, 72] overview the equations that can be used to define G_0 and G for cohesionless, gravel and cohesive soil depending on their conditions. In some works [154], equation (3.76) is complemented by additional approximation parameter a which is

an exponent of $\frac{\gamma}{\gamma_{ref}}$ transforming equation (3.76)to the form:

$$G = G_0 \frac{1}{1 + (\frac{\gamma}{\gamma_{ref}})^a}, \tag{3.77}$$

In this case, more experiments are required to correctly approximate soil behaviour by equation (3.77). Additionnaly, other ways of approximating the dependency of soil shear modulus on shear strain are used. In terms of conventional triaxial tests (here the tests used in engineering practice are mentioned), the variant proposed by Ishibashi et. al., [61] is one of the most convenient, as it takes into account the effect of hydrostatic pressure and plasticity index (0 for cohesionless soils) on the shear modulus degradation with the increase in shear strains. The law introduced by Ishibashi et al. has the following form:

$$G = G_0 * K(\gamma, PI) * (\sigma_m)^{m(\gamma,PI)-m_0}, \tag{3.78}$$

where

$$K(\gamma, PI) = 0.5 * \left\{ 1 + \tanh \left[\ln \left(\frac{0.000102 + n(PI)}{\gamma} \right)^{0.492} \right] \right\} \tag{3.79}$$

$$m(\gamma, PI) - m_0 = 0.272 * \left\{ 1 - \tanh \left[\ln \left(\frac{0.000102 + n(PI)}{\gamma} \right)^{0.4} \right] \right\} * \exp(-0.0145 * PI^{1.3}) \tag{3.80}$$

Here G_0 is initial shear modulus, based on geophysical data; PI is plasticity index for clays (for sands $PI = 0$) and $n(PI)$ is defined as:

$$n(PI) = \begin{cases} 0 & \text{if } PI = 0 \\ 3.37 * 10^{-6} * PI^{1.404} & \text{if } 0 < PI \leq 15 \\ 7 * 10^{-7} * PI^{1.976} & \text{if } 15 < PI \leq 70 \\ 2.7 * 10^{-5} * PI^{1.115} & \text{if } PI > 70 \end{cases} \tag{3.81}$$

Figures 3.26,3.27 and 3.28 show the degradation of shear moduli at different values of PI and confining pressure σ_m. It is worth noting that for triaxial stress-strain condition the maximum shear strain should be used. These formulas are quite convenient since they do not require

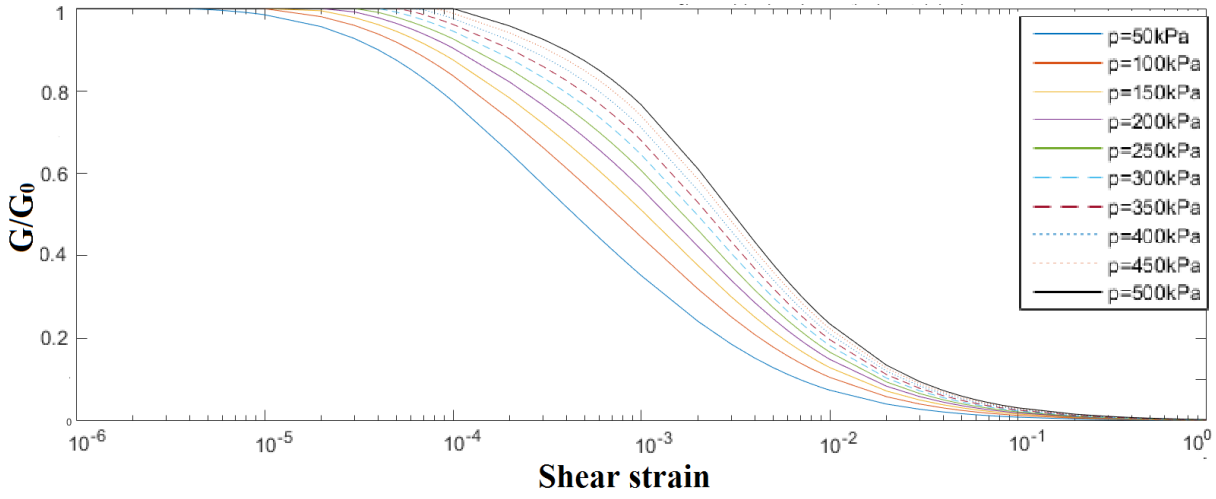

Figure 3.26: Shear modulus degradation for sands at different confining pressures

additional parameters to obtain in soil tests, but they can lead to an increase in the calculation

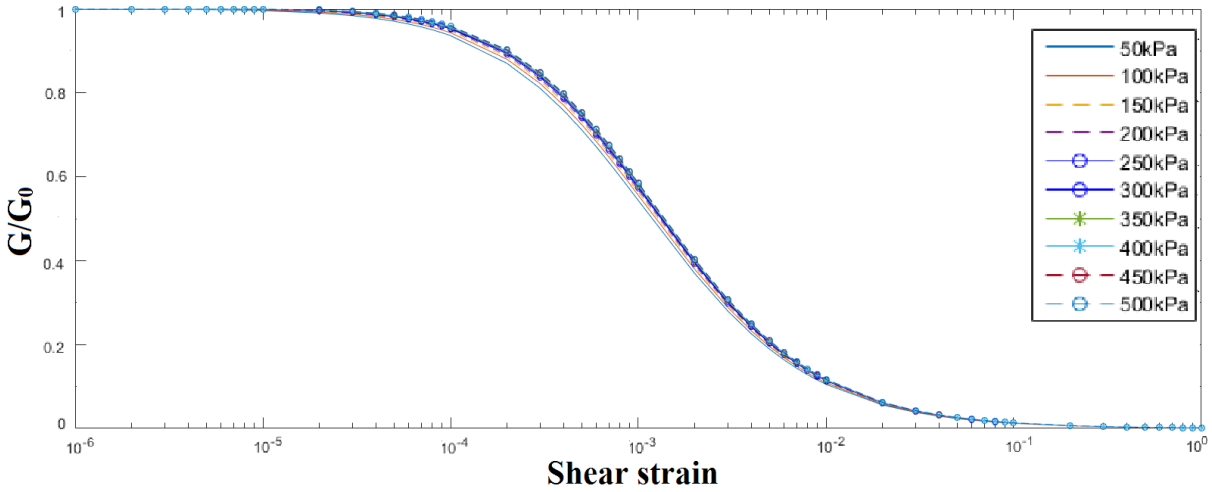

Figure 3.27: Shear modulus degradation for clay with $PI = 50$ at different confining pressures

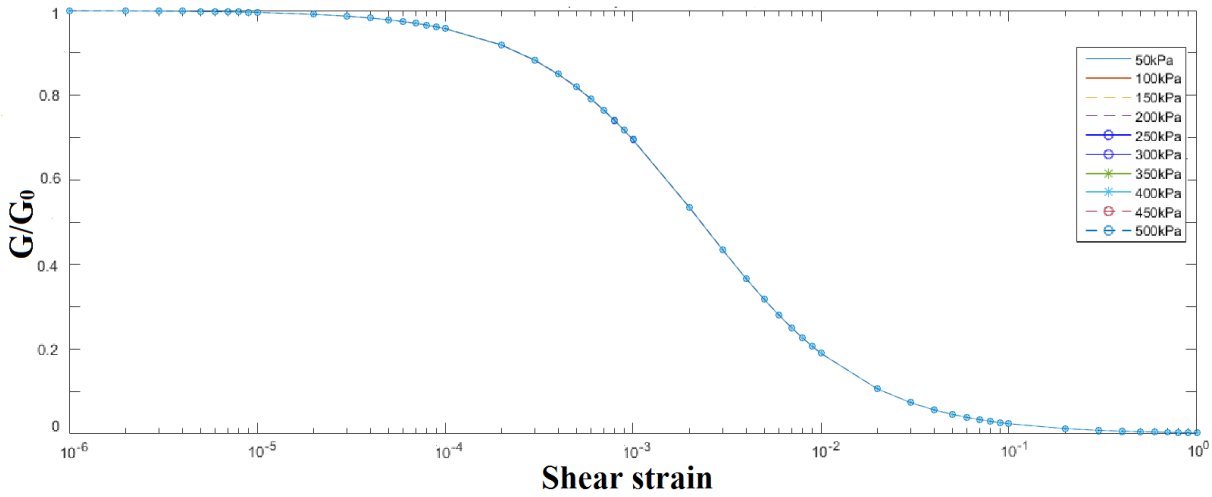

Figure 3.28: Shear modulus degradation for clay with $PI = 100$ at different confining pressures

time. On the other hand, models based on equation (3.76) are more more frequently used. For example, it is implemented in the widely used soil model "small strain hardening soil" [14].

According to table 2.1.2 in Chapter 2 and figure 3.25, artificial vibrations caused by construction works, traffic, as well as heavy dynamic equipment, generate vibrations with shear deformations in the ground not exceeding 10^{-4} during its propagation . Thus, for these vibration sources it is sufficient to use elastic or viscoelastic models,which also allow to use linear equivalent method instead numerical simulation in the time domain. Additionally, within this shear strain range shear modulus varies insignificantly (figures 3.26-3.28).

In contrast to that, earthquakes and explosions generate vibrations of a higher level, which can induce shear strains up to 10^{-2}. Therefore, elastoplastic models are required to take into account nonlinear behavior of the soil. Apart from that, it is important to underline that viscous properties dominates over the plastic ones of the soil skeleton at sufficiently high speeds of pore fluid flow in the channels, which corresponds to high frequencies. At the same time, according to table 2.1.2 the main frequencies of earthquakes that are dangerous for constructions do not exceed $20Hz$ [132]. Therefore, plasticity models are required to correctly account for the dissipation of energy and soil behaviour within the shear strain range $10^{-4} \div 2 * 10^{-3}$. On the other hand it is worth noting that damage models are needed to simulate soil behaviour in the source zone.

Conclusion

Based on the analysis of the models and approaches used in the mechanics of granular media and soil mechanics, as well as the analysis of experimental works on the behaviour of soils under dynamic loading, the following conclusions can be made:

1. For any type of anisotropy, there is no "forbidden" direction for Rayleigh waves (the direction in which Rayleigh wave does not propagate) in the material; hence,the only possibility of protection with vertical seismic barriers is to dissipate and reflect the energy of seismic waves by obstacles.

2. The analysis of vertical seismic barriers interaction with Rayleigh waves within the framework of hyperelastic models (even with account of damping) has significant limitations related to range of the shear strains ($< 10^{-4}$). Therefore, this formulation of the problem is only possible for analysing and design of vibration protection from the vibrations generated by artificial sources producing surface waves of low amplitude, for example, railway transport.

3. At high shear strains exceeding 10^{-4}, plastic behaviour of soils and the degradation of the shear modulus with an increase in shear strains must be taken into account.One of the most accurate approaches in that case is the one based on hypoplasticity theory for granular and cohesive soils proposed in [97, 107], but their use is rather difficult because of the large number of the input parameters and the complexity of the experiments to obtain all the parameters (additionally,the database on different soils for these models is small, which also complicates the possibility of detailed analysis).

4. Modified Cam-Clay model requires more complex set of experiments than conventional engineering triaxial tests. Additionally, it takes into account the effect of soil damage at high confining pressures, which is practically not observed in the near-surface zone where the Rayleigh wave propagates.

5. Models based on perfect plasticity and Drucker-Prager or Mohr-Coulomb approaches are the most suitable for analysis of interaction of surface waves with vertical seismic barriers. Because they approximate the degradation of the soil shear modulus and are quite convenient, since they do not require a large number of input parameters. In addition to that, these models allow to simulate the hysteresis behaviour of soils under cyclic loading. However, these models do not account for the different elastic moduli for loading and unloading, as well as their accuracy in approximation of the shear modulus degradation with the increase in shear strains is less compared to [97, 107, 14]. However, the model based on Mohr-Coulomb approach is chosen for the numerical simulation of the vertical seismic barrier or pile fields interaction with Rayleigh waves at different strain ranges.

6. Numerical damping introduced into the solution algorithm to ensure its convergence may affect the calculation results significantly. Therefore, the minimal value of damping factor should be selected to ensure the convergence of the solution procedure without a significant effect on the final results.

7. Numerical parameters implemented in the Mohr-Coulomb model (meridional and deviatoric eccentricities), as well as the eccentricity of the plastic flow introduced in Drucker-Prager model, have hardly no effect on the results of the calculation. However, in the case of Mohr-Coulomb model these values should be chosen accurately as in some cases the instabilitiy of the solution can take place.

CHAPTER 4

VERTICAL SEISMIC BARRIERS

Contents

In this chapter the results of numerical simulation of surface Rayleigh wave interaction with vertical seismic barriers under hyperelastic material behaviour assumption are presented.The parameters affecting vibration reduction effect are determined and the recommendations towards practical barrier design are given. Additionally, a method for multi parametric optimization of the barrier geometry is presented and adopted for specific soil conditions and design vibration loading.

Simulation methods and FE models

FE models

Mathematical formulation including constitutive equations, boundary and initial conditions for the problem of interaction of surface Rayleigh waves with vertical seismic barriers can be described by the system of equations including equations (3.25), (3.15),(3.18) and (3.19). The analysis is performed in time domain for surface Rayleigh waves generated by fully harmonic surface loading in the form defined by equation below:

$$f(x,t) = Ae^{i\omega t}\delta(\mathbf{x}), \tag{4.1}$$

where i is the imaginary unit; A is the vibration amplitude;ω is the circular frequency of the loading; $\delta(\mathbf{x})$ is the Dirac delta function; is the vector of a unit normal to the free surface and t

is time. In equation (4.1), $\delta(\mathbf{x})$ defines concentrated character of the loading. This means that equation (4.1) defines concentrated point loading in the case of plane strain condition, meanwhile, harmonic line loading generating Rayleigh waves with planar wavefront is considered in the case of spatial stress-strain condition.

Numerical solution for the problem of surface Rayleigh waves interaction with vertical seismic barriers is carried out using an explicit finite-difference procedure for integration in time domain and spatial discretization using finite element method (FEM) in Abaqus 2016 software [1].

Explicit finite-difference procedure used in the analysis rests on the second order explicit central difference integration scheme involving the Lax-Wendroff method [75], [1]. Time integration is performed using many small time increments, which size is selected automatically by the program satisfying the stability condition for the numerical scheme also called the Courant–Friedrichs–Lewy (CFL) condition [35]. At a given element size Δx , this condition takes the following form:

$$\Delta t = C\frac{\Delta x}{c_S}, \tag{4.2}$$

where Δt and c_S are the time step and the shear wave speed in the considered material; C is a some constant. The disadvantages of the selected time integration scheme and the effect on the final results are discussed in the next section.

Spatial discretization is performed with CPE4R and C3D8R element types [1] for plane-strain and 3D conditions respectively. Elements of the type CPE4R are four-node quadrilateral elements with a linear shape function reduced by the integration scheme with control of deformations and the energy equal to zero at the integration point [1].Elements of the type C3D8R are eight-node hexahedral elements with a linear shape function reduced by the integration scheme with control of deformations and the energy equal to zero at the integration point [1]. The meshed reproduced for plane-strain and 3d conditions are structural and quite accurate with maximum length ratio (k_l) in the range $k_l \in [0.99, 1]$. Numerical error given by this type of discretization along with the selection of optimal element size is discussed in the next section.

It is worth noting that a vertical barrier can act as a vibration mitigation measure if the wavelength is comparable or less than the barrier depth and the dimensions of the protected zone in plane. According to [95] the minimum frequency in the earthquake elastic response spectrum starts at approximately $2Hz$. At the same time, the artificial vibration sources usually generate vibrations with larger frequencies (table 2.1.2). Therefore, the lowest frequency $2Hz$ is chosen as it generates Rayleigh waves with large enough wavelength corresponding to the real vibration sources both natural and anthropogenic nature and for lower frequencies the construction of a barrier is not possible even in soft soils as it will require large barrier depth's which is too expensive or impossible for large wavelengths ($l > 100$). It is worth noting, that higher frequencies correspond to shorter wavelengths and require smaller protective barriers. The results in the present chapter are presented in relation to the maximum Rayleigh wavelength l equalling to $50m$ and corresponding to minimum vibration frequency $f = 2Hz$.

In addition to that, two main assumptions are made: (i) the size of the protected zone does not change which implies that the barrier volume can be replaced by its cross-section area as the barrier length remains constant; (ii) the same soil conditions are used for all the calculations. This allow simulation of Rayleigh wave interaction with seismic barriers under plain strain conditions at the first stage of the analysis to estimate the effect of geometrical sizes of a barrier as well mechanical parameters of its material on vibration reduction in the protected zone Δ.

Plane strain condition is simulated in a plate (figure 4.1) with vertical and horizontal sizes equalling to $18 * l$ and $11 * l$ respectively, where l is the considered Rayleigh wavelength. To decrease the sizes of the model a symmetry condition is applied on the left edge of the plate (3). The source of waves is simulated using harmonic point loading (1), which is defined according to equation (4.1) and applied on the top of the left edge (on the top of the symmetry axis). At a distance L_1 from the symmetry axis (3) a vertical seismic barrier is created (2). The protected

zone Δ of the size l is located directly beyond the vertical barrier (2). On the bottom and right edges of the plate (4) "infinite elements" of CINPE4 type [1] are used to avoid reflections from the boundaries. Defining the considered boundaries as $\mathbf{\Gamma_\chi}$ with a normal $\boldsymbol{\chi}$,these non-reflected boundary conditions can be written the following form [46]:

$$\left(\frac{\partial \mathbf{u}}{\partial \boldsymbol{\chi}} + \left(\sqrt{\lambda + 2\mu} \cdot \boldsymbol{\chi} \otimes \boldsymbol{\chi} + \sqrt{\mu}(\mathbf{I} - \boldsymbol{\chi} \otimes \boldsymbol{\chi})\right) \cdot \dot{\mathbf{u}}\right)_{\mathbf{x} \in \mathbf{\Gamma_\chi}} = 0, \tag{4.3}$$

where $\mathbf{x}$ and $\mathbf{u}$ are the coordinates and displacements vectors; λ and μ are Lame's constants. This conditions is imposed only for longitudinal waves incident on this boundary virtually normal. Thus,to be absorbed, the unit wave vector that determines the direction of wave propagation ($\mathbf{n}$) must satisfy the condition:

$$(\mathbf{n}; \boldsymbol{\chi})|_{\mathbf{x} \in \mathbf{\Gamma_\chi}} \leq 15^0, \tag{4.4}$$

everywhere on the boundary $\mathbf{\Gamma_\chi}$. Taking into account that several types of waves (longitudinal, transverse and Rayleigh waves) simultaneously propagate near the boundary in the considered problem, the boundary condition defined by equation(4.3) is partly applicable only P-waves. Therefore,the dimensions of the model are chosen in a way that the waves reflected from the boundaries of the model should not return to the observation zone $2 * \Delta$ during the calculation time. In addition to that, during the calculation time $\mathbf{t_1}$ several waves go through the observation zone $2*\Delta$ and the oscillation process becomes steady. The interaction of body waves with vertical seismic barrier is neglected. Therefore, vertical model size satisfies the condition $H \geq \frac{C_p \mathbf{t_1}}{2}$; the distance between the barrier (2) and the left border (L_1) is calculated taking into account the symmetry condition (3) $L_1 \geq \frac{C_p \mathbf{t_1}}{3}$. If the size of the observation zone 2Δ is $L_2 = 2l$, the distance from the observation zone to the right border of the model is L_3 and the general horizontal size of the model is $L_1 + L_2 + L_3$, then $L_3 \geq \frac{C_p \mathbf{t_1} - L_1 - L_2}{2}$.The mesh size is less than $\frac{l}{10}$ where l is the wavelength. Figures 4.2 and 4.3 represent the picture of Rayleigh wave propagation and interaction with the barrier in the planar model under plane strain condition.

It is possible to implement more complicated absorption techniques such as perfectly matched layer (PML) proposed by Berenger [15], Absorbing Layers using Increasing Damping (ALID) introduced by Semblat et al. in [131] and implemented by Rajagopal et al. in [120] into commercial software or Hybrid Asynchronous Absorbing Layers with Increasing Damping (HA-ALID) introduced in [87] by Li et al. All these methods, are more efficient than the one used in this work, however, they are not implemented in Abaqus/explicit and would require writing additional subroutines. Meanwhile, the available computing power allowed to eliminate "reflection effect" by increasing the model size.

Remark 4.1 This work concerns the interaction of Rayleigh waves with vertical seismic barriers outside of the source vicinity. This is primarily due to the fact that the behaviour of waves in the source zone has difficult to predict complex nature which is strongly affected by geological conditions along with the source itself. In the considered case, the source determines only the frequency range and shear strain amplitude in the soil during wave propagation. Additionally, it is possible to distinguish the major waves that carry the energy of vibration source. As a result, the distance between the seismic barrier and the source has virtually no effect on the final reduction effect in the protected zone. This is the case for homogeneous media, while for stratified media the situation is different which is, however, beyond the scope of this research.

Remark 4.2 Hereinafter, if the variable dimension is not explicitly specified, it is presented in the dimensionless form. The main dimensionless complex is given in the section 4.1.3 (equations (4.5) and (4.6)). By default, geometrical variables are given in relation to the Rayleigh wave wavelength, which maximum value considered in this work equals to $50m$.

The spatial model is used to assess the results of numerical simulation carried out using the planar model. The model is a parallelepiped with the dimensions chosen based on the same principle as in the planar model. Hence, the interaction of surface waves with a barrier takes

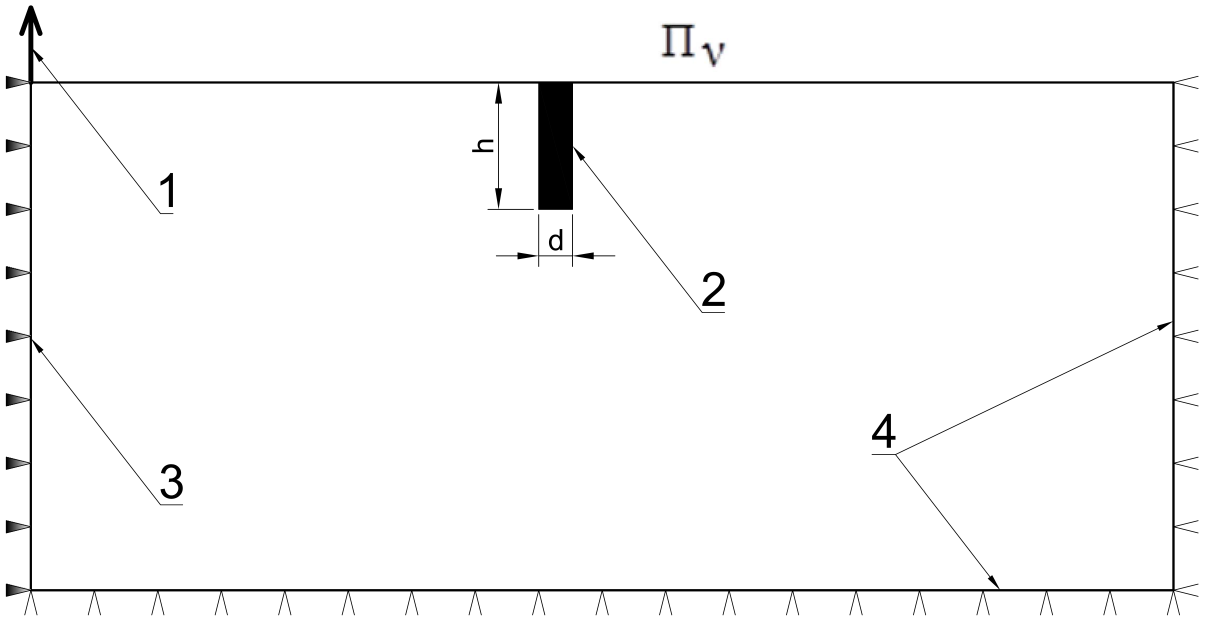

Figure 4.1: Planar FE model configuration.
1. Existing force. 2. Vertical barrier. 3. Condition of symmetry. 4. Infinite boundaries.

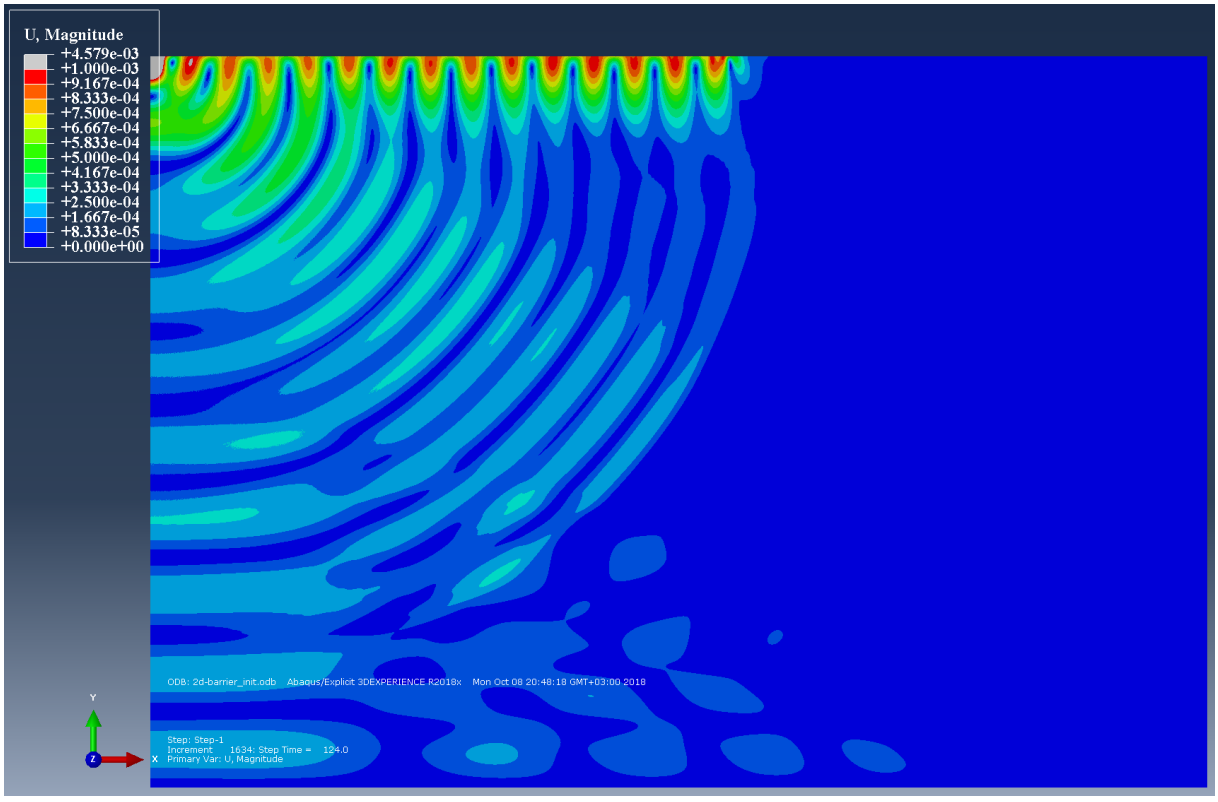

Figure 4.2: Rayleigh wave propagation in planar model.Amplitude of displacements,m.

place in the zone remote enough from the source and the distance from the barrier to the edges of the model ensures that the reflected waves do not return to the observation zone. The sizes of the model along the x, y and z axis equal to $9l$, $3l$ and $5l$ respectively with the diameter of the protected zone equalling to l. To reduce the model size two symmetry planes (4) and (5) are introduced (figure 4.4). On the top of the symmetry plane (4), a concentrated or line loading

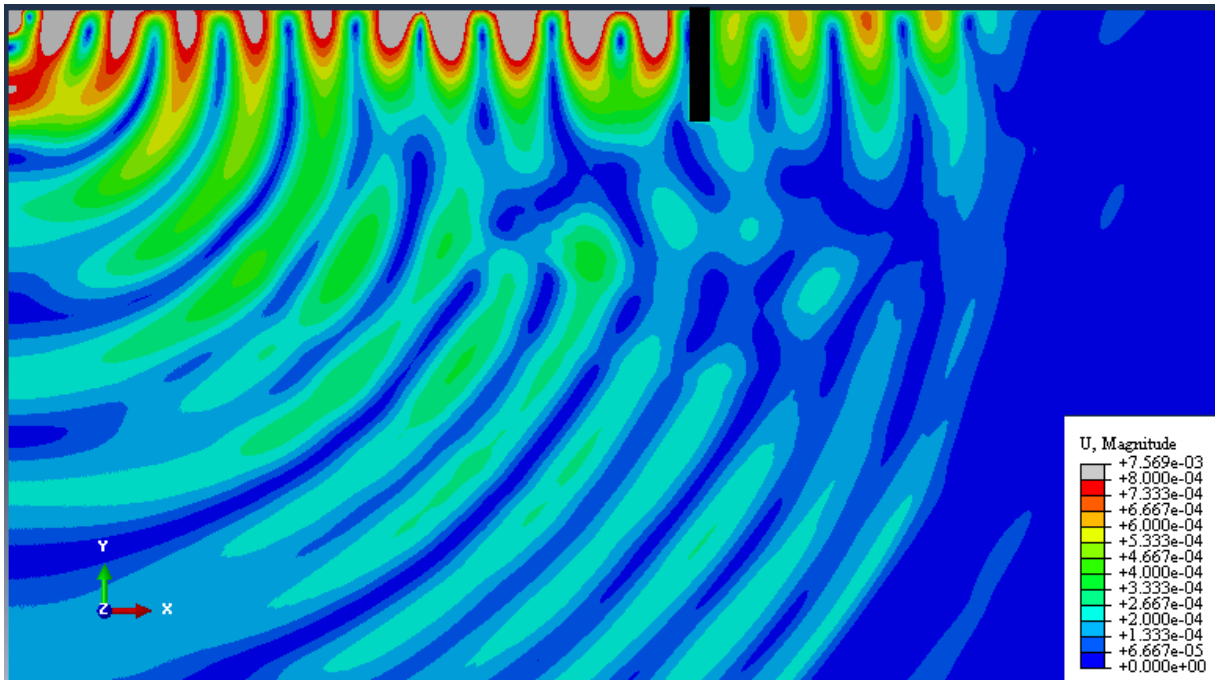

Figure 4.3: Rayleigh wave interaction with the vertical barrier.Amplitude of displacements,m.

defined by equation 4.1 is applied (3) to simulate a Rayleigh wave with a plane or spherical wavefronts, respectively. Primary calculations show that there is hardly no difference in the vibration reduction effect for plane and spherical waves. Therefore, taking into account the requirements to the model size, Rayleigh waves with a plane front are considered in the following text. The propagation of plane Rayleigh waves and their interaction with a vertical seismic barrier in the spatial model is shown in figures 4.5 and 4.6 respectively.

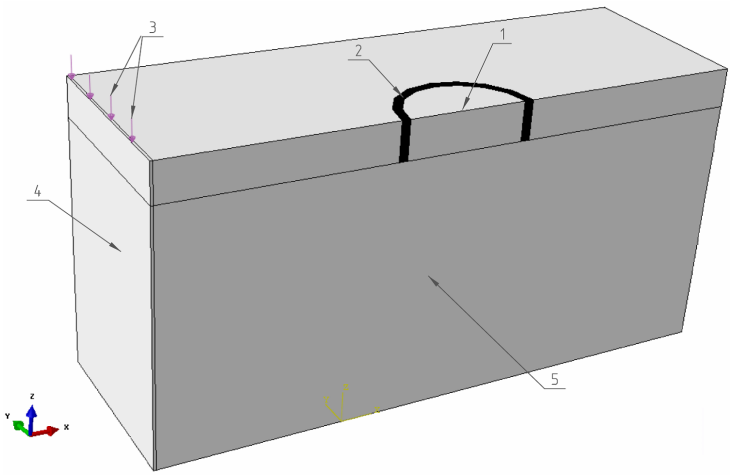

Figure 4.4: 3D numerical model of the vertical seismic barriers
(1. Observation point 2. Vertical barrier. 3. Harmonic loading 4,5. The conditions of symmetry with respect to YoZ and XoZ planes respectively). The bottom of the model is fixed.

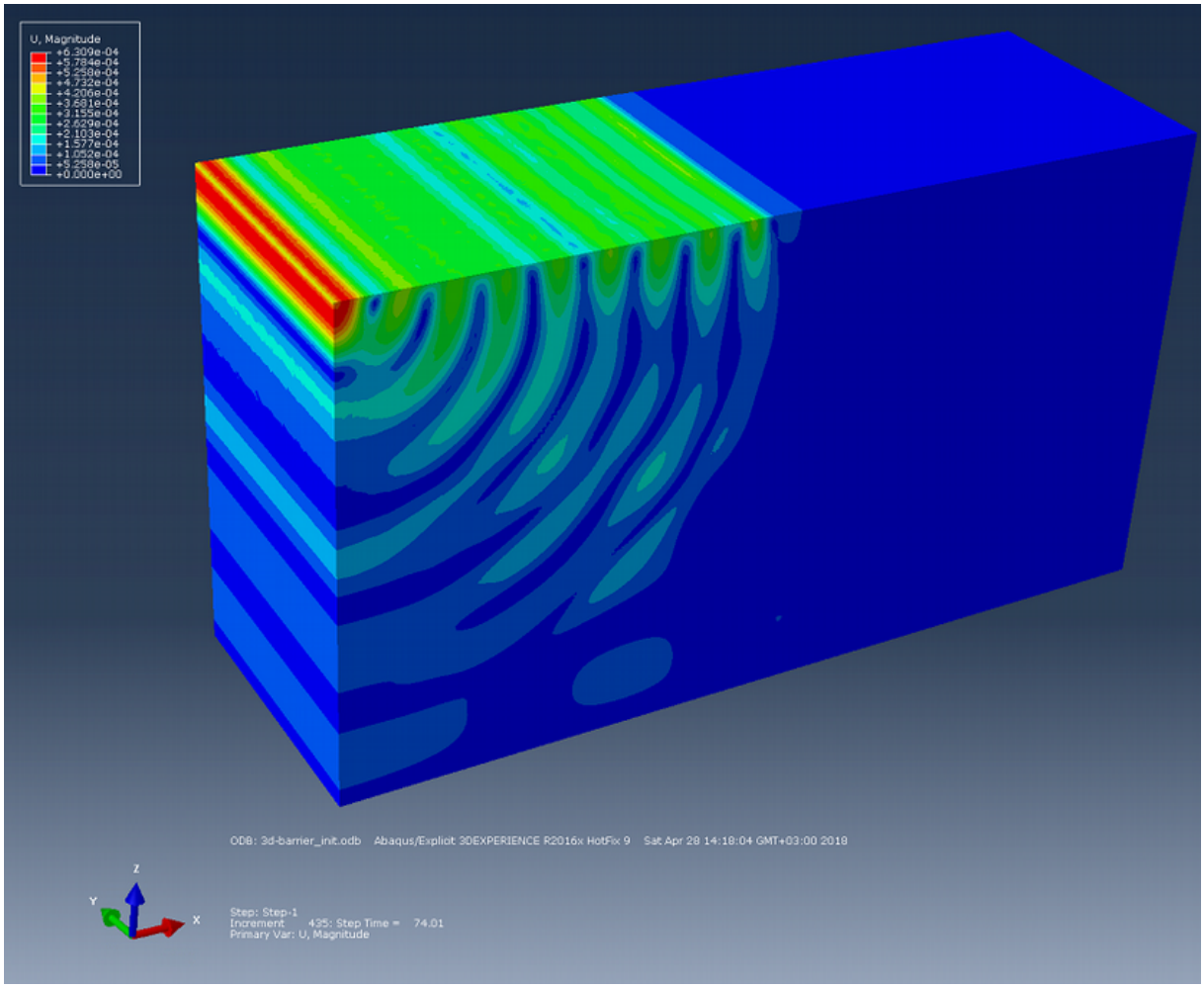

Figure 4.5: Plane Rayleigh wave propagation in the spatial case.Amplitude of displacements,m.

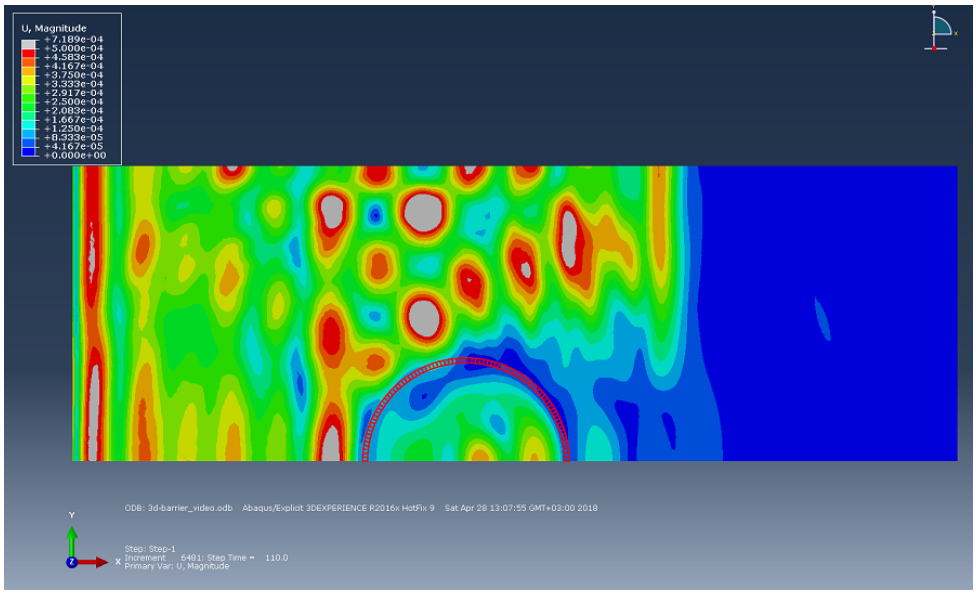

Figure 4.6: Plane Rayleigh wave interaction with the vertical barrier in the spatial case..Amplitude of displacements,m.

The influence of the numerical methods

Detailed analysis of numerical errors caused by explicit central difference scheme of the second order with FE element discretization with quadrilateral and hexahedral elements with a linear shape function is presented in [152], [36] and [75] including such effects as error control, convergence,stability, numerical damping etc. for elastic and elastoplastic constitutive models. Here, the analysis of element size is presented to show number of elements used in the computations for discretazing key parameters of the wavelength, barrier and model. It is worth noting that a minimal barrier size requires at least $2-3$ elements for correct stiffness approximation and a minimal wavelength requires at least $8-10$ elements for the correct simulations [73].

Figure 4.7 represents the amplitude of displacements of a point in the protected zone without a barrier at different number of elements per wavelength. According to the graphs in figure 4.7, it can be seen that the number of elements per Rayleigh wavelength equalling to 100 provides sufficient accuracy of the solution under plain strain conditions and further reduction of the element size gives virtually no effect on the results. Therefore, the element size equalling to $0.01l$ is chosen for the plane case .

Reducing the element size in the spatial case affects the results till the element size of $0.025l$. Further decrease in the element size gives virtually no effect, but leads to the appearance of non-physical high-frequency noise (figure 4.8) which is inherent to the second order finite difference schemes [75]. Figure 4.9 shows the amplitude of displacements of the point in the frequency domain at the element size equalling to $0.01l$. Taking into account that the loading frequency is $2Hz$, the "numerical noise" in the frequency range $f = 3 \div 35Hz$ is observed at this element size. However, this noise is easy to control at the considered harmonic loading and element size. Additionally, it gives hardly no affect on the maximum values of displacements amplitude and kinetic energy. Thus, for the spatial model, the element size is chosen to be $0.01l$ as for less element sizes the "numerical noise" increases along with the calculation time. The effect of numerical noise is eliminated in this work by using Butterworth's filter [108] with account of loading frequencies.

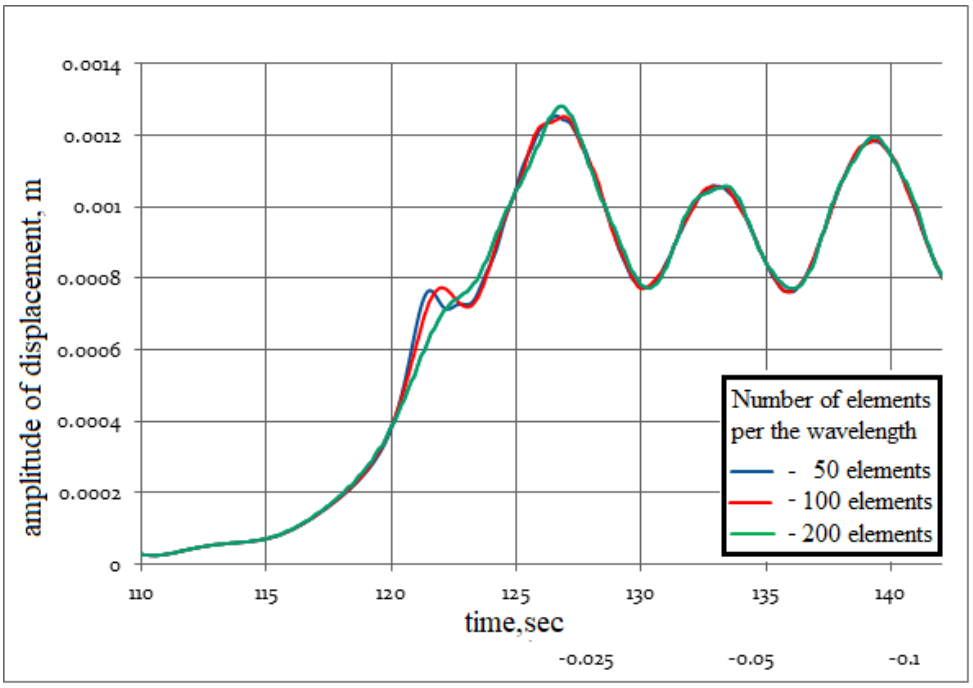

Figure 4.7: The amplitude of displacements in the protected zone without a barrier at different number of elements per Rayleigh wavelength in the planar model.

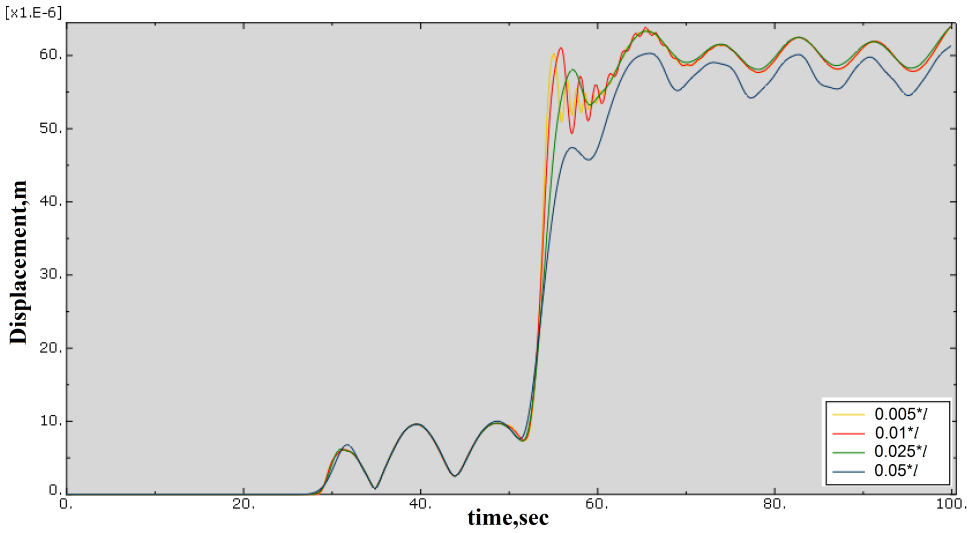

Figure 4.8: The amplitude of displacements in the protected zone without a barrier at different sizes of the element Δx in the spatial model.

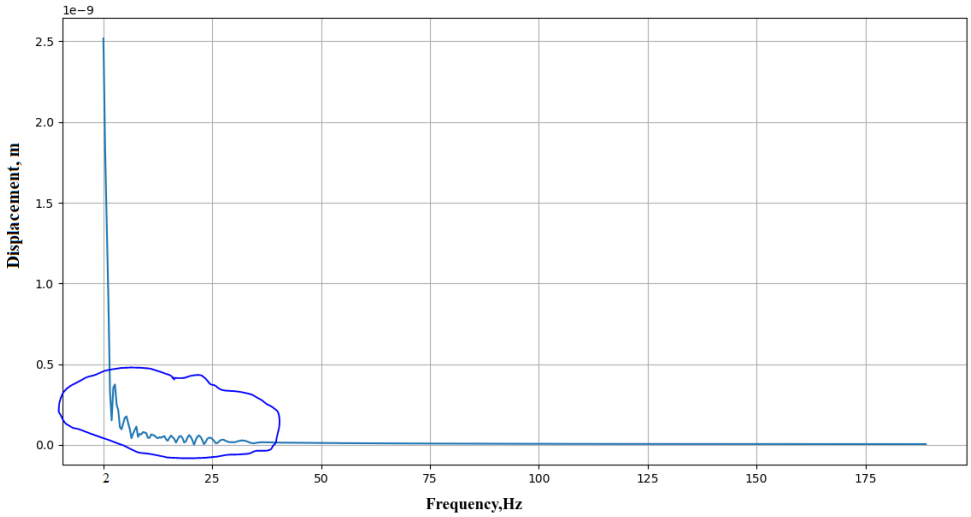

Figure 4.9: High frequency noise caused by the spatial discretization with FEM (circled in blue).

Principal dimensionless complex

According to π-theorem [49] which states that a physical law does not depend on the form of units as well as [80] the kinetic energy field of an area Δ beyond the barrier can be described by the following group of dimensionless parameters:

$$K_{bar} = f\left(\frac{E_{bar}}{E_{soil}}; \frac{\rho_{bar}}{\rho_{soil}}; \frac{d \times h}{l^2}; \frac{h}{l}; \nu_{bar}; \nu_{soil}\right), \tag{4.5}$$

where the index *soil* indicates the soil material of the half-space, while the index *bar* corresponds to the parameters of the barrier; l is the wavelength of Rayleigh wave in a half-space (this wavelength can be solved from the Bergmann-Viktorov equation); E_{bar}, E_{soil} correspond respectively to Young's modulus of the barrier and of the soil ; ν_{bar}, ν_{soil} are Poisson's ratios; ρ_{bar}, ρ_{soil} are the densities; d and h are the thickness and the depth of the barrier accordingly. Displacement field in the protected zone Δ can be defined similarly:

$$u_{bar} = g\left(\frac{E_{bar}}{E_{soil}}; \frac{\rho_{bar}}{\rho_{soil}}; \frac{d \times h}{l^2}; \frac{h}{l}; \nu_{bar}; \nu_{soil}\right), \tag{4.6}$$

According to the analyses performed in[80], both Poisson's ratios have hardly any influence on the kinetic energy field. Therefore both Poisson's ratios are then eliminated in this work. That is why the expressions (4.5) and (4.6) can be simplified to the following:

$$K_{bar} = f\left(\frac{E_{bar}}{E_{soil}}; \frac{\rho_{bar}}{\rho_{soil}}; \frac{d \times h}{l^2}; \frac{h}{l}\right), \tag{4.7}$$

$$u_{bar} = g\left(\frac{E_{bar}}{E_{soil}}; \frac{\rho_{bar}}{\rho_{soil}}; \frac{d \times h}{l^2}; \frac{h}{l}\right), \tag{4.8}$$

The optimization problems can be described by introducing several dimensionless variables. The principle geometric dimensionless complexes:

$$\tilde{h} = \frac{h}{l}; \tilde{d} = \frac{d}{l}, \tag{4.9}$$

where $\tilde{h}$ and $\tilde{d}$ are the dimensionless barrier depth and width respectively;h and d are barrier depth and width accordingly; l is the wavelength.

The dependent geometrical dimensionless complexes:

$$\tilde{A} = \tilde{h} \times \tilde{d} = \frac{h \times d}{l^2}; \tilde{r} = \frac{h}{d}, \tag{4.10}$$

which are the dimensionless cross-section area and geometrical ratio accordingly.

In the first stage of computations involving linear elastic constitutive law (equation (3.25)) and planar model (figure 4.1) the following ranges for material parameters are considered: $\tilde{E} \in [0.01, 1000]$ and $\tilde{\rho} \in [0.01, 3]$ at geometrical ratios $\tilde{r} = 0.1 \div 18$ and constant dimensionless volume equalling to $\tilde{A} = 0.08$. Total number of computations performed equals to roughly 2000. Then, at the second stage the principal results obtained from the 2d model are checked using 3d model (figure 4.4) to verify and analyse shadow zone behind the barrier. Total number of computations performed in that case is virtually 30.

AS it is written in chapter 3 analysis of material and geometrical parameters of the barriers is carried out in terms of reduction ratio. In this chapter, energy reduction ratio $k_{ref,E}$ equation (3.13) is used for the assessment of vibration reduction effect given by a barrier.

The influence of the barrier material

The main mechanical barrier parameters that determine its effectiveness in terms of vibration reduction are its density and modulus of elasticity (as it was mentioned before, the case of hyperelastic materials obeying Hooke's law is considered here). Variation of the energy reduction ratio in the area Δ due to variation of the barrier relative Young's modulus $\tilde{E} = \frac{E_{bar}}{E_{soil}}$ and relative density $\tilde{\rho} = \frac{\rho_{bar}}{\rho_{soil}}$ with other parameters in (4.7) fixed is shown in (figure 4.10). The contour plot in figure 4.10 is plotted at $\nu_{bar} = \nu_{soil} = 0.25$, $\tilde{\omega} = 0.324$, $\tilde{r} = 6.35$, $\tilde{A} = 0.08$ (here $\tilde{\omega} = 0.324$ is the dimensionless circular frequency).

The obtained results show that the barrier is most effective if the difference between the mechanical characteristics of the barrier material and the soil increases. Which means that both decrease and increase in relative Young's modulus as well decrease and increase in relative density leads to the decline in the reduction ratio, thus, increasing the barrier effectiveness. Therefore, the minimum of the reduction ratio at fixed geometrical parameters can be achieved on the border of the considered range of relative Young's modulus $\tilde{E}_{bar}$ along with the relative density $\tilde{\rho}_{bar}$.

At the same time, it is worth noting that a barrier made of low dense and non stiff material (lesser than those of the soil) is more effective than a heavy rigid barrier if the sizes are equal for the geometry considered. However, as it will be shown below, at some values of the cross-section area and geometrical ratios vibration decrease for a rigid barrier can be higher than that of the barrier made of light and non-rigid material. Hence, in case of small wavelengths, when construction of an empty trench is possible, an empty trench is recommended which is in agreement with the previous studies presented in chapter 2.

More detailed charts in the figures 4.11 and 4.12 confirm better barrier reduction effect in the case of the maximum difference in the density and stiffness of its material parameters from those of the soil.

The curves in figure 4.11 shows that the dependency of the reduction ratio on relative Young's modulus of the barrier has a single maximum at $\tilde{E}_{bar} = 1$. If Young's modulus increases, the reduction ratio demonstrates more than two times decrease at all the densities followed by less rapid decline after $\tilde{E}_{bar} = 10$. If relative Young's modulus decreases from 1 to 0, the reduction ratio decreases at all the densities. However, even in this case there are no additional extremes in the graph.

In the case of high dense barrier material, $k_{red,E}$ attains lower values if relative Young's modulus is large. If the barrier is made of a material with a low density, $k_{red,E}$ reaches its minimum values at smaller relative Young's modulus. It can be also seen from the curves in figure 4.12 with a minimum of the reduction ratio achieved at the boundary of the considered range.

To confirm the previous conclusion, two limit cases are considered which are (i) an empty trench($\tilde{E}_{bar} = 0; \tilde{\rho}_{bar} = 0$)) , (ii) a trench with fixed borders ($\tilde{E}_{bar} \longrightarrow \infty; \tilde{\rho}_{bar} \longrightarrow \infty$)). The curves in figure 4.13 are plotted for these limit cases at $\tilde{\omega} = 0.324$, $\tilde{r} = 6.35$, $\tilde{A} = 0.08$. The obtained results confirm the conclusions that the higher the difference in the mechanical parameters of barrier material and the soil the higher the reduction effect given by the barrier.

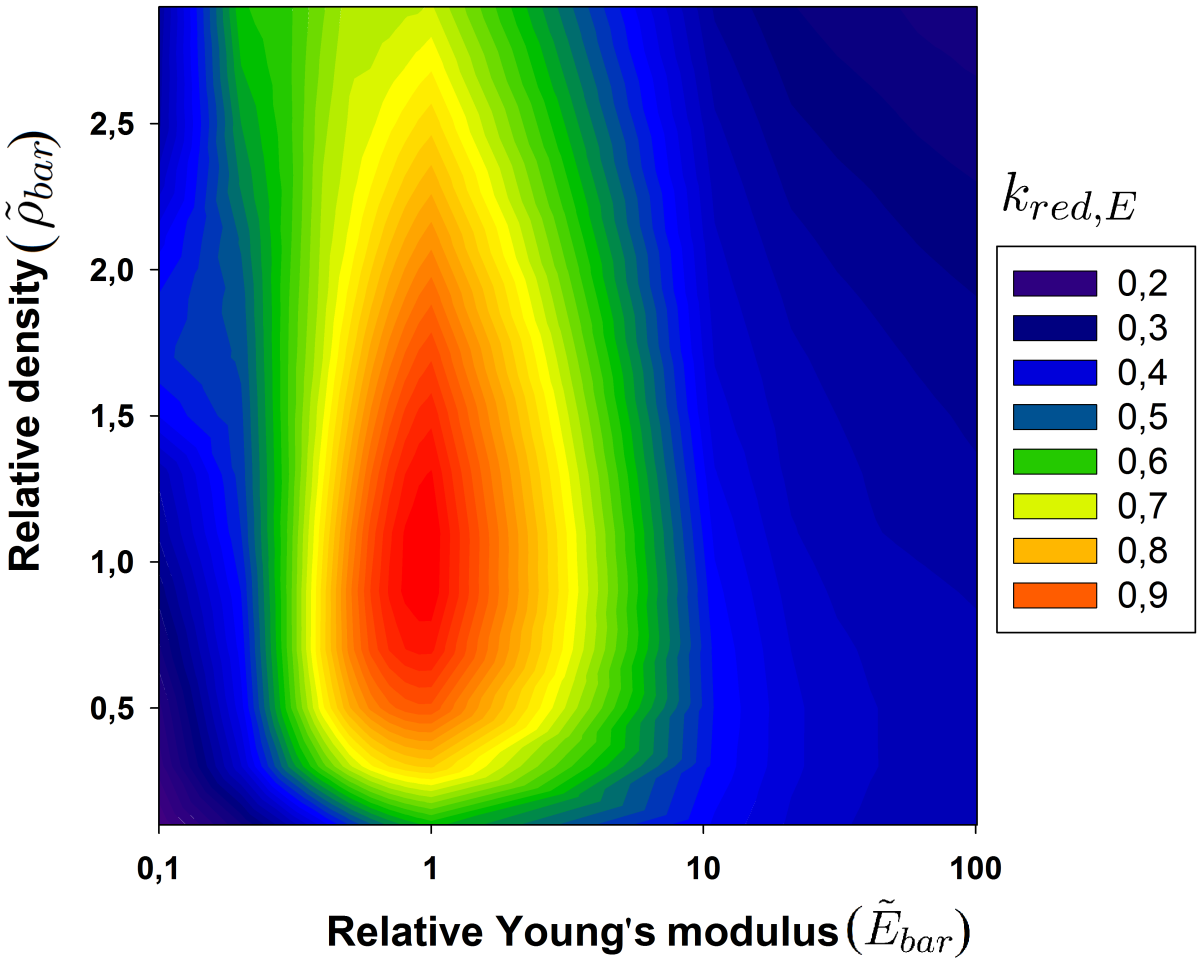

Figure 4.10: Reduction ratio versus dimensionless density and Young's modulus (barrier geometrical ratio $\tilde{r} = 6.35$; barrier dimensionless cross-section area $\tilde{A} = 0.08$; dimensionless circular frequency $\tilde{\omega} = 0.324$).

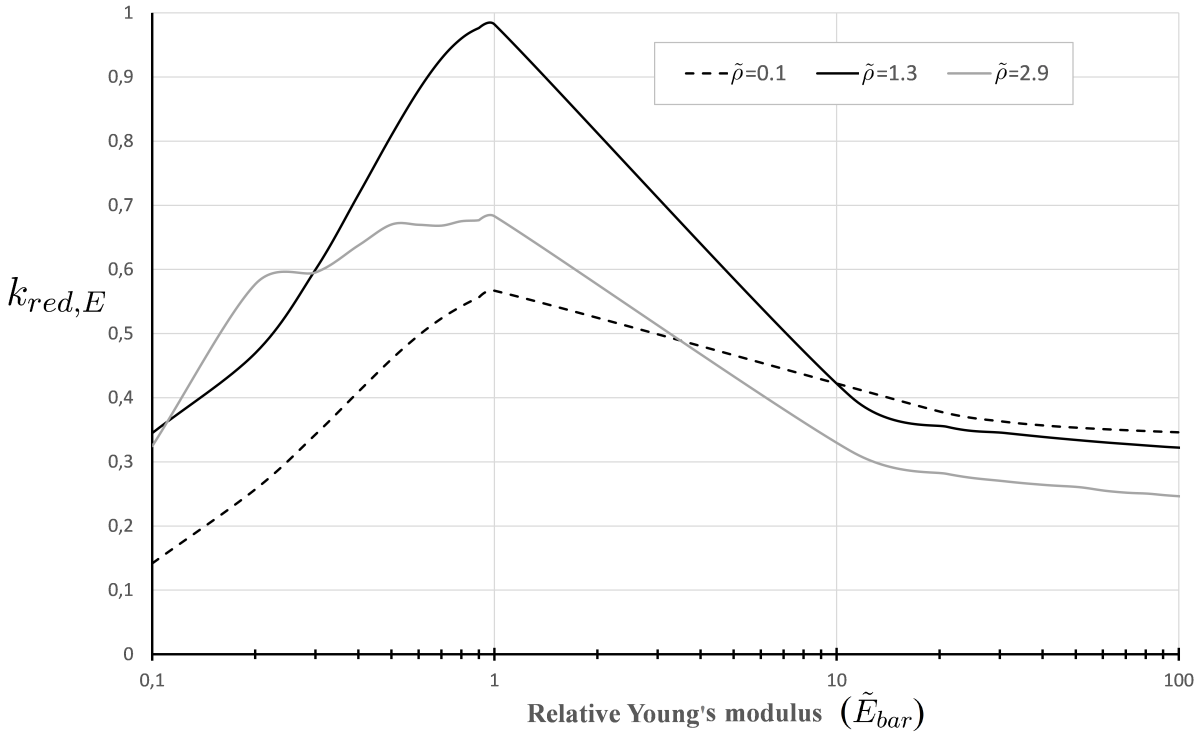

Figure 4.11: Reduction ratio at various relative densities versus dimensionless Young's modulus (barrier dimensionless depth $\tilde{r} = 6.35$; barrier dimensionless cross-section area $\tilde{A} = 0.08$; dimensionless circular frequency $\tilde{\omega} = 0.324$).

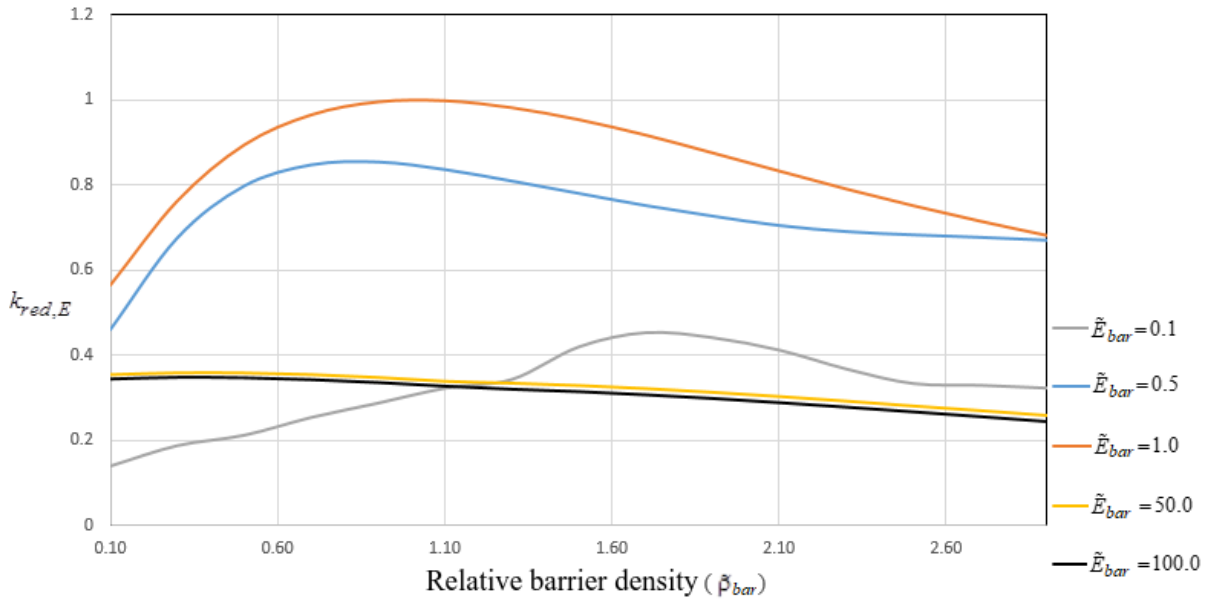

Figure 4.12: Reduction ratio at various relative Young's modulus versus dimensionless density (barrier dimensionless depth $\tilde{r} = 6.35$; barrier dimensionless cross-section area $\tilde{A} = 0.08$; dimensionless circular frequency $\tilde{\omega} = 0.324$).

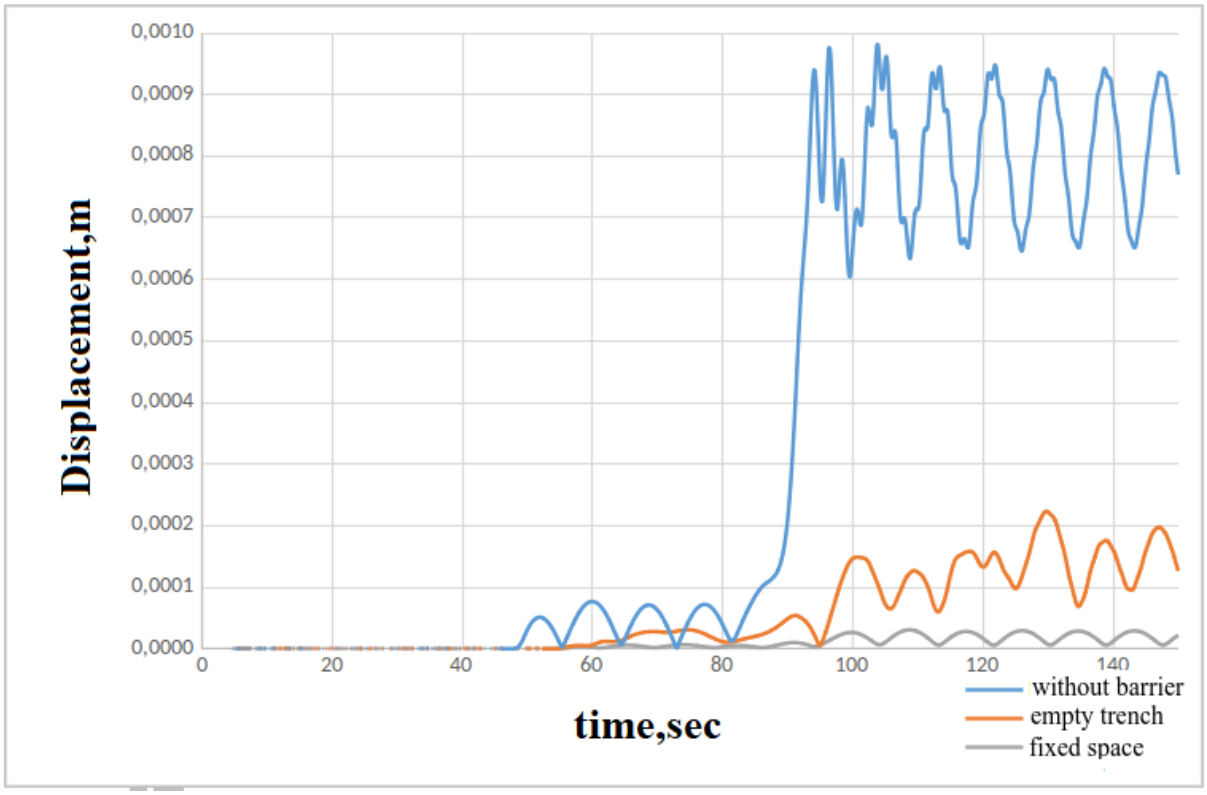

Figure 4.13: Displacements in the case of empty and fixed trench (trench dimensionless depth $\tilde{r} = 6.35$; trench dimensionless cross-section area $\tilde{A} = 0.08$; dimensionless circular frequency $\tilde{\omega} = 0.324$).

The influence of barrier geometry

According to the results obtained in the previous section, the higher the difference in the mechanical parameters of the barrier material from those of the soil the better reduction effect can be obtained. If "exotic" materials are not considered (high dense and non stiff materials, stiff and light weight materials, meta materials, etc.), two types of construction materials are possible: (1) heavy and rigid material; (2) light and non stiff material. Excluding expensive materials (lead or similar metals characterized by high density and stiffness), then two construction materials are best suited for the barrier: reinforced high density concrete and expanded polystyrene foam (EPS).

According to the Eurocode 8 [138] seismic shear wave speeds for soft soils are shown in the table 4.1. Then, these data are recalculated to Young's modulus. The elastic parameters for Expanded Polystyrene Geofoam (EPG) and reinforced high density concrete are shown in table 4.2. Therefore, the normalized parameters used for "rigid material" are $\tilde{E}_{bar} = \frac{E_{bar}}{E_{soil}} = 100$, $\tilde{\rho}_{bar} = \frac{\rho_{bar}}{\rho_{soil}} = 3$, while the ones chosen for "soft material" are $\tilde{E}_{bar} = \frac{E_{bar}}{E_{soil}} = 0.1$, $\tilde{\rho}_{bar} = \frac{\rho_{bar}}{\rho_{soil}} = 0.1$.

Soil type	Density ρ, kg/m^3	Poisson's ratio ν	c_S, m/s
Deposits consisting, or containing a layer at least 10 m thick, of soft clays/silts with a high plasticity index ($PI > 40$) and high water content	1750	0.45	< 100
Deposits of loose-to-medium cohesionless soil (with or without some soft cohesive layers), or of predominantly soft-to-firm cohesive soil.	1880	0.3	< 180
Deep deposits of dense or medium dense sand, gravel or stiff clay with thickness from several tens to many hundreds of metres.	2000	0.2	$180-360$

Table 4.1: Dynamic properties of soils

Material	Density ρ, kg/m^3	Poisson's ratio ν	Young's Modulus, MPa
EPS	45.7	0.05	12.8
Reinforced high density concrete	4650-6090	0.23	35500-57000

Table 4.2: Dynamic properties of barrier materials.

Taking into account that the sizes of the protected area for linear and circular barriers are fixed , its relative volume can be replaced by the relative cross-section area of the barrier $\tilde{A} = \frac{h \times d}{l^2}$. Figures 4.14 and 4.15 represent the reduction ratio evolution with the ratios $\tilde{r} = \frac{h}{d}$ and $\tilde{h} = \frac{h}{l}$ at $\tilde{A} = 0.08$. The obtained results reveal that for soft materials one minimum that corresponds to the vertical trench can be observed at $\tilde{r} = 3.55$. Meanwhile, for rigid material there are two local minimums corresponding to horizontal and vertical seismic barriers at $\tilde{r} = 0.25$ and $\tilde{r} = 4.5$ respectively.

Horizontal barriers are considered in [80] and it is shown that this type of protection is effective

for soft soils. However, the optimal material for such barrier has high density and low Young's modulus, which is difficult to implement in practice. As for the cases considered above, the local minimum value of reduction ratio for rigid material corresponding to the horizontal barrier $\frac{h}{d} = 0.25$ is higher than the one relating to the vertical seismic barrier $\frac{h}{d} = 4.5$. Additionally, k_{redE} continue decreasing with the increase in $\tilde{r}$ for rigid materials, while for soft materials k_{redE} slightly increases.

According to the figure 4.15, the barrier depth is the most important size at fixed cross-sectional area and mechanical parameters of the material. Therefore,an increase in the barrier depth to the above-mentioned minima at a constant volume improves its effectiveness in terms of vibration reduction.

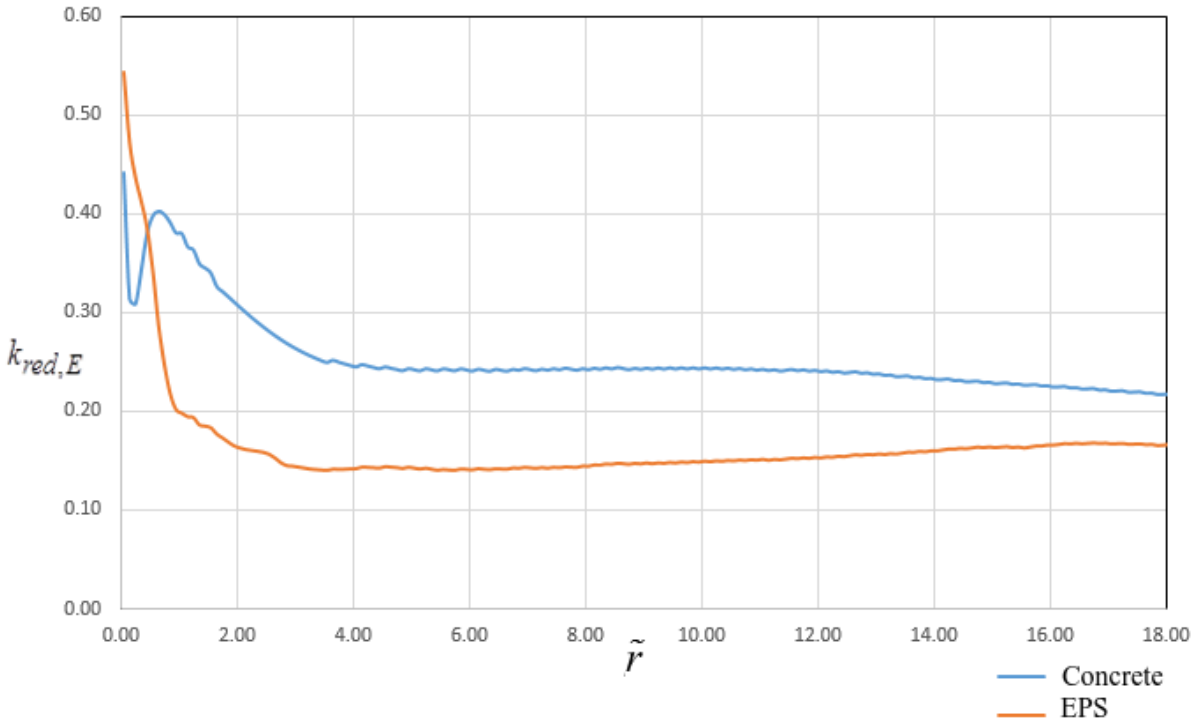

Figure 4.14: Reduction ratio versus dimensionless barrier depth ($\tilde{A} = 0.1$;).

Figure 4.16 demonstrates how the increase in the relative cross-section area of the barrier $\frac{h \times d}{l^2}$ from $\tilde{A} = 0.08$ to $\tilde{A} = 0.3$ significantly reduces the kinetic energy in the protected zone for the both considered barrier types. Then, the reduction ratio decreases less rapidly with the relative cross-section area for rigid materials. Meanwhile, the reduction ratio remains virtually the same at relative cross-section area higher than $\tilde{A} = 0.38$ for soft materials .

Remark 4.3.The main drawback of the plane model is the absence of the so-called shadow zone (figure 4.15). At the same time it can be important for linear barriers (figure 4.15) and zone behind the ring barriers (figure 4.6). Except this effect, the results obtained under plane strain assumption are confirmed by the results obtained using spatial models.

Remark 4.4. In the case of multi-layered media, wavelengths, Rayleigh wave velocity, and mechanical parameters of the soil should be determined for the layer with the highest velocity of longitudinal and transverse waves obtained from geophysical tests. Based on this, barrier parameters ensuring required vibration level are identified. Another way is based on numerical modelling accounting for real stratification of the media and the full frequency range.

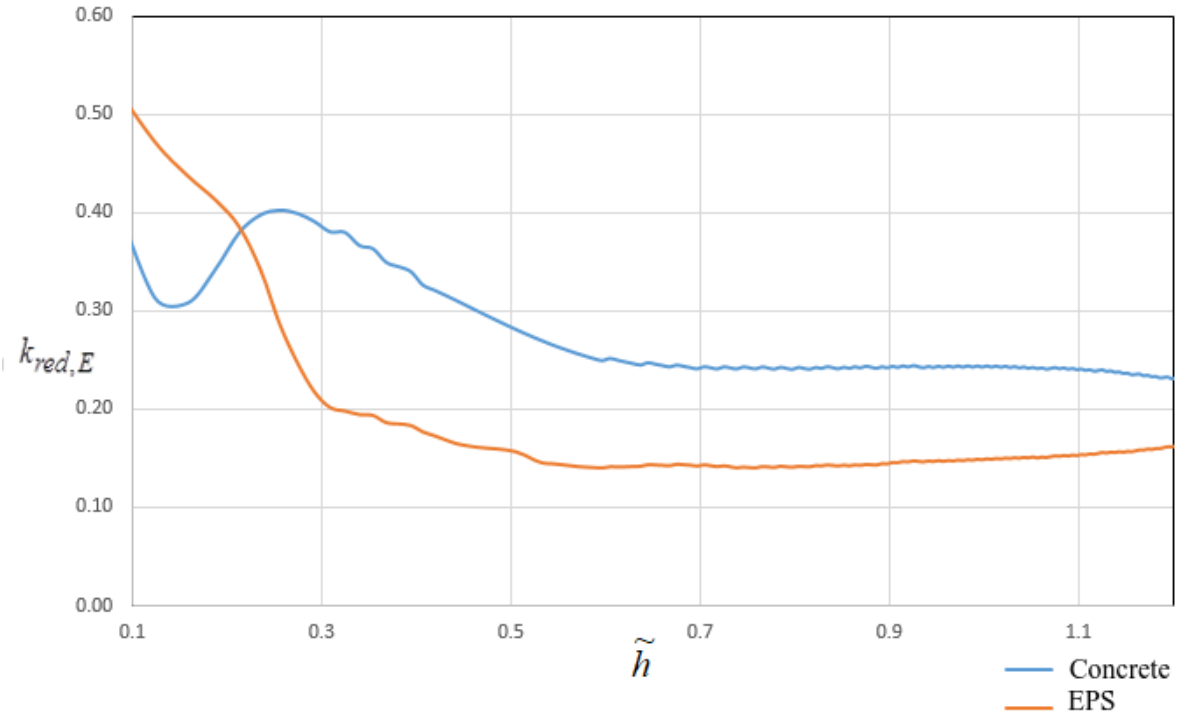

Figure 4.15: Reduction ratio relative barrier depth ($\tilde{A} = 0.1; \omega = 0.324$).

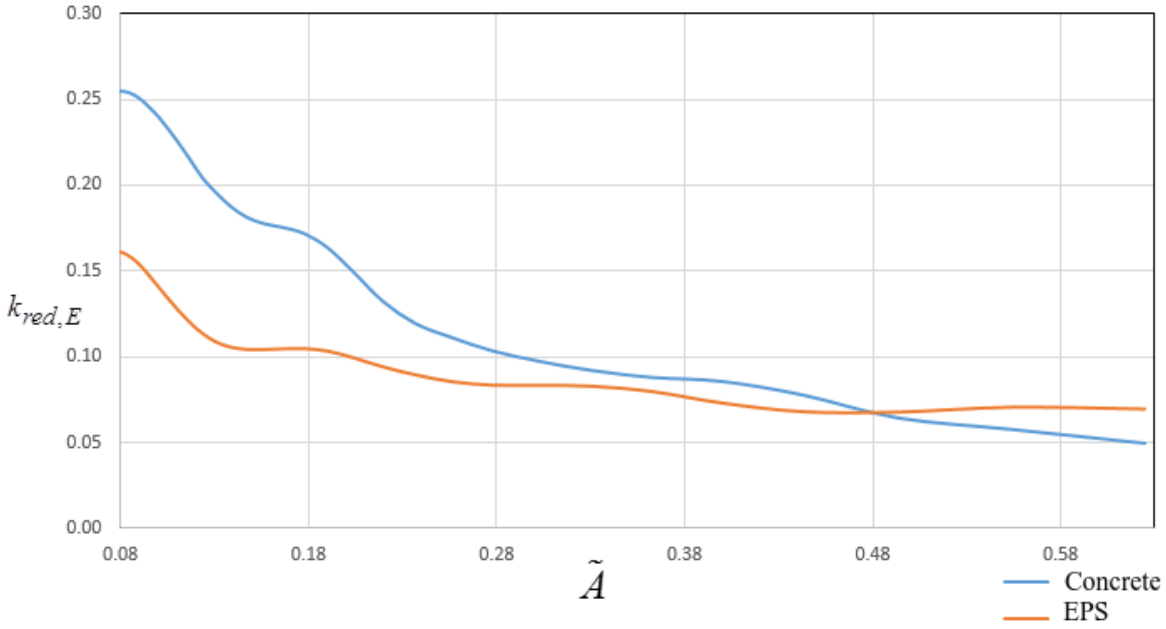

Figure 4.16: Reduction ratio versus dimensionless barrier cross-section area ($\tilde{r} = 6.4; \tilde{\omega} = 0.324$).

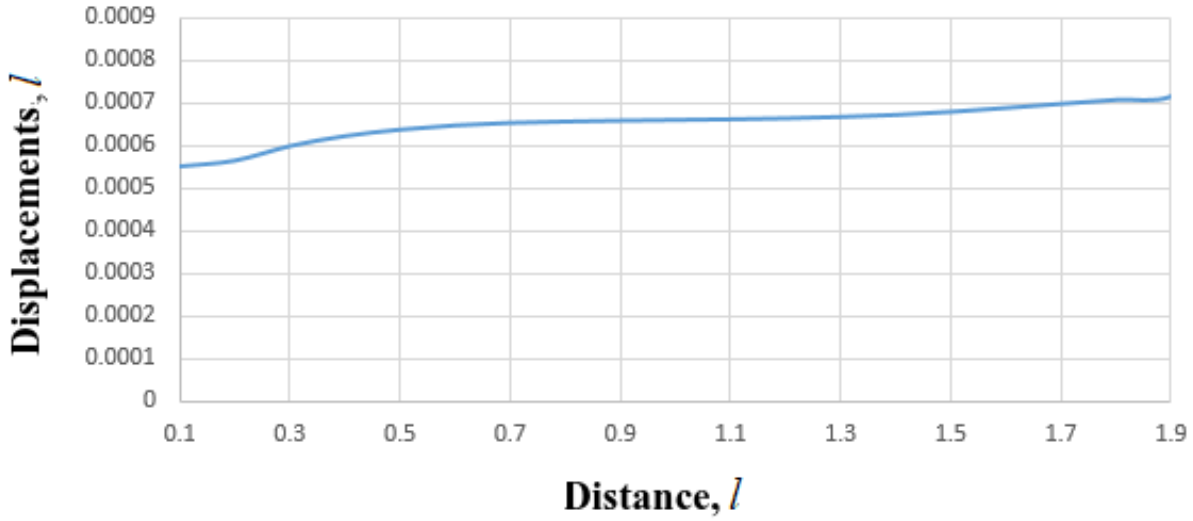

Figure 4.17: The amplitude of displacement at different distances from the barrier ($\tilde{A} = 0.1; \tilde{r} = 6.4$ and $\tilde{\omega} = 0.324$).

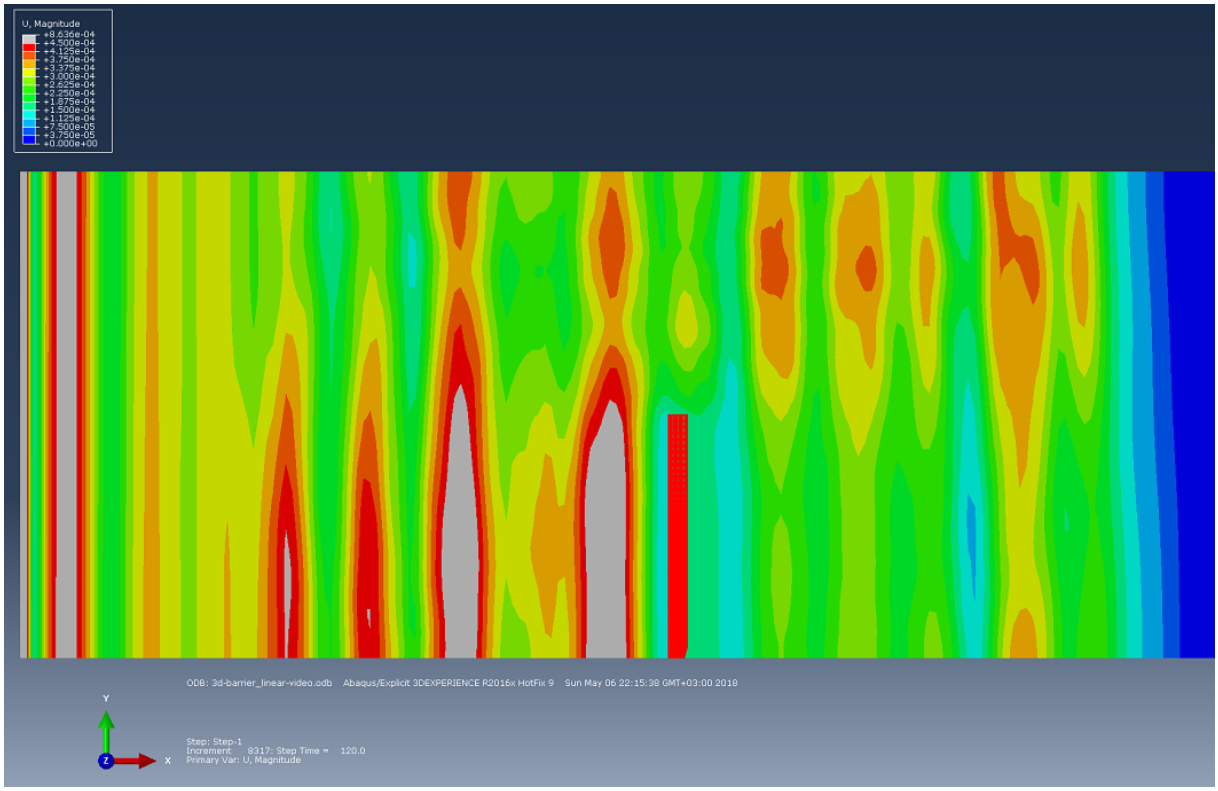

Figure 4.18: Shadow zone behind the linear seismic barrier ($\tilde{A} = 0.1; \tilde{r} = 6.4$ and $\tilde{\omega} = 0.324$).

Optimization of a vertical seismic barrier for prescribed soil conditions and vibration loading.

Problem formulation

Here, a possible method for the optimization of a vertical seismic barrier is considered at a given soil conditions and the size of the protected zone. This problem relates to multi-objective optimization under possible constraints imposed on the target functions:

$$V_{bar}(\tilde{x}), k_{red}(\tilde{x}), \tag{4.11}$$

where $V_{bar}(\tilde{x})$ is the barrier volume, $k_{red}(\tilde{x})$ is the reduction ratio (it is possible to account for k_{redE} and k_{redu} defined in equations 4.7 and 4.8 respectively). Now it is possible to formulate two objective functions that relate to optimization of the volume of the barrier material and reduction ratio. In this case, the volume of both vertical and horizontal seismic barriers can be determined in the following way:

$$V_{bar} = \pi H_{bar} W_{bar}(W_{bar} + 2R), \tag{4.12}$$

where ρ is the material density, H_{bar} and W_{bar} are the barrier depth and width (length for the horizontal barrier) respectively and R is the radius of the protected zone. Because the size of the protected zone remains the same it is possible to eliminate R from the target function. Therefore, to formulate optimization problem [114] two objective functions can be introduced :

$$V_{bar}(\tilde{A}, \tilde{r}), k_{red}(\tilde{E}_{bar}, \tilde{\rho}_{bar}, \tilde{A}, \tilde{r}), \tag{4.13}$$

where V_{bar} is the barrier volume, $\tilde{A}$ and $\tilde{r}$ are determined using (4.10), $\tilde{E}_{bar}$ and $\tilde{\rho}_{bar}$ are the dimensionless barrier Young's modulus and density respectively:

$$\tilde{E}_{bar} = \frac{E_{bar}}{E_{soil}}, \tilde{\rho}_{bar} = \frac{\rho_{bar}}{\rho_{soil}} \tag{4.14}$$

In contrast to single objective optimization problems no single solution may exist for the multi objective ones. Therefore, various optimality criteria are considered. One of the most used is Pareto's optimality (efficiency) condition [114, 20] which states that the solution $x_0 \in \mathbf{X}$ ($\mathbf{X}$ is the considered parameter space) is Pareto's effective(optimal) for the set of target functions $\mathbf{F}(\mathbf{x}) = (F_1(\mathbf{x}), F_2(\mathbf{x}), ..., F_n(\mathbf{x}))$ if there is no x for at least one function so that $F(x) \leq F(x_0)$ and $F_i(x) < F_i(x_0)$.

One of the methods to solve Pareto's optimality problem is the constraint method [20]. In that case the initial problem (4.11) is divided into two:

Problem I: Finding optimal solution is to deliver conditional minimum to the function of reduction ratio under the restriction on the barrier volume (in that case the cross-section area):

$$\min_{\tilde{E}_{bar}, \tilde{\rho}_{bar}, \tilde{A}, \tilde{r}} \left(k_{red}(\tilde{E}_{bar}, \tilde{\rho}_{bar}, \tilde{A}, \tilde{r}) \right) \text{ subject to } \quad V_{bar}(\tilde{A}, \tilde{r}) \leq V_0 \tag{4.15}$$

In that case, using the Karush-Kuhn-Tucker conditions [114], [20] yields the condition of optimal solution:

$$\begin{gathered} \nabla \left(k_{red}(\tilde{E}_{bar}, \tilde{\rho}_{bar}, \tilde{A}, \tilde{r}) \right) + \alpha_1 \left(V_{bar}(\tilde{A}, \tilde{r}) \right) = 0 \\ \alpha_1 \left(V_{bar}(\tilde{A}, \tilde{r}) - V_0 \right) = 0, \alpha_1 \geq 0, \end{gathered} \tag{4.16}$$

where α_1 is Lagrangian multiplier. This formulation can be used when the main factor of optimization is the appropriate volume of the barrier.

Problem II: Finding optimal solution is to deliver conditional minimum to the function of the barrier volume under the restriction on the barrier reduction ratio:

$$\min_{\tilde{A},\tilde{r}} \left(V_{bar}(\tilde{A},\tilde{r}) \right) \text{ subject to } \quad k_{red}((\tilde{E}_{bar},\tilde{\rho}_{bar},\tilde{A},\tilde{r})) \leq k_0 \tag{4.17}$$

Similarly to the Problem I (4.16), the condition of optimal solution has the following form:

$$\begin{aligned} \nabla \left(V_{bar}(\tilde{\nu},\tilde{r}) \right) + \alpha_2 \left(k_{red}(\tilde{E}_{bar},\tilde{\rho}_{bar},\tilde{\nu},\tilde{r}) \right) = 0 \\ \alpha_2 \left(V_{bar}(\tilde{A},\tilde{r}) - V_0 \right) = 0, \quad \alpha_2 \geq 0, \end{aligned} \tag{4.18}$$

where α_2 is Lagrangian multiplier. This formulation can be used when the main factor of optimization is the vibration reduction level, therefore it is fixed. These two problems will permit to choose and analyse the optimal configuration of the barrier. It is worth noting that these restrictions on the vibration level and barrier volume are usually imposed on the barrier in practical design to ensure appropriate vibration level or the final cost of the protection.

In order to ensure the minimum corresponding to the initial problem (4.11) it is necessary to add the following verification condition of the positive definiteness of the quadratic form :

$$\forall_{\vec{a}\in R^n, \vec{a}\neq 0} \vec{a} \quad \vec{a} \cdot H \cdot \vec{a} > 0 \tag{4.19}$$

where H - Hessian matrix of the function $C(a_1...a_n) + \alpha D(a_1...a_n)$, the functions $C(a_1...a_n)$ and $D(a_1...a_n)$ are the objective functions depending upon the variables $a_1...a_n$ [114],[20].

$$H \equiv \nabla\nabla \left(C(a_1...a_n) + \alpha D(a_1...a_n) \right) \tag{4.20}$$

The solution of these optimization problems reveals that both of them have no global minimums if the restrictions are not used. On the contrary, the minimum can be obtained if the restrictions are adopted.

It is clear that the barrier volume does not depend on the mechanical characteristics of its material. Additionally, according to the results obtained in section 4.2 optimal material parameters lay on the borders of the considered range for the relative density and Young's modulus. Therefore, equations (4.16), (4.18) are simplified to the form:

$$\min_{\tilde{E}_{bar},\tilde{\rho}_{bar},\tilde{A},\tilde{r}} \left(k_{red}(\tilde{A},\tilde{r}) \right) @V_{bar}(\tilde{A},\tilde{r}) \leq V_0 \tag{4.21}$$

$$\min_{\tilde{A},\tilde{r}} \left(V_{bar}(\tilde{A},\tilde{r}) \right) @k_{red}((\tilde{A},\tilde{r})) \leq k_0 \tag{4.22}$$

with Hessian matrix defined as:

$$H = \nabla_x \nabla_x (L_{1,2}(\tilde{A},\tilde{r}), \tag{4.23}$$

where $\mathbf{x} = \tilde{A},\tilde{r}$ is the argument vector; $L_1 = k_{red}(\tilde{A},\tilde{r}) + \alpha_1 V_{bar}((\tilde{A},\tilde{r}))$ and $L_2 = V_{bar}((\tilde{A},\tilde{r})) + \alpha_2 k_{red}(\tilde{A},\tilde{r})$ the functions corresponding to the first (4.21) and the second (4.22) problems respectively.

Finite difference form

In order to solve the optimization problems (4.16), (4.18), it is necessary to write equations for (4.21), (4.22) and (4.23) in finite difference form. In that case, equations (4.16) accounting for equation (4.21) can be written as:

$$\begin{cases} \frac{k_{red}(\tilde{A}+\triangle\tilde{A},\tilde{r})-k_{red}(\tilde{A},\tilde{r})+\alpha_2(V_{bar}(\tilde{A}+\triangle\tilde{A},\tilde{r})-V_{bar}(\tilde{A},\tilde{r}))}{\triangle\tilde{A}} = 0 \\ \frac{k_{red}(\tilde{A},\tilde{r}+\triangle\tilde{r})-k_{red}(\tilde{A},\tilde{r})+\alpha_1(V_{bar}(\tilde{A},\tilde{r}+\triangle\tilde{r})-V_{bar}(\tilde{A},\tilde{r}))}{\triangle\tilde{r}} = 0, \end{cases} \tag{4.24}$$

with the components of Hessian matrix of the function L_1 defined as:

$$\begin{aligned} h_{11} &= \frac{k_{red}(\tilde{A}+2\Delta\tilde{A},\tilde{r})+k_{red}(\tilde{A},\tilde{r})+\alpha_1(V_{bar}(\tilde{A}+2\Delta\tilde{A},\tilde{r})+V_{bar}(\tilde{A},\tilde{r}))}{\Delta\tilde{A}^2} \\ h_{22} &= \frac{k_{red}(\tilde{A},\tilde{r}+2\Delta\tilde{r})+k_{red}(\tilde{A},\tilde{r})+\alpha_1(V_{bar}(\tilde{A},\tilde{r}+2\Delta\tilde{r})+V_{bar}(\tilde{A},\tilde{r}))}{\Delta\tilde{r}^2} \\ h_{12} = h_{21} &= \frac{1}{\Delta\tilde{r}\Delta\tilde{A}}(k_{red}(\tilde{A}+\Delta\tilde{A},\tilde{r}+\Delta\tilde{r})-k_{red}(\tilde{A},\tilde{r}+\Delta\tilde{r})+ \\ &\alpha_1(V_{bar}(\tilde{A}+\Delta\tilde{A},\tilde{r}+\Delta\tilde{r})-V_{bar}(\tilde{A},\tilde{r}+\Delta\tilde{r})-k_{red}(\tilde{A}+\Delta\tilde{A},\tilde{r})+ \\ &k_{red}(\tilde{A},\tilde{r})-\alpha_1(V_{bar}(\tilde{A}+\Delta\tilde{A},\tilde{r})-V_{bar}(\tilde{A},\tilde{r}))). \end{aligned} \tag{4.25}$$

In that case the condition of the positive definiteness of the form (4.20) can be written as:

$$\begin{aligned} h_{11} &> 0 \\ h_{11} * h_{22} - h_{12} * h_{21} &> 0 \end{aligned} \tag{4.26}$$

In the case of the second optimization problem, equation (4.26) remains the same, while equations (4.24) and (4.25) are written as:

$$\begin{cases} \frac{V_{bar}(\tilde{A}+\triangle\tilde{A},\tilde{r})-V_{bar}(\tilde{A},\tilde{r}))+\alpha_2(k_{red}(\tilde{A}+\triangle\tilde{A},\tilde{r})-k_{red}(\tilde{A},\tilde{r}))}{\triangle\tilde{A}} = 0 \\ \frac{V_{bar}(\tilde{A},\tilde{r}+\triangle\tilde{r})-V_{bar}(\tilde{A},\tilde{r})+\alpha_2(k_{red}(\tilde{A},\tilde{r}+\triangle\tilde{r})-k_{red}(\tilde{A},\tilde{r}))}{\triangle\tilde{r}} = 0 \end{cases} \tag{4.27}$$

$$\begin{aligned} h_{11} &= \frac{V_{bar}(\tilde{A}+2\Delta\tilde{A},\tilde{r})+V_{bar}(\tilde{A},\tilde{r})+\alpha_2(k_{red}(\tilde{A}+2\Delta\tilde{A},\tilde{r})+k_{red}(\tilde{A},\tilde{r}))}{\Delta\tilde{A}^2} \\ h_{22} &= \frac{V_{bar}(\tilde{A},\tilde{r}+2\Delta\tilde{r})+V_{bar}(\tilde{A},\tilde{r})+\alpha_2(k_{red}(\tilde{A},\tilde{r}+2\Delta\tilde{r})+k_{red}(\tilde{A},\tilde{r}))}{\Delta\tilde{r}^2} \\ h_{12} = h_{21} &= \frac{1}{\Delta\tilde{r}\Delta\tilde{A}}(V_{bar}(\tilde{A}+\Delta\tilde{A},\tilde{r}+\Delta\tilde{r})-V_{bar}(\tilde{A},\tilde{r}+\Delta\tilde{r})+ \\ &\alpha_2(k_{red}(\tilde{A}+\Delta\tilde{A},\tilde{r}+\Delta\tilde{r})-k_{red}(\tilde{A},\tilde{r}+\Delta\tilde{r})-V_{bar}(\tilde{A}+\Delta\tilde{A},\tilde{r})+ \\ &V_{bar}(\tilde{A},\tilde{r})-\alpha_2(k_{red}(\tilde{A}+\Delta\tilde{A},\tilde{r})-k_{red}(\tilde{A},\tilde{r}))). \end{aligned} \tag{4.28}$$

Equations (4.24 -4.26) and (4.26-4.28) form the closed system sufficient to solve optimization problems (4.21 and 4.22) respectively.

Solution of the optimization problem for a particular soil conditions

Assuming that the soil corresponds to the deposits of loose-to-medium cohesionless soils the following mechanical parameters (the second case in table 4.1) are used:

$$\rho_{soil} = 1885kg/m^3 \quad E_{soil} \approx 60MPa \quad \nu_{soil} = 0.35 \tag{4.29}$$

and the minimum design vibration frequency equals to $f = 2Hz$. The solution of the optimization problem for rigid and soft barriers with the characteristics defined in table 4.2. The results of solution are shown in the table below:

.

Material	$\tilde{A}$	$\tilde{r}$	h, m	d, m
EPS	0.596	3.58	29.810	6.450
Reinforced concrete	0.596	18.05	67.175	2.870

Table 4.3: Optimization results.

Conclusion

According to the obtained results , the following conclusions can be drawn:

1. Vertical seismic barrier can be used as a measure to decrease the vibrations transferred by surface Rayleigh waves reducing kinetic energy and displacements in the protected zone up to $5-6$ times and $2-2.5$ times respectively. At the same time, these results are valid for low level of shear strains in the soil induced in the process of wave propagation as the elastic formulation is appropriate for this case.

2. The maximum vibration reduction in the protected zone at fixed geometrical parameters is achieved by providing the maximum difference in the mechanical characteristics of the barrier material and those of the soil. It can be seen from the obtained dependencies of the reduction ratio.It monotonically decreases with an increase in the relative density and Young's modulus of the barrier material from 1 to $+\infty$ as well as a decreases with the relative density and Young's modulus decline from 1 to 0. Therefore, the dependency of the reduction ratio on the relative Young's modulus and density can be called a uni modal with the minimum on the borders of the considered range for $\tilde{E}, \tilde{\rho}$.

3. Based on the foregoing, it can be concluded that the optimization of vertical seismic barriers for the prescribed soil condition and vibration loading can be performed by separating the barrier parameters into geometric and material ones. In the case of material parameters, it is sufficient to ensure the maximum difference in the density and Young's modulus of the barrier material from those of the soil. It guarantees the minimum for the optimization part related to the material and, then, to search for the optimal barrier geometry.

4. If "exotic" construction materials (metamaterials, materials with high density and low stiffness, etc.) as well as expensive structural materials (steel, lead, etc.) are not considered, a barrier can be made of light and non-rigid materials (extruded polystyrene foam) as well as heavy and rigid materials (reinforced concrete).

5. In the case of light and non-stiff barrier, the cross-section area affects the reduction ratio k_{red} in the protected area up to the value of $\tilde{A} = 0.3$, then at $\tilde{A} \in [0.3, 0.48]$ the effect of the cross-sectional area decreases and at $\tilde{A} > 0.48$ it becomes insignificant. The optimal dimensionless barrier height is $\tilde{r} \approx 3.55$.

6. For a rigid heavy barrier (reinforced heavy concrete), two configurations are possible: horizontal ($\tilde{r} \approx 0.25$) and vertical ($\tilde{r} \approx 4.5$). The vertical wave barrier demonstrates higher effectiveness in terms of vibration reduction. At the same time, further increase in the depth leads to a slight decrease in reduction ratio. Hence,the reduction effect of a heavy and rigid barrier increases with the cross-section area non linearly and exceeds the efficiency of a soft and light barrier.

7. The proposed technique for the optimization of vertical seismic barriers accounting for specific soil conditions and design vibration loading allows to find optimal barrier configuration under required restrictions upon the barrier volume or vibration level.

8. The proposed optimization method is valid for the vibration sources generating low amplitude vibrations with shear strains in the soil not exceeding 10^{-4}. As for high intensity vibrations such as earthquakes and explosions additional computations accounting for non linear soil deformation character are necessary.

CHAPTER 5

THE INTERACTIONS OF PILES AND PILE FIELDS WITH SURFACE RAYLEIGH WAVES

Contents

Numerical simulation and analysis of surface Rayleigh wave interaction with piles and pile fields using Finite Element Method is presented in this chapter to show the attenuation effect of this wave barrier along with the possibility to implement pile rows as a method of vibration protection of buildings and underground structures from the surface waves of Rayleigh type. Spatial FE models are used to analyse the influence of pile field parameters such as pile length, diameter, spacing number of rows on the vibration reduction effect of the field with respect to the wavelength, that depends on the frequency characteristics of the vibration loading and soil conditions. Apart from that, it is shown how additional pile rows can decrease internal forces in the piles inside the protected zone which can be important for deep foundations. It is worth noting that the remarks 4.1 and 4.2 from chapter 4 take place in this chapter either.

Simulation methods and FE models

Finite element models.

Mathematical formulation including constitutive equations as well as boundary and initial conditions for the considered problem is is defined by system equations including equations (3.25), (3.15),(3.18) and (3.20) shown in chapter 3. The analysis is performed in time domain for surface Rayleigh waves, generated by fully harmonic surface line loading defined by equation 4.1.

Numerical solution for the problem of surface Rayleigh waves interaction with piles and pile fields is performed using an explicit finite-difference procedure for integration in time domain and spatial discretization using finite element method (FEM) in Abaqus 2016 software [1].

Similarly to the problem considered in chapter 4 explicit finite-difference procedure used in the analysis is based on the second order explicit central difference integration scheme involving the Lax-Wendroff method [75], [1]. Time increment size is selected automatically by the program satisfying the Courant–Friedrichs–Lewy (CFL) condition 4.2 [35].

The standard finite element library of Abaqus/Explicit software package is used in the calculations [1]. The region is meshed with finite elements of the C3D8R type which are eight-node hexahedral elements with a linear shape function reduced by the integration scheme with control of deformations and the energy equal to zero at the integration point. In contrast to the models used for the analysis in chapter 4 (figures 4.1 and 4.4), mesh quality is lower with maximum length ratio in the range $k_l \in [0.95, 1]$. Numerical error given by the element size is analysed given in section 5.1.3.

In the subsequent analysis two types of 3d models are used (figures 5.1 and 5.2. The first model represents a piece of a pile field with several rows with three planes of symmetry used to decrease model size (figure 5.1). The first plane of symmetry passes through the wave source perpendicularly to the direction of Rayleigh wave propagation and parallel to the pile row. It is assumed that there are several piles in a row located along the same straight line at the same distance from each other(the length of the row can be compared with the dimensions of the wave front or larger than it, so the effect of the row length can be neglected).This allows to introduce two additional planes of symmetry passing through the pile axis and middle of the interval between the piles parallel to the direction of propagation of surface waves substantially reducing the number of elements. On the free surface at the top of the symmetry plane fully harmonic line loading defined by equation 4.1 is applied. Meanwhile, the remaining part of the top surface is free. On the bottom and right planes of the model non reflecting boundaries for P waves defined by equation 4.3 are used. These boundary conditions are discussed in more detailed in chapter 4. This model is used to analyse the influence of pile diameter, spacing and length on the reduction ratio of a pile field and bending moments in piles as well as to determine the optimal values of these parameters for the following analysis involving the model of a more realistic pile field (figure 5.1). At the second stage, a full scale spatial model of the homogeneous pile field is adopted to simulate a real finite size pile field which may surround a construction or be the foundation of a structure (figure 5.2). For this model the main parameters are set based on the results obtained from the analysis using the first model (figure 5.1). Basically, the full scale 3d model is used to confirm the main results and trends identified in the first calculation stage.

Similarly to the first model the second one figure 5.2 is a three-dimensional with the condition of symmetry applied on the left plane perpendicularly to the direction of Rayleigh wave propagation to reduce the model size. On the free surface at the top surface of the symmetry plane, fully harmonic line loading defined by equation 4.1 is applied. The second plane of symmetry passes through the middle of the pile field parallel to the direction of surface Rayleigh wave propagation, which is not shown in figure 5.2. On the other surfaces non reflecting boundaries for P waves defined by equation 4.3 are applied.

The models presented in figures 5.1 and 5.2 allow to analyse the influence of pile field planar shape (square (figure 5.2) and circular pile field planar shapes can considered, however, as the results are virtually the same, the results for square field are presented in this work) and pile field planar configuration (quadratic or triangular cells (figure 5.3)) on the vibration reduction effect along with the interaction with surface waves. Vertical and horizontal sizes of the first model (figures 5.1) equals to $9l$ and $18l$ respectively (l is the wavelength of Rayleigh wave), while the width of the model varied according to the pile distance. The sizes of the second model (figure 5.2) along the X, Y and Z axis equals to $9l$, $6l$ and $5l$. The size of the protected zone Δ is l,

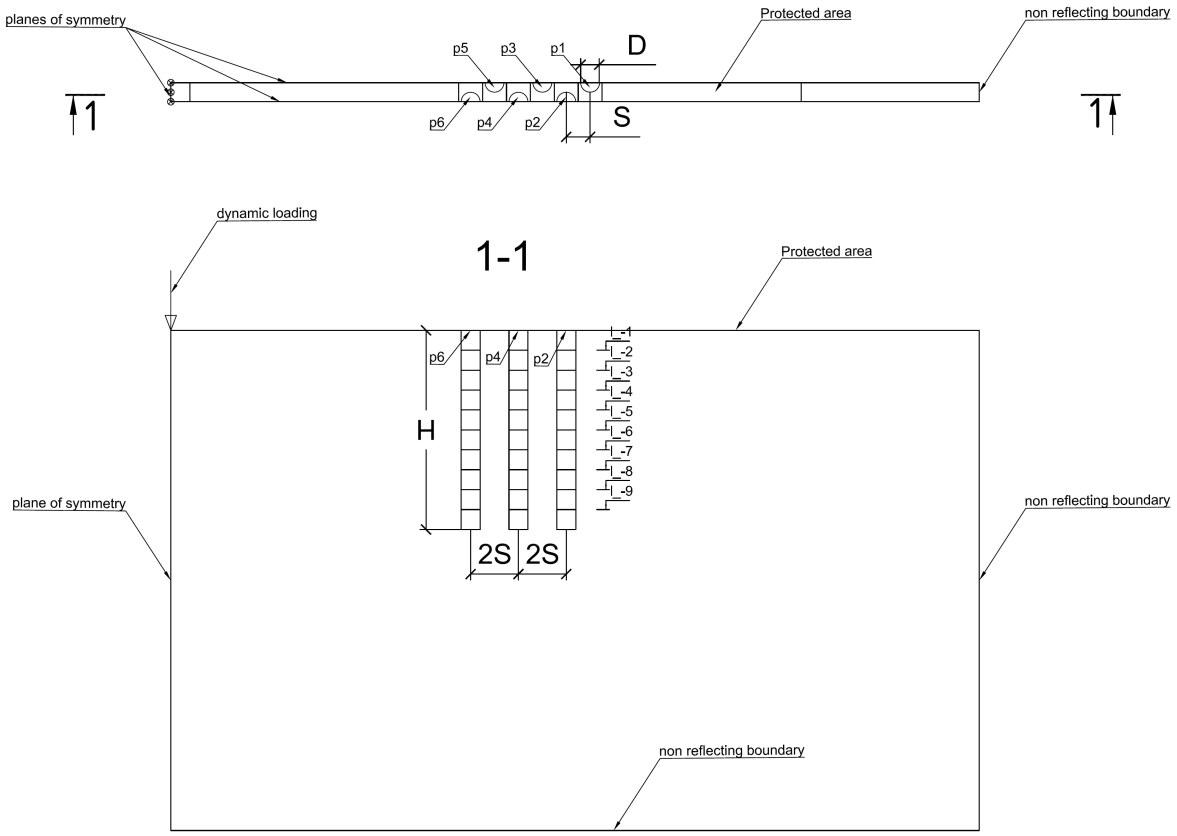

Figure 5.1: The scheme of simplified spatial model of pile field.

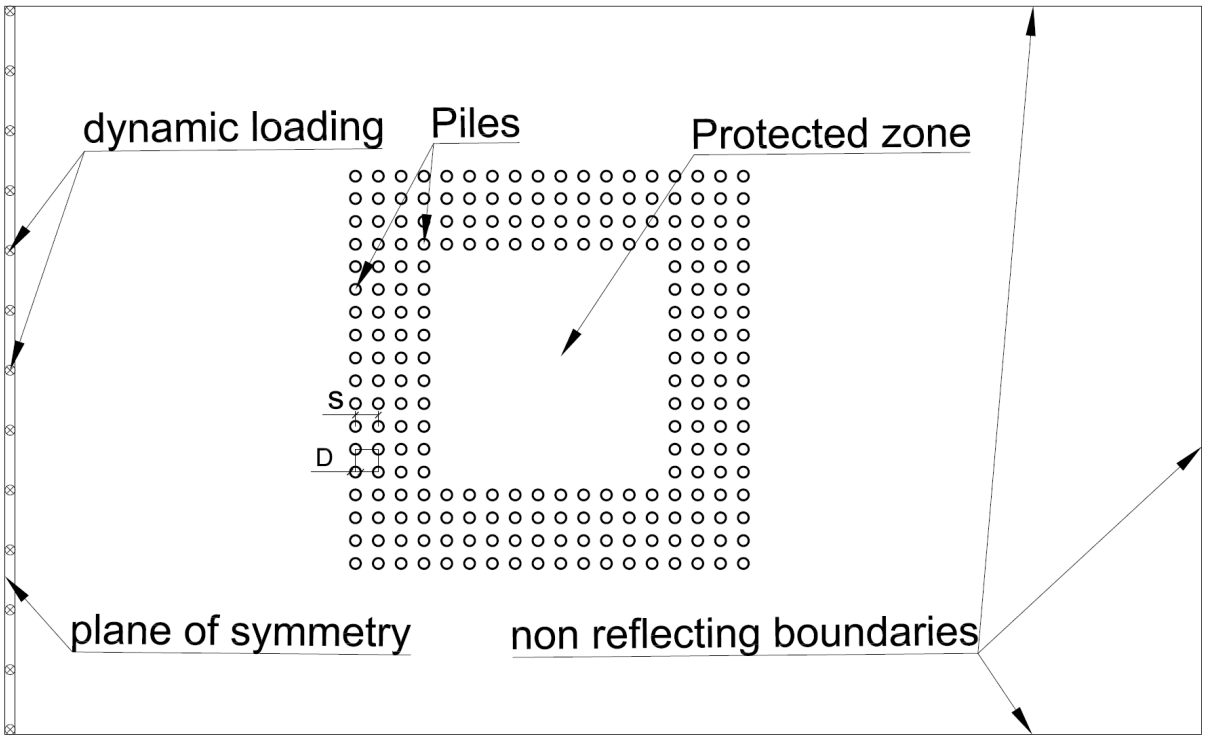

Figure 5.2: The scheme of spatial model for real full scale pile field.

while the observation zone size equals to $2l$

A pile rows are created at a distance from the symmetry plane (left plane) so that the interaction of the waves and the piles would occur remote enough from the source with account of symmetry condition. Similarly to the previous problem discussed in chapter 4, the dimensions of the models are chosen in a way that the waves reflected from the boundaries of the model could not return to the points of observation during the calculation time. In addition to that, two main assumptions are also made: (1) the size of the protected zone does not change; (2) the same soil conditions are used for all the calculations.

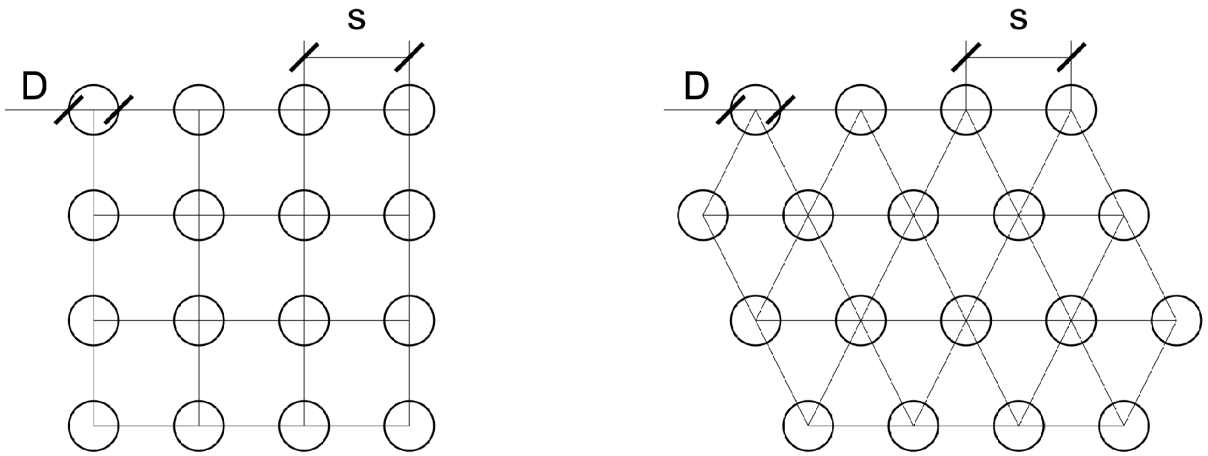

Figure 5.3: The types of pile field configuration: square cells (on the left) and triangular cells (on the right).

It is worth noting that a pile field can act as a barrier if the wavelength is comparable or less than the pile length and the dimensions of the pile field in plane. For low frequency range corresponding to earthquakes $f = 2 \div 10Hz$ the wavelength of Rayleigh wave varies from 100 m to 10 m in soft soils, while in rigid soils it can exceed 200 m. At the same time, pile depth which is more than 50 m is difficult to implement in practice. Therefore, the lowest frequency $2Hz$ is chosen as it generates Rayleigh waves with large enough wavelength corresponding to the real vibration sources both natural and anthropogenic nature. While, construction of a pile field providing reasonable vibration reduction effect is not possible even in soft soils for lower frequencies as it will require large pile lengths. At the same time, higher frequencies correspond to shorter wavelengths and require smaller protective pile barriers. The results in the present chapter are presented in relation to the maximum Rayleigh wavelength l equalling to $50m$ and corresponding to minimum vibration frequency $f = 2Hz$.

Young's modulus and density for soft soils are chosen according to the seismic shear wave speeds that are given in Eurocode 8 [138].The attenuation effect of the field is analysed using the value of the kinetic energy reduction ratio $k_{red,E}$ defined by equation 3.13 for the elements beyond the pile field at the surface layer of the protected zone Δ placed behind the pile rows and an underground layer which is placed directly beneath the protected zone Δ at the depth $l/10$. The reduction of bending moments in piles are estimated through the comparison of normalized bending moments in the piles when they are installed in a row and after installation of addtional rows of piles. The bending moments are normilized in relation to the maximum value of bending moment in the pile of the single row pile barrier.

According to the results obtained by Kattis et al. in [67], it is possible to replace a pile row with an effective trench, thus basic qualitative results obtained in chapter 4 regarding the influence of the depth, width and mechanical material parameters can be extrapolated to pile rows. Which means, the higher the difference in the mechanical parameters of the piles and the

soil the better vibration reduction effect can be observed. However, the range of materials for a pile field is quite narrow. Therefore, further analysis is limited by piles made of reinforcement concrete, which are more widely used. Mechanical parameters of concrete and a possible soft soil are shown in table 5.1 in agreement with [138].

Material	Density ρ, kg/m^3	Poisson's ratio ν	Young's modulus, MPa
Soil	1800	0.25	55
Concrete	2450	0.23	30000

Table 5.1: Dynamic parameters of materials.

Dimensional analysis.

Similarly to chapter 3 kinetic energy field of an area beyond the pile field can be described by the following group of dimensionless parameters:

$$K_{pile} = f\left(\frac{E_{pile}}{E_{soil}}; \frac{\rho_{pile}}{\rho_{pile}}; \frac{D}{l}; \frac{H}{l}; \frac{S}{l}; \nu_{pile}; \nu_{soil}\right), \tag{5.1}$$

where the index *soil* indicates the soil material of the half-space, while the index *pile* corresponds to the parameters of the pile field; l is the wavelength of the Rayleigh wave in a half-space (this wavelength can be solved from the Bergmann-Viktorov's equation); E_{pile}, E_{soil} correspond respectively to Young's modulus of the piles and of the soil ; ν_{pile}, ν_{soil} are Poisson's ratios; ρ_{pile}, ρ_{soil} are the densities; D , H and S are the diameter,length and spacing of the field accordingly. A pile field interacts with seismic waves as a uniform composite barrier, thus it is convenient to introduce the value of pile fraction - $\alpha = \frac{\pi \cdot D^2}{4 \cdot S^2}$ showing the density of the pile field. Afterwards, all the geometric values are normalized in relation to the wavelength of Rayleigh's wave.

As it was mentioned before, the main attention is paid to the geometrical parameters of a pile field and their influence on the vibration attenuation. Thus the functions of reduction ratio for the surface and underground layers are analysed:

$$k_{red} = \frac{K_{pile}}{K_{init}}. \tag{5.2}$$

where K_{pile} and K_{init} are the kinetic energies before and after pile field installation.

Model verification and element size influence.

Similarly to chapter 4 the analysis of element size is presented to show number of elements used in the computations for discretazing key parameters of the wavelength, pile and model supplemented by the comparison with the results of S.E. Kattis et al., [67] obtained using boundary element method (BEM).

Figure 5.4 shows how the kinetic energy of the surface and underground layers change with variation of the element size. Figure 5.5 demonstrates the effect of mesh size variation on the displacement amplitudes of the point beyond the field. The graphs in figures 5.4 and 5.5 are plotted at $\nu_{pile} = 0.2, \nu_{soil} = 0.25, \quad \tilde{\omega} = 0.324, \quad \alpha = 0.1632, \quad \tilde{D} = 0.06, \quad \tilde{H} = 1.0$. Kinetic energy in the plot is normalized in relation to the kinetic energy of the underground layer at the element size equalling to 0.05 and the displacement values are normalized in relation to the maximum magnitude of displacements which is obtained for the element size 0.05.

The obtained results reveal that the element size affects the solution up to the value of $0.01l$ at the considered size of the model (maximum linear size is $18l$, where l is the wavelength).Further

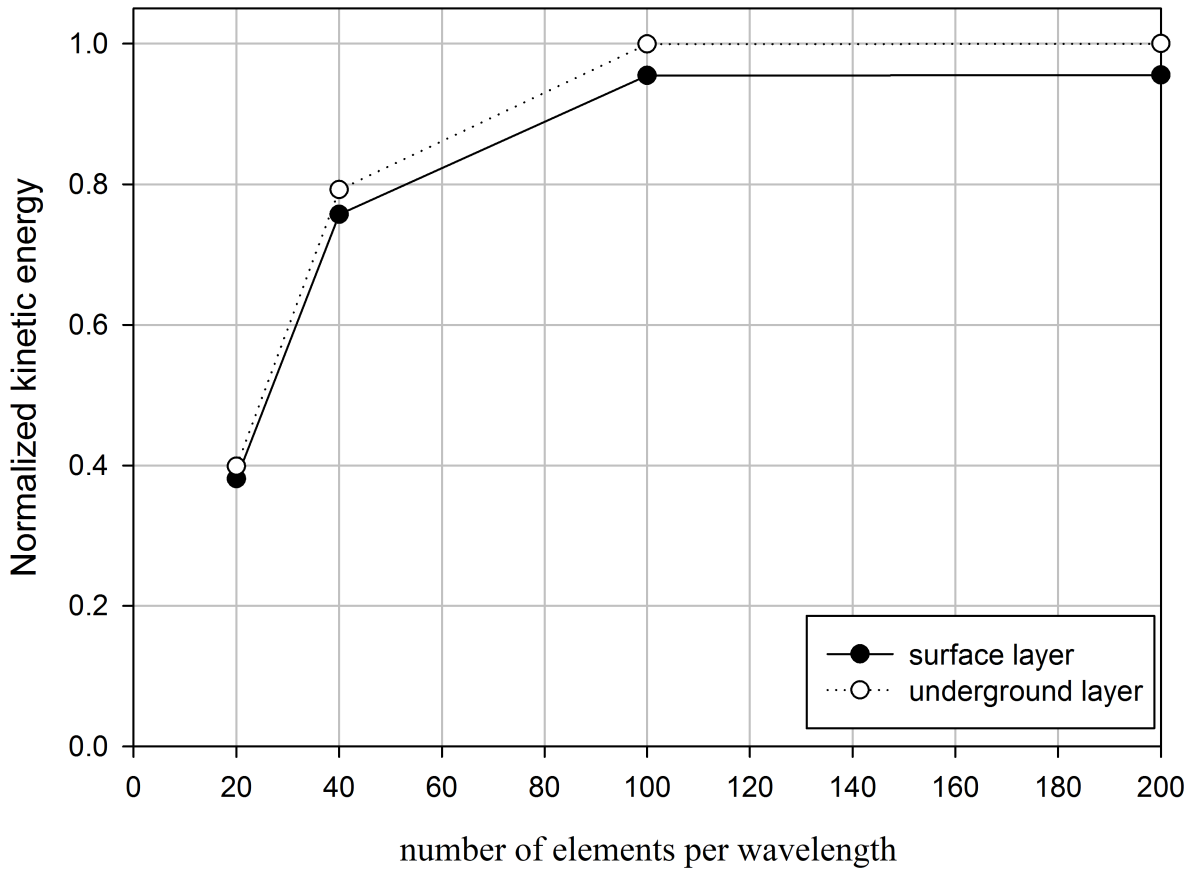

Figure 5.4: The variation of the kinetic energy with the size of the mesh.

decrease in the mesh size does not change the results significantly and the values of energy as well as displacements maintain the same level with further decrease of the mesh size, while the computation time goes up. At the same time, a decrease in the element size gives additional parasite fluctuations caused by the time integration scheme. Such fluctuations can be observed even with a mesh size of $0.01l$, meanwhile the level of displacements remains the same. Therefore, in further calculations the element size of $0.005l$ is used for both the 3D models (figures 5.1 and 5.2). This satisfies Kramer's suggestion [72] as it is less than $0.1 * l$, where l - is the wavelength. In order to avoid the effect of non-physical fluctuations, Butterworth's filter of the second order is used to clear the final graphs. This method is appropriate because the excitation loading is harmonic and it is easy to choose the filtering frequency.

To compare the results obtained in this work and the ones of Kattis et al., [67] the model shown in figure 5.6 is created. The material parameters used for the computations are chosen as follows: frequency $f = 50Hz$, shear modulus of the soil $G_{soil} = 132MPa$, Poisson's ratio $\nu_{soil} = \nu_{pile}$, radius of the protected zone for the estimation of the vibration reduction $R = 7.5m$, pile diameter $D = 1m$, pile length $H = 5m$ and pile distance $S = 0.5m$. The obtained average amplitude reduction factor equals to $\overline{AR} = 0.719$ while Kattis et al. obtained $\overline{AR} = 0.712$. The difference in the average amplitude reduction factors is less than 1.0% which shows that the presented results and the results of Kattis et al. are in a good agreement. In the following sections it will be shown that the increase in the pile fraction and diameter results in the decline of the reduction ratio which means that isolation effectiveness of pile barrier approaches to that of an underground concrete walls one [28].

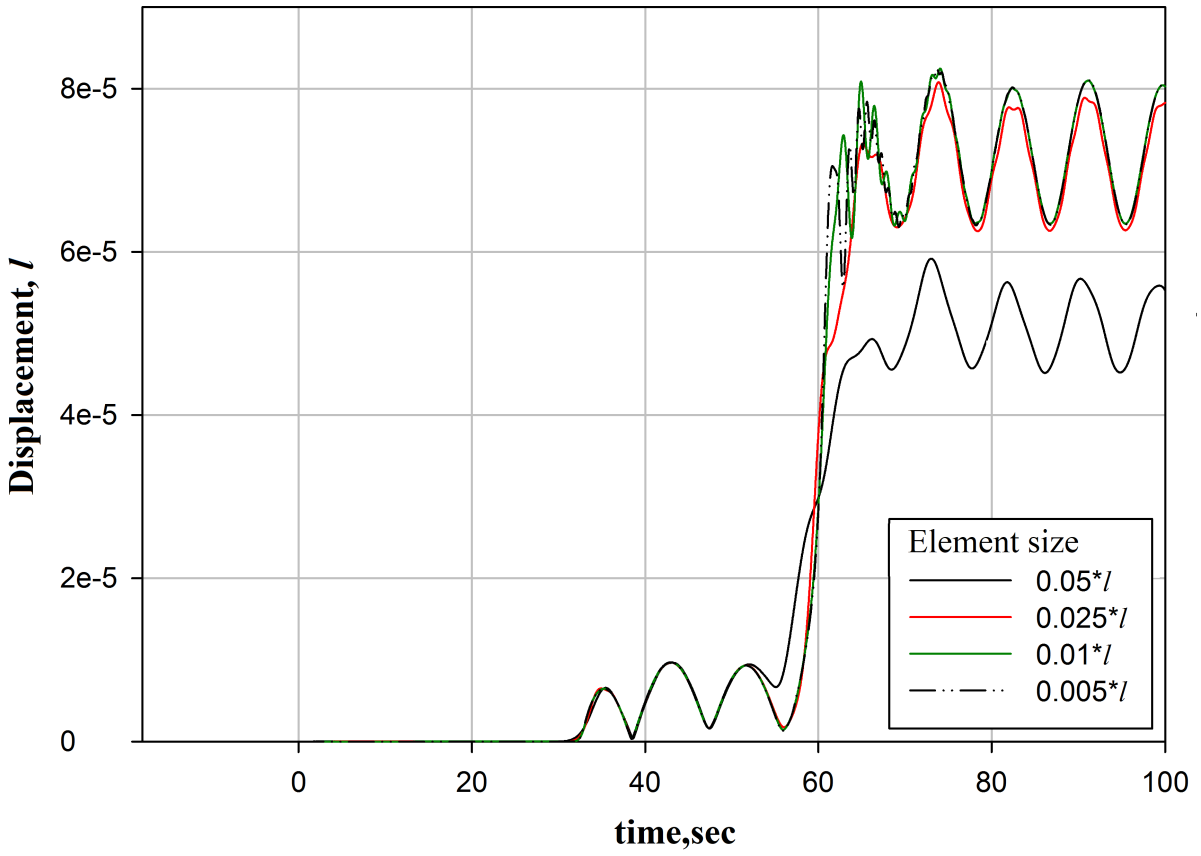

Figure 5.5: The variation of the displacement amplitudes with the size of the mesh.

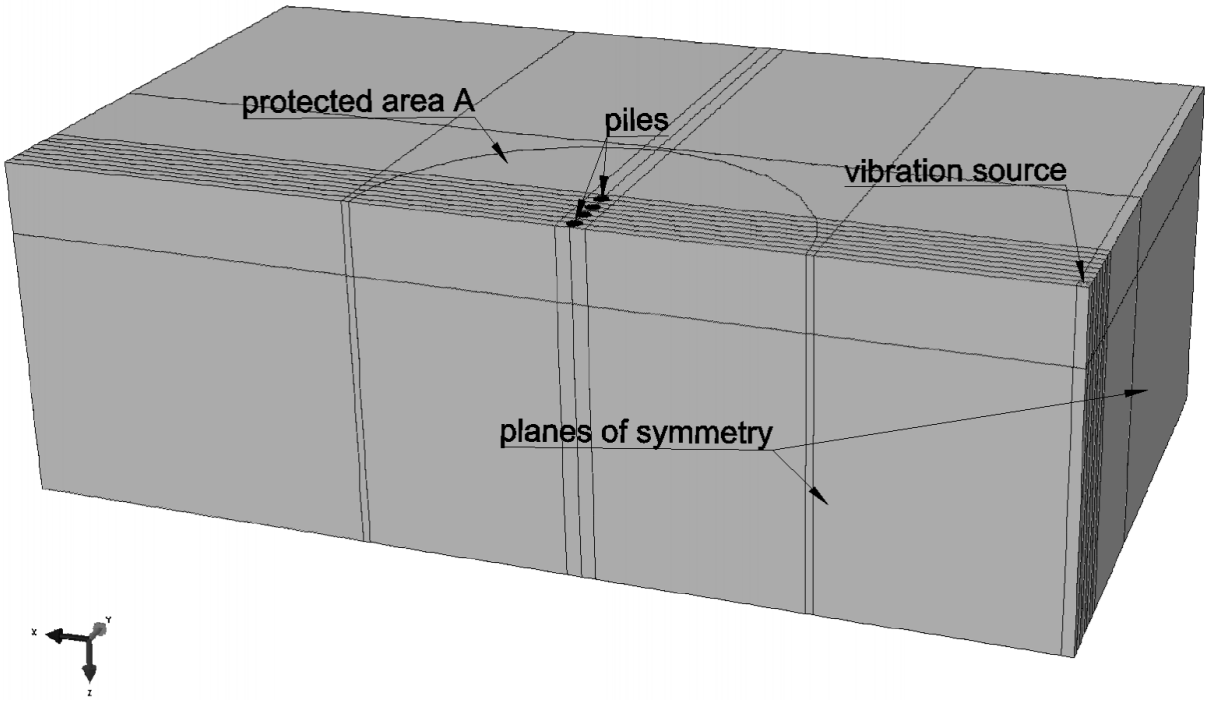

Figure 5.6: The scheme of FE model.

The computed results.

Planar configuration of the field.

As a starting point, the influence of pile diameter ($\tilde{d} = DL$), fraction ($\alpha = \frac{\pi \cdot D^2}{4 \cdot S^2}$) and pile distance ($S$) are considered. In order to estimate the influence of these parameters, the reduction ratio are calculated at the surface level in the protected zone Δ and underground level, which is located at the depth of $l/10$ beneath the surface layer, (figure 5.1). Figures 5.7 and 5.8 represent the reduction ratios for these layers. Contour plots in figures 5.7 and 5.8 are plotted at $\frac{E_{pile}}{E_{soil}} = 550, \frac{\rho_{pile}}{\rho_{soil}} = 1.3$, $\nu_{pile} = 0.2, \nu_{soil} = 0.25$ and $\frac{H}{l} = 1$.

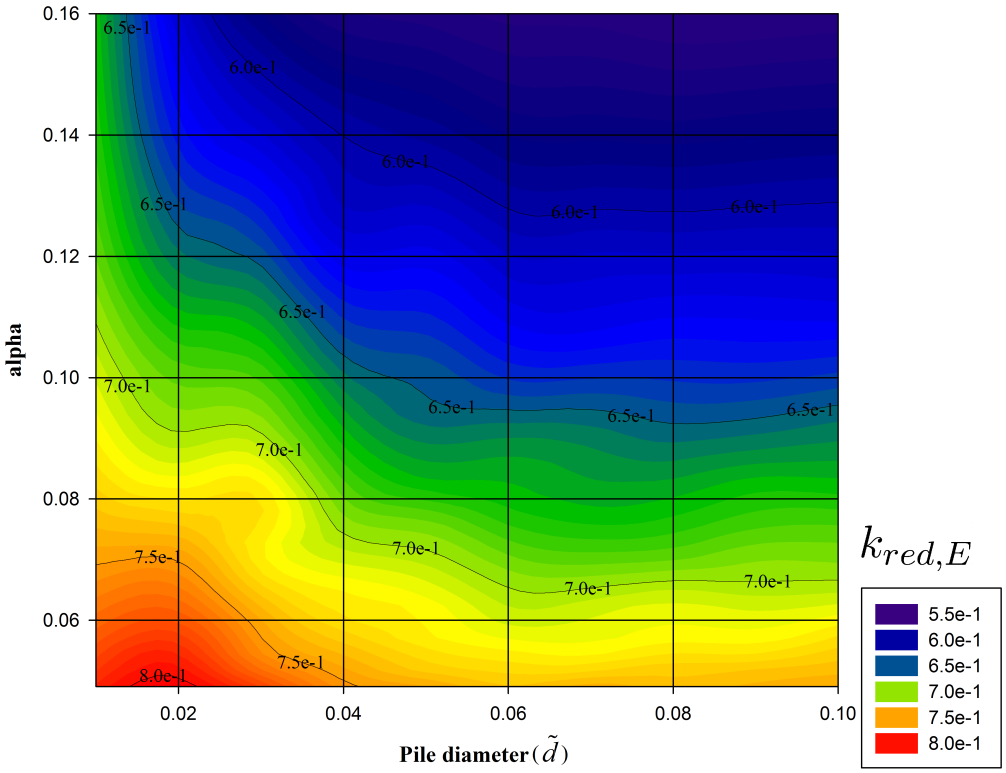

Figure 5.7: Reduction ratio for the surface layer.

The obtained results reveal that for a single row pile barrier, both diameter and pile fraction play and important role as the maximum vibration decrease is observed at the following values of pile fraction and diameter $\alpha = 0.16, \quad \tilde{d} = 0.1$ respectively. However, as it will be shown in the following text, pile diameter is less important if a pile barrier is composed of more than 2 rows (figure 5.9). In addition to that, it can be seen from figures 5.7 and 5.8 that the reduction ratio for the surface and underground layers decline with the increase in the diameter at the constant alpha significantly up to the value of normalized diameter equaling to 0.06. Then it maintains the same level slightly fluctuating around it. At the same time, pile fraction significantly affects the reduction effect which is growing with the increase of alpha. Comparing figures 5.7 and 5.8 shows that low normalized pile diameters are less effective for the protection of underground layer than the surface one. If $\tilde{d}$ is located in the range $[0, 0.03]$ such one row pile barrier is not effective even if pile fraction is high.

Figures 5.9 and 5.10 show the influence of pile row number on the reduction effect at different pile configurations (figure 5.3) and two pile diameters - small and large which correspond to $\tilde{d} = 0.01$ and $\tilde{d} = 0.06$ respectively. Curves in figures 5.9 and 5.10 are plotted at $\frac{E_{pile}}{E_{soil}} = 550, \frac{\rho_{pile}}{\rho_{soil}} = 1.3$, $\nu_{pile} = 0.2, \nu_{soil} = 0.25, \frac{H}{l} = 1$ and $\alpha = 0.162$.

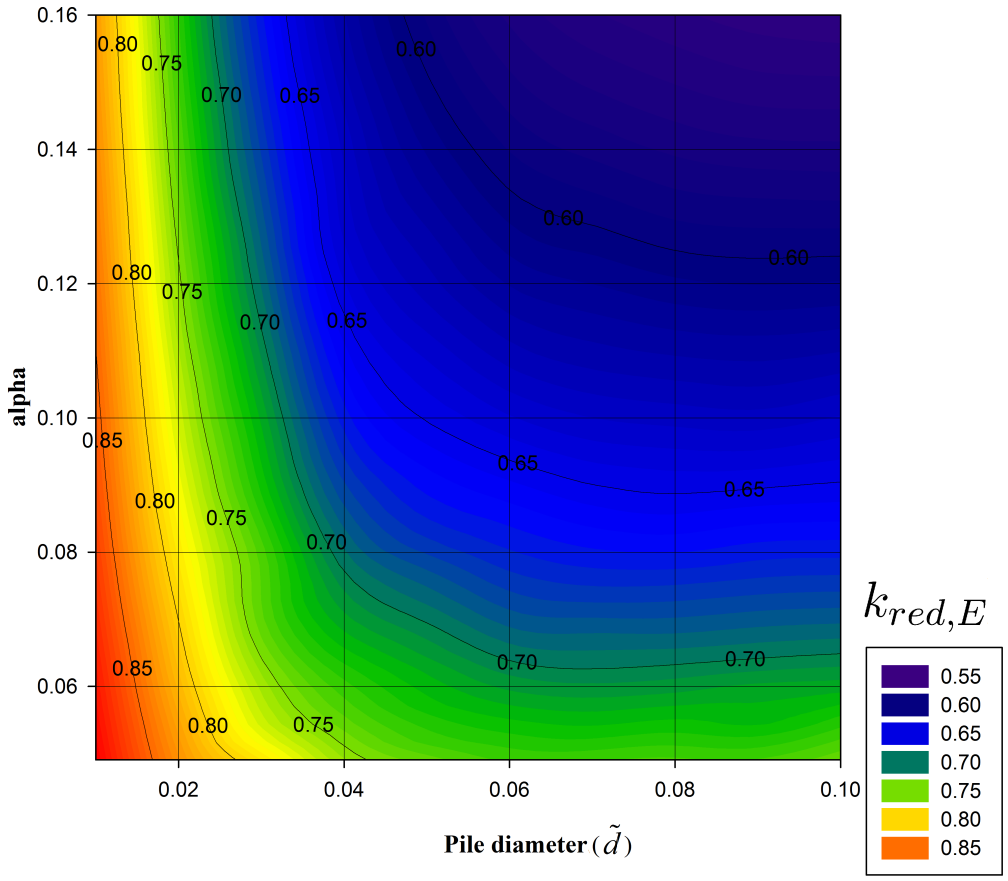

Figure 5.8: Reduction ratio for the underground layer.

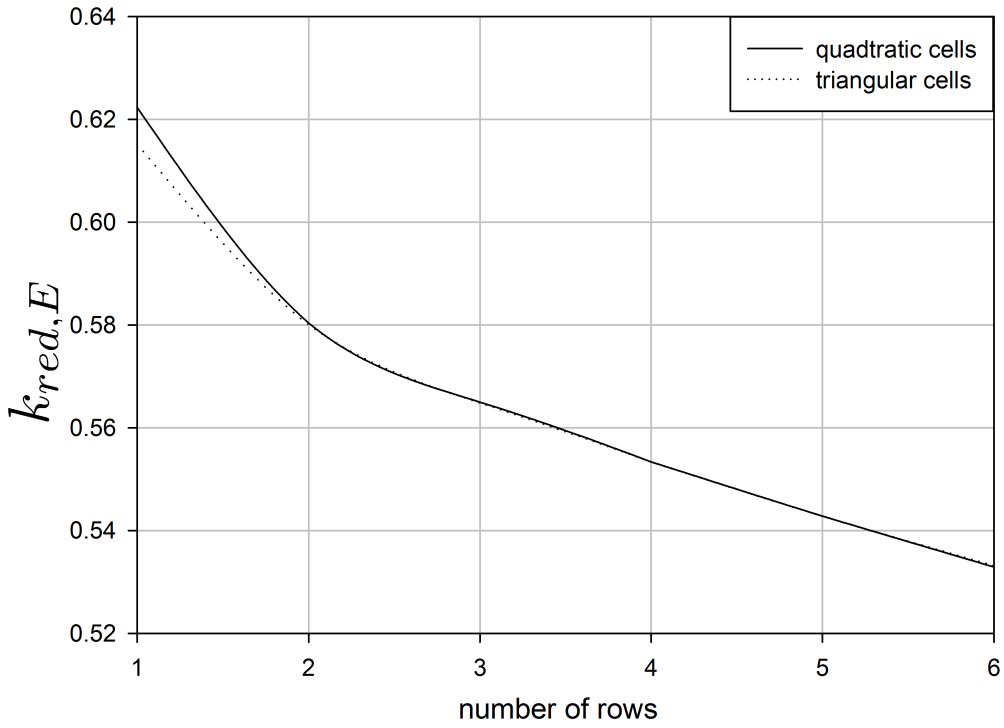

Figure 5.9: The influence of row number on the vibration reduction for low diameter piles. $\tilde{d} = 0.01; \tilde{\alpha} = 0.162; \tilde{l} = 1$

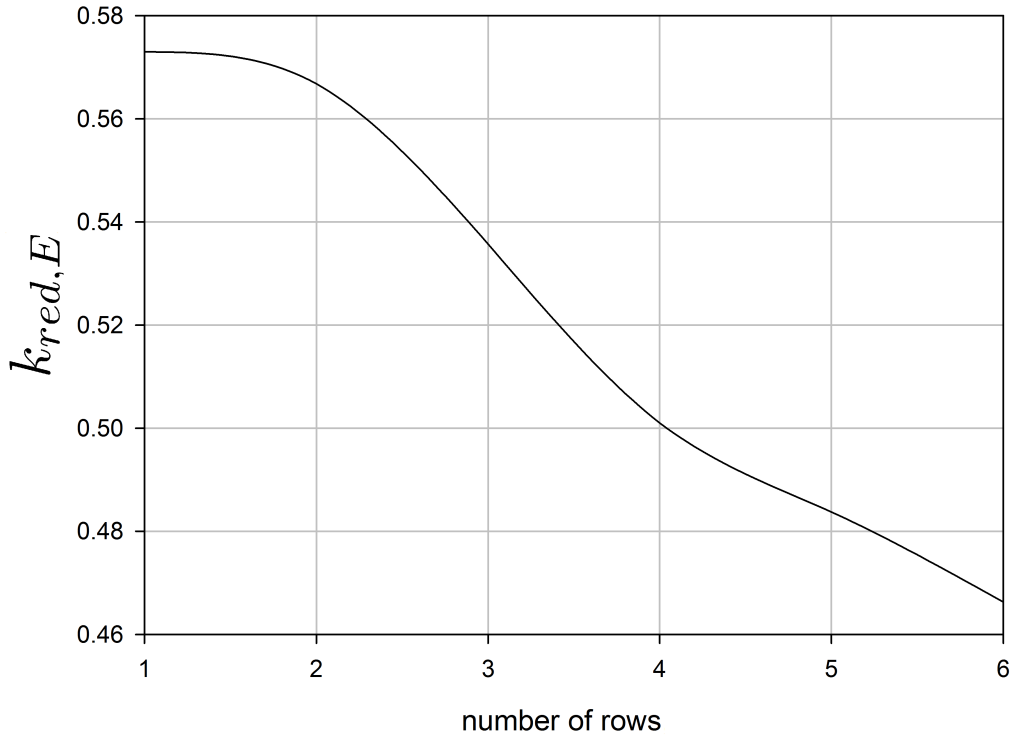

Figure 5.10: The influence of row number on the vibration reduction for high diameter piles. $\tilde{d} = 0.06; \tilde{\alpha} = 0.162; \tilde{l} = 1$

Figure 5.9 shows that the pile configurations (triangular and quadratic cells) have virtually no

effect on the reduction ratio. Therefore, the curve in figure 5.10 is plotted only for the quadratic configuration. Apart from that, the increase in the number of rows leads to a better vibration reduction effect of the pile field and even the barriers designed of low diameter piles but having several rows can give the same reduction effect as a single row barrier one with high diameter piles. However, high diameter piles give better reduction effect at the same number of rows (figure 5.10). Therefore, it is important to estimate the optimal configuration of pile field in terms of material volume, designed vibration reduction level and technology for each practical case.

Another interesting effect of the multi row pile barrier is the reduction of bending moments in piles which is presented in figure 5.11 showing the envelopes of bending moments in inner piles (the piles that are related to the first row which is the closest to the protected zone; they can be considered as the boarder piles of the foundation). This figure is plotted at the same values of the variables as figures 5.9 and 5.10. All the values in figure 5.11 are normalized in relation to the maximum bending moment for the case of the single row barrier. The graphs show that the value of the maximum bending moment in a pile may be decreased by 4 times due to the installation of 5 additional rows, while bending moments at deeper layers does not change significantly. Taking into account that the piles are simulated using 3D elements, bending moments are calculated from stress in the pile volume.

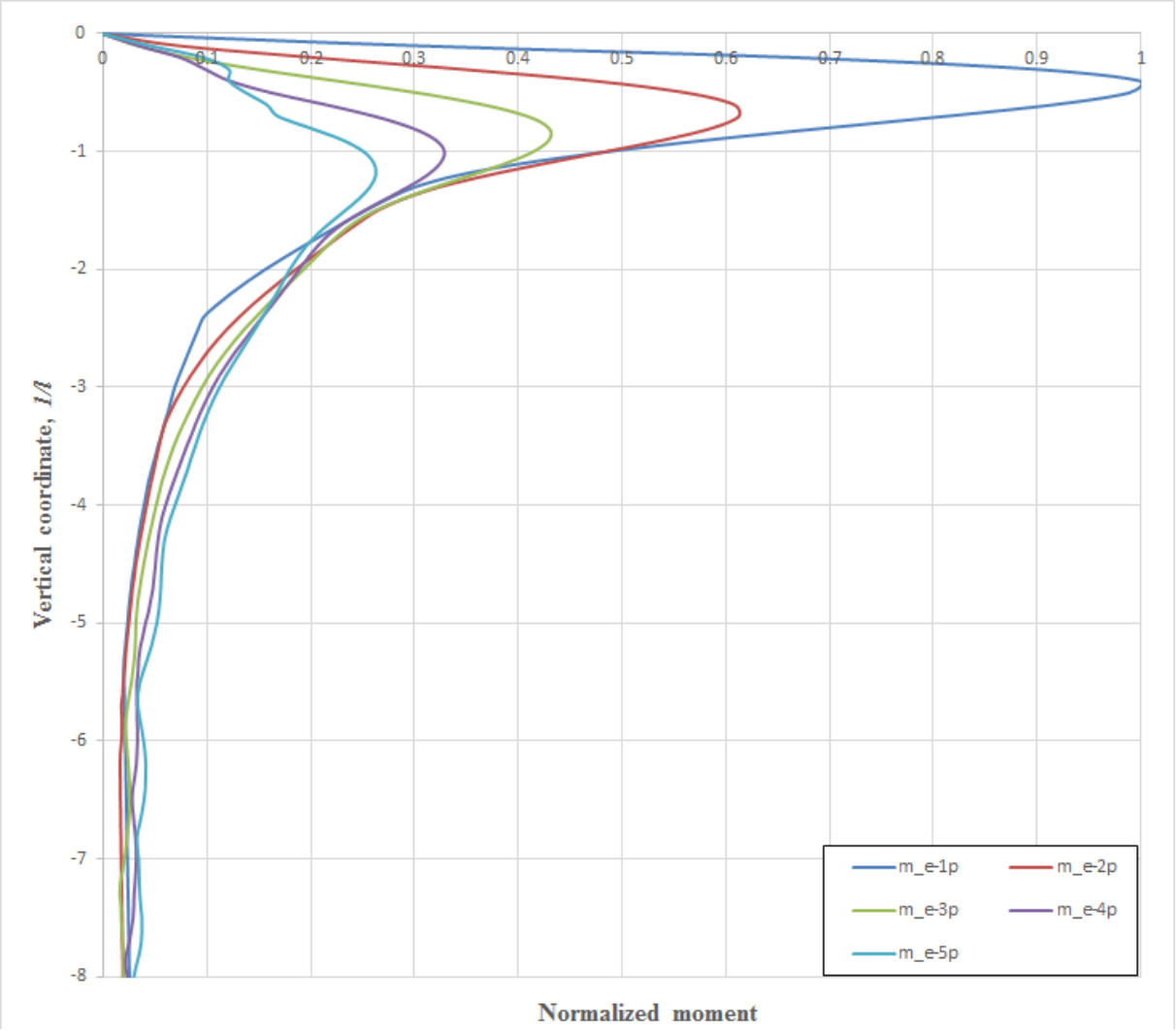

Figure 5.11: Envelops of maximum bending moments in the pile of the first row at different number of additional rows. Bending moments in the pile are normalized in relation to the maximum bending moment in this pile without additional rows.
$\tilde{d} = 0.01; \tilde{\alpha} = 0.162; \tilde{l} = 1$

Influence of the pile length.

It is clear that the pile length should be comparable with the wavelength, otherwise there will be virtually no diffraction and scattering of Rayleigh waves by the piles. Hence, the field itself cannot be used as a vibration barrier. Therefore, it is important to determine the connection between pile length and the attenuation effect. Figure 5.12 shows the change in the reduction ratio with the increase in the pile length. The curves in this figure are plotted at $\frac{E_{pile}}{E_{soil}} = 550, \frac{\rho_{pile}}{\rho_{soil}} = 1.3$, $\nu_{pile} = 0.2, \nu_{soil} = 0.25$, $\alpha = 0.162$ and $\tilde{D} = 0.1$.

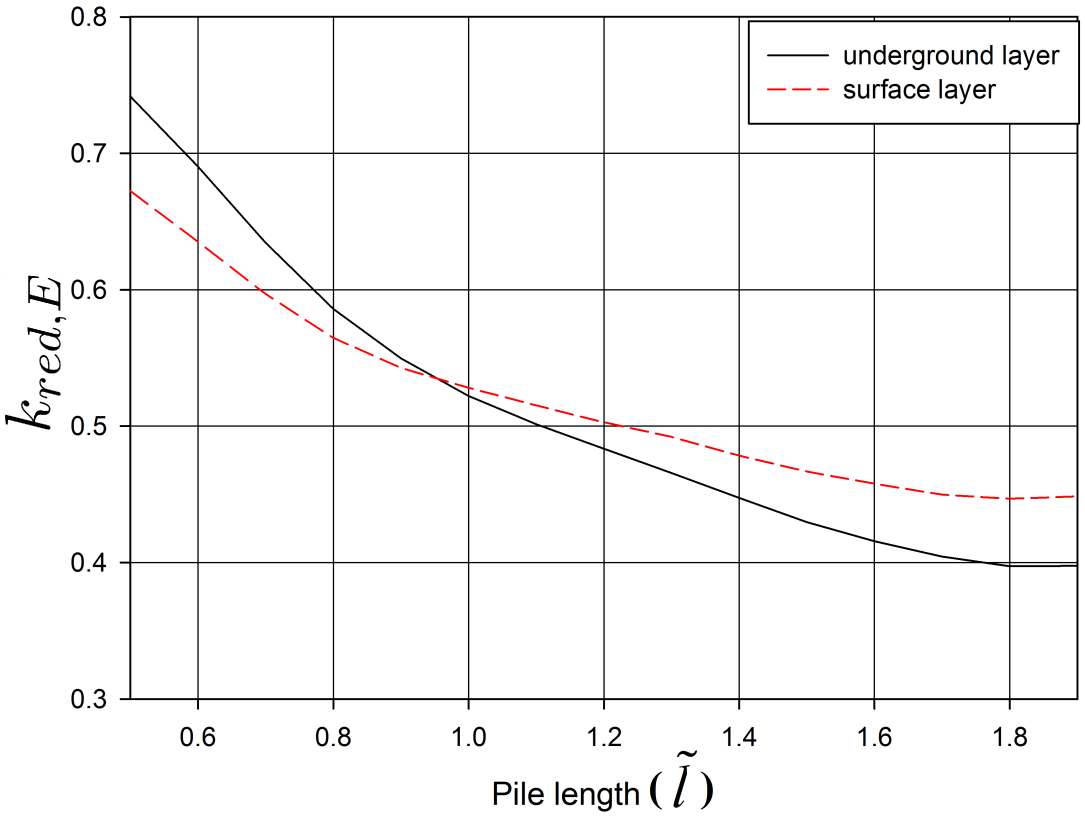

Figure 5.12: The change of screening effect with increase in the pile length.
$\tilde{d} = 0.1; \tilde{\alpha} = 0.162; \tilde{l} = 1$

According to the graphs in figure 5.12, reduction effect increases with the pile length significantly up to the reduction ratio of 0.3 at $\tilde{l} = 1.6$ reaching an asymptotic limit. It means that further increase in the pile length will not change the reduction effect noticeably. Additionally, for pile length which is less than the wavelength $\tilde{l} = 1.0$ better reduction is observed at the surface layer while for longer piles underground layer shows better vibration reduction.

Full scale 3d model.

Full scale 3d model shown in figure 5.2 is used to compare the results from the previous section for infinite length pile field with the results for finite length field that may surround the construction. The calculations are performed for $\frac{E_{pile}}{E_{soil}} = 550, \frac{\rho_{pile}}{\rho_{soil}} = 1.3$, $\nu_{pile} = 0.2, \nu_{soil} = 0.25$, $\alpha = 0.162$ and $\tilde{D} = 0.06$. Figure 5.13 shows the variation of the reduction ratio of the protected zone inside the field.

Figure 5.13 shows that the results for a finite size pile field surrounding the protected region (figure 5.2) are in a good agreement with those for the "infinite length pile field" (figure 5.1) shown in figure 5.10. It can be seen from the shapes of the curves and the range of the values

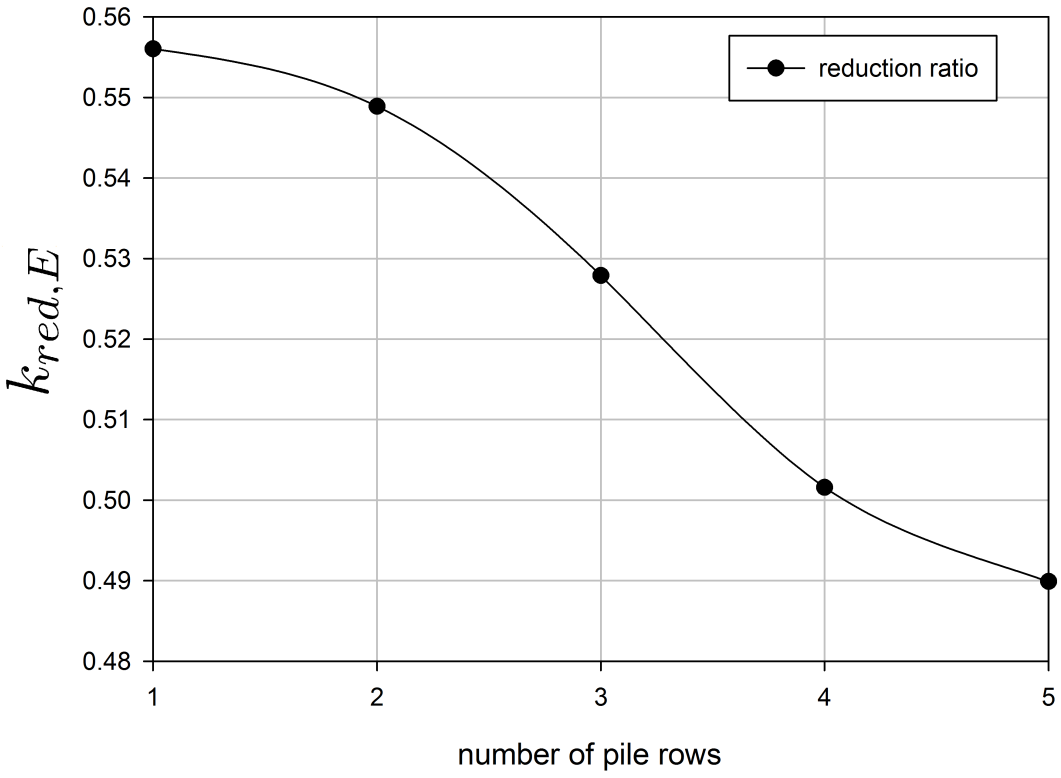

Figure 5.13: Full scale 3D model. The variation of the reduction ratio with the number of pile rows.
$\tilde{d} = 0.06; \tilde{\alpha} = 0.162; \tilde{l} = 1$

of the reduction ratio at different row numbers. Therefore, all the calculations conducted in the previous sections are valid for real finite size pile barriers. At the same time, if a barrier does not surround the protected area, the value of the reduction ratio will be different and the results from this work can be used only for a rough estimation. Therefore, additional calculations for the specific geometry should be carried out.

The comparison of wave barriers and pile fields in terms of vibration protection.

In order to compare two types of vibration barriers including underground walls and pile fields, the reduction effects of the both methods are compared assuming their material volumes to be equal. Let L is the length of a vibration barrier, then the volume of the pile field and seismic barrier (underground wall) are calculated as:

$$V_{bar} = L * h_{bar} * d_{bar} // V_{pile} = \frac{L}{s} * \frac{\pi * D^2}{4} H, \tag{5.3}$$

where V_{bar} and V_{pile} the volumes of the barrier and pile field materials; h_{bar} and d_{bar} are the barrier height and depth; D,H and s are the diameter, length and distance between piles respectively. At fixed parameters of the single row pile field $\tilde{d} = 0.06; \tilde{\alpha} = 0.162; \tilde{l} = 1$ and equal depth for the all barrier types, the parameters of the barrier can be obtained $\tilde{A} = 0.02; \tilde{r} = 46.7; \tilde{h} = 1$. Table 5.2 represents the reduction ratios of the pile field, EPS geofoam and concrete barriers.

The obtained results demonstrate that vertical seismic barriers are more effective than pile fields in vibration reduction. Although, in some cases the use of pile fields can be more beneficial

	Pile field	EPS geofoam barrier	Concrete barrier
Reduction ratio	0.557	0.477	0.335

Table 5.2: The comparison of the different type of vibration barriers.

as they additionally can protect a construction from body waves which, however, is beyond the scope of this research.

Conclusions.

The obtained results reveal that:

1. Pile field can be an effective measure to protect structures from surface Rayleigh waves as it decreases the transmission of wave energy, that is carried out by the surface waves into the protected region , thus, declining the amplitude of displacements, velocities and accelerations of the points in this zone. Simplified and full scale spatial models are used in the calculations and the results obtained using the both models are in a good agreement. Thus, it is possible to extrapolate the results from the simplified model to the full scale pile field that may surround a structure.

2. This way of protection shows good effectiveness when the maximum possible wavelength is comparable with the planar dimensions of a protected area along with the geometrical parameters of the pile field. This is the case for seismic waves in soft soils, such as clays with low plasticity index, loose and medium sands etc. as well as high frequency artificial vibration sources generating vibrations in stiffer soils, like clays with high plasticity index, dense sands etc. At the same time, for both cases of application, acoustical density of the pile barrier must be different to that of the soil. In that case, the pile field satisfying this condition can provide up to 50% decrease in the vibration energy transmitted to the protected zone. It is possible to improve vibration reduction effect of a pile field increasing pile diameter, length and fraction. However, further rise of these values may lead to inappropriate cost of the structure along with the additional complexity in the construction technology.

3. The main parameters that affect vibration reduction are the pile fraction, length, diameter as well as the number of pile rows.It is shown that pile length should be more than half of the wavelength to ensure at least 20% reduction in the kinetic energy, meanwhile the influence of the pile fraction and diameter is strongly affected by the number of rows. It means that for a single row pile barrier, the diameter of piles plays an important role up to the value of diameter equalling to $0.06 * l$. Then it has virtually no effect on the reduction ratio of the surface layer, while for the underground layer it affects the vibration decrease up to the diameter of $0.08 * l$ (here l is the design wavelength).

4. In the case of multi row pile barriers, the effect of pile diameter still exists, but becomes less important because the reduction ratio of low diameter piles installed in several rows can be the same as that of high diameter piles but designed as one row barrier. Therefore, there are no strict limitations on pile diameters. However, the volume of the material for the pile field will be equal for a single and multi rows pile fields if the same vibration reduction is provided. Therefore, it is possible to use lower diameters for the piles which is a better solution from technological point of view.

5. An additional important result from the use of such barrier is a decrease in bending moments in the inner piles, that can be used as a deep foundation. It is shown that the possible reduction effect in bending moments of the inner piles can reach 80%.

6. A pile field is a less effective measure than seismic barriers in terms of vibration reduction. Although, they can protect constructions from body waves which, however, is beyond the scope of this research.

CHAPTER 6

INTERACTION OF VERTICAL SEISMIC BARRIERS (INCLUDING PILE FIELDS) WITH SURFACE RAYLEIGH WAVES

Contents

Present chapter summarizes the results of numerical simulation of vertical seismic barriers and pile fields interaction with surface Rayleigh waves accounting for plastic character of soil deformation at high shear strain levels that correspond to earthquakes and explosions. Two reference cases which relate to cohesive and cohesionless soils are considered using Mohr-Coulomb model to simulate elasto-plastic soil behaviour. Pile field and barrier geometries as well as materials are chosen based on the simulation results obtained in chapters 4 and 5.

FE models and initial conditions

FE models

The models used for numerical simulation of vertical seismic barrier and pile field interaction with surface Rayleigh waves are shown in figures 6.1 and 6.2 accordingly. In general, these models are similar to the ones described in chapters 4 and 5 (Figures 4.1 and 5.1), except finite element types and boundary conditions on the bottom and right sides. Therefore, general principles such as the size and location of the protected zone, symmetry axis and planes, model sizes are applicable to the models used in this part of the work.

Planar model implementing plane strain condition (Figure 6.1) is used to simulate interaction of Rayleigh waves with vertical seismic barriers. Spatial discretization is performed using eight node elements of CPE8R type with bi-quadratic shape function reduced by the integration scheme

with control of deformations [1]. Final mesh is structural with maximum length ratio in the range $k_l \in [0.99, 1]$. As in the simplified model shown in figure 4.1, the condition of symmetry is applied on the left edge (Figure 6.1). However, the right and the bottom edges are fixed.

To simulate interaction of pile fields with surface Rayleigh waves "simplified" model of a pile field (Figure 6.2) is used. This model is similar to the one shown in figure 5.1 including three planes of symmetry which pass parallel to the direction of wave propagation through pile center and between piles as well as perpendicular to the direction of wave propagation at the distance from the pile row. At the same time, the right and bottom sides of the model are fixed. Spatial discretization is performed using twenty node elements of C3D20R type with quadratic shape function reduced by the integration scheme with control of deformations [1].The mesh is of an appropriate quality with maximum length ratio in the range $k_l \in [0.97, 1]$.

Similarly to the problems considered in chapters 4 and 5 explicit finite-difference procedure is used in the analysis. Time increment size is selected automatically by the program satisfying the Courant–Friedrichs–Lewy (CFL) condition 4.2 [35]. Detailed analysis of numerical errors caused by explicit central difference scheme of the second order with FE element discretization with quadrilateral 8-node and hexahedral 20-node elements with a quadratic shape functions is shown in [152], [36] and [75] for elastic and elastoplastic constitutive models.

The kinematic surface loading that generates Rayleigh waves in the both models (Figures 6.1 and 6.2) is specified in the form (4.1) as in chapters 5 and 4. It is worth noting, that in the source zone shear strain can achieve high values, thus, soil behaviour in this area is highly non-linear. This zone is shown in figures 6.1 and 6.2 hatched with dash-dotted lines. The size of this region may achieve $l \div 2 * l$, which is, however, less than the distance required by symmetry condition and specified in the previous chapters. Therefore, the observation zone is remote enough from the loading zone (more than $5l$) and the level of shear strains in the soil within the surface area in the observation zone is stable and defined by the loading amplitude. The observation zone is shown in figures 6.1 and 6.2 hatched with cross hatching.

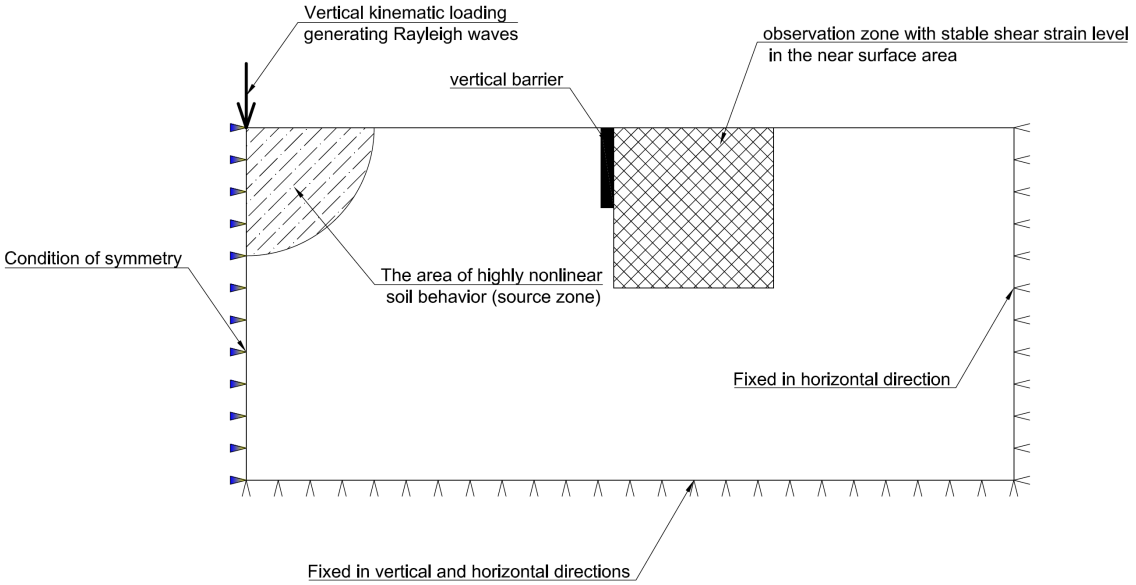

Figure 6.1: Vertical barrier. The scheme of the FE model for the non-linear case.

Initial stress field

Numerical simulation is performed for two soil types shown in table 6.1 at loading frequency equalling $2Hz$. Prior to the dynamic analysis, the calculation of the initial stress field along

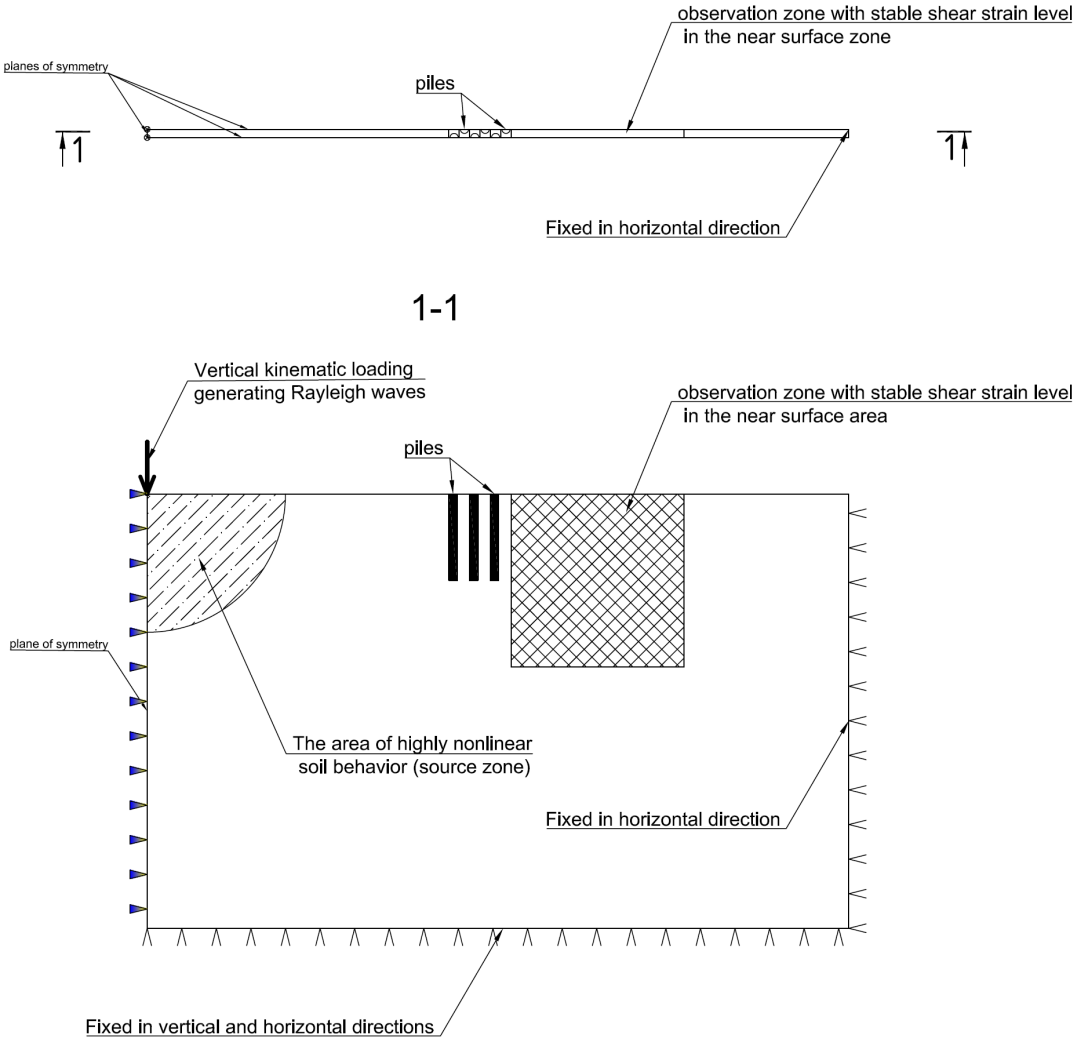

Figure 6.2: Pile field. The scheme of the FE model the non-linear case.

with the stress field after barrier installation is conducted. Initial stress field presented in the following text are calculated for plane strain case using model in figure 6.1. Initial stress fields for the problem of Rayleigh wave interaction with pile fields (Figure 6.2) is not presented here as they are is similar to the planar case.

Soil type	Density, kg/m^3	Young's modulus, MPa	Poissin's ratio	Cohesion, KPa	Friction angle
Cohesive(clay)	1800	87.22	0.35	50	23
Cohesionless(sand)	1750	24	0.32	1	30

Table 6.1: The comparison of the different type of vibration barriers.

Cohesionless soil

Vertical and horizontal initial stresses in the soil prior to the installation of the barrier in the case of cohesionless soil are shown in figures 6.3 and 6.4 respectively. Vertical and horizontal stresses in the soil after construction of the barrier are shown in figures 6.5 and 6.6 respectively.

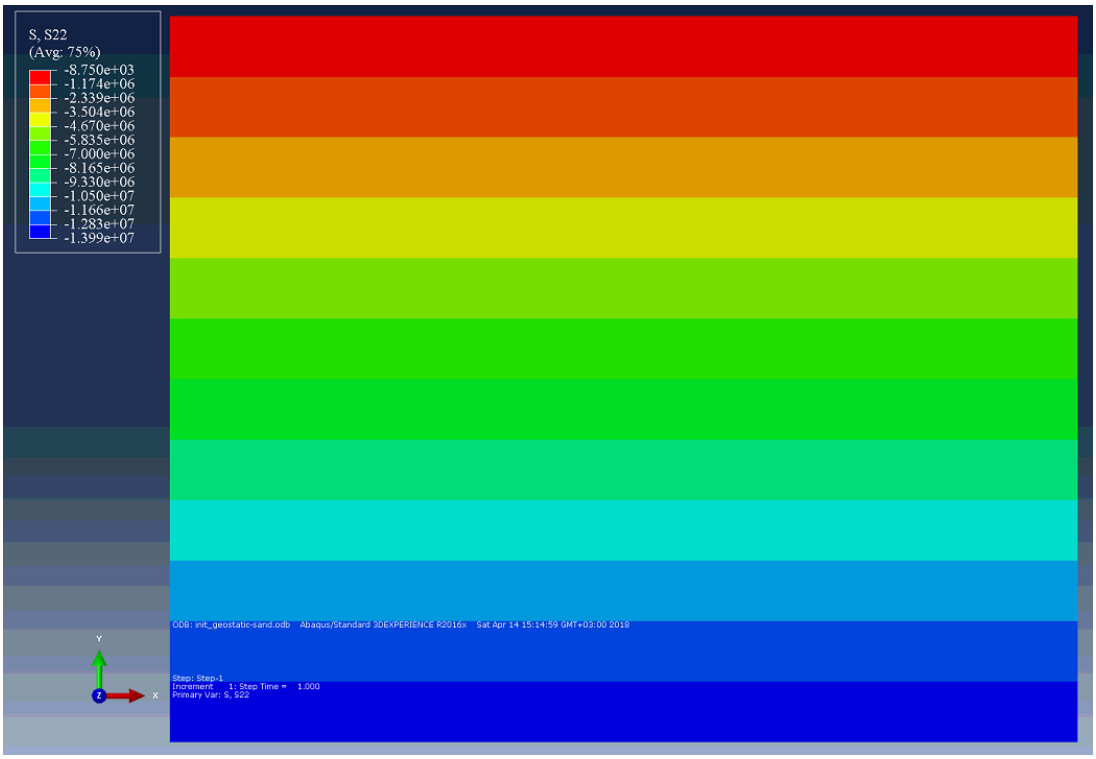

Figure 6.3: Initial vertical stresses in the soil before installation of the barrier (Pa).

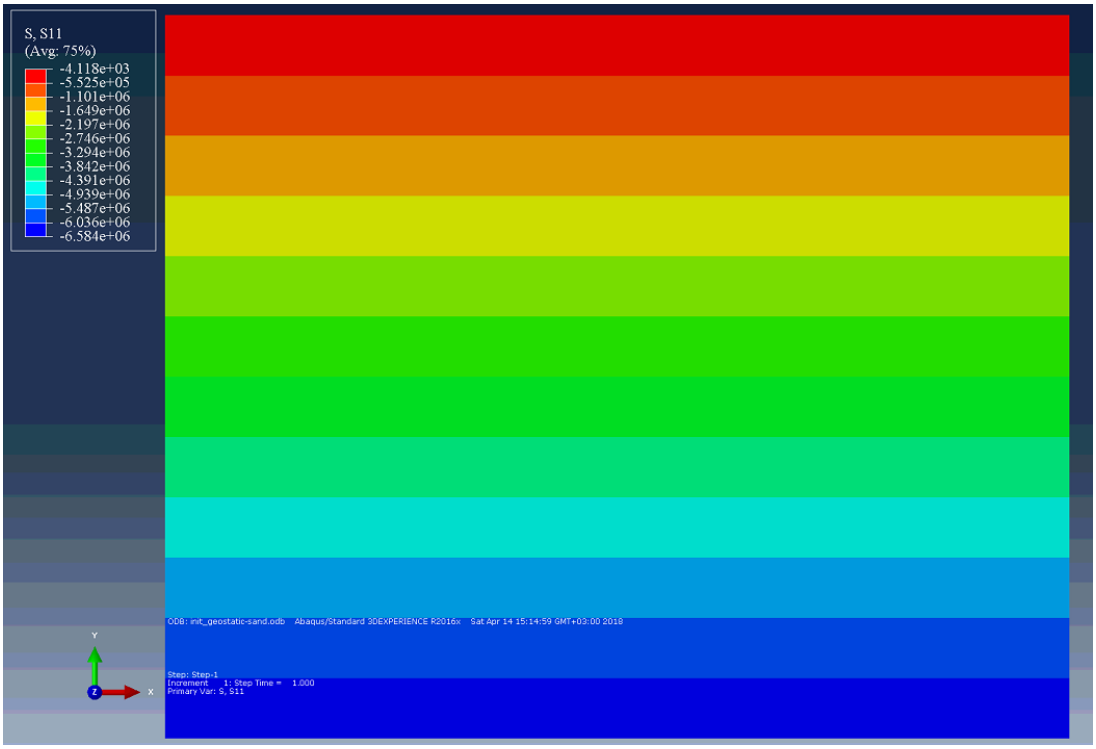

Figure 6.4: Initial horizontal stresses in the soil before installation of the barrier (Pa).

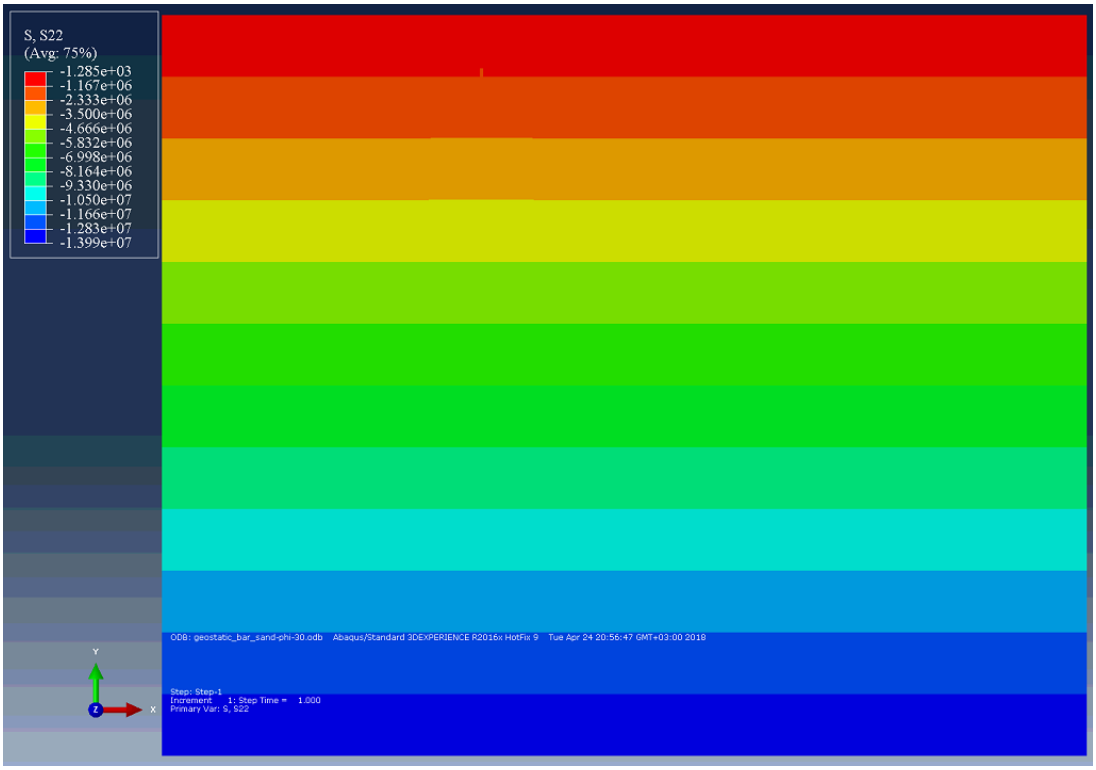

Figure 6.5: Vertical stresses in the soil after installation of the barrier (Pa).

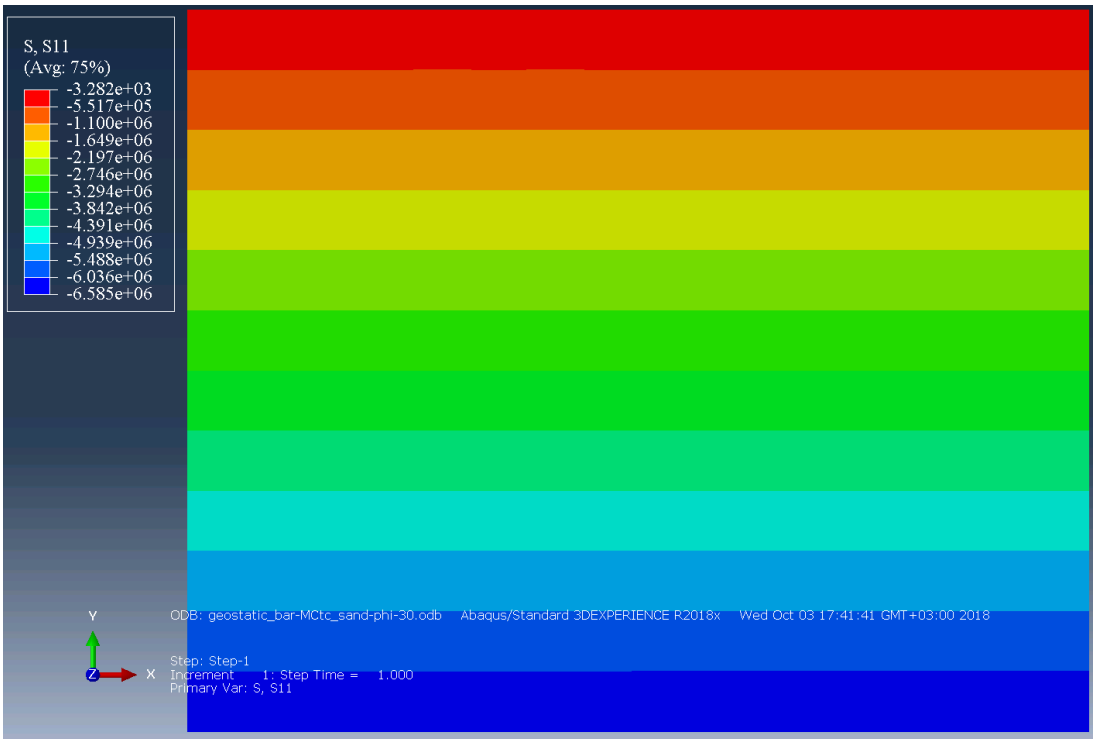

Figure 6.6: Horizontal stresses in the soil after installation of the barrier (Pa).

Cohesive soil

Vertical and horizontal initial stresses in the cohesive soil before barrier installation are shown in figures 6.7 and 6.8 respectively, their change after barrier installation is shown in figures 6.9 and 6.10.

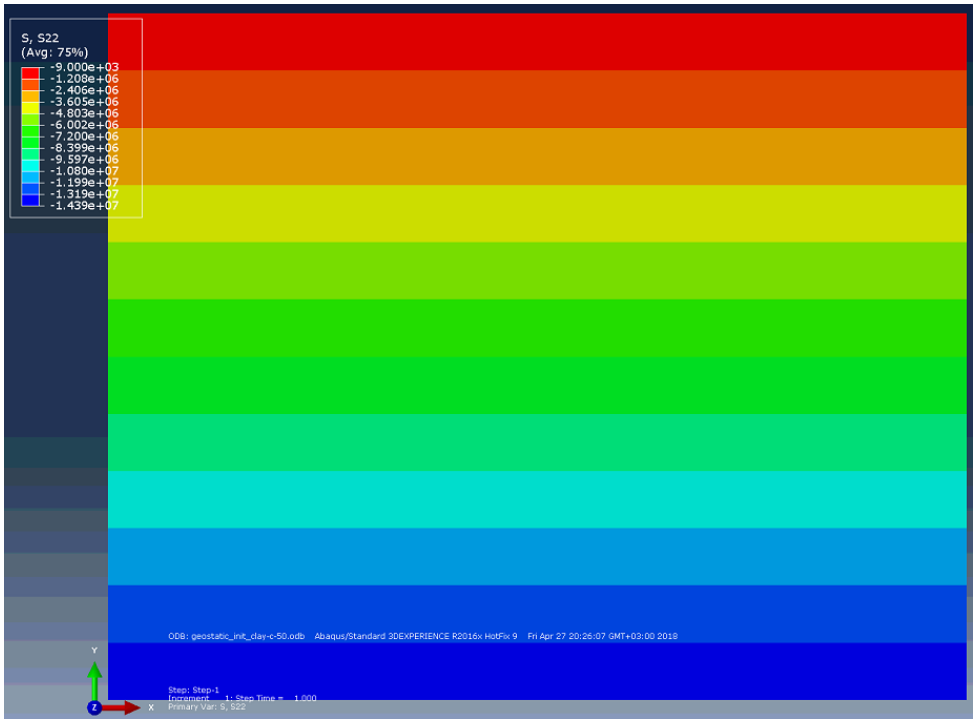

Figure 6.7: Initial vertical stresses in the soil before installation of the barrier (Pa).

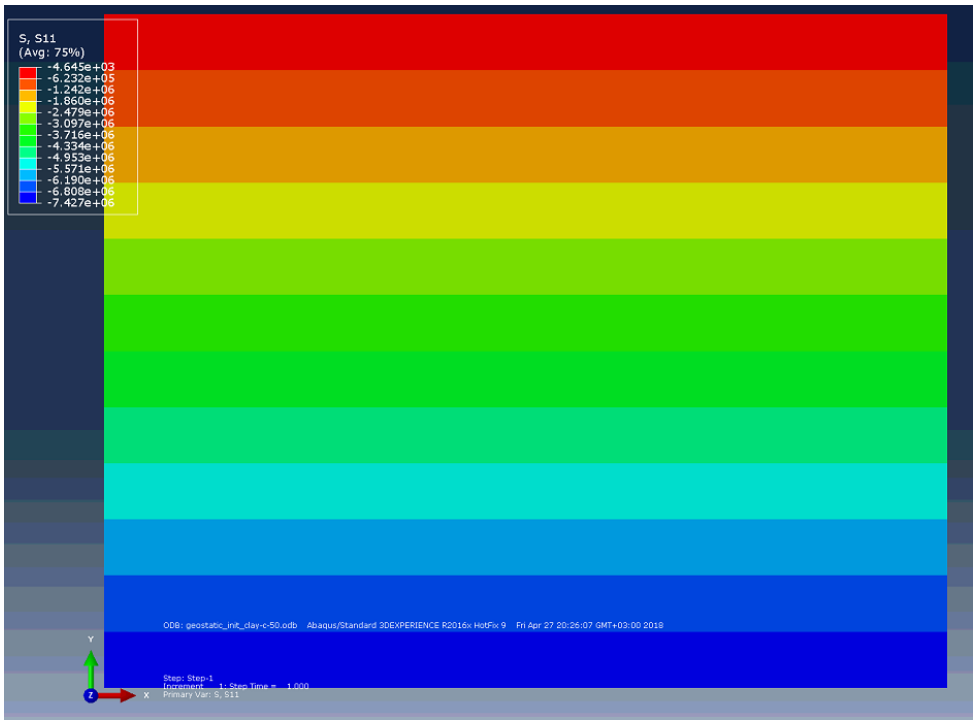

Figure 6.8: Initial horizontal stresses in the soil before installation of the barrier(Pa).

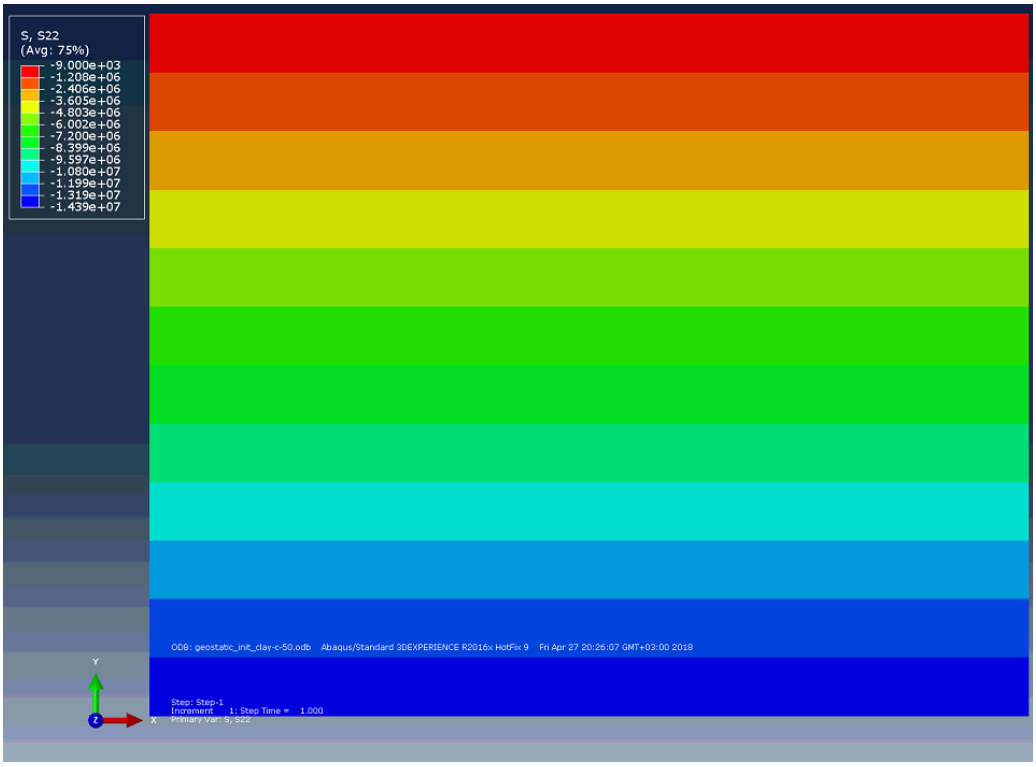

Figure 6.9: Horizontal stresses in the soil after installation of the barrier (Pa).

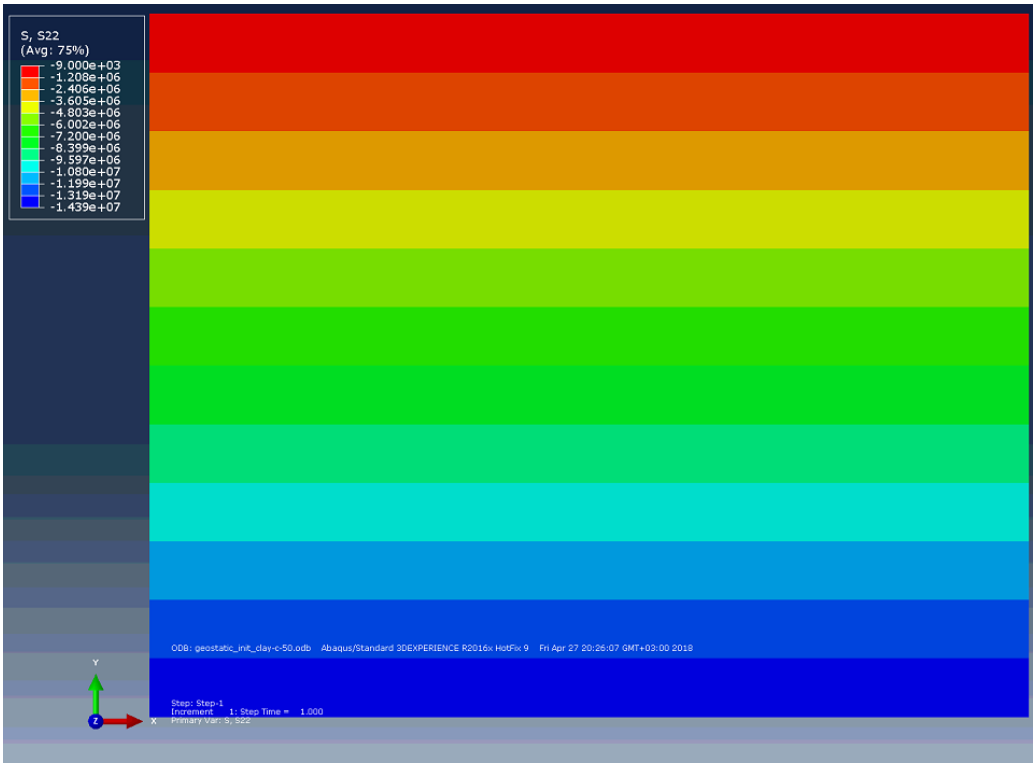

Figure 6.10: Vertical stresses in the soil after installation of the barrier (Pa).

Calculation algorithm

As a starting point, numerical simulation of surface Rayleigh wave propagation without barrier is performed using the planar model (Figure 6.1) to analyse displacement and velocity fields at different shear strain levels. Also, it is shown that, because of plane strain type of the model, no effect of shadow zone is observed (this is also the case for pile field model 6.1 as it simulates an infinite length pile field). The results also show that the reduction effect can be represented by displacement curves for any surface point in the protected zone ($x \in [0.1l, l]$), where x is the distance from the barrier or the pile field) and kinetic energy for the surface layer in this zone.

Then, numerical simulation of surface Rayleigh wave interaction with the vertical barrier is performed for the cohesionless and cohesive soils. The curves representing amplitude of displacements and kinetic energy in the protected zone show the reduction effect given by the barrier at various shear strain levels.

Afterwards, based on the results obtained from the simulation of Rayleigh wave interaction with vertical seismic barriers, the modelling of pile field interaction with the surface waves is performed. The results are shown for the cohesionless soil as the results for the considered cohesive and cohesionless soils are qualitatively similar at high shear strain level.

Initial displacement and velocity distributions in the observation zone

Although, the character of wave propagation in the framework of elastoplasticity is more complex, it is possible to underline main components of vibration in the observation zone. When the distance between the points in the observation zone and wave velocities are known, waves can be determined according to their theoretical velocities and the velocities calculated from the results obtained using the FE model (Figure 6.1). Figure 6.11 represents amplitude of displacements of a point in the observation zone. According to the theoretically calculated body and surface wave velocities, arrivals of body and surface waves are specified. Figure 6.11 is plotted for the sand shown in table 6.1 at shear strain equalling $\gamma = 0.0005$. It can be seen that, although, body waves carry more energy than in the linear elastic case, Rayleigh waves still dominates in displacements even at this shear strain level. So, the considered models are still appropriate for the analysis of Rayleigh wave interaction with vertical barriers and pile fields, however, the analysis of barrier interaction with body waves must be performed using other models of the source, preferably more realistic underground source.

It is worth noting, that the appearance of residual strains caused by plastic deformations in the soil results in a slight increase in vibration displacements is observed when new wave comes to the observation points (each of the following peaks are slightly higher then previous one 6.11). This effect also takes place in the case of cohesive soils 6.31. Therefore, vibration velocities are also estimated through kinetic energy in the protected zone to avoid accumulating effect of the residual strains and possible error in estimation of the vibration reduction effect.

Figures 6.12 - 6.15 represent the envelopes of normalized displacement and velocity amplitudes change with depth at low and high shear strain levels. As these graphs are targeted to show displacement and velocity distribution character change with depth they are normalized in relation to its maximum values for the considered time interval. These figures are plotted for the cohesionless soil with mechanical parameters defined in table 6.1 and the loading frequency equalling $2Hz$. During the considered time interval four Rayleigh waves pass through the observation zone.

The obtained results reveal that at high shear strain in the soil vibration energy is redistributed to deeper layers, which can be seen from slow displacement decay with depth placed in the range from $0.1l$ to $1.5l$, followed by its stabilization at depth which is more than $1.5l$ (figure 6.14). On the contrary, at low shear strain level (figure 6.12) displacements in the soil decrease

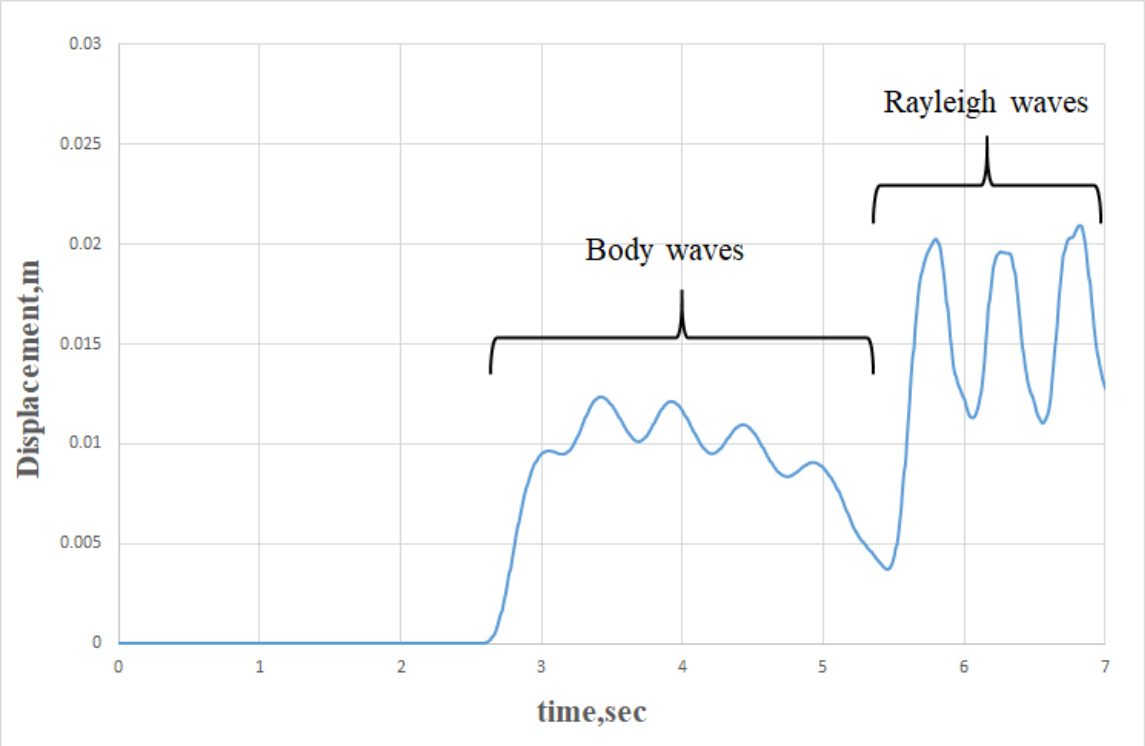

Figure 6.11: Cohesionless soil. Amplitude of displacement in the observation zone at $\gamma = 0.0005$

much faster with an increase in the depth. At the same time, the change of velocity distribution character is less significant. This can be explained by the limitation on stresses in the subsurface layer imposed by the yield function, which means that plasticity zone propagates to deeper layer at high shear strains. Velocity distribution character is strongly affected at higher shear strain levels $\gamma > 0.005$, at which velocity decay with depth is slower. For the cohesive soil this also takes place, but at higher shear strains.

This trend can be observed for the cohesive soil in figures 6.16 - 6.21 which represent the envelopes of normalized displacement and velocity amplitude change with depth at low and high shear strain levels for the cohesive soil (table 6.1). These graphs are also normalized in relation to its maximum values for the considered time interval and plotted at the loading frequency equalling $2Hz$.

At high shear strain in the soil vibration energy is redistributed to deeper layers, which can be seen from slower displacement decay with depth, however, its value continue decreasing with depth (figure 6.14) in contrast to the cohesionless soil. Shear strain increase in cohesive soil affect the character of velocity amplitude versus depth curve also less than in the case of the cohesionless soil.

The obtained results are especially important taking into account that barrier reduction effect occurs in subsurface layer at depths $z \in [0, 0.6l]$ (Figures 6.22 and 6.23), where l is the wavelength of Rayleigh wave. This means that at high shear strain in the soils, seismic barriers and pile fields tend to be ineffective in terms of vibration reduction 6.24 and 6.25.

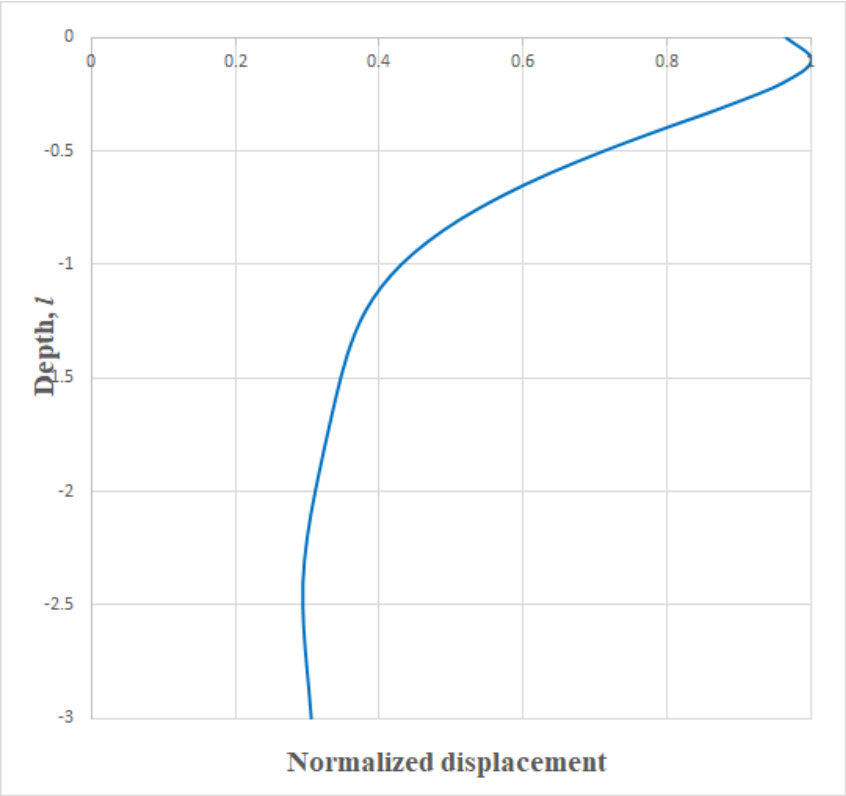

Figure 6.12: Cohesionless soil, $\gamma = 10^{-5}$. Envelopes of normalized amplitude of displacement at different depths l. (Amplitude of displacement is normalized in relation to its maximum value during the considered time period.)

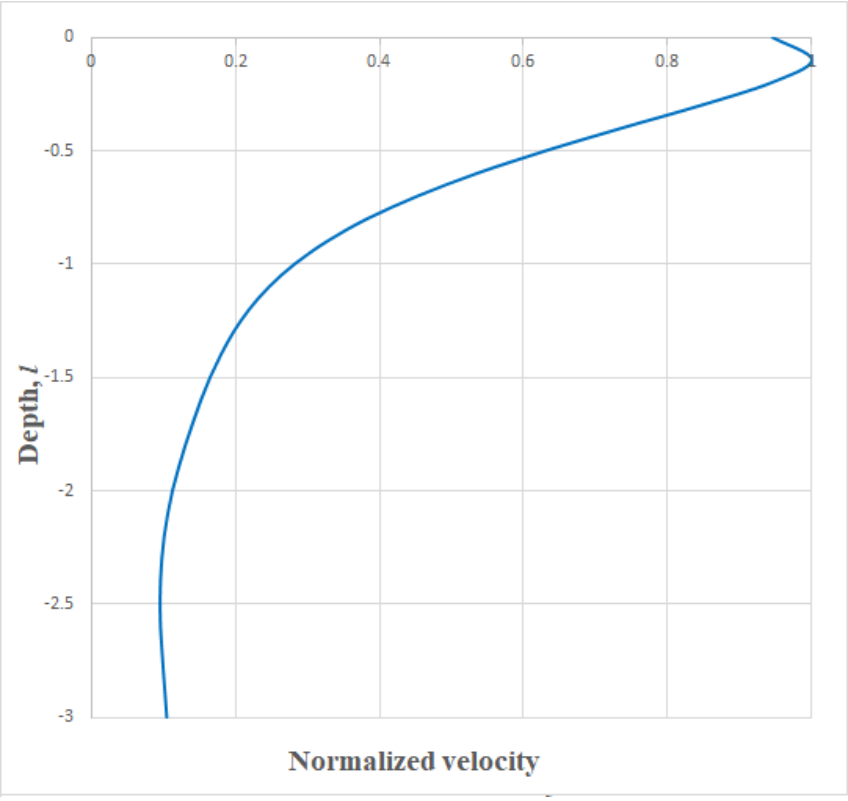

Figure 6.13: Cohesionless soil, $\gamma = 10^{-5}$. Envelopes of normalized amplitude of velocities at different depths l. (Amplitude of velocities is normalized in relation to its maximum value during the considered time period.)

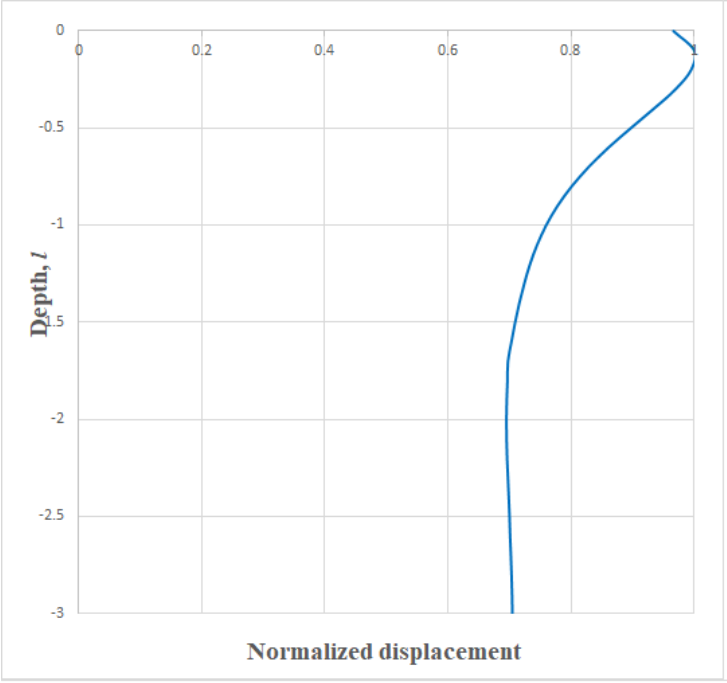

Figure 6.14: Cohesionless soil, $\gamma = 5 * 10^{-4}$. Envelopes of normalized amplitude of displacement at different depths l. (Amplitude of displacement is normalized in relation to its maximum value during the considered time period.)

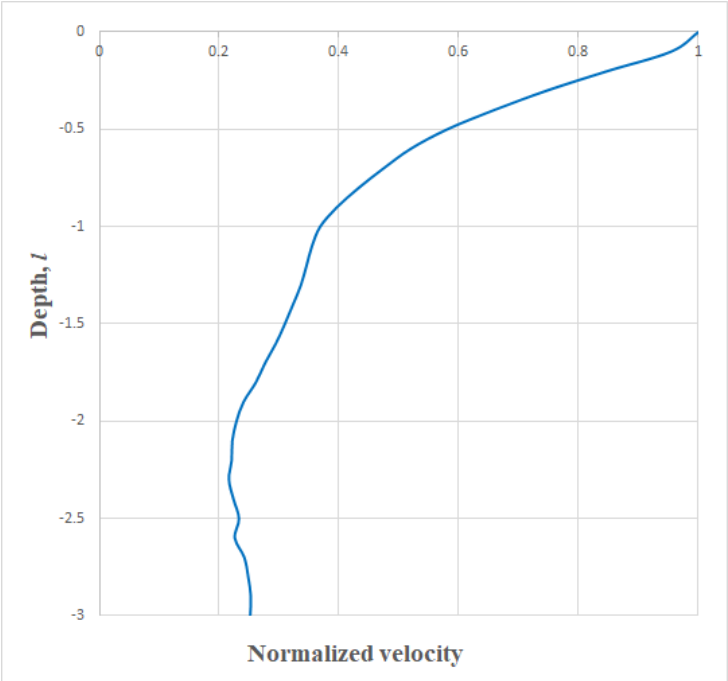

Figure 6.15: Cohesionless soil, $\gamma = 5 * 10^{-4}$. Envelopes of normalized amplitude of velocities at different depths l. (Amplitude of velocities is normalized in relation to its maximum value during the considered time period.)

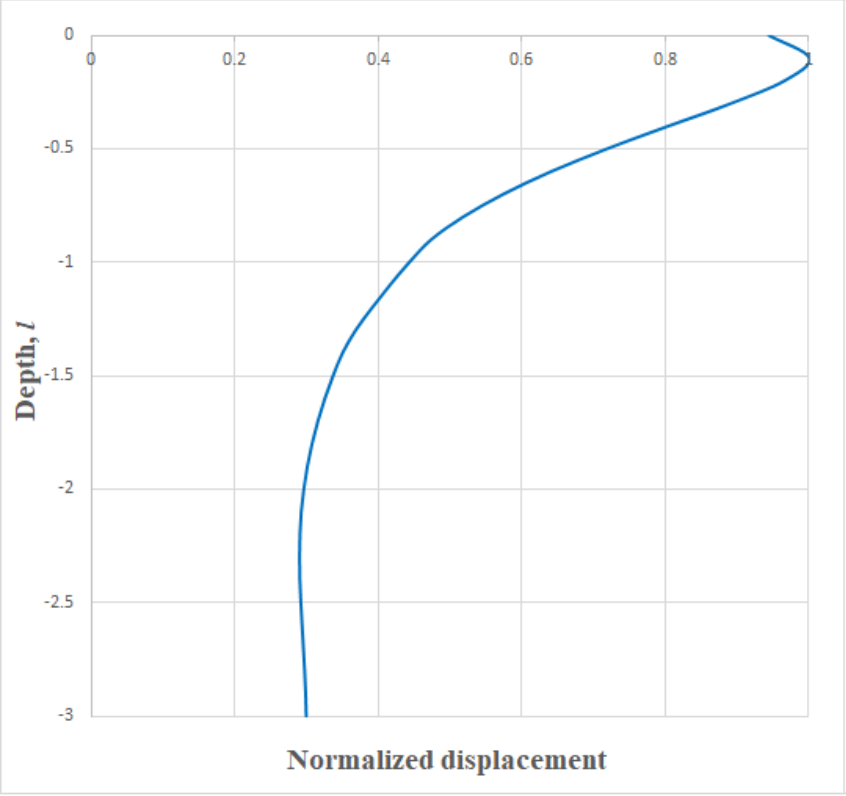

Figure 6.16: Cohesive soil, $\gamma = 10^{-5}$. Envelopes of normalized amplitude of displacement at different depths l. (Amplitude of displacement is normalized in relation to its maximum value)

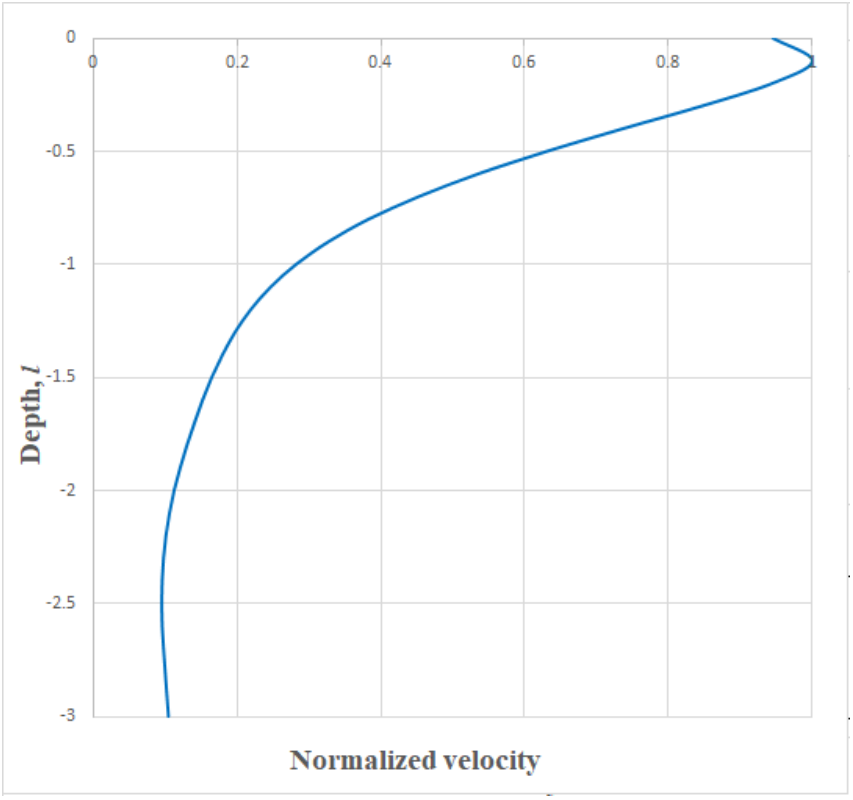

Figure 6.17: Cohesive soil, $\gamma = 10^{-5}$. Envelopes of normalized amplitude of velocities at different depths l. (Amplitude of velocities is normalized in relation to its maximum value)

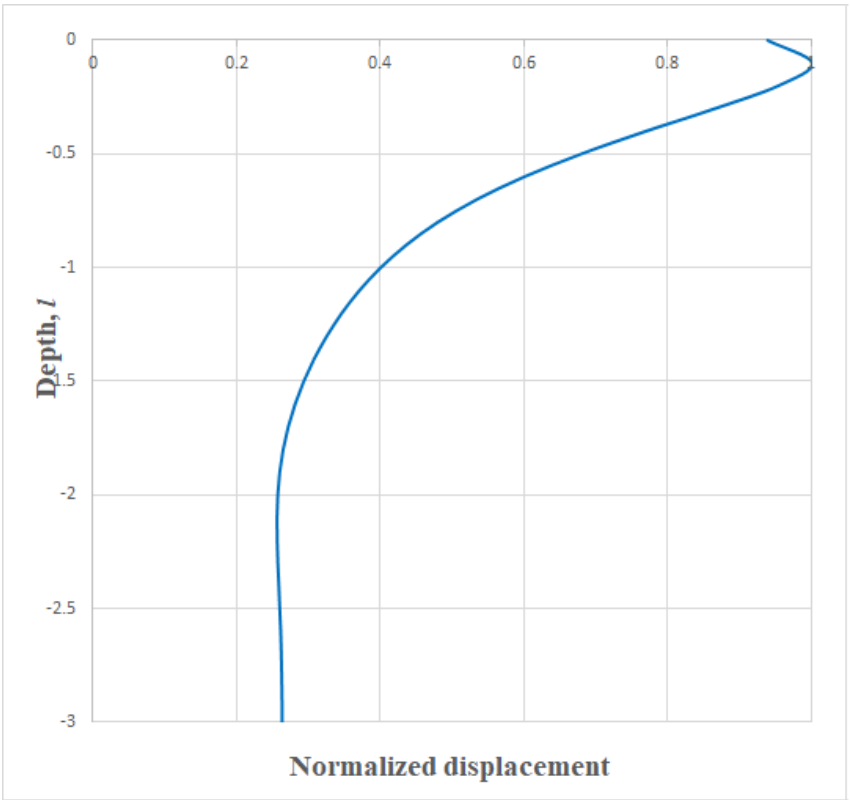

Figure 6.18: Cohesive soil, $\gamma = 5 * 10^{-5}$. Envelopes of normalized amplitude of displacement at different depths l. (Amplitude of displacement is normalized in relation to its maximum value)

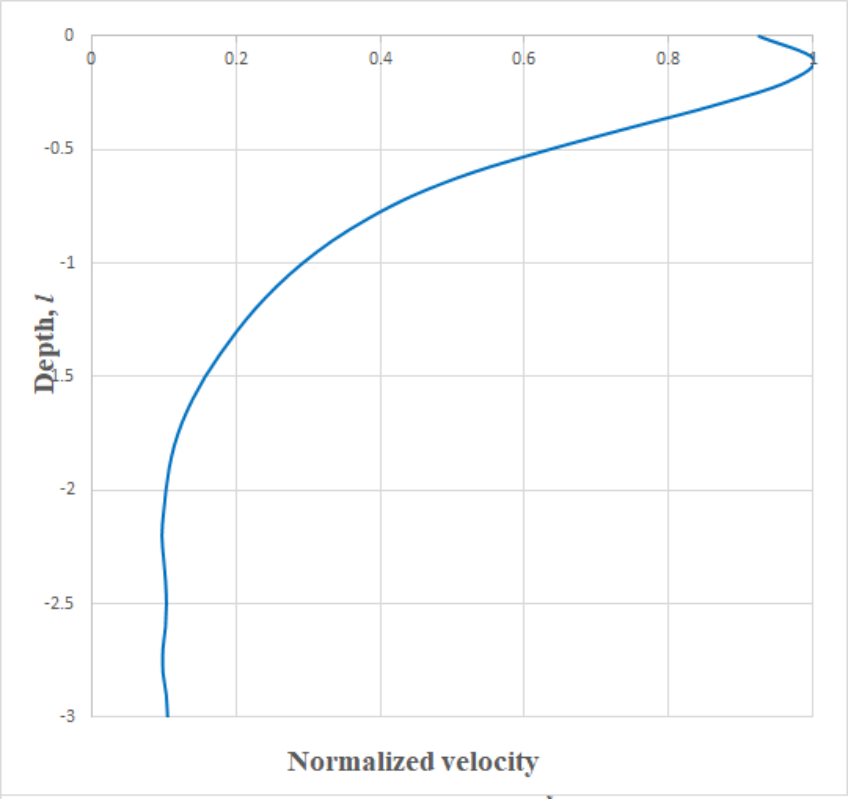

Figure 6.19: Cohesive soil, $\gamma = 5 * 10^{-4}$. Envelopes of normalized amplitude of velocities at different depths l. (Amplitude of velocities is normalized in relation to its maximum value)

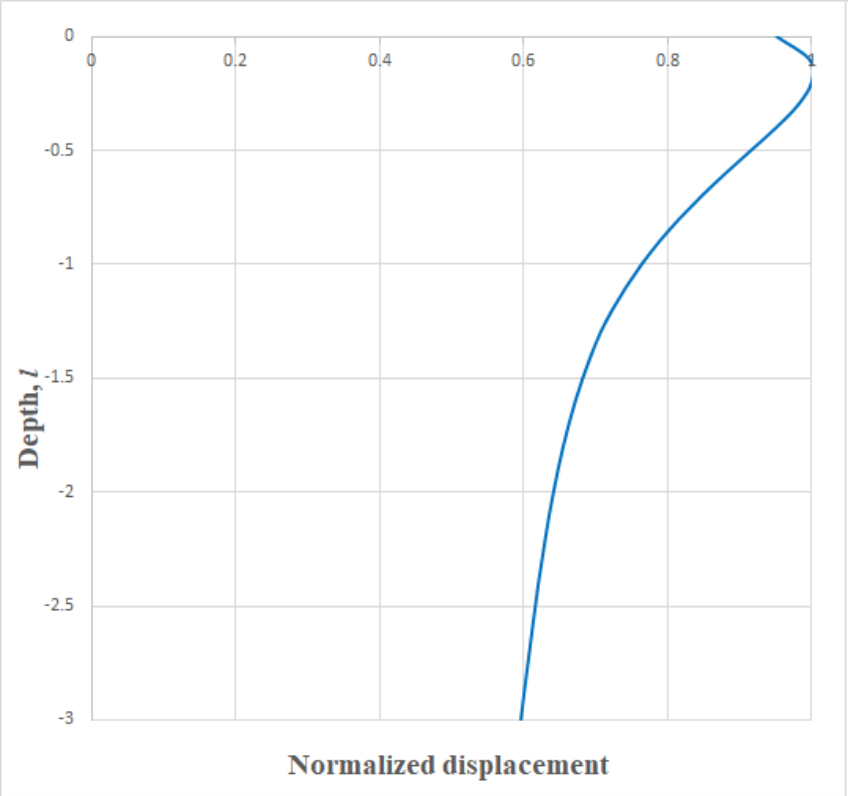

Figure 6.20: Cohesive soil, $\gamma = 2 * 10^{-3}$. Envelopes of normalized amplitude of displacement at different depths l. (Amplitude of displacement is normalized in relation to its maximum value)

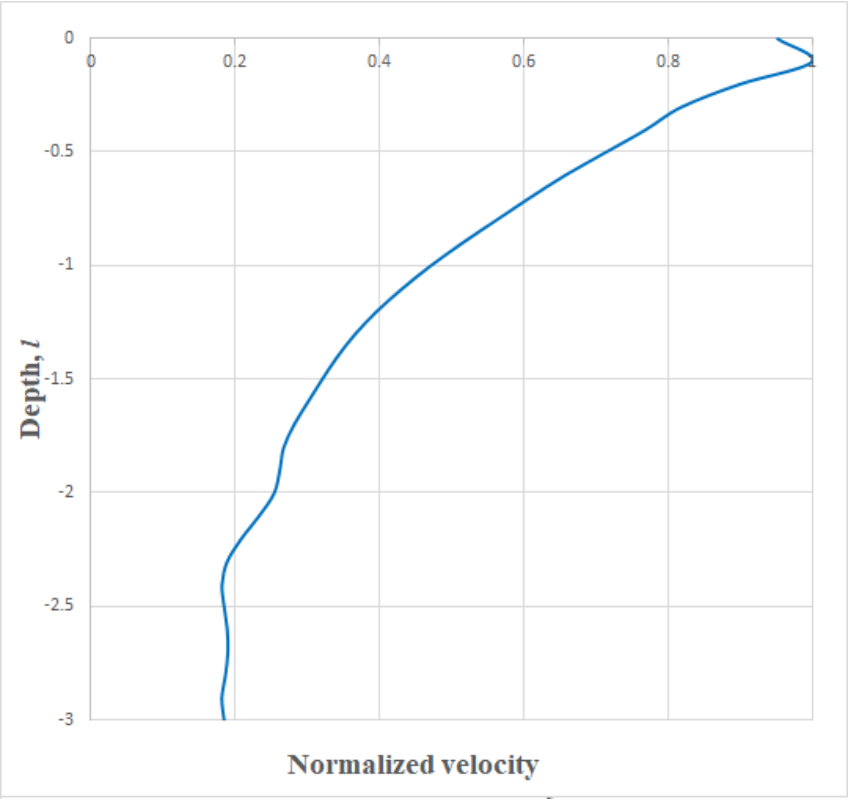

Figure 6.21: Cohesive soil, $\gamma = 2 * 10^{-3}$. Envelopes of normalized amplitude of velocities at different depths l. (Amplitude of velocities is normalized in relation to its maximum value)

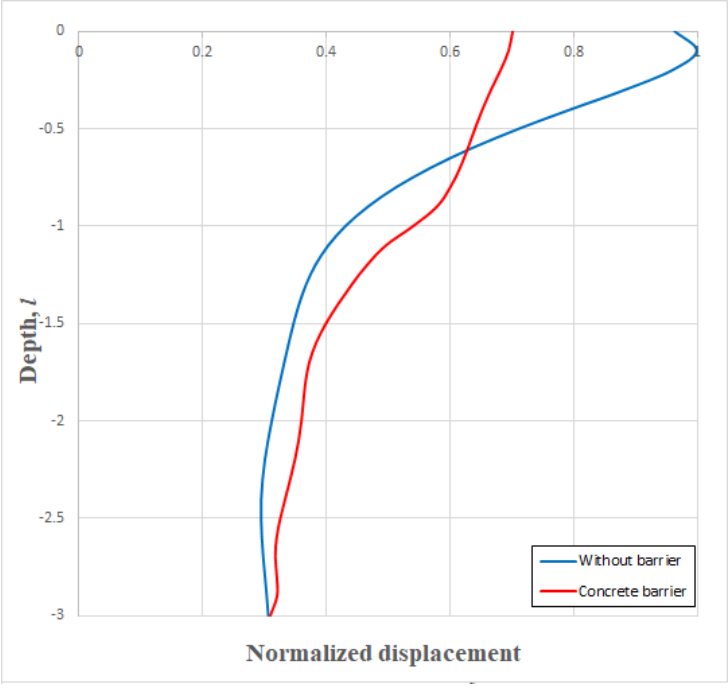

Figure 6.22: Cohesionless soil, $\gamma = 10^{-5}$. Envelopes of normalized amplitude of displacement at different depths l. (Amplitude of displacement is normalized in relation to its maximum value)

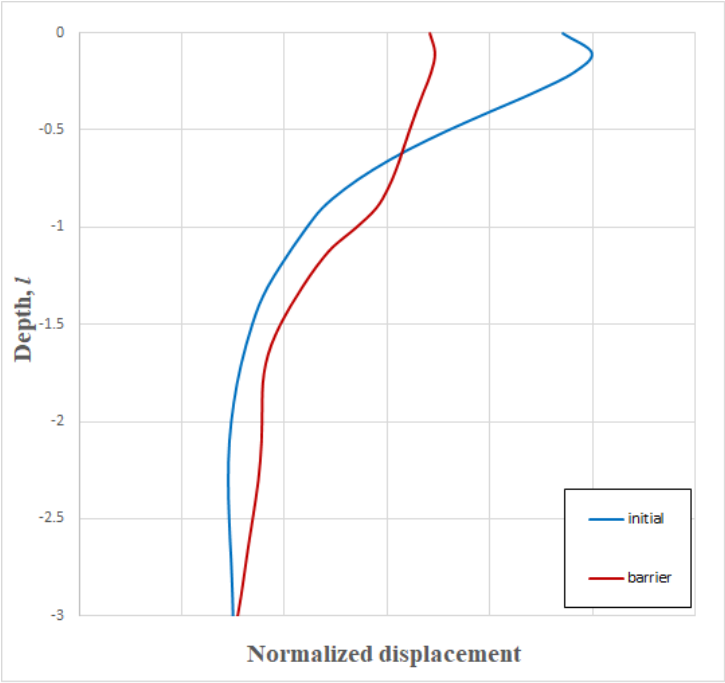

Figure 6.23: Cohesive soil, $\gamma = 10^{-5}$. Envelopes of normalized amplitude of displacement at different depths l. (Amplitude of displacement is normalized in relation to its maximum value)

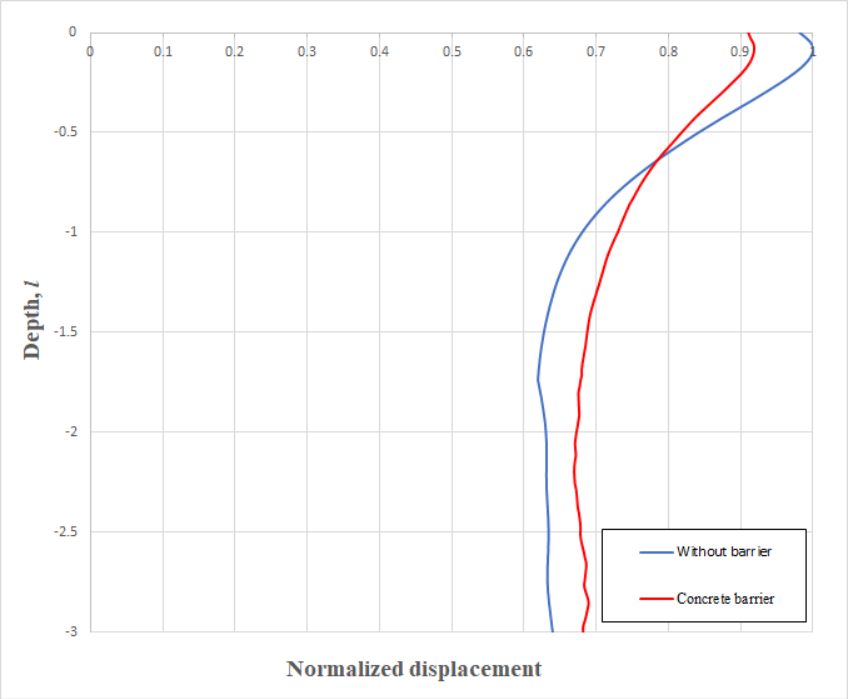

Figure 6.24: Cohesionless soil, $\gamma = 5{*}10^{-4}$. Envelopes of normalized amplitude of displacement at different depths l before and after barrier installation. (Amplitude of displacement is normalized in relation to its maximum value)

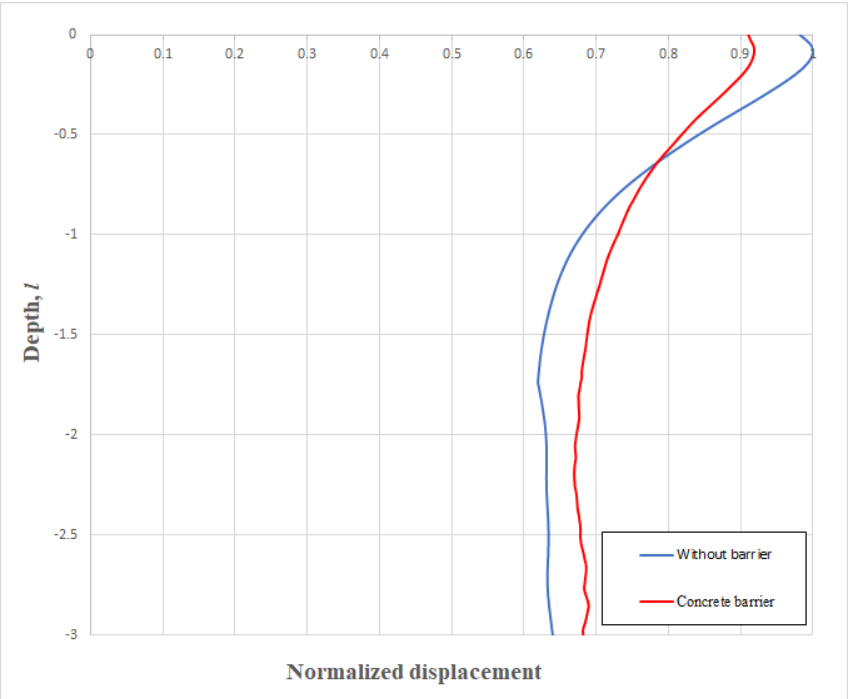

Figure 6.25: Cohesive soil, $\gamma = 2 * 10^{-3}$. Envelopes of normalized amplitude of displacement at different depths l before and after barrier installation. (Amplitude of displacement is normalized in relation to its maximum value)

Figures 6.26 and 6.27 represent the envelops of displacement amplitude versus distance from the barrier at high shear strain levels equalling to $\gamma = 5{*}10^{-4}$ and $\gamma = 2{*}10^{-3}$ for the cohesionless and cohesive soils respectively before and after barrier installation. These figures are plotted for the soils with mechanical parameters defined in table 6.1 and the loading frequency equalling $2Hz$. During the considered time interval four Rayleigh waves pass through the observation zone.

According to the character of the curves, the amplitude of displacement in the protected zone change insignificantly with the distance from the barrier. This is caused by the type of the considered models (plane strain) and allow showing vibration decrease by the graphs for the amplitude of displacements at any point in the protected zone ($x \in [0.1l, l]$, where x is the distance from the barrier or the pile field).

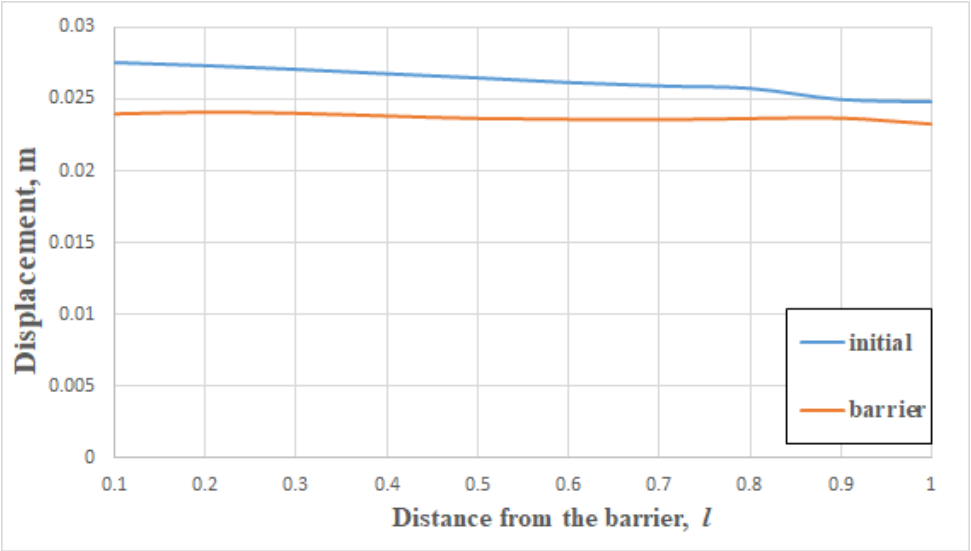

Figure 6.26: Cohesionless soil, $\gamma = 5 * 10^{-4}$. Envelopes of amplitude of displacement at different distance from the barrier l.

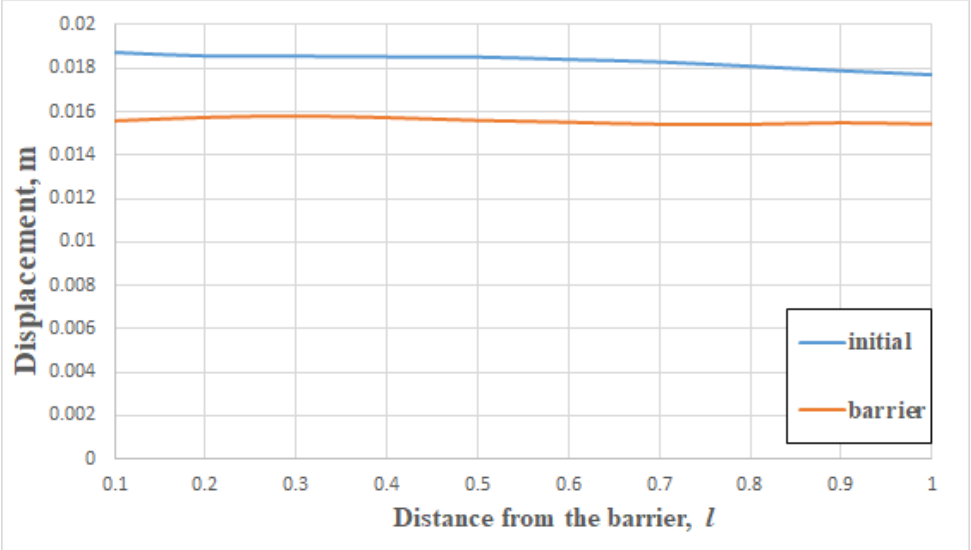

Figure 6.27: Cohesive soil, $\gamma = 2 * 10^{-3}$. Envelopes of amplitude of displacement at different distance from the barrier l.

Vertical seismic barriers

Cohesionless soil

The calculations is carried out for the following range of shear deformations: $\gamma = 10^{-6} \div 10^{-3}$. It is worth noting that at shear strains less than $\gamma = 10^{-5}$ the results are equal to the ones obtained under elastic conditions. The results presented for shear strains $\gamma = 10^{-5} \div 10^{-4}$ to show a decrease in the barrier reduction effect.

Figures 6.29 –6.30 show the amplitude of displacements at a distance $l/2$ from the barrier before and after its installation . The curves in these figures are plotted at $\frac{h}{l} = 1.0; \frac{d}{l} = 0.09$ and $\omega = 12.56 rad/sec$.(l- Rayleigh wavelength, h, d - barrier height and width respectively).

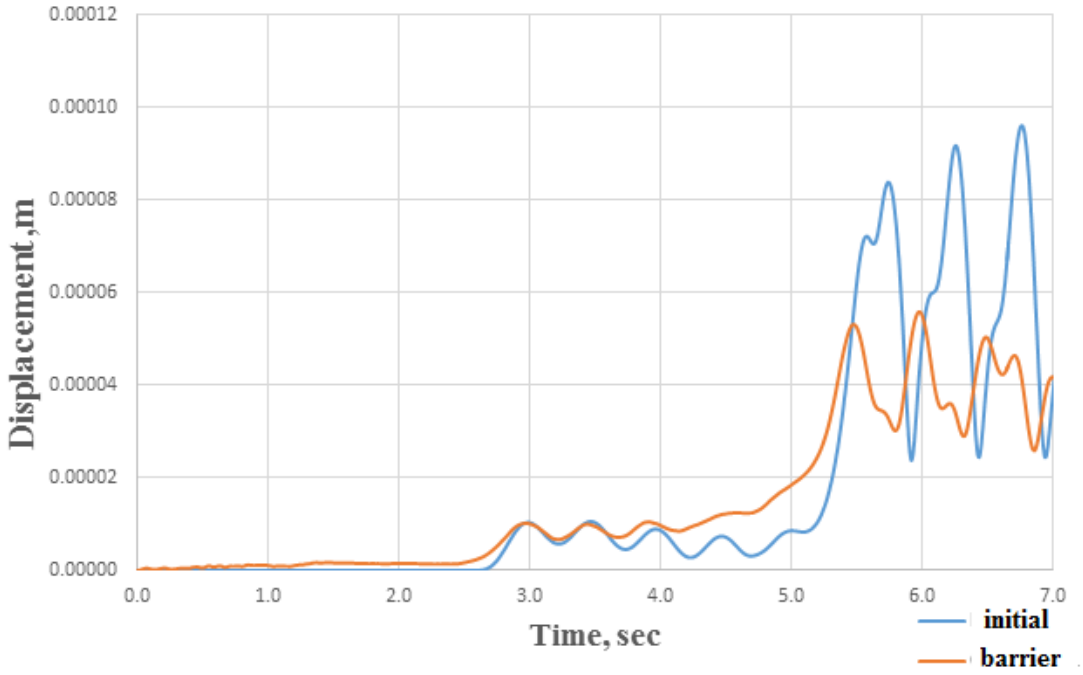

Figure 6.28: The amplitude of displacements at the distance $l/2$ from the barrier before and after its installation ($\frac{h}{l} = 1.0, \frac{d}{l} = 0.09, \omega = 12.56 rad/sec, \gamma = 10^{-5}$).

The obtained results reveal that the effectiveness of the vertical seismic barrier decreases at high levels of shear strains and for the barrier depths comparable with the wavelength of the surface wave, the loss of barrier efficiency occurs at low shear strains 10^{-4}. In this case, for weaker loose soils (with small values of the internal friction angle), the loss of seismic barrier efficiency occurs earlier. The width of the barrier practically does not affect the limit strain after which the barrier efficiency diminishes significantly, while the increase in the barrier height increases the value of the critical strain.

At the same time, another effect concerning $k_{red,E}$ is observed. While the value of $k_{red,u}$ increases with the increase in shear strain level, the value of $k_{red,E}$ remains virtually the same up to the shear strain value of 0.0005, then it moderately increases almost up to 0.8 at shear strain equalling to 0.005. Which means that the barrier still provides vibration reduction effect on the velocities and accelerations while the amplitudes of displacements are not affected by the barrier up to the value of the shear strain equalling to 0.0005 for the considered sand and $h/l = 1$, but then, the reduction effect decreases even for the kinetic energy. It can be explained by the transition of the subsurface region into the plastic state (the formation of plastic zone in the barrier vicinity) and the extension of the surface wave propagation zone deeper than in case of pure elasticity because of the limitations on shear strains given by Mohr-Coulomb yield surface.

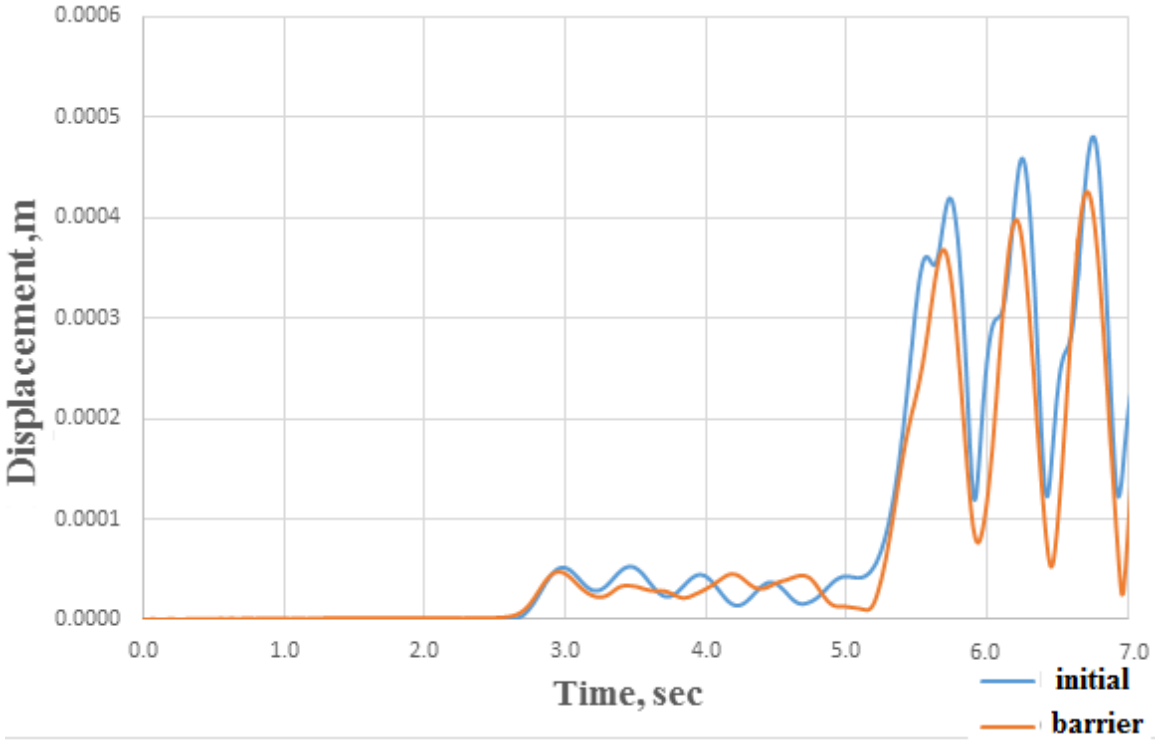

Figure 6.29: The amplitude of displacements at the distance $l/2$ from the barrier before and after its installation ($\frac{h}{l} = 1.0, \frac{d}{l} = 0.09, \omega = 12.56 rad/sec, \gamma = 5 * 10^{-5}$).

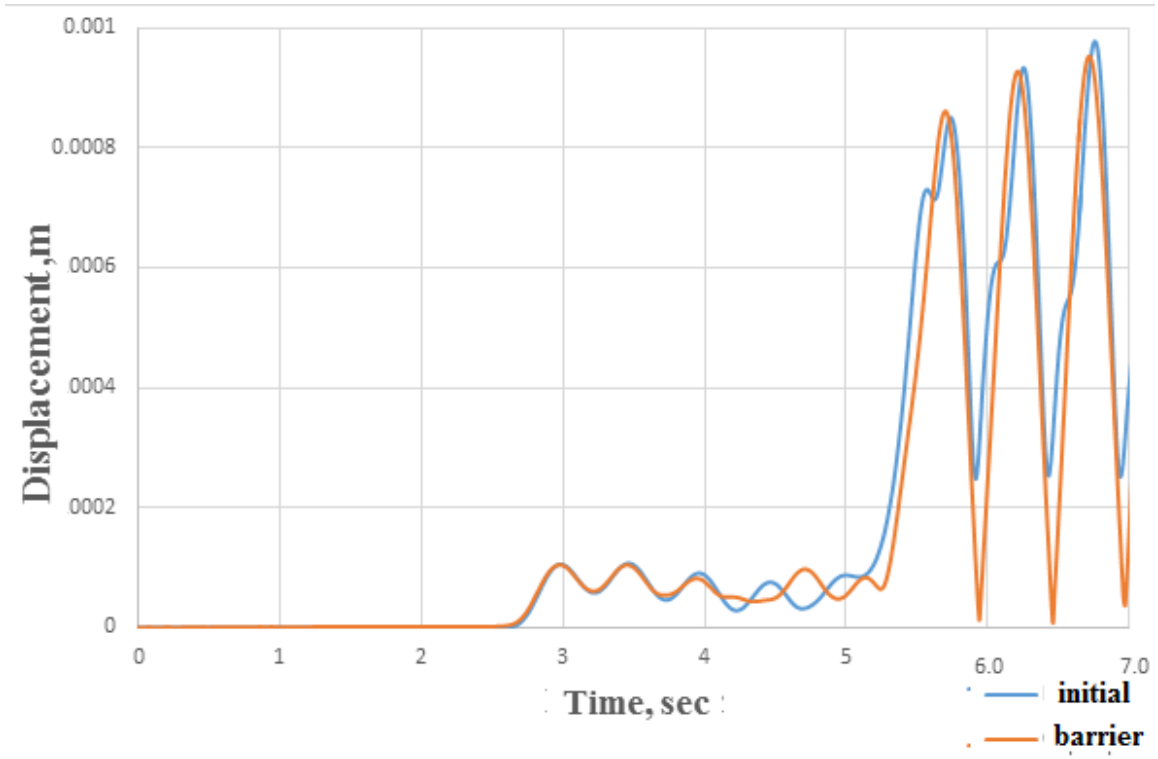

Figure 6.30: The amplitude of displacements at the distance $l/2$ from the barrier before and after its installation ($\frac{h}{l} = 1.0, \frac{d}{l} = 0.09, \omega = 12.56 rad/sec, \gamma = 1 * 10^{-4}$).

Cohesive soil

The calculations are performed for shear strain range $\gamma = 10^{-6} \div 10^{-3}$. At shear strains less than $\gamma = 5 * 10^{-5}$ the results are similar to the ones obtained under the assumption of linear elastic soil and barrier deformation behaviour. The results presented for shear strains $\gamma = 10^{-4} \div 10^{-3}$ to show a decrease in the barrier reduction effect.

Figures

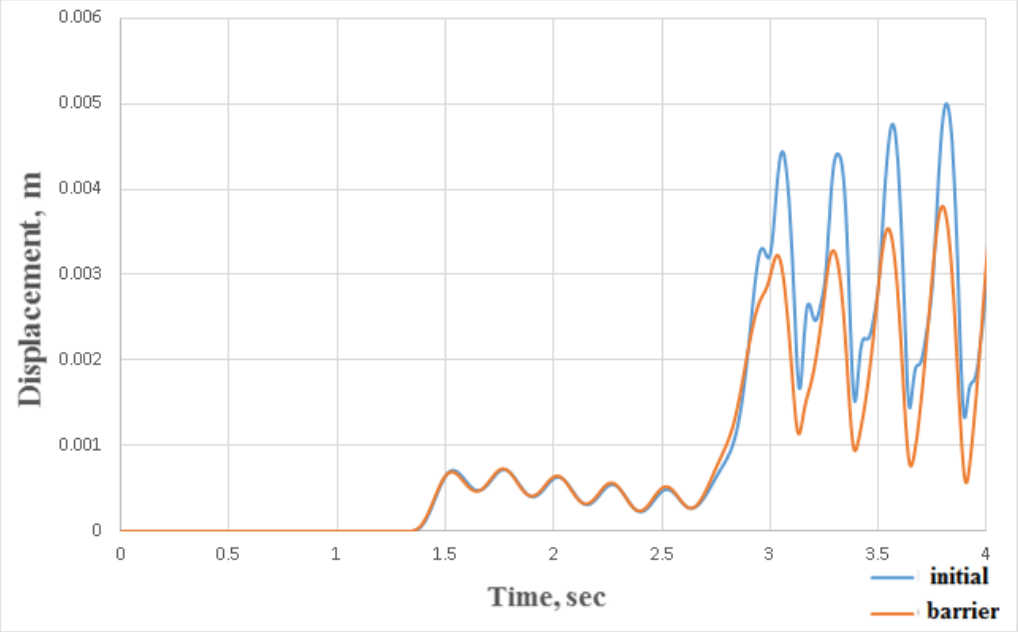

Figure 6.31: The amplitude of displacements at the distance $l/2$ from the barrier before and after its installation ($\frac{h}{l} = 1.0, \frac{d}{l} = 0.09, \omega = 25.12 rad/sec, \gamma = 4 * 10^{-4}$).

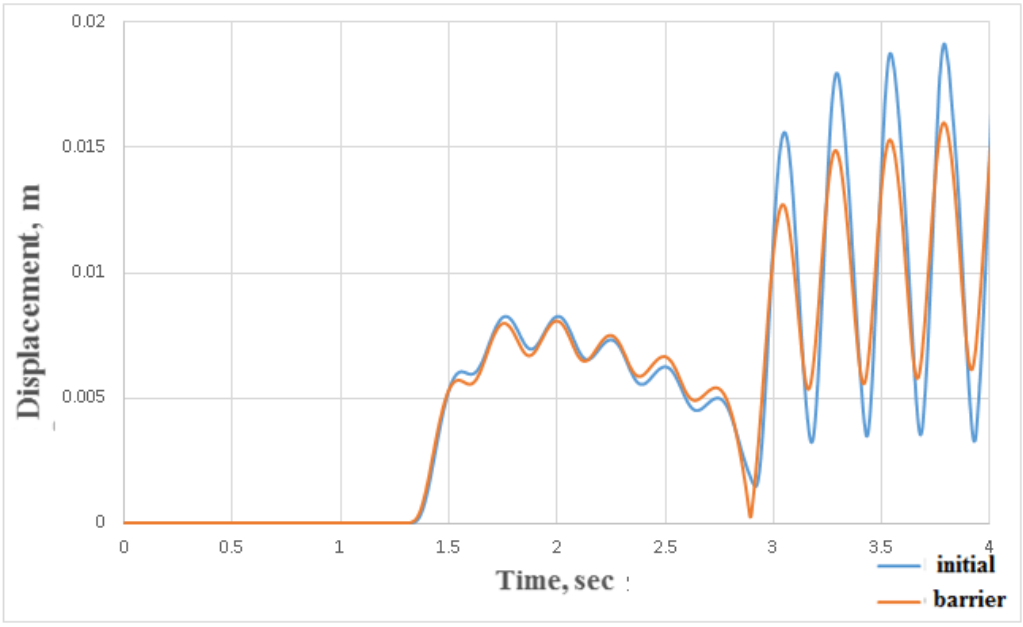

Figure 6.32: The amplitude of displacements at the distance $l/2$ from the barrier before and after its installation ($\frac{h}{l} = 1.0, \frac{d}{l} = 0.09, \omega = 25.12 rad/sec, \gamma = 2 * 10^{-3}$).

The obtained results reveal that the effectiveness of vertical seismic barriers decreases at high values of shear strain in the soil. However, for cohesive soils the negative effect can be observed at higher shear strains than for cohesionless ones. Barrier reduction effect upon the kinetic energy in this case shows the same trend as for the cohesionless soils significantly decreasing after shear strain in the soil exceeding $\gamma = 0.001$, which is higher than that of the cohesionless soils.

In sum, for each particular soil conditions the calculations determining the level of shear strains within which the barrier remains effective should be performed. This is essential for high amplitude vibrations like earthquakes and explosions. At the same time, seismic barriers are less effective for cohesionless soils at high shear strains as the plastic zone due to the process of barrier - Rayleigh wave interaction occurs at lower shear strains.

As the barrier demonstrates similar qualitative effect for cohesive and cohesionless soil and according to the results of [67] as well as rough calculations performed in the present analysis, pile field behaviour is similar to the behaviour of a vertical seismic barrier. Therefore, in the following paragraph the results of pile field interaction with surface Rayleigh waves is shown only for cohesionless soil.

Pile fields

The calculation of the initial stress field is performed similarly to the case of the vertical seismic barriers considered in the previous paragraph. Numerical simulation of the pile field interaction with Rayleigh waves is carried out at the following values of shear strains $\gamma = 10^{-6} \div 10^{-3}$ induced during wave propagation. As it will be shown in the following part, the single row pile field behaves similarly to the vertical seismic barrier with the sharp decrease of reduction effect at a some critical value of the shear strain.

Figures 6.33 - 6.36 show the amplitudes of displacements at the point located at the distance $l/2$ from the pile field before and after its installation as well as the kinetic energy of the subsurfcace layer in the protected zone. The curves in the figures 6.33 - 6.36 are plotted at $\frac{h}{l} = 1.0$; $\frac{d}{l} = 0.06\alpha = 0.16$ and $\omega = 12.56 rad/sec.$(l- Rayleigh wavelength, h, d - pile length and diameter respectively).

The obtained results reveal that the single row pile field demonstrates the same trend as the seismic barrier if the shear strain in the soil increases (figure 6.33). After a certain value of shear strain in the soil (this value depends on the soil mechanical properties) the effect of pile field installation upon vibration displacements diminishes (figure 6.33). In that case, the pile field gives virtually no effect on vibration displacements at $\gamma = 0.00004$. On the other hand, kinetic energy is still reduced (figure 6.34).

The range of shear strain within which the pile field still provides displacement reduction can be expanded by installation of additional pile rows (Figure 6.35). According to the figure 6.35, 5 row pile field becomes ineffective in terms of vibration reduction at $\gamma = 0.0007$ while kinetic energy is still reduced. Further increase in shear strains in the soil decreases the reduction effect upon the kinetic energy in the protected zone.

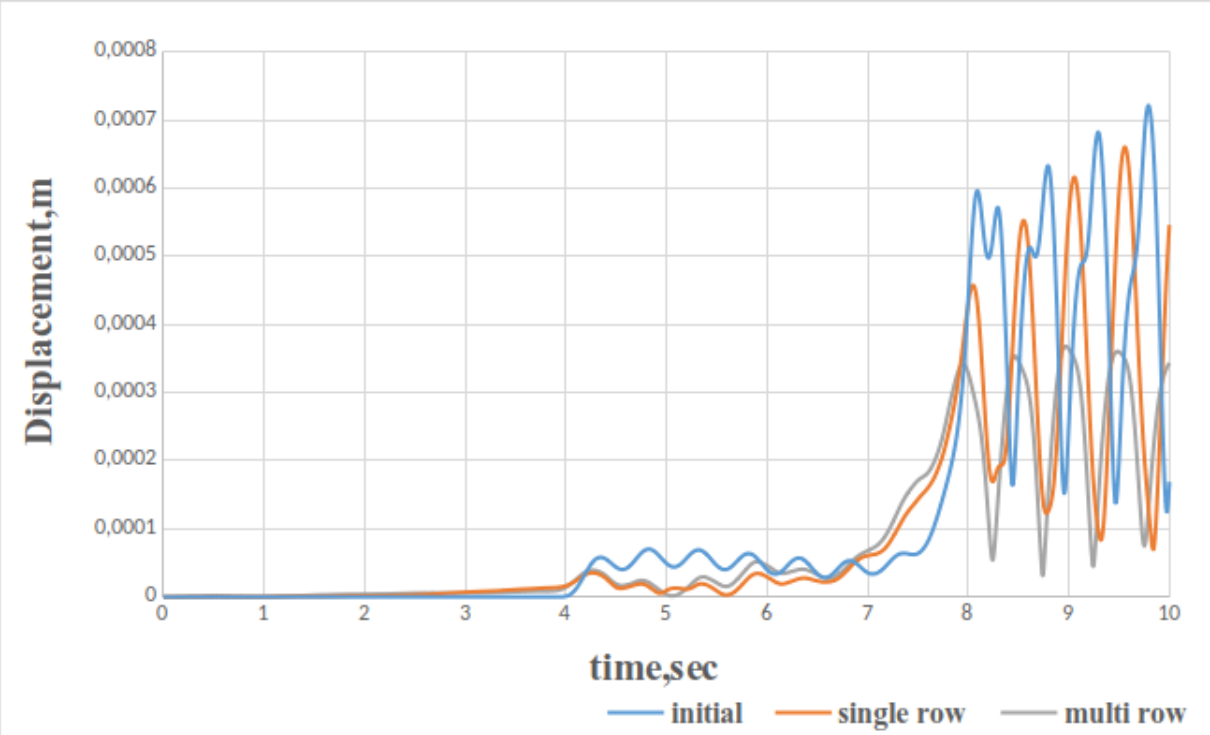

Figure 6.33: The amplitude of displacements at the distance $l/2$ from the pile row before its installation and after installation of single or 5 row pile fields ($\frac{h}{l} = 1.0; \frac{d}{l} = 0.06$ and $\omega = 12.56 rad/sec$, $\gamma = 4 * 10^{-5}$).

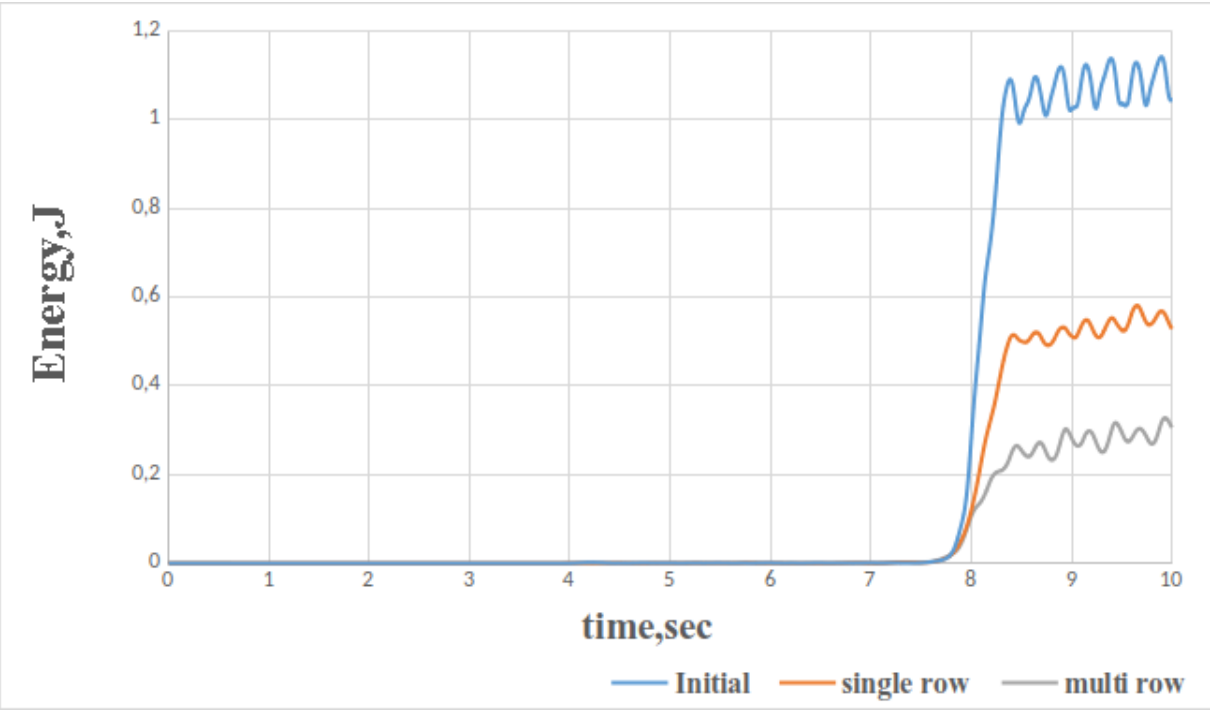

Figure 6.34: The variation of the kinetic energy of the surface layer in the protected zone without pile field and after installation of the single or 5 row pile fields($\frac{h}{l} = 1.0; \frac{d}{l} = 0.06$ and $\omega = 12.56 rad/sec$, $\gamma = 4 * 10^{-5}$).

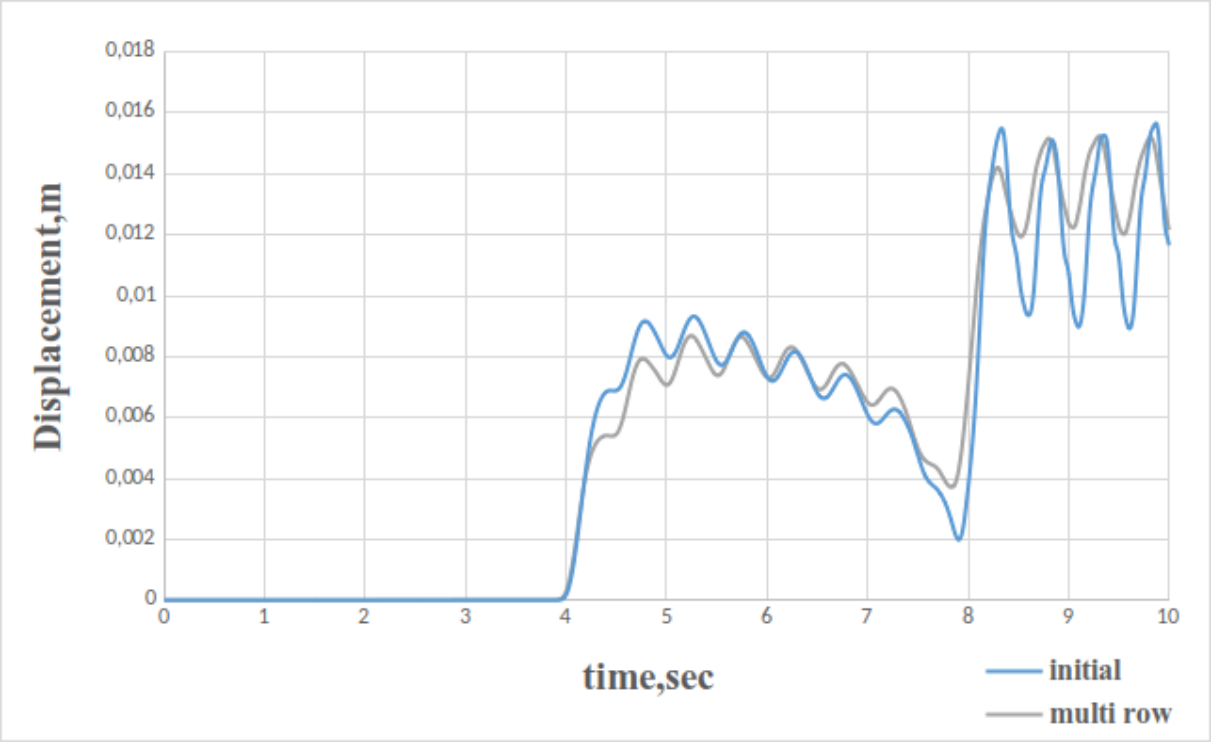

Figure 6.35: The amplitude of displacements at the distance $l/2$ from the piles without the pile field and after installation of the 5 row pile field ($\frac{h}{l} = 1.0; \frac{d}{l} = 0.06$ and $\omega = 12.56 rad/sec$, $\gamma = 7 * 10^{-4}$).

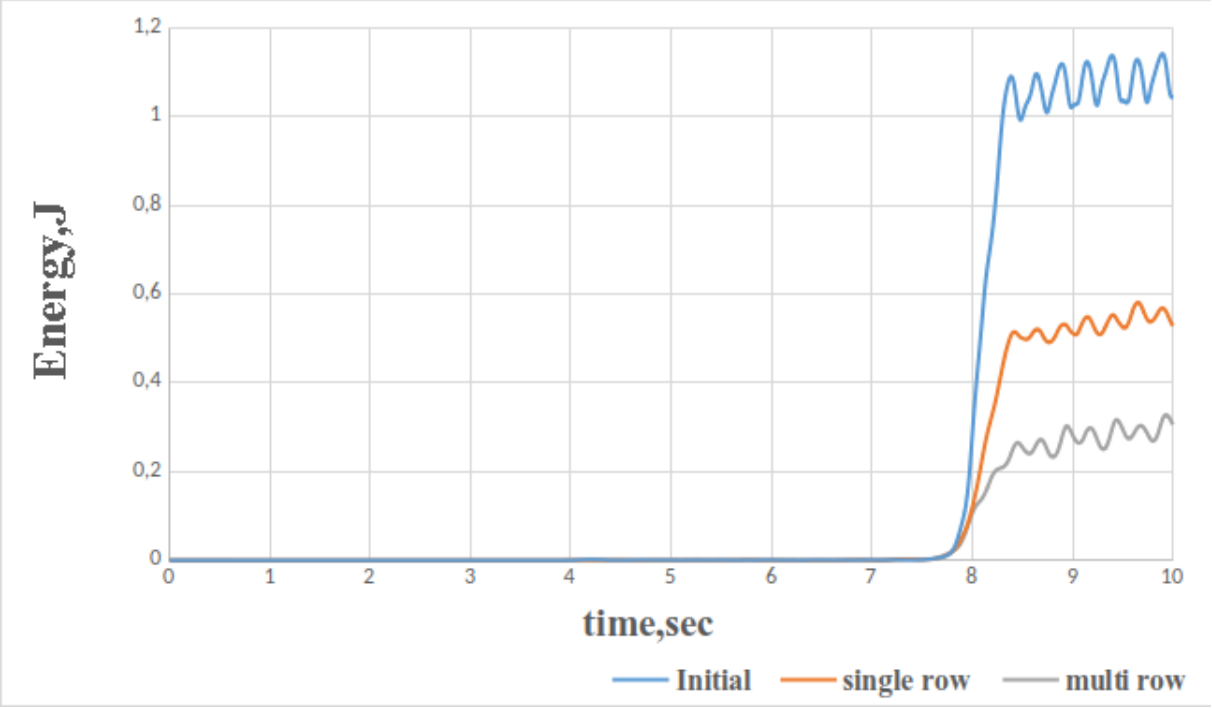

Figure 6.36: The variation of kinetic energy of the surface layer in the protected zone without pile field and in the case of the 5 row pile field ($\frac{h}{l} = 1.0; \frac{d}{l} = 0.06$ and $\omega = 12.56 rad/sec$, $\gamma = 7 * 10^{-4}$).

Conclusions.

In sum, plastic character of soil behaviour significantly affects vibration reduction effect of the both vertical seismic barrier and pile field significantly at high shear strain level ($\gamma \geq 10^{-4}$). Such level of shear strain relates to earthquakes and explosions. On the other hand, in the case of low shear strains in the soil ($\gamma \leq 10^{-4}$) during wave propagation, the calculations within the elastic framework are sufficient.

Therefore, in the case of vibrations affecting comfort in residential and industrial buildings it is possible to follow the recommendations in the chapters 4 and 5 or to adopt the optimization method implemented in the finite difference form. Both of these ways are based on the assumptions that soil and barrier materials deform according to the linearly elastic constitutive law.

The formation of plastic zones at high shear strains in soil leads to the decrease in displacement reduction effect given by a barrier or a pile field. For cohesionless soils this effect occurs at lower shear strains as the subsurface zone starts yielding at lower shear stresses than in the case of cohesion soils. At the same time, these barriers still reduce kinetic energy in the protected zone even at high values of shear strains in the soil during wave propagation. However, this effect tends to decrease at high values of shear strains ($\gamma \geq 5 * 10^{-4}$) depending on soil. This can be explained by the limitation on the stress in soil given by yield surface, while the deformations and displacements are not limited. Therefore, the formation of plastic zone in the barrier region leads to the transmission of the vibration energy to the deeper layers.

The range of shear strains within which a barrier remains effective can be expanded by increase of the barrier depth. The same effect for a pile field can be achieved by installation of additional rows.

One important remark is that the results are obtained using simplified model of the source, hence, the character of energy distribution among various types of waves will differ from that can take place in the case of an earthquake or underground explosion. At the same time, the results allow to estimate how a barrier or pile field interacts with Rayleigh waves at various shear strains, while, the effect of body wave interaction with these barrier will require more realistic vibration source.

CHAPTER 7

CONCLUSION AND PERSPECTIVES

Conclusion

The thesis is primarily concerned with numerical simulation of Rayleigh wave interaction with vertical seismic barriers and pile fields. Planar and spatial models are used to analyse the possibility to protect the territories from surface Rayleigh waves of various intensity and generated by different vibration sources. The thesis object is achieved by fulfilling the following objectives:

- review and comparative study of plasticity models, that are used in soil mechanics, along with their parameters that was resulted in the selection of Mohr-Coulomb model as the most appropriate in terms of the existing experimental database for various soils as well as its applicability to model soil hysteresis behaviour and the degradation of the shear modulus with the increase in shear strains;
- verification of the FE models as well as the analysis of numerical parameters influence on the displacement and energy fields along with non-physical effects to exclude it from the final results and decrease the final numerical error;
- formulation of the principal dimensionless complex that determines the final barrier reduction effect in case of linear elastic behaviour of barrier material and soil, followed by parametric analysis of vertical seismic barrier in terms of vibration reduction;
- formulation of multi parametric optimization problem related to the practical barrier design for particular soil conditions and design frequency accounting for possible prescribed restrictions on the material volume or vibration reduction level;
- use of the constrained method [20] and the Karush-Kunn-Tucker condition [114] formulating it in the finite difference form to obtain the optimality criteria allowing to solve the optimization problem;
- formulation of the principal dimensionless complex that determines the final pile field reduction effect within the framework of linear elastic constitutive law and the parametric analysis of vertical seismic barrier in terms of vibration reduction;
- numerical simulation of Rayleigh wave interaction with vertical seismic barriers as well as pile fields using the chosen plasticity model to analyse the influence of shear strain level upon the vibration reduction effect.

The obtained results confirm the applicability of vertical seismic barriers as well as pile fields for protection of territories from surface Rayleigh waves in the case of low amplitude vibrations

(shear strains in the soil do not exceed 10^{-5}), such as transport vehicles, construction activities and operating equipment. In that case, vertical seismic barriers are more effective than the pile fields allowing to obtain $5-6$ times kinetic energy decrease in the protected zone or to decrease vibration displacements by $2-2.5$ times. Meanwhile, pile fields can produce 50% kinetic energy decrease in the protected zone.

On the other hand, the results of numerical computations performed within the framework of linear elastic constitutve law are valid for low amplitude vibrations when plastic soil properties can be neglected and vibration energy dissipation can be described by using viscous models. This is also the limitation upon the optimization criteria considered in the work. The reason behind this is that the reduction effect of a vertical seismic barrier or a pile field tends to decrease with the increase in shear strain level in case of high amplitude vibrations (shear strains in the soil equal to $10^{-4} \div 10^{-2}$) which is the case for earthquakes and explosions. This effect is more significant for cohesionless soils rather than for cohesive ones. At the same time, the possible shear strain range within which the barrier or pile field reduces vibrations can be extended by an increasing barrier (pile) length or by installing additional rows in the case of pile fields.

Therefore, for each particular soil conditions and vibration sources it must be estimated whether this way of protection is appropriate or not. For low amplitude vibration the appropriate barrier configuration can be obtained from the graphs or optimization procedure presented in chapter 4. For high amplitude vibration sources the optimization procedure must be supplemented by the calculations accounting for plastic behaviour of soils which may correct the final geometry.

In general, these approaches towards vibration protection demonstrate good performance for high frequency and low amplitude vibration sources as well as for protection from Rayleigh waves propagating in soft soils due to earthquakes and blasts at moderate shear strain level $10^{-5} \div 10^{-4}$ depending on the depth (pile length in case of a pile field) - wavelength ratio.

Future Works

Barrier type

This work does not investigate the effect of non-linear behaviour of the barrier or pile field material which can significantly affect the final reduction effect. It is presented in [69] where the authors demonstrated a significant reduction of the barrier made of meta materials or in [63] where composite wave barriers are studied. Hence, two possible directions can be underlined: (1)analysis of a composite barrier as well as (2)analysis of the barrier made of meta materials or materials demonstrating high dissipation properties.

Mechanical models improvement

Numerical simulation involving Biot's theory of poroelasticity [17, 18] can be an additional perspective of the present work . This will allow accounting for the energy dissipative mechanism in soils at different frequency ranges more accurately. This is important as the viscous properties dominate over the plastic ones of the soil skeleton at high pore fluid flow velocities in the channels which corresponds to high frequencies. Meanwhile, for lower frequencies it is sufficient to use plastic models of soil. Therefore, it is important to separate this frequency ranges and specify the difference for the reduction effect. At the same time, the use of Rayleigh damping to account for dissipative soil behaviour at low shear strain level is not sufficient enough and the indifference of vibration reduction effect towards damping ratio can be obtained.

Plastic behaviour of the soil skeleton can be approximated more precisely by using hypoplasticity models [97, 107]. However, they have to be modified to solve the coupled system of equations for Biot's porous media and the database for these models needs to be extended by

additional experiments. Moreover, the analysis seems to be to complicated because of the number of the parameters in the models. Otherwise, it is possible to modify Hardening soil small-strain model [14] (which is appropriate for the simulation of dynamic soil behaviour) with the dependencies obtained in [61] thus reducing the number of parameters making it appropriate for the analysis.

As a result, the shear strain range within which the considered vibration barriers demonstrate reduction effect can be refined and generalized to the form of the functional dependencies on the soil parameters. That will allow to formulate the recommendations for practical civil engineering avoiding complicated dynamic computations for each particular case.

BIBLIOGRAPHY

[1] A. Abaqus. Standard user manual, abaqus. *Inc., USA*, 2016.

[2] J. Aboudi. The motion excited by an impulsive source in an elastic half-space with a surface obstacle. *Bulletin of the Seismological Society of America*, 61(3):747–763, 1971.

[3] J. Aboudi. Elastic waves in half-space with thin barrier. *Journal of the Engineering Mechanics Division*, 99(1):69–83, 1973.

[4] A. Alzawi and M. H. El Naggar. Full scale experimental study on vibration scattering using open and in-filled (geofoam) wave barriers. *Soil Dynamics and Earthquake Engineering*, 31(3):306–317, 2011.

[5] L. Andersen and S. R. Nielsen. Reduction of ground vibration by means of barriers or soil improvement along a railway track. *Soil Dynamics and Earthquake Engineering*, 25(7-10):701–716, 2005.

[6] Y. Angel and J. Achenbach. Reflection and transmission of obliquely incident rayleigh waves by a surface-breaking crack. *The Journal of the Acoustical Society of America*, 75(2):313–319, 1984.

[7] Australian and N. Z. E. Council. The technical basis for guidelines to minimize annoyance due to blasting overpressure and ground vibration, 1990.

[8] J. Avilés and F. J. Sánchez-Sesma. Piles as barriers for elastic waves. *Journal of Geotechnical Engineering*, 109(9):1133–1146, 1983.

[9] J. Avilés and F. J. Sánchez-Sesma. Foundation isolation from vibrations using piles as barriers. *Journal of Engineering Mechanics*, 114(11):1854–1870, 1988.

[10] P. Banerjee, S. Ahmad, and K. Chen. Advanced application of bem to wave barriers in multi-layered three-dimensional soil media. *Earthquake engineering & structural dynamics*, 16(7):1041–1060, 1988.

[11] D. D. Barkan. Dynamics of bases and foundations. 1960.

[12] D. Barnett and J. Lothe. Consideration of the existence of surface wave (rayleigh wave) solutions in anisotropic elastic crystals. *Journal of physics F: Metal physics*, 4(5):671, 1974.

[13] D. Barnett and J. Lothe. An image force theorem for dislocations in anisotropic bicrystals. *Journal of Physics F: metal physics*, 4(10):1618, 1974.

[14] T. Benz. *Small-strain stiffness of soils and its numerical consequences*, volume 5. Univ. Stuttgart, Inst. f. Geotechnik Stuttgart, 2007.

[15] J.-P. Berenger. A perfectly matched layer for the absorption of electromagnetic waves. *Journal of computational physics*, 114(2):185–200, 1994.

[16] D. Beskos, B. Dasgupta, and I. Vardoulakis. Vibration isolation using open or filled trenches. *Computational mechanics*, 1(1):43–63, 1986.

[17] M. A. Biot. Theory of propagation of elastic waves in a fluid-saturated porous solid. ii. higher frequency range. *The Journal of the acoustical Society of america*, 28(2):179–191, 1956.

[18] M. A. Biot. Theory of propagation of elastic waves in a fluid-saturated porous solid. ii. higher frequency range. *The Journal of the acoustical Society of america*, 28(2):179–191, 1956.

[19] R. I. Borja. *Plasticity: modeling & computation*. Springer Science & Business Media, 2013.

[20] S. Boyd and L. Vandenberghe. *Convex optimization*. Cambridge university press, 2004.

[21] S. Brule, S. Enoch, and S. Guenneau. Flat lens for seismic waves. *arXiv preprint arXiv:1602.04492*, 2016.

[22] S. Brûlé, S. Enoch, and S. Guenneau. Sols structurés sous sollicitation dynamique: des métamatériaux en géotechnique. *Revue Française de Géotechnique*, (151):4, 2017.

[23] S. Brûlé, E. Javelaud, S. Enoch, and S. Guenneau. Experiments on seismic metamaterials: molding surface waves. *Physical review letters*, 112(13):133901, 2014.

[24] R. Buildings. Standarts in civil engineering. *Law(Zakon)*, 19:91, 1996.

[25] P. Cacciola and A. Tombari. Vibrating barrier: a novel device for the passive control of structures under ground motion. *Proceedings of the Royal Society A: Mathematical, Physical and Engineering Sciences*, 471(2179):20150075, 2015.

[26] Y.-Q. Cai, G.-Y. Ding, and C.-J. Xu. Amplitude reduction of elastic waves by a row of piles in poroelastic soil. *Computers and Geotechnics*, 36(3):463–473, 2009.

[27] Y.-Q. Cai, G.-Y. Ding, C.-J. Xu, and J. Wang. Vertical amplitude reduction of rayleigh waves by a row of piles in a poroelastic half-space. *International Journal for Numerical and Analytical Methods in Geomechanics*, 33(16):1799–1821, 2009.

[28] E. Çelebi, S. Fırat, G. Beyhan, İ. Çankaya, İ. Vural, and O. Kırtel. Field experiments on wave propagation and vibration isolation by using wave barriers. *Soil Dynamics and Earthquake Engineering*, 29(5):824–833, 2009.

[29] P. Chadwick and D. Jarvis. Surface waves in a pre-stressed elastic body. *Proc. R. Soc. Lond. A*, 366(1727):517–536, 1979.

[30] P. Chadwick and G. Smith. Foundations of the theory of surface waves in anisotropic elastic materials. In *Advances in applied mechanics*, volume 17, pages 303–376. Elsevier, 1977.

[31] P. Chadwick and T. Ting. On the structure and invariance of the barnett-lothe tensors. *Quarterly of Applied Mathematics*, 45(3):419–427, 1987.

[32] W.-F. Chen and D.-J. Han. *Plasticity for structural engineers*. J. Ross publishing, 2007.

[33] D. Connolly, A. Giannopoulos, W. Fan, P. Woodward, and M. Forde. Optimising low acoustic impedance back-fill material wave barrier dimensions to shield structures from ground borne high speed rail vibrations. *Construction and Building Materials*, 44:557–564, 2013.

[34] P. Coulier, V. Cuéllar, G. Degrande, and G. Lombaert. Experimental and numerical evaluation of the effectiveness of a stiff wave barrier in the soil. *Soil Dynamics and Earthquake Engineering*, 77:238–253, 2015.

[35] R. Courant, K. Friedrichs, and H. Lewy. Über die partiellen differenzengleichungen der mathematischen physik. *Mathematische annalen*, 100(1):32–74, 1928.

[36] M. A. Crisfield, J. J. Remmers, C. V. Verhoosel, et al. *Nonlinear finite element analysis of solids and structures*. John Wiley & Sons, 2012.

[37] B. M. Das and Z. Luo. *Principles of soil dynamics*. Cengage Learning, 2016.

[38] B. Dasgupta, D. Beskos, and I. Vardoulakis. Vibration isolation using open or filled trenches part 2: 3-d homogeneous soil. *Computational Mechanics*, 6(2):129–142, 1990.

[39] DEC. Assessing vibration: A technical guideline, 2006.

[40] E. DIN. 1683: Bevorzugte bezugswerte für pegel in der akustik und schwingungstechnik (iso 1683: 2015). *Deutsche Fassung EN ISO*, 1683, 2015.

[41] I. Djeran-Maigre and S. V. Kuznetsov. A new principle for protection from seismic waves.

[42] H. Dolling. Schwingungsisolierung von bauwerken durch tiefe auf geeignete weise stabilisierte schiltze. *VDI-Berichte*, 88:3741, 1965.

[43] H.-J. Dolling. Abschirming von erschitterungen durch bodenschlitze. *Die Bautecnic*, 5:151–158, 1970.

[44] F. Dunne and N. Petrinic. *Introduction to computational plasticity*. Oxford University Press on Demand, 2005.

[45] S. D. Ekanayake, D. Liyanapathirana, and C. J. Leo. Attenuation of ground vibrations using in-filled wave barriers. *Soil Dynamics and Earthquake Engineering*, 67:290–300, 2014.

[46] B. Engquist and A. Majda. Absorbing boundary conditions for numerical simulation of waves. *Proceedings of the National Academy of Sciences*, 74(5):1765–1766, 1977.

[47] W. Ewing et al. Elastic waves in layered media,(1957), 328-363, 2.

[48] M. Fuyuki and Y. Matsumoto. Finite difference analysis of rayleigh wave scattering at a trench. *Bulletin of the Seismological Society of America*, 70(6):2051–2069, 1980.

[49] J. C. Gibbings. *Dimensional analysis*. Springer Science & Business Media, 2011.

[50] R. Goldshtein and S. Kuznetsov. Continuum models in dynamics of granular media. review. *International Journal for Computational Civil and Structural Engineering*, 10(3):82–104, 2014.

[51] R. Goldstein and J. Lewandowski. Surface roughness induced attenuation and changes in the propagation velocity of long rayleigh-type waves. *Acta mechanica*, 91(3-4):235–243, 1992.

[52] C. E. Hanson, J. C. Ross, D. A. Towers, M. Harris, et al. High-speed ground transportation noise and vibration impact assessment. Technical report, United States. Federal Railroad Administration. Office of Railroad Policy and Development, 2012.

[53] B. O. Hardin and V. P. Drnevich. Shear modulus and damping in soils: design equations and curves. *Journal of Soil Mechanics & Foundations Div*, 98(sm7), 1972.

[54] W. Haupt. Isolation of vibrations by concrete core walls. In *Proceedings of the ninth international conference on soil mechanics and foundation engineering*, volume 2, pages 251–256, 1977.

[55] R. Hill. *The mathematical theory of plasticity*, volume 11. Oxford university press, 1998.

[56] W. Hu, R. Song, Y. Wu, Y. Wu, and Z. Kang. Numerical analysis on vibration reduction of isolation trench along train tracks.

[57] J. Huang and Z. Shi. Application of periodic theory to rows of piles for horizontal vibration attenuation. *International Journal of Geomechanics*, 13(2):132–142, 2011.

[58] J. Huang and Z. Shi. Attenuation zones of periodic pile barriers and its application in vibration reduction for plane waves. *Journal of Sound and Vibration*, 332(19):4423–4439, 2013.

[59] J. Hudson. Scattered surface waves from a surface obstacle. *Geophysical Journal of the Royal Astronomical Society*, 13(4):441–458, 1967.

[60] J. Hudson and L. Knopoff. Transmission and reflection of surface waves at a corner: 2. rayleigh waves (theoretical). *Journal of Geophysical Research*, 69(2):281–289, 1964.

[61] I. Ishibashi and X. Zhang. Unified dynamic shear moduli and damping ratios of sand and clay. *Soils and Foundations*, 33(1):182–191, 1993.

[62] K. Ishihara. Soil behaviour in earthquake geotechnics. oxford engineering science series. 1996.

[63] E. N. Its and J. S. Lee. Screening of surface waves by composite wave barriers. In *Proceedings of the 10th World Conference on Earthquake Engineering*, pages 1987–1992, 1992.

[64] M. Jesmani, A. M. Fallahi, and H. F. Kashani. Effects of geometrical properties of rectangular trenches intended for passive isolation in sandy soils. *Earth Science Research*, 1(2):137, 2012.

[65] A. Karlström and A. Boström. Efficiency of trenches along railways for trains moving at sub-or supersonic speeds. *Soil Dynamics and Earthquake Engineering*, 27(7):625–641, 2007.

[66] S. Kattis, D. Polyzos, and D. Beskos. Structural vibration isolation by rows of piles. *WIT Transactions on The Built Environment*, 15, 1970.

[67] S. Kattis, D. Polyzos, and D. Beskos. Modelling of pile wave barriers by effective trenches and their screening effectiveness. *Soil Dynamics and Earthquake Engineering*, 18(1):1–10, 1999.

[68] S. Kattis, D. Polyzos, and D. Beskos. Vibration isolation by a row of piles using a 3-d frequency domain bem. *International Journal for Numerical Methods in Engineering*, 46(5):713–728, 1999.

[69] S.-H. Kim and M. P. Das. Artificial seismic shadow zone by acoustic metamaterials. *Modern Physics Letters B*, 27(20):1350140, 2013.

[70] L. Knopoff. Scattering of compression waves by spherical obstacles. *Geophysics*, 24(1):30–39, 1959.

[71] L. Knopoff. Scattering of shear waves by spherical obstacles. *Geophysics*, 24(2):209–219, 1959.

[72] S. L. Kramer. Geotechnical earthquake engineering. in prentice–hall international series in civil engineering and engineering mechanics. *Prentice-Hall, New Jersey*, 1996.

[73] A. Kravtsov, S. Kuznetsov, and S. Y. Sekerzh-Zen'kovich. Finite element models in lamb's problem. *Mechanics of solids*, 46(6):952–959, 2011.

[74] R. D. Krieg. *A simple constitutive description for cellular concrete*. Sandia National Laboratories Albuquerque, NM, 1972.

[75] V. N. Kukudzhanov. *Numerical continuum mechanics*, volume 15. Walter de Gruyter, 2012.

[76] S. Kuznetsov. Seismic waves and seismic barriers. *Acoustical Physics*, 57(3):420–426, 2011.

[77] S. Kuznetsov and E. Terentjeva. Planar internal lamb problem: Waves in the epicentral zone of a vertical power source. *Acoustical Physics*, 61(3):356–367, 2015.

[78] S. V. Kuznetsov. Subsonic lamb waves in anisotropic plates. *Quarterly of Applied Mathematics*, 60(3):577–587, 2002.

[79] S. V. Kuznetsov. Surface waves of non-rayleigh type. *Quarterly of Applied Mathematics*, 61(3):575–582, 2003.

[80] S. V. Kuznetsov and A. E. Nafasov. Horizontal acoustic barriers for protection from seismic waves. *Advances in Acoustics and Vibration*, 2011, 2011.

[81] H. Lamb. On the propagation of tremors over the surface of an elastic solid. *Proceedings of the Royal Society of London*, 72(477-486):128–130, 1904.

[82] H. Lamb. Xliv. on waves due to a travelling disturbance, with an application to waves in superposed fluids. *The London, Edinburgh, and Dublin Philosophical Magazine and Journal of Science*, 31(184):386–399, 1916.

[83] V. W. Lee. A note on the scattering of elastic plane waves by a hemispherical canyon. *International Journal of Soil Dynamics and Earthquake Engineering*, 1(3):122–129, 1982.

[84] G. Lefeuve-Mesgouez, A. Peplow, and D. Le Houédec. Surface vibration due to a sequence of high speed moving harmonic rectangular loads. *Soil Dynamics and Earthquake Engineering*, 22(6):459–473, 2002.

[85] K. Leung, D. Beskos, and I. Vardoulakis. Vibration isolation using open or filled trenches. *Computational Mechanics*, 7(2):137–148, 1990.

[86] J. Lewandowski. Propagation velocity and attenuation coefficient of rayleigh-type waves on rough solid surfaces. In *Physical Acoustics*, pages 461–465. Springer, 1991.

[87] S. Li, M. Brun, I. Djeran-Maigre, and K. Sergey. Numerical modelling of wave barrier in 2d unbounded medium using explicit/implicit multi-time step co-simulation. In *IOP Conference Series: Materials Science and Engineering*, volume 365, page 042062. IOP Publishing, 2018.

[88] X. Liu, Z. Shi, H. Xiang, and Y. Mo. Attenuation zones of periodic pile barriers with initial stress. *Soil Dynamics and Earthquake Engineering*, 77:381–390, 2015.

[89] G. Lombaert, G. Degrande, S. François, and D. Thompson. Ground-borne vibration due to railway traffic: a review of excitation mechanisms, prediction methods and mitigation measures. In *Noise and vibration mitigation for rail transportation systems*, pages 253–287. Springer, 2015.

[90] J. Lothe and D. Barnett. On the existence of surface-wave solutions for anisotropic elastic half-spaces with free surface. *Journal of Applied Physics*, 47(2):428–433, 1976.

[91] A. E. H. Love. *Some Problems of Geodynamics: Being the Essay to which the Adams Prize in the University of Cambridge was Adjudged in 1911.* CUP Archive, 1911.

[92] J.-F. Lu, B. Xu, and J.-H. Wang. Numerical analysis of isolation of the vibration due to moving loads using pile rows. *Journal of Sound and Vibration*, 319(3):940–962, 2009.

[93] S. Maiolino and M. P. Luong. Measuring discrepancies between coulomb and other geotechnical criteria: Drucker-prager and matsuoka-nakai. In *7th Euromech solid mechanics conference, Lisbon, Portugal*, pages 09–07, 2009.

[94] A. U. Manual. Abaqus theory guide, 2014.

[95] S. D. F. B. Manual. Unified facilities criteria (ufc). 2010.

[96] A. Maradudin and D. Mills. The attenuation of rayleigh surface waves by surface roughness. *Annals of Physics*, 100(1-2):262–309, 1976.

[97] D. Mašín. Clay hypoplasticity model including stiffness anisotropy. *Géotechnique*, 64(3):232–238, 2014.

[98] K. R. Massarsch. Vibration isolation using gas-filled cushions. In *Soil dynamics symposium in honor of professor Richard D. Woods*, pages 1–20, 2005.

[99] T. W. May and B. A. Bolt. The effectiveness of trenches in reducing seismic motion. *Earthquake Engineering & Structural Dynamics*, 10(2):195–210, 1982.

[100] R. MCNEILL, B. MARGASON, and F. BABCOCK. The role of soil dynamics in the design of stable test pads. In *Guidance Control Conference*, page 1239, 1965.

[101] D. Mendelsohn, J. Achenbach, and L. Keer. Scattering of elastic waves by a surface-breaking crack. *Wave motion*, 2(3):277–292, 1980.

[102] G. Miller, H. Pursey, and E. C. Bullard. On the partition of energy between elastic waves in a semi-infinite solid. *Proc. R. Soc. Lond. A*, 233(1192):55–69, 1955.

[103] R. Motamed, K. Itoh, S. Hirose, A. Takahashi, and O. Kusakabe. Evaluation of wave barriers on ground vibration reduction through numerical modeling in abaqus. In *Proceedings of the SIMULIA Customer Conference 2009*, pages 402–441, 2009.

[104] C.-C. Mow and Y.-H. Pao. The diffraction of elastic waves and dynamic stress concentrations. Technical report, RAND CORP SANTA MONICA CALIF, 1971.

[105] H. Nakano. On rayleigh waves. *Jap. J. Astr. Geophys.*, 2:1–94, 1925.

[106] H. Neumeuer. Untersuchungen uber die abschirmung eines bestehenden gebaudes gegen erschutterungen beim bau und betrieb einer u-bahnstrecke. *Baumaschine and Bautechnik-10, Jahrgang*, (1), 1963.

[107] A. Niemunis and I. Herle. Hypoplastic model for cohesionless soils with elastic strain range. *Mechanics of Cohesive-frictional Materials: An International Journal on Experiments, Modelling and Computation of Materials and Structures*, 2(4):279–299, 1997.

[108] A. V. Oppenheim. *Discrete-time signal processing*. Pearson Education India, 1999.

[109] M. Ostoja-Starzewski. Propagation of rayleigh, scholte and stoneley waves along random boundaries. *Probabilistic engineering mechanics*, 2(2):64–73, 1987.

[110] Y.-H. Pao and C. Mow. Scattering of plane compressional waves by a spherical obstacle. *Journal of Applied Physics*, 34(3):493–499, 1963.

[111] R. Paolucci and D. Spinelli. Ground motion induced by train passage. *Journal of engineering mechanics*, 132(2):201–210, 2006.

[112] G. Pflanz, K. Hashimoto, and N. Chouw. Reduction of structural vibrations induced by a moving load. *Journal of applied mechanics*, 5:555–563, 2002.

[113] W. Pilant, L. Knopoff, and F. Schwab. Transmission and reflection of surface waves at a corner: 3. rayleigh waves (experimental). *Journal of Geophysical Research*, 69(2):291–297, 1964.

[114] V. Podinovskii and V. Nogin. Pareto-optimal solutions of multicriteria problems. *Moscow: Sci*, 1982.

[115] S.-D. Poisson. Memoir on the theory of sound. *J. Ecole Polytech. Paris*, 7:319–370, 1808.

[116] S. D. Poisson. *Traité de mécanique*. Société belge de librairie, 1838.

[117] A.-R. public organization "Tunnel Association of Russia". Sp 23-105-2004. an assessment of vibration in the design, construction and operation of underground facilities. 2004.

[118] N. Puzyrev. *Methods and Objects of Seismic Investigations: Introduction to General Seismology*.

[119] B. Qiu. *Numerical study on vibration isolation by wave barrier and protection of existing tunnel under explosions*. PhD thesis, Lyon, INSA, 2014.

[120] P. Rajagopal, M. Drozdz, E. A. Skelton, M. J. Lowe, and R. V. Craster. On the use of absorbing layers to simulate the propagation of elastic waves in unbounded isotropic media using commercially available finite element packages. *NDT & E International*, 51:30–40, 2012.

[121] R. S. Rani, K. Prasad, and T. Krishna. Applicability of mohr-coulomb & drucker-prager models for assessment of undrained shear behaviour of clayey soils. *International Journal of Civil Engineering and Technology*, 5(10):104–123, 2014.

[122] F. E. Richart, J. R. Hall, and R. D. Woods. Vibrations of soils and foundations. 1970.

[123] K. Roscoe. Mechanical behaviour of an idealized'wet'clay. In *Proc. 3rd Eur. Conf. Soil Mech. Wiesbaden, 1963*, volume 1, pages 47–54, 1963.

[124] K. ROSCOE. On the generalized stress-strain behavior of wet clays. *Proceedings of Engineering Plasticity*, pages 535–609, 1968.

[125] K. H. Roscoe, A. Schofield, and C. Wroth. On the yielding of soils. *Geotechnique*, 8(1):22–53, 1958.

[126] R. K. Roy. *A primer on the Taguchi method.* Society of Manufacturing Engineers, 2010.

[127] A. Saikia. Numerical study on screening of surface waves using a pair of softer backfilled trenches. *Soil Dynamics and Earthquake Engineering*, 65:206–213, 2014.

[128] H. Schweiger. On the use of drucker-prager failure criteria for earth pressure problems. *Computers and geotechnics*, 16(3):223–246, 1994.

[129] H. B. Seed, R. T. Wong, I. Idriss, and K. Tokimatsu. Moduli and damping factors for dynamic analyses of cohesionless soils. *Journal of Geotechnical Engineering*, 112(11):1016–1032, 1986.

[130] G. Segol, J. F. Abel, and P. C. Lee. Amplitude reduction of surface waves by trenches. *Journal of the Engineering Mechanics Division*, 104(3):621–641, 1978.

[131] J.-F. Semblat, L. Lenti, and A. Gandomzadeh. A simple multi-directional absorbing layer method to simulate elastic wave propagation in unbounded domains. *International Journal for Numerical Methods in Engineering*, 85(12):1543–1563, 2011.

[132] J. F. Semblat and A. Pecker. Waves and vibrations in soils: earthquakes, traffic, shocks, construction works, 2009.

[133] J. Shen and A. A. Maradudin. Multiple scattering of waves from random rough surfaces. *Physical Review B*, 22(9):4234, 1980.

[134] T. Smirnova. Noise in the workplace, in residential, public buildings and residential areas.

[135] K. Sobczyk. Scattering of reyleigh waves at a random boundary of an elastic body. In *Proc. of Vibr. Probl*, volume 4, pages 363–374, 1966.

[136] B. Standard. Evaluation and measurement for vibration in buildings. *BS7385 Part*, 2, 1993.

[137] B. Standard. Eurocode 1: Actions on structures—, 2005.

[138] B. Standard. Eurocode 8: Design of structures for earthquake resistance". 2005.

[139] M.-m. Sun, C. Chen, W.-y. Chen, X. Ping, et al. Analysis on multiple scattering by an arbitrary configuration of piles as barriers for vibration isolation. *Soil Dynamics and Earthquake Engineering*, 31(3):535–545, 2011.

[140] D. Systémes. Abaqus theory guide. *Abaqus 6.13 Documentation*, 2013.

[141] M. Trifunac. Scattering of plane sh waves by a semi-cylindrical canyon. *Earthquake Engineering & Structural Dynamics*, 1(3):267–281, 1972.

[142] C. Truesdell and W. Noll. The non-linear field theories of mechanics. In *The non-linear field theories of mechanics*, pages 1–579. Springer, 2004.

[143] P.-h. Tsai, Z.-y. Feng, and T.-l. Jen. Three-dimensional analysis of the screening effectiveness of hollow pile barriers for foundation-induced vertical vibration. *Computers and Geotechnics*, 35(3):489–499, 2008.

[144] I. A. Viktorov. *Rayleigh and Lamb Waves: Physical Theory and Applications. Transl. from Russian. With a Foreword by Warren P. Mason.* Plenum press, 1967.

[145] J. Wang, W. Sun, and S. Anand. Numerical investigation on active isolation of ground shock by soft porous layers. *Journal of sound and vibration*, 321(3-5):492–509, 2009.

[146] M. Wojciechowski. A note on the differences between drucker-prager and mohr-coulomb shear strength criteria. *Studia Geotechnica et Mechanica*, 2018.

[147] H. Wong and M. Trifunac. Scattering of plane sh waves by a semi-elliptical canyon. *Earthquake Engineering & Structural Dynamics*, 3(2):157–169, 1974.

[148] R. D. Woods. Screening of suface waves in soils. 1968.

[149] R. D. Woods, N. E. Barnett, and R. Sagesser. Holography–a new tool for soil dynamics. *Journal of Geotechnical and Geoenvironmental Engineering*, 100(Proc. Paper 10949), 1974.

[150] R. D. Woods and F. E. Richart. *Screening of elastic surface waves by trenches*. University of Michigan, Department of Civil Engineering, 1967.

[151] G. Wu. *Finite element study of vibration isolation using an underground trench*. PhD thesis, Texas Tech University, 1997.

[152] S. R. Wu and L. Gu. *Introduction to the explicit finite element method for nonlinear transient dynamics*. John Wiley & Sons, 2012.

[153] Y.-B. Yang and H.-H. Hung. A parametric study of wave barriers for reduction of train-induced vibrations. *International Journal for Numerical Methods in Engineering*, 40(20):3729–3747, 1997.

[154] J. Zhang, R. D. Andrus, and C. H. Juang. Normalized shear modulus and material damping ratio relationships. *Journal of Geotechnical and Geoenvironmental Engineering*, 131(4):453–464, 2005.

[155] O. C. Zienkiewicz and R. L. Taylor. *The finite element method for solid and structural mechanics*. Elsevier, 2005.

[156] O. C. Zienkiewicz, R. L. Taylor, and R. L. Taylor. *The finite element method: solid mechanics*, volume 2. Butterworth-heinemann, 2000.